

# **Synthesis of metal-organic frameworks and monolithic composite materials for water sorption applications**

Inaugural-Dissertation

zur Erlangung des Doktorgrades  
der Mathematisch-Naturwissenschaftlichen Fakultät  
der Heinrich-Heine-Universität Düsseldorf

vorgelegt von

**Martin Wickenheisser**

aus Bonn

Düsseldorf, April 2015

aus dem Institut für Anorganische Chemie und Strukturchemie I  
der Heinrich-Heine-Universität Düsseldorf

Gedruckt mit der Genehmigung der  
Mathematisch-Naturwissenschaftlichen Fakultät der  
Heinrich-Heine-Universität Düsseldorf

Referent: Prof. Dr. Christoph Janiak

Korreferent: Prof. Dr. Christian Ganter

Tag der mündlichen Prüfung: 27.05.2015

Die vorliegende Arbeit wurde in der Zeit von März 2012 bis April 2015 an der Heinrich-Heine Universität Düsseldorf im Institut für Anorganische Chemie und Strukturchemie I im Arbeitskreis von Prof. Dr. Christoph Janiak angefertigt. Im November 2014 wurde ein Teil der praktischen Arbeiten an der Wuhan University of Technology (China) in der Arbeitsgruppe von Prof. Dr. Xiao-Yu Yang im Rahmen eines Austauschprogramms durchgeführt.

## Eidesstattliche Erklärung

Ich versichere an Eides statt, dass die Dissertation von mir selbstständig und ohne unzulässige fremde Hilfe unter der Beachtung der „Grundsätze zur Sicherung guter wissenschaftlicher Praxis“ an der Heinrich-Heine Universität Düsseldorf erstellt worden ist. Die aus fremden Quellen direkt oder indirekt übernommenen Gedanken sind als solche kenntlich gemacht. Die Arbeit wurde bisher weder im Inland noch im Ausland in gleicher oder ähnlicher Form einer anderen Prüfungsbehörde vorgelegt. Es wurden keine früheren erfolglosen Promotionsversuche unternommen.

.....

Ort, Datum

.....

Unterschrift

## Danksagung

Mein besonderer Dank gilt Herrn Prof. Dr. Christoph Janiak, der mir die Möglichkeit gegeben hat meine Dissertation in seinem Arbeitskreis anzufertigen. Weiterhin bedanke ich mich bei ihm für die interessante Themenvergabe, die zahlreichen Ideenanstöße und die nützlichen Diskussionen. Für das Korrekturlesen von Manuskripten und für die Zusammenarbeit in den Publikationen danke ich ihm sehr.

Herrn Prof. Dr. Christian Ganter danke ich recht herzlich für die freundliche Übernahme des Koreferates.

Meinem damaligen Masterstudenten, Sebastian Glomb, danke ich für die gemeinsame, sehr angenehme Zeit in Labor und Büro. Für die zahlreichen Gespräche und für den einen oder anderen lustigen Abend zwischen Hürth, Köln, Dormagen, Neuss oder Düsseldorf möchte ich mich bei dem Jung bedanken ;).

Ein weiterer großer Dank geht an Tanja Paul, die ich während ihrer Bachelorarbeit betreut habe. Die tolle gemeinsame Zusammenarbeit und die Kaffeegespräche werde ich stets in Erinnerung behalten!

Natürlich möchte ich mich auch bei einigen Mitarbeitern für das angenehme Arbeitsklima, die nette Zeit und die Mithilfe bei Messungen für das Zustandekommen meiner Doktorarbeit recht herzlich bedanken. Bei Frau Schäfer möchte ich mich recht herzlich für ihre nette Hilfe bei organisatorischen Fragestellungen bedanken. Hajo Meyer danke ich für die schönen Motorradtouren durchs Bergische Land oder durch die Eifel. Für die erfolgreiche Zusammenarbeit im Xerogel-Projekt gilt ein besonderer Dank an Annika Herbst. Bei Raquel Marcos Esteban bedanke ich mich herzlich für die lustigen Bahngespräche, welche die Zeit des Pendelns schneller vergingen ließ. Subarna Dey danke ich für das tolle Chicken Curry Rezept. Für die AAS Messungen und den REM Aufnahmen bedanke ich mich ebenfalls bei Annette Ricken und Steffen Köhler. Ein weiterer Dank geht auch an Janina Dechnik, Kai Schütte, Dennis Dietrich, Anna Christina Kautz und Christina Rutz, die dafür sorgten, dass die Zeit wie im Flug verging ;).

Meinen Eltern und meiner Schwester danke ich für die seelische und finanzielle Unterstützung und dafür, dass Ihr stets an mich geglaubt habt.

Mein allergrößter Dank geht an meine liebe Freundin Svenja Theele, die immer ein Ohr für mich hatte, auch wenn mal etwas nicht gut lief. Für die tolle und liebevolle Unterstützung bedanke ich mich bei Ihr von ganzem Herzen. Unsere schönen gemeinsamen Urlaube und das Tanzbeinschwingen auf dem Parkett, sorgten stets für den perfekten Ausgleich. Dankeschön für Alles ☺!

## Kurze Zusammenfassung

Metallorganische Gerüstverbindungen (MOFs) wurden in den letzten Jahren als Adsorbentien für zyklische Wasserad- und desorptionvorgänge für potentielle Wärmetransformations-anwendungen umfassend erforscht. Trotz ihrer vielen Vorteile gegenüber klassischen Adsorbentmaterialien wie Silikagele oder Zeolithe, bleiben die Wasseraufnahmekapazitäten besonders bei geringem bis mittlerem Feuchtigkeitsgehalt vergleichsweise gering. Als zukünftiges Adsorbentmaterial in Wärme/Kältemaschinen muss die Wasseraufnahme im Partialdruckbereich von  $0.05 < P \cdot P_0^{-1} < 0.35$  durch eine Steigerung des hydrophilen Charakters des MOFs durch chemische Modifizierungen erhöht werden.

Zwei Vertreter aus der Klasse der MIL-MOFs (MIL = Matériaux de l'Institut Lavoisier), MIL-100(Cr) und MIL-101(Cr) wurden wegen ihrer ausgeprägten Wasserstabilität ausgewählt und postsynthetisch durch Substitution der terminal gebundenen Wassermoleküle durch hydrophile Glykole und Amine an den koordinativ ungesättigten Metallzentren modifiziert. Diese Art der postsynthetischen Modifikation wird auch als „Grafting“ bezeichnet. Trotz des starken Verlustes der BET-Oberflächen und der Gesamtporenvolumina der modifizierten MILs zeigen MIL-100(Cr)-EG, MIL-100(Cr)-DEG und MIL-100(Cr)-EN (EG = Ethylenglycol, DEG = Diethylenglycol, EN = Ethylendiamin) fast unveränderte Wasseraufnahmekapazitäten mit einer leicht bevorzugten Wasseraufnahme im Druckbereich von  $0.17 < P \cdot P_0^{-1} < 0.30$  im Vergleich zu nicht modifiziertem MIL-100. Die zugehörigen Wasseradsorptionsisothermen konnten zu niedrigeren Partialdrücken verschoben werden. Die hohen Wasserbeladungen und die ausgeprägte Verringerung der inneren BET-Oberflächen können nur dadurch erklärt werden, dass die Größe der MIL-100 Poren nicht der ausschlaggebende Faktor für hohe Wasseraufnahmekapazitäten ist. Ethylendiamin weist eine stabilere Bindung gegenüber Chrom(III) auf als die entsprechenden Glykole, jedoch zeigt ein zyklischer Ad- und Desorptions-Stabilitätstest von MIL-100(Cr)-EN, dass eine mögliche Anwendung auf Grund teilweiser Zersetzung kritisch betrachtet werden muss.

Die Formgebung von metallorganischen Gerüstverbindungen in mechanisch stabile und handhabbare Körper ist ein weiterer wichtiger Schritt für zukünftige Anwendungen von MOFs. Auf Grund der Nachteile eines möglichen MOF-Adsorbent in Pulverform ist es notwendig diese in eine handhabbare Form (z.B. Monolithe) zu überführen. Solche Polymere können beispielweise der Klasse der „high internal phase emulsions“ (HIPEs) oder der „Xerogele“ angehören.

Eine Reihe wasserstabiler MOFs wurden daher in poröse, organische und anorganische Polymere/Bindemittel eingebettet, welche in der Lage sind, monolithische Körper auszubilden.

MOFs des MIL-Typs, MIL-100(Fe,Cr) und MIL-101(Cr), wurden in poröses Si(HIPE), poly(HEMA)HIPE (HEMA = 2-Hydroxyethylmethacrylat), poly(NIPAM)HIPE (NIPAM = *N*-Isopropylacrylamid) und einem Xerogel, basierend auf Resorcin und Formaldehyd, über zwei unterschiedliche Syntheserouten eingebettet: Erstens über die direkte Route (Route A), in der das aktivierte MIL-Pulver während der Synthese des porösen Polymeres diesem direkt vor Aushärtung hinzugefügt wurde. Die zweite *in situ* Route (Route B) beschreibt die *in situ* Kristallisation von MOF-Partikeln direkt in den Poren des polymeren Bindemittels. Die Synthese der MIL@Si(HIPE) Komposite erwies sich als problematisch auf Grund der starken Kontraktion während des Trocknungsprozesses. Komposite konnten nur in granulierter Form oder als Monolithe mit starken Rissen, und kleinen BET-Oberflächen erhalten werden. Bei den MIL@poly(NIPAM)HIPE Kompositen führte die ausgeprägte Kontraktion zu deformierten Materialien, obwohl hier gezeigt werden konnte, dass das Vorpolymerisieren der HIPE Emulsion vor Zugabe der MIL-Pulver bei der direkten Syntheseroute zu Kompositen mit höheren inneren Oberflächen führt.

Poly(HEMA)HIPE und R,F-Xerogel erwiesen sich als die am besten geeigneten Kandidaten für die Synthese von monolithischen Kompositen mit hohen MOF Beladungen. Sowohl die reinen Polymere als auch die Komposite zeigen nur eine vernachlässigbar kleine Kontraktion durch gewöhnliches Trocknen im Ofen unter Ausbildung von mechanisch stabilen Monolithen. Porenblockierung der MIL-Poren durch HIPE oder Xerogel-Monomere konnte bei der direkten Route durch Vorpolymerisieren des Bindemittels weitestgehend verhindert werden. Es konnten zwar auch monolithische MIL@HEMA Komposite über die *in situ* Methode dargestellt werden, diese zeigen jedoch im Vergleich zu den Materialien, die über den direkten Weg erhalten wurden, geringere BET-Oberflächen. Dampfsorptionsmessungen zeigten, dass MIL@HEMA Komposite auf Grund des eher hydrophoben Charakters des reinen poly(HEMA)HIPE, die Adsorption von Methanoldampf gegenüber von Wasserdampf bevorzugen. Reine R,F-Xerogele weisen im Vergleich zu reinem poly(HEMA)HIPE einen stärker hydrophilen Charakter auf, welcher die hohen Wasserbeladungen der MIL@R,F-Xerogele erklärt.



## Short summary

Metal-organic frameworks (MOFs) have been well investigated as adsorbents for cyclic water ad-, desorption processes in potential heat transformation applications during the last years. In spite of their advantages over traditional adsorbents, the total water uptakes remain comparably low in environments of low to medium humidity. For intended practical applications, the water loading lifts have to be maximized in the partial pressure range of  $0.05 < P \cdot P_0^{-1} < 0.35$  through increasing the hydrophilic nature of MOFs by chemical modifications.

Two water stable MOFs of the MIL-family ((MIL = Matériaux de l'Institut Lavoisier)), MIL-100(Cr) and MIL-101(Cr) were chosen and post-synthetically modified by substitution of terminal, coordinated water molecules through hydrophilic glycols and amines, so-called 'grafting', at their coordinatively unsaturated metal sites. In spite of the decrease of the BET surface areas and total pore volumes of the modified MILs, MIL-100(Cr)-EG, MIL-100(Cr)-DEG and MIL-100(Cr)-EN (EG = ethylene glycol, DEG = diethylene glycol, EN = ethylenediamine) showed almost unchanged water loading capacities with slightly favored water uptakes in the range of  $0.17 < P \cdot P_0^{-1} < 0.30$  compared to non-modified MIL-100. The corresponding water adsorption isotherms could be shifted to lower partial pressures, accompanied with a higher slope of the adsorption isotherms in comparison to bulk MIL-100(Cr). The high water loading lifts in combination with the decrease of the surface areas can only be explained by the fact that the size of the MIL-100 pores is not the essential factor for high water uptakes. Ethylenediamine has shown a more stable bonding towards chromium(III) over glycols, but an ad-, desorption cycling stability test of MIL-100(Cr)-EN have shown that a practical application has to be critically regarded due to some degradation.

We also focused on shaping of metal-organic frameworks into mechanically stable and manageable bodies due to the disadvantages of the powdery appearance of MOFs (e.g. dust problems). Shaping of MOFs into a more utilizable form, like monoliths, is an indispensable requirement for potential applications like heat transformation purposes.

Therefore, different, water stable MOFs were embedded into porous organic and inorganic polymers (so-called binding agents), which can be manufactured in monolithic shape. These polymers can either be synthesized by high internal phase emulsions (HIPEs) or by xerogels.

MOFs of the MIL-type such as MIL-100(Fe,Cr) and MIL-101(Cr) were incorporated into porous Si(HIPE), poly(HEMA)HIPE (HEMA = 2-hydroxyethyl methacrylate), poly(NIPAM)HIPE (NIPAM = *N*-Isopropylacrylamide) and a xerogel, based on resorcinol and formaldehyde, through two different synthetic approaches: Firstly, the direct route, 'Route A', whereas activated MIL powders were added to the binding agents before curing and secondly an *in situ* route, 'Route B', in which MOF particles were *in situ* grown in the pores of monolithic polymers. The syntheses of MIL@Si(HIPE) composites has turned out to be problematic due to large shrinking effects during the drying process. Composites could only be obtained in granulated shape or monoliths with big cracks and relative low surface areas. MIL@poly(NIPAM)HIPE materials were also largely deformed during drying, although it could be shown that porous composites were obtained using the direct route, if the HIPE emulsion was highly pre-polymerized before addition of the powdery MILs.

Only poly(HEMA)HIPE and R,F-xerogel have shown to be the most suitable candidates for monolithic composites with high MOF loadings. Pure polymers as well as the composite materials show negligible shrinking effects by conventional oven drying, resulting in mechanically stable monoliths. Pore blocking effects of the MIL pores by HIPE or xerogel monomers could be largely avoided in the direct route by pre-polymerization of the binding agents. Monolithic MIL@HEMA composites could also be synthesized by the *in situ* route, but this method yielded less porous materials in comparison to the direct route. Vapor sorption experiments have shown that MIL@HEMA composites favor the adsorption of methanol vapor over water due to the rather hydrophobic nature of the pure poly(HEMA)HIPE. Native R,F-xerogel reveals a more hydrophilic character in comparison to native poly(HEMA)HIPE, which explains the high water loading lifts in MIL@R,F-xerogels.

## List of abbreviations and symbols

AAS	Atomic absorption spectrometry
AHP	Adsorption heat pump
APS	Ammonium persulfate
ATR	Attenuated total reflection
bar	Unit of pressure (1 bar $\cong$ 100000 Pa $\cong$ 100 kPa)
BDC	1,4-Benzenedicarboxylate
BET	Brunauer-Emmett-Teller
BTC	1,3,5-Benzenetricarboxylate
cC <sub>6</sub>	Cyclohexane
CUS	Coordinatively unsaturated (metal) sites
d	Day(s)
DEG	Diethylene glycol
DETA	Diethylenetriamine
DMF	<i>N,N'</i> -Dimethylformamide
EG	Ethylene glycol
EN	Ethylenediamine
EtOH	Ethanol
Fig.	Figure(s)
FT-IR	Fourier transform infrared
GM	Gravimetical quantification
h	Hour(s)
HEMA	2-Hydroxyethyl methacrylate
HIPE(s)	High internal phase emulsion(s)
IUPAC	International Union of Pure and Applied Chemistry
K	Degree Kelvin
mA	(Milli)ampere
MBA	<i>N,N'</i> -Methylenebisacrylamide
mg	(Milli)gram
MIL	Matériaux de l'Institut Lavoisier
min	Minute(s)
mL	Milliliter(s)
mm	Millimeter(s)
(m)mol	(Milli)mol, unit of amount of substance (1 mol $\cong$ 6.022·10 <sup>23</sup> particles)
MOF	Metal-organic framework
NIPAM	<i>N</i> -Isopropylacrylamide

NL(DFT)	(Nonlocal) density functional theory
nm	Nanometer(s)
NMR	Nuclear Magnetic resonance
p	Pressure
pp-	Pre polymerized-
(P)XRD	(Powder) X-ray diffraction
r.t.	Room temperature
R,F-xerogel	Resorcinol-formaldehyde based xerogel
Route A <sup>1</sup>	Direct synthesis by adding pre-formed MOFs during synthesis of porous templates
Route B	<i>In situ</i> synthesis of MOFs into pre-formed porous templates
s	Second(s)
SBU	Secondary building unit
SEM	Scanning electron microscopy
TDC	Thermally driven adsorption chiller
TEG	Triethylene glycol
TEOS	Tetraethyl orthosilicate
TETA	Triethylenetetramine
TGA	Thermogravimetric analysis
TMAOH	Tetramethylammonium hydroxide
TMEDA	<i>N,N,N',N'</i> -Tetramethylethylenediamine
TTAB	Tetradecyltrimethylammonium bromide
VBC	4-Vinylbenzyl chloride
wt%	Weight percentage (weight%)
Å	Ångström
$\delta$	Delta (stands for chemical shift)
$\theta$	Theta (stands for (i) surface coverage, e.g. in the Langmuir equation or (ii) angle of diffracted wave, e.g. in the Bragg's equation)
$\lambda$	Lambda (stands for wavelength)
$\mu\text{m}$	Micrometer(s)
$\nu$	Nu (stands for wavenumber)
$\rho$	Rho (stands for density)

---

<sup>1</sup> Route A and B refer to the syntheses of the monolithic composite materials. Porous templates studied in this work are either HIPE materials [Si(HIPE), HEMA(HIPE) and NIPAM(HIPE)] or R,F-xerogels.

## Table of contents

Eidesstattliche Erklärung .....	I
Danksagung .....	II
Kurze Zusammenfassung.....	IV
Short summary.....	VI
List of abbreviations and symbols.....	VIII
1. Introduction .....	1
1.1 Basic theory of gas adsorption .....	2
1.1.1 General definitions and terminology.....	2
1.1.2 Types of physisorption isotherms .....	5
1.1.3 Mathematical models of sorption isotherms.....	7
1.1.3.1 Langmuir model .....	7
1.1.3.2 BET model.....	8
1.2 Water adsorption in porous materials.....	10
1.2.1 Silica gels .....	12
1.2.2 Silica aerogels .....	14
1.2.3 Zeolites.....	15
1.2.4 Aluminophosphates (AIPO), silica-aluminophosphates (SAPO).....	17
1.2.5 Other mesoporous materials .....	18
1.3 Metal-organic frameworks for diverse applications.....	19
1.3.1 Concepts and properties of MOFs .....	19
1.3.2 Post-synthetic modification in metal-organic frameworks.....	22
1.3.3 Water adsorption in MOFs for heat pump applications .....	27
1.4 Metal-organic framework composites for various applications.....	36
1.4.1 Pure binding agents.....	37
1.4.1.1 High internal phase emulsions (HIPES) .....	37
1.4.1.2 Aero-/Xerogels based on resorcinol and formaldehyde .....	39
1.4.2 Polymeric MOF composites.....	41
2. Assignment of tasks .....	45

3. Cumulative part .....	47
3.1 Grafting of hydrophilic ethylene glycols or ethylenediamine on coordinatively unsaturated metal sites in MIL-100(Cr) for improved water adsorption characteristics .....	48
3.2 Hierarchical embedding of micro-mesoporous MIL-101(Cr) in macroporous poly(2-hydroxyethyl methacrylate) for high internal phase emulsions with monolithic shape for vapor adsorption applications .....	67
3.3 Hierarchical MOF-xerogel monolith composites from embedding MIL-100(Fe,Cr) and MIL-101(Cr) in resorcinol-formaldehyde based xerogels for water adsorption applications .....	96
4. Unpublished work .....	148
4.1 Grafting of MIL-101(Cr) with ethylene glycols.....	148
4.2 Meso-/Macroporous Si(HIPE) .....	152
4.2.1 MIL-101(Cr)@Si(HIPE) (Route A).....	156
4.2.2 MIL-100(Cr)/101(Cr)@Si(HIPE) (Route B).....	160
4.3 Macroporous Poly(HEMA)HIPE .....	165
4.3.1 MIL-100(Fe,Cr)/101(Cr)@HEMA (Route B) .....	168
4.4 Macroporous Poly(NIPAM)HIPE .....	175
4.4.1 MIL-100(Fe,Cr)/101(Cr)@NIPAM (Route A) .....	179
4.5 Experimental part.....	189
4.5.1 General section .....	189
4.5.2 Analytical methods .....	192
4.5.2.1 Powder X-ray diffraction (PXRD).....	192
4.5.2.2 Fourier transform infrared spectroscopy (FT-IR) .....	192
4.5.2.3 Nitrogen, water and methanol sorption analyses.....	192
4.5.2.4 Water cycling measurement.....	193
4.5.2.5 NMR spectroscopy.....	193
4.5.2.6 Scanning electron microscopy .....	193
4.5.2.7 Thermogravimetric analyses .....	194
4.5.2.8 Atomic absorption spectrometry .....	194
4.5.3 Syntheses.....	195
4.5.3.1 Syntheses of MIL-101(Cr)-x, x = EG, DEG, TEG.....	195

4.5.3.2 Synthesis of meso-/macroporous Si(HIPE) .....	195
4.5.3.3 Syntheses of MIL-101(Cr)@Si(HIPE) composites via route A .....	196
4.5.3.4 Syntheses of MIL-100(Cr)/101(Cr)@Si(HIPE) composites via route B .....	198
4.5.3.5 Synthesis of macroporous Poly(HEMA)HIPEs .....	199
4.5.3.6 Syntheses of MIL-100(Fe,Cr)/101(Cr)@HEMA composites via route B.....	200
4.5.3.7 Synthesis of macroporous Poly(NIPAM)HIPEs .....	202
4.5.3.8 Syntheses of MIL-100(Fe,Cr)/101(Cr)@NIPAM composites via route A.....	203
5. Summary .....	205
5.1 Grafting of MIL-100(Cr) and MIL-101(Cr) .....	205
5.2 MIL@Si(HIPE) .....	207
5.3 MIL@Poly(HEMA)HIPE .....	209
5.4 MIL@Poly(NIPAM)HIPE .....	211
5.5 MIL@R,F-Xerogel.....	213
5.6 Overall summary .....	215
6. Outlook.....	217
6.1 Water sorption based applications .....	217
6.2 Other applications.....	219
7. References.....	220

# 1. Introduction

The introductory section of this thesis gives the reader an understanding beginning of basic principles and fundamentals of gas adsorption up to current research studies, which are essential in the context of this work.

Section 1.1 describes the basic theory of gas adsorption. Herein essential terms, physical processes, gas sorption isotherm types and important mathematical models are shortly introduced. In section 1.2 the adsorption processes in porous materials are extended onto water vapor. Typical well-studied porous compounds such as silica gels, zeolites, silica aerogels or aluminophosphates are presented concerning their water sorption characteristics. Concepts, properties and water adsorption in metal-organic frameworks and the usage of MOFs as potential adsorbents for heat transformation applications are exposed in section 1.3. A selection of well examined MOFs is presented together with an analysis of advantages and disadvantages over traditional porous water adsorbents. Furthermore, metal-organic frameworks can be post-synthetically modified, which allows a fine-tuning of the chemical and porous nature of these hybrid materials. The last section 1.4 of the introduction presents the chemistry of MOF composite materials, using an additional second component. The usage of a second component, or binding agent, is often accompanied with shaping effects of the original powdery MOF particles into monoliths, beads, fibers or membranes. Chemical and physical properties of these MOF composites are introduced together with an overview of possible applications.



## 1.1 Basic theory of gas adsorption

### 1.1.1 General definitions and terminology

Gas adsorption processes of pure as well as mixed gases on porous solid materials are of growing importance and interest in science and industrial fields.<sup>1-3</sup> A growing number of chemical, biochemical and petrochemical applications are based on gas adsorption processes. The most important are: gas separation processes,<sup>4-7</sup> drying of gases and solids,<sup>8</sup> cleaning processes of air and water,<sup>9,10</sup> adsorption based energetic processes and air conditioning refrigerating techniques,<sup>11,12</sup> gas storage<sup>13</sup> and characterization of porous solid materials.<sup>14</sup>

This section contains an overview of the theory of gas adsorption and is projected to give the reader a basic understanding of adsorption chemistry. It is not intended to be a comprehensive tract. For a detailed in-depth treatment of this topic, the reader is referred to other literature.<sup>15</sup>

Sticking of molecules of gases or liquids onto a solid (or in some cases a liquid) surface is called **adsorption**. **Adsorption** should not be confused with **absorption**, in which gaseous or liquid molecules are dissolved in another liquid or solid material. Adsorption phenomena occur in principle at any temperature and pressure and for all chemical species known so far.<sup>4,14,16</sup> The adsorbed molecules can return to the gaseous phase, which is called desorption. In many cases, one can observe a dynamic equilibrium between the rates of adsorption- and desorption processes. Such a situation is called adsorption equilibrium. In figure 1 a schematic illustration of an adsorption system is shown. The following essential terms have to be defined in advance:

*Adsorptive:* Gaseous or liquid molecules, which have not been adsorbed onto the surface yet.

*Adsorbent:* (Porous) solid phase with external or internal surface, which is exposed to the gaseous or liquid molecules.

*Adsorbate:* Two component system, consisting of the solid adsorbent and the adsorbed molecules.<sup>11</sup>

---

<sup>11</sup> The term 'adsorbate' can also be referred to the sole molecules in the adsorbed state.

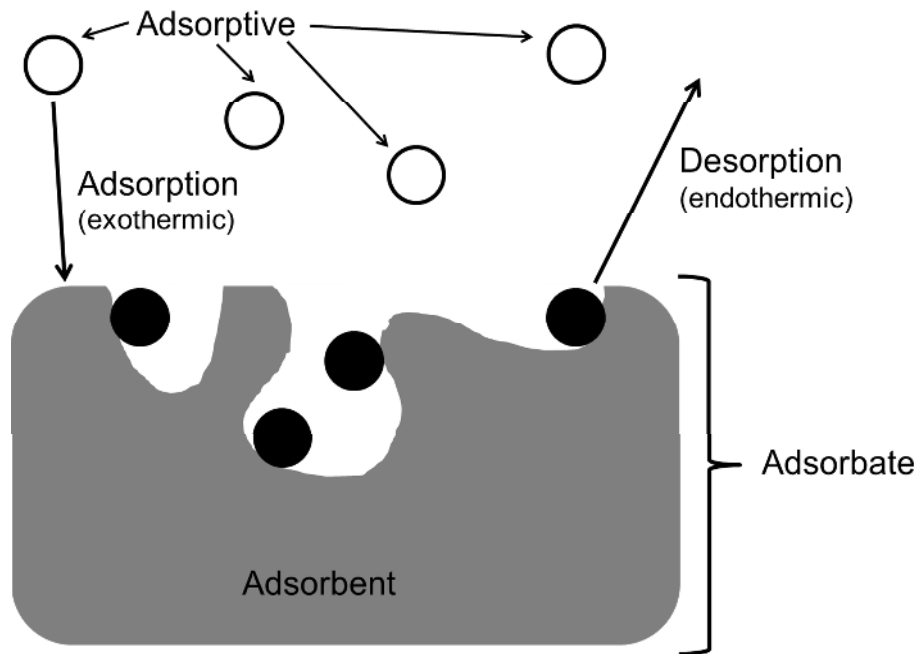


**Fig. 1.** Adsorption system of a gas (adsorptive), a (porous) solid phase (adsorbent) and the adsorbate, which describes a complex consisting of the adsorbent and the adsorbed gas molecules. Adsorption is an exothermic, desorption an endothermic thermodynamic process.

Depending on the strength or binding energy by which molecules are bound onto a surface, one can differentiate between chemisorption, physisorption phenomena and capillary condensation.<sup>6,17,18</sup>

In *chemisorption* molecules are strongly bound to the adsorbent and desorption from the surface is an energy-demanding process. Strong, irreversible binding between adsorbent and adsorptive via covalent bonds exists with binding energies of 60–450 kJ·mol<sup>-1</sup>.<sup>19</sup> Due to the covalent bonds, only monolayer adsorption is obtained. For the gas phase the following correlation can be assumed:<sup>4</sup>

*Chemisorption:* Binding energy > 2–3 enthalpy of evaporation of adsorptive

In *physisorption* molecules are bound by relatively weak interactions as van der Waals- and dispersion forces due to (induced) dipole-dipole interactions. Desorption can take place reversibly by lowering the sorptive gas pressure or enhancing the temperature. Physisorption phenomena are characterized by low binding energies of <50 kJ·mol<sup>-1</sup>.<sup>19</sup> Physisorbed molecules generally tend to form a monolayer on the surface, which can interact further with additional adsorptives to form multilayers. Binding energies are slightly above the enthalpy of evaporation of the adsorptive for gas phase processes:<sup>4</sup>

*Physisorption:* Binding energy ≈ 1.5 enthalpy of evaporation of adsorptive

A third mechanism, the capillary condensation, can also occur in the gas phase. It describes a classical phase transition from the gaseous to the liquid phase in the capillaries of the adsorbent. This effect does not occur until all adsorption sites are occupied and multilayer adsorption has come to an advanced state. Interactions between the adsorbent and the adsorptive play a minor role compared to the interactions of the adsorptive molecules among each other. Binding energies and the enthalpy of evaporation are of the same magnitude.

*Capillary condensation:* Binding energy  $\approx$  enthalpy of evaporation of adsorptive

In this work only physisorption phenomena and capillary condensation effects appear during the sorption procedure. It is convenient to characterize the pores of the porous adsorbent according to their sizes:

- (i) *Micropores* are pores with diameters not exceeding 20 Å (= 2 nm).
- (ii) Pores with diameters of 20–500 Å (2 – 50 nm) are called *mesopores*.
- (iii) *Macropores* have diameters exceeding 500 Å (= 50 nm).

Porous solids can be characterized by gas adsorption studies. For the evaluation of the porosity of solid materials, nitrogen (N<sub>2</sub>) at 77 K is the most appropriate adsorptive gas. The free and adsorbed gas can be described as a dynamic equilibrium, in which the *surface coverage* ( $\theta$ ) is defined in Formula 1:

$$\theta = \frac{\text{Number of occupied adsorption sites}}{\text{Number of available adsorption sites}}$$

**Formula 1.** Definition of surface coverage  $\theta$ .

The surface coverage is dependent on the partial pressure of the free gas. The shape of  $\theta$  as a function of the partial pressure of the gaseous phase at a constant temperature is called *adsorption isotherm*.

### 1.1.2 Types of physisorption isotherms

Based on the early work by Brunauer et al. in 1940, in which five types of adsorption isotherms are introduced, recommendations on the definition of adsorption isotherm types were treated by an IUPAC report in 1985 with the extension to a sixth type.<sup>20,21</sup> A new IUPAC task group has recently been assembled with revising this 1985 report to update classifications of pore size and isotherm types. This publication is not yet available but should be published in 2015.<sup>22</sup> Within the scope of this work, we will refer to the 1985 classifications of adsorption isotherms by Sing et al. as shown in figure 2.<sup>21</sup>

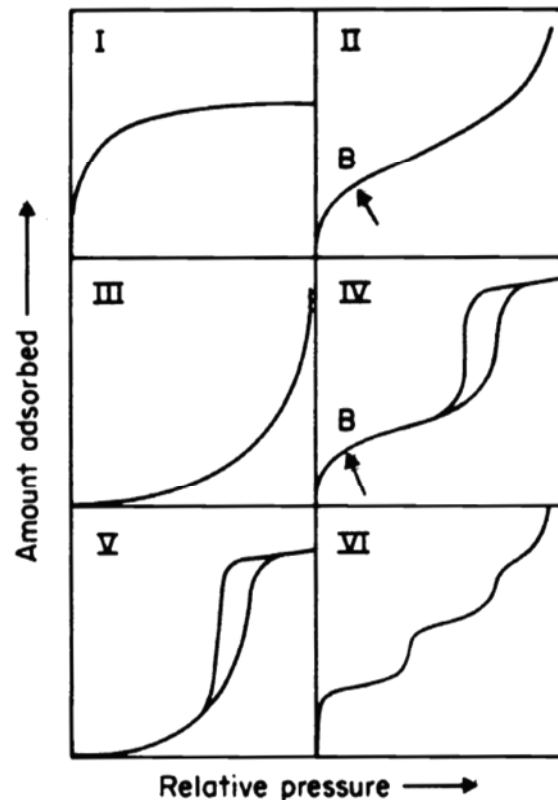


**Fig. 2.** Main types of physisorption isotherms (IUPAC). Reprinted from ref. 21, Copyright 1985, with permission from De Gruyter.

Three isotherm types (I, II, III) describe reversible processes. The type I isotherm is concave to the  $P \cdot P_0^{-1}$  axis and saturation of the adsorbed amount of gas is reached when  $P \cdot P_0^{-1}$  approaches 1 with an almost linear rise at the initial part. Type I isotherms are obtained when adsorption is limited, e.g. for chemisorption processes. If only physical adsorption occurs, the adsorbents are of microporous nature and only monolayer adsorption takes place with relatively strong interactions between adsorbent and adsorbed particles. Filling of the micropores and therefore high gas uptakes are observed at low relative pressures due to the narrow pore width and the high adsorption potential. Adsorption processes of water on zeolites follow a type I shape.<sup>23</sup>

Type II sorption isotherms are normally obtained for non-porous or macroporous materials, where unlimited multilayer adsorption can develop. The knee of type II isotherms is called point B, where a complete filling of the monolayer is indicated and multilayer adsorption starts.

Sorption isotherms of type III are convex to the  $P/P_0^{-1}$  axis. Attractive interactions between adsorbed particles and the adsorbent are relatively weak and the interactions of adsorbed gases or molecules among each other play a major role. Type III isotherms are rather uncommon, but there are some examples, e.g. nitrogen on polyethylene.

Mesoporous adsorbents typically show an irreversible type IV sorption behavior. The most characteristic feature is the hysteresis loop, which is induced by capillary pore condensation in the mesopores. Complete pore filling is reached at high relative pressures, which results in a plateau of the sorption isotherm. The primary part of a type IV isotherm follows a type II shape according to multilayer adsorption. The sorption of water vapor on silica gel follows a type IV shape.<sup>24</sup>

Type V isotherms are featured by pore condensation effects similar to type IV sorption isotherms but the initial part reflects relatively weak interactions between the porous materials and the adsorbed particles as shown for type III. Water-vapor adsorption on activated carbons shows a type V sorption isotherm.<sup>24,25</sup>

The IUPAC task group added a sixth type of sorption isotherm in 1985 (type VI), which is described by a stepwise multilayer adsorption on a non-porous, homogeneous surface. Typical examples of this type are argon or krypton adsorbed on graphitized carbon black at 77 K.

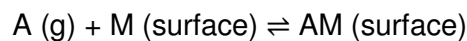
## 1.1.3 Mathematical models of sorption isotherms

### 1.1.3.1 Langmuir model

One of the simplest mathematical descriptions for sorption isotherms was derived by Irving Langmuir in 1918.<sup>26</sup> The Langmuir equation is based on the following assumptions:

- (i) All adsorption sites are energetically equal.
- (ii) All adsorption sites can be occupied.
- (iii) There are no interactions between adsorptives among each other.
- (iv) The fluid phase can be described as an ideal gas.
- (v) Only monolayer coverage occurs (no capillary condensation).

The following dynamic equilibrium exists between gas molecules 'A' and the surface 'M':



The rate of change of the surface coverage  $\theta$  for the adsorption process is directly proportional to the partial pressure of A ' $p_A$ ' and to the amount of free adsorption sites ' $N(1-\theta)$ ' on the surface 'M'. The number of all adsorption sites is given by 'N'. The rate constants for ad- and desorption are described by ' $k_{Ad}$ ' and ' $k_{Des}$ '.

$$\frac{d\theta}{dt} = k_{Ad}p_A N(1 - \theta)$$

A similar description can be given for the desorption process. Herein, the rate of change of the surface coverage  $\theta$  is proportional to the number of adsorbed gas molecules ' $N\theta$ '.

$$\frac{d\theta}{dt} = -k_{Des}N\theta$$

If the dynamic equilibrium is reached, the rate of adsorption is equal to the rate of desorption. From this, the Langmuir equation can be expressed as:

$$\theta = \frac{Kp_A}{1 + Kp_A} \text{ with } K = \frac{k_{Ad}}{k_{Des}}$$

**Formula 2.** Langmuir equation.

Type I sorption isotherms can be described by the Langmuir equation (Formula 2).

### 1.1.3.2 BET model

The most famous mathematical method for the determination of a specific surface area of porous solids is based on the so-called 'Brunauer-Emmett-Teller' (BET) model. In 1938 Brunauer, Emmett and Teller derived an equation in which the surface area of porous materials can be calculated from the weight of adsorbed gas molecules constituting a monolayer of surface coverage ' $W_m$ ',<sup>27</sup>

The BET model is based on the Langmuir model with further assumptions:

- (i) Adsorption is localized.
- (ii) Multilayer adsorption can occur.
- (iii) The surface is homogeneous.
- (iv) The heat of adsorption of the first monolayer is independent from the surface coverage  $\theta$ .
- (v) The heat of adsorption of further multilayers corresponds to the heat of condensation of adsorbed gas molecules.
- (vi) There are no interactions between adsorbed particles among each other.

The BET equation (Formula 3) is often displayed in the linearized form where ' $W$ ' is the weight of the adsorbed gas at a relative pressure  $P \cdot P_0^{-1}$ . ' $W_m$ ' is the weight of adsorbed gas molecules, which cover the monolayer of the surface. The BET ' $C$ ' constant is related to the energy of adsorption in the monolayer and its value indicates the magnitude of the interaction between adsorbed gas molecules and adsorbent.

$$\frac{1}{W \left( \left( \frac{P_0}{P} \right) - 1 \right)} = \frac{1}{W_m} + \frac{C - 1}{W_m C} \left( \frac{P}{P_0} \right)$$

**Formula 3.** Linearized BET equation.

Traditionally nitrogen gas is used at 77 K for the determination of the BET surface area from the gas sorption isotherms. The BET model should only be applied on type II (non-porous) and type IV (mesoporous) sorption isotherms and is theoretically not valid for type I (microporous) and type III isotherms. The BET equation requires a linear plot of  $1/[W(P_0 \cdot P^{-1}) - 1]$  against  $P \cdot P_0^{-1}$  usually in the linear region of  $0.05 < P \cdot P_0^{-1} < 0.30$ . ' $W_m$ ', the

weight of adsorbed gas molecules in the monolayer, can be calculated from the slope 's' and the intercept 'i' of the linear BET plot:

$$s = \frac{C - 1}{W_m C}; \quad i = \frac{1}{W_m C}$$

The weight of the monolayer ' $W_m$ ' can therefore be obtained by combining the equations for the slope 's' and the intercept 'i'.

$$W_m = \frac{1}{s + i}$$

From ' $W_m$ ', it is possible to calculate the total surface area ' $S_t$ ' (Formula 4, left). ' $N_A$ ' is the Avogadro constant and ' $M$ ' the molar mass of the adsorbed gas (nitrogen). ' $A_{cs}$ ' is the cross-sectional area for nitrogen. For a hexagonal close packed nitrogen monolayer at 77 K, ' $A_{cs}$ ' is  $16.2 \text{ \AA}^2$ . The specific surface area ' $S$ ' can be obtained from ' $S_t$ ' by dividing it by the weight of the sample mass ' $w$ ' (Formula 4, right).

$$S_t = \frac{W_m N_A A_{cs}}{M}; \quad S = \frac{S_t}{w}$$

**Formula 4.** Calculation of the total surface area ' $S_t$ ' (left) and the specific surface area ' $S$ ' (right).



## 1.2 Water adsorption in porous materials

Water adsorption in porous materials is essential for many kinds of applications in dehumidification, delivery of fresh drinking water by attraction/removing of contaminants or as adsorption-driven heat exchangers for the usage in air-conditioning devices.<sup>28–30</sup> In the focus of this work, the latter application is discussed in detail.

Before the discussion of the relatively new members of porous materials (MOFs) for heat transformation applications in section 1.3, the reader is given a short overview of the water sorption properties of traditional, porous, inorganic materials in this section: Silica gels, silica aerogels and zeolites. Aluminophosphates (AlPOs) and silicaluminophosphates (SAPOs) are also presented as relatively new, porous materials referring to their water sorption characteristics.

Criteria for achieving high performing porous materials for water adsorption, the basic principle of a water sorption based heat pump and pros and cons of MOFs versus traditional porous materials are discussed in section 1.3.

The water sorption behavior of an adsorbent depends on many factors such as the structure, the chemical composition, the presence of charged species, type of framework structure and the hydration level. The hydrophilicity and water uptake of porous adsorbents have to be discussed independently. Hydrophilic materials do not necessarily have high water sorption capacities. Water sorption capacity is mostly dictated by the pore volume of the adsorbent. The hydrophilicity of porous materials is defined based on its selectivity to water compared to other adsorptives at a specific relative pressure. For porous materials, the shape of the water vapor isotherm can provide direct information on the hydrophilicity or hydrophobicity of the solid. This was quantitatively and qualitatively classified by the IUPAC based on seven types of sorption isotherms, shown in figure 3a.<sup>23</sup>

The isotherm of type I shows a material with a steep rise at low relative pressure, which indicates a highly hydrophilic material. Type II and IV can be described as hydrophilic due to high water uptakes at low (type II) or medium partial pressure (type IV). The uncommon type VI isotherm is also classified as hydrophilic with a stepwise adsorption of water vapor. On the other hand, sorption isotherms of type III and V describe hydrophobic or weakly hydrophilic materials with low water uptakes at low  $P/P_0^{-1}$  and sometimes moderate adsorption at medium  $P/P_0^{-1}$  with a sudden water uptake at high  $P/P_0^{-1}$  close to 1. Type VII sorption isotherms reflect highly hydrophobic solids.

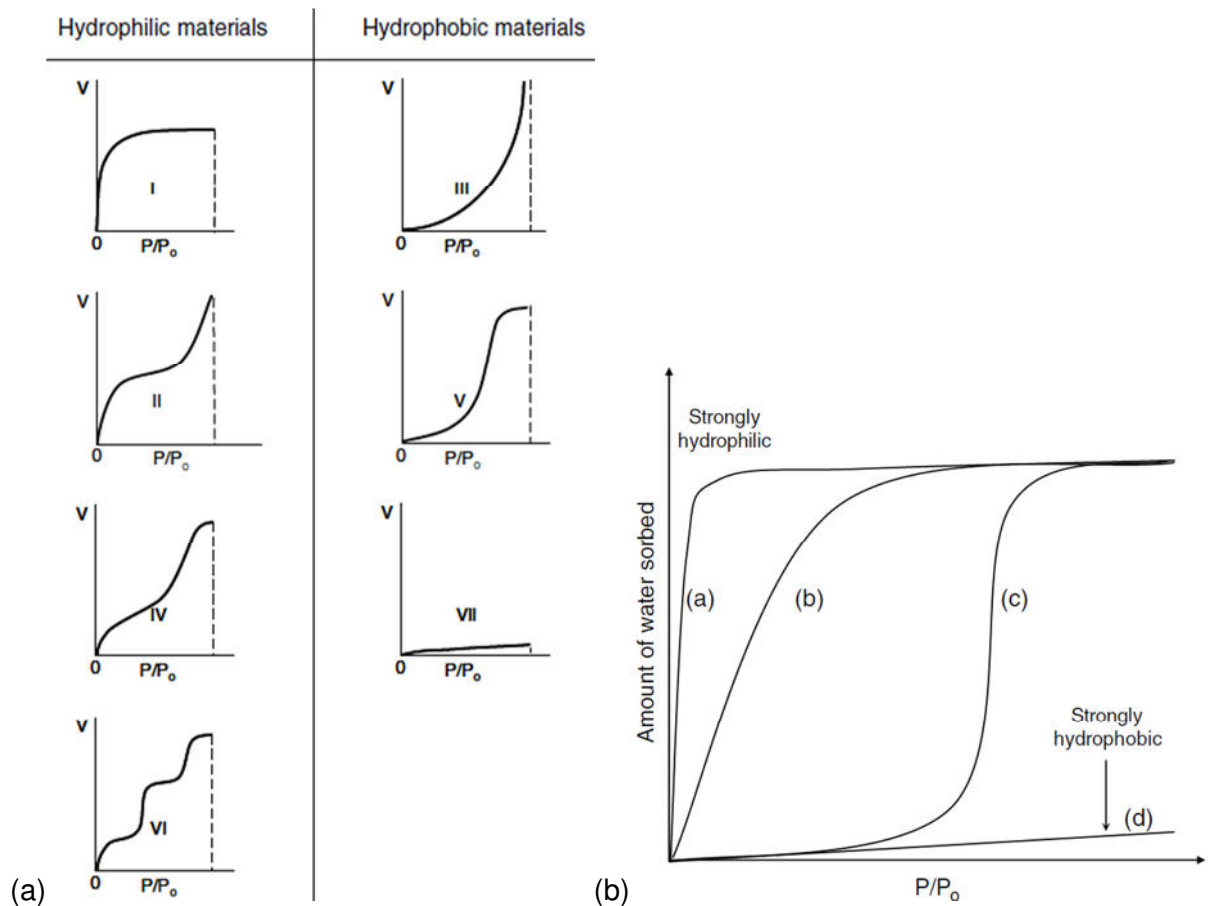


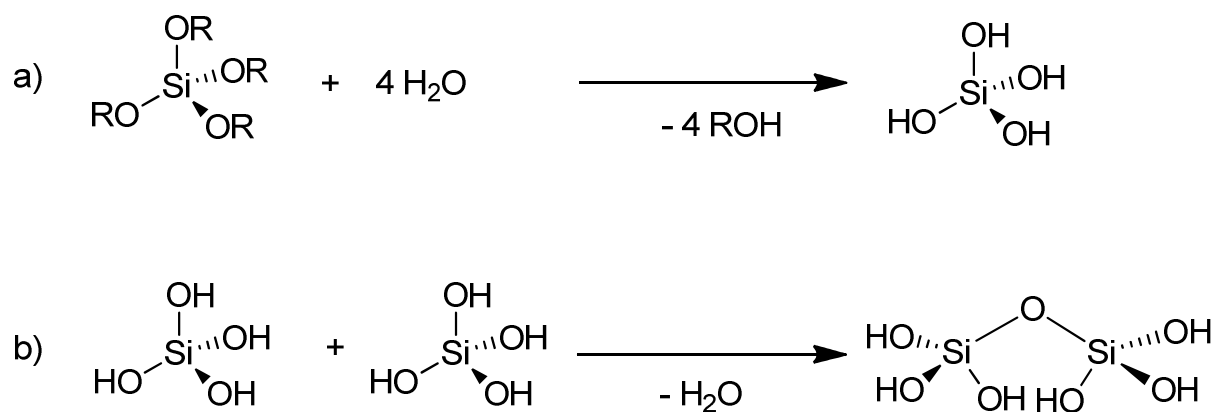
**Fig. 3.** (a) Seven types of water adsorption isotherms according to the IUPAC classification. Type I, II, IV and VI show a hydrophilic behavior. Type III, V and VII display hydrophobic adsorbents. (b) Water sorption isotherms of four porous adsorbents with different degrees of hydrophilicity. Reprinted from ref. 23, Copyright 2008, with permission from Elsevier.

As shown for example in figure 3b, material (a) of type I is more hydrophilic than (b) due to the steep rise at relatively low pressure for (a), possibly because of a higher concentration of hydrophilic sites. Adsorbent (c) reflects a type V water adsorption isotherm with low water uptakes up to the medium pressure range. In spite of the low hydrophilicity of (c), the water uptake capacity at high pressures is similar to (a) and (b) because of similar pore volumes of the three materials. Hydrophobic material (d) shows a type VII isotherm with only small water uptake over the entire pressure range.

## 1.2.1 Silica gels

Amorphous silica gels with the empirical formula  $\text{SiO}_2 \cdot x\text{H}_2\text{O}$  can be synthesized via two different methods. In the first approach silicic acid  $\text{Si}(\text{OH})_4$  is polymerized and the second approach is based on coagulation of silica particles.<sup>31</sup>

Through hydrolysis of silicon alkoxides silicic acid  $\text{Si}(\text{OH})_4$  can be prepared (Scheme 1a), which spontaneously polymerizes to form a siloxane network ( $\text{Si}-\text{O}-\text{Si}$ ) (Scheme 1b). Some of the silanol groups ( $\text{Si}-\text{OH}$ ) remain unreacted on the surface to contribute to the hydrophilic nature of silica gels.



**Scheme 1.** Synthesis of silica gels.

The second approach is based on a polymerization of a silica source (e.g. sodium silicate) with mineral acids (e.g. hydrochloric acid) through aggregation of colloidal silica particles. Herein, silica gel beads can be obtained by dropping the liquid silica source into a bath containing the diluted acid. Silica gels can be obtained with different surface areas, pore volumes and particles sizes depending on the synthesis conditions, silica concentration, temperature, pH and activation steps.<sup>31</sup>

Silica gels are well-studied hydrophilic materials with a pronounced affinity towards water vapor, cheap synthesis conditions and easy regeneration at approximately 100 °C.<sup>32,33</sup> As mentioned before, the amount of free silanol groups of the silica gels determines the hydrophilic behavior and therefore the water uptake capacity.

Various chemical modifications can improve the water sorption capacities. It has been shown that reducing the pore sizes of silica gels, which usually possess pores in the mesoporous range, leads to improvements in their water sorption characteristics. Several approaches were made to decrease the pore size of silica gels.<sup>32,34</sup> Through decreasing the solubility of silica during the polymerization steps, the pore sizes could be successfully reduced.<sup>32</sup> The introduction of aluminum ions during the silica synthesis, which act as a growth inhibitor of

primary silica particles, also leads to decreased pore sizes.<sup>32</sup> It has been shown that the water uptake capacity in microporous silica is highly enhanced compared to traditional, mesoporous silica because of a simultaneous increase of the pore volume, when reducing the pore size to the microporous range (Figure 4).<sup>34</sup> High pore volumes and surface areas are indispensable for high water uptake capacities in porous materials.<sup>35</sup> Commercially available mesoporous silica gels approach water uptakes of  $0.40\text{--}0.45\text{ g}\cdot\text{g}^{-1}$  ( $25\text{ }^\circ\text{C}$ ,  $P\cdot P_0^{-1} = 1$ ).<sup>35</sup>

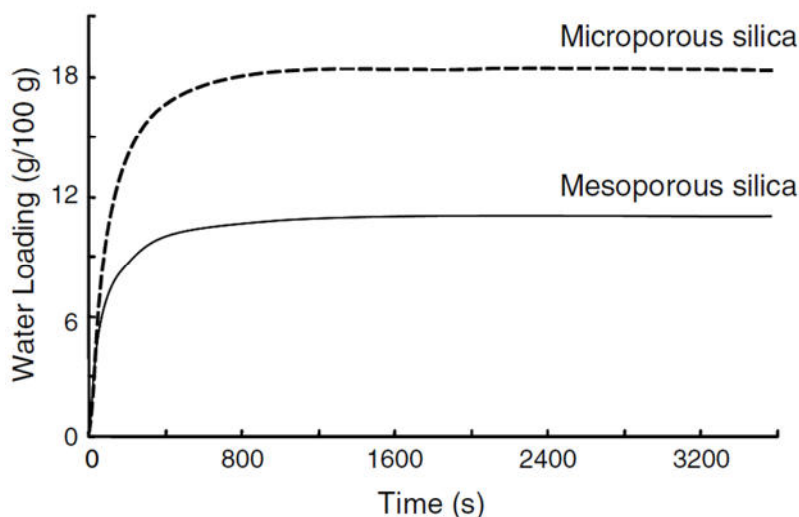


**Fig. 4.** Sorption kinetics of water adsorption in microporous (dashed) and mesoporous (line) silica gel at  $35\text{ }^\circ\text{C}$ . The x-axis refers to the time of exposure of the porous materials to saturated water vapor. Reprinted from ref. 23, Copyright 2008, with permission from Elsevier.

Highly hydrophilic and hygroscopic salts such as LiBr or  $\text{CaCl}_2$  can be introduced into silica gels by impregnation or sol-gel techniques, which are accompanied by an increased total water uptake of the composites compared to native silica.  $\text{CaCl}_2$ -silica gels show water loadings of  $0.60\text{--}0.80\text{ g}\cdot\text{g}^{-1}$  ( $25\text{ }^\circ\text{C}$ ,  $P\cdot P_0^{-1} = 1$ ).<sup>36,37</sup> The embedding of transition metal salts into porous silica gels was studied as humidity indicator, such that reversible water uptake and release is indicated by a color change.<sup>38</sup>

## 1.2.2 Silica aerogels

Silica aerogels are highly porous amorphous materials with surface areas up to  $1600 \text{ m}^2 \cdot \text{g}^{-1}$  with several applications such as insulators, support as catalyst or adsorbent for various vapors.<sup>39–41</sup>

The synthesis contains a two-step process: Firstly, an alcogel is prepared via a sol-gel method using tetraethylorthosilicate or a sodium silicate solution as silica source followed by an acidic hydrolysis to form a Si–O–Si network. Secondly, a supercritical drying step is performed to obtain a monolithic silica aerogel.<sup>42</sup>

Comparable to silica gels, silica aerogels possess a large number of active silanol groups featuring a highly hydrophilic character with water uptake capacities of  $1.35 \text{ g} \cdot \text{g}^{-1}$  ( $25 \text{ }^\circ\text{C}$ ,  $P \cdot P_0^{-1} = 1$ ).<sup>43</sup> Nevertheless, the usage of pure silica aerogels as water adsorbent is limited due to the collapse of the structure during exposure to moisture accompanied by cleavage of the siloxane bridges through hydrolysis.<sup>44</sup> Several modifications such as the incorporation of inorganic salts ( $\text{CaCl}_2$ ,  $\text{LiBr}$ ) yield to a mechanical stabilization effect of the modified silica aerogels during reversible water ad- and desorption processes.<sup>45,46</sup> Introduction of heteroatoms such as Al, a significant stabilization of the aerogels can be achieved. Knez and Novak synthesized pure alumina aerogels, as well as mixed silica-alumina aerogels, which show an improved hydrostability and satisfying water sorption capacities.<sup>43</sup>

For a further discussion of the chemistry and properties of aerogels the reader is referred to section 1.4.

### 1.2.3 Zeolites

Microporous zeolite molecular sieves are crystalline aluminosilicates built out of  $\text{SiO}_4$  and  $\text{AlO}_4$  tetrahedra forming different zeolitic structures with the empirical formula  $\text{M}^{n+}_{x/n}[(\text{AlO}_2)^-_{x}(\text{SiO}_2)_y] \cdot z\text{H}_2\text{O}$  and pores in the range of 2.5–10 Å (Figure 5). Zeolites are based on the sodalite cage (SOD) as secondary building unit yielding types A, X and Y. Zeolites X and Y belong to the faujasite (FAU) type, which are the most common, commercially available synthetic zeolites. Zeolitic type A materials feature a LTA structure.

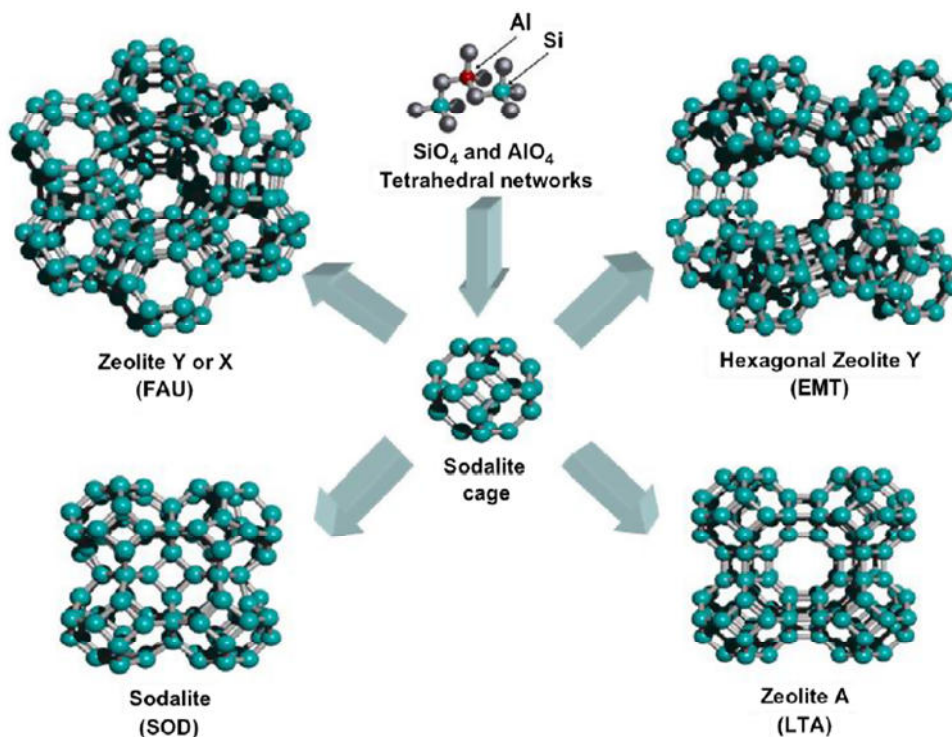


**Fig. 5.** Zeolite structures based on the sodalite cage, which consists of  $\text{SiO}_4$  and  $\text{AlO}_4$  tetrahedral networks. Reprinted from ref. 23, Copyright 2008, with permission from Elsevier.

Besides classical applications such as ion-exchange, separation and catalysis, other research topics such as host-guest chemistry and chemical sensors make use of zeolites. In addition to approximately 40 natural zeolites, more than 170 synthetic types of zeolites are known so far, which are synthesized by hydrothermal treatment with an alumina (e.g. aluminum hydroxide) and a silica source (e.g. silicic acid) followed by calcination at elevated temperature, which is an evidence for their high thermal stability.<sup>47</sup>

Zeolites are well-known highly hydrophilic adsorbents because of the extra-framework charge balancing cations with strong adsorption sites for water molecules. Water uptake capacities lie in the range of 0.20–0.45  $\text{g}\cdot\text{g}^{-1}$  (25 °C,  $P/P_0 = 1$ ) and zeolites show type I water sorption isotherms, indicating the pronounced affinity of water to these microporous

molecular sieves. The water uptake is dictated by the pore size, where large pores (e.g. in ZSM-20) show very high water loadings with  $0.46 \text{ g}\cdot\text{g}^{-1}$  ( $25 \text{ }^\circ\text{C}$ ,  $P\cdot P_0^{-1} = 1$ ).<sup>48</sup> Due to the high affinity towards water, the regeneration of zeolites requires elevated temperatures (approximately  $200 \text{ }^\circ\text{C}$ ).

The extra-framework cations, which occupy the microporous channels, play a key role in the zeolite chemistry due to their exchangeable properties and interactions with water molecules. Water loading capacity is a function of the cation size. NaA of the 'Zeolite A' type features the same LTA ring size as MgA, but substitution of two  $\text{Na}^+$  cations by the smaller  $\text{Mg}^{2+}$  cation increases the total pore volume accompanied by a 50 % enhancement in water adsorption capacity.<sup>49</sup> Replacement of small cations, by e.g.  $\text{K}^+$ ,  $\text{Rb}^+$  and  $\text{Cs}^+$  shows that diffusion of water molecules into the channels is hindered.<sup>50-53</sup> Jänchen et al. studied the effect of different cations on water loading capacities. It was found that the water uptake is proportional to the cation loadings.<sup>54</sup>

Also, the  $\text{SiO}_2:\text{Al}_2\text{O}_3$  ratio in the zeolite framework affects their hydrophilicity. Water adsorption isotherms have proven an increased hydrophilicity for the high aluminum containing zeolitic framework HZSM-5 due to the presence of more hydrophilic, active tetrahedral aluminum sites.<sup>55</sup>

Further factors such as defect sites in the crystal structure, presence of coke deposits from organic templates, crystal size and the degree of hydration can tune the water sorption characteristics in a very sensitive way.<sup>23</sup>

## 1.2.4 Aluminophosphates (AIPO), silica-aluminophosphates (SAPO)

Aluminophosphates (AIPOs) and silica-aluminophosphates (SAPOs), which possess zeolite-like structures with regular pore systems, have been studied as water adsorbents within the last decade.<sup>56</sup>

More than 30 types of AIPOs composed of Al-O-P networks have been prepared so far.<sup>47</sup> AIPOs are typically synthesized by hydrothermal reactions using an aluminum source, phosphoric acid and an amine based organic template. The organic template is then removed in a calcination step. Compared to zeolites, which have extra framework cations, microporous AIPOs are neutral with a low concentration of surface hydroxyl groups. Due to this fact, AIPOs are expected to be rather hydrophobic, but they are often described as hydrophilic because of water adsorption even under low humidity.<sup>57,58</sup> Most of the AIPO sorbents are not hydrothermally stable, but materials such as AIPO-5, AIPO-17 and AIPO-18 feature moderate stability and high water loading capacities (often higher than zeolites) with s-shaped water adsorption isotherms, which means that the adsorption isotherms have a steep increase within a narrow range of relative pressure.<sup>59-61</sup> The water loadings for AIPOs can strongly vary with  $0.15\text{--}0.54\text{ g}\cdot\text{g}^{-1}$  ( $25\text{ }^\circ\text{C}$ ,  $P/P_0 = 1$ ) and water sorption isotherms show type I or type V behavior due to the lower hydrophilicity compared to zeolites, but some of them (e.g. AIPO-5) are able to adsorb large amounts of water.<sup>58</sup>

Microporous SAPOs can be obtained by isomorphous substitution of some phosphorous atoms by silicon atoms, which leads to a negatively charged zeolite-like framework (e.g.  $\text{SiO}_4^{4-}$  sites). The essential charge balancing extra cations can increase the polarity and hydrophilicity of the framework. Therefore SAPOs are usually more hydrophilic than AIPOs. SAPO-34, for example shows a good water sorption behavior with an s-shaped water sorption isotherm.<sup>62,63</sup>

The usage of AIPOs and SAPOs for intended applications is hampered by the high costs of the solvothermal or hydrothermal syntheses, which require the use of expensive template molecules or salts, such as morpholine or tetramethylammonium hydroxide.<sup>64-66</sup>



## 1.2.5 Other mesoporous materials

Mesoporous semi-crystalline, silica based adsorbents such as MCM-48, MCM-41, SBA-15, KIT-1, etc. are synthesized by using long-chain surfactants as templates.<sup>67</sup> They have pore sizes in the range of 20–100 Å, BET surface areas of  $>500 \text{ m}^2\cdot\text{g}^{-1}$  and specific pore geometries.<sup>67–70</sup> MCM-41 is one of the most studied materials among these mesoporous solids with hexagonal pore channels and easy synthetic preparation.<sup>68,71–74</sup> Due to the high number of surface active silanol groups, a large amount of water can be adsorbed followed by capillary condensation. These materials show hydrophobic type V water adsorption isotherms with water uptake capacities in the range of  $0.45\text{--}0.84 \text{ g}\cdot\text{g}^{-1}$  ( $25 \text{ }^\circ\text{C}$ ,  $P/P_0 = 1$ ), which is higher compared to zeolites (Figure 6).<sup>68</sup> It has to be mentioned that these mesoporous materials face several difficulties as water adsorbents, because of the high sensitivity towards moisture and low hydrothermal stability.<sup>75,76</sup>

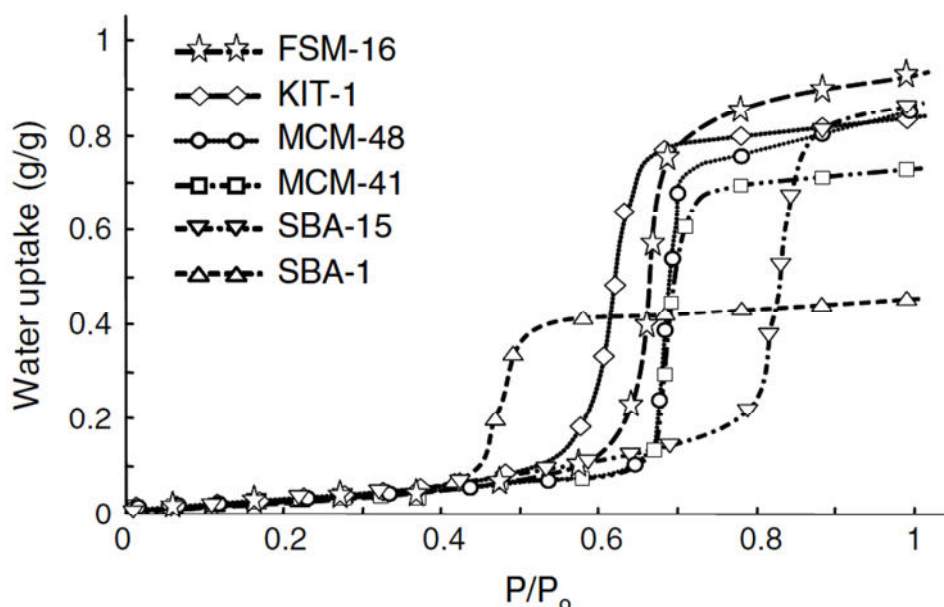


**Fig. 6.** Water sorption isotherms of various mesoporous silicas, measured at  $25 \text{ }^\circ\text{C}$ . Reprinted from ref. 23, Copyright 2008, with permission from Elsevier.

## 1.3 Metal-organic frameworks for diverse applications

### 1.3.1 Concepts and properties of MOFs

Besides classical porous materials, such as purely inorganic and carbon materials, metal-organic frameworks (MOFs) have gained an important position in the field of porous materials during the last 10–15 years (Figure 7).

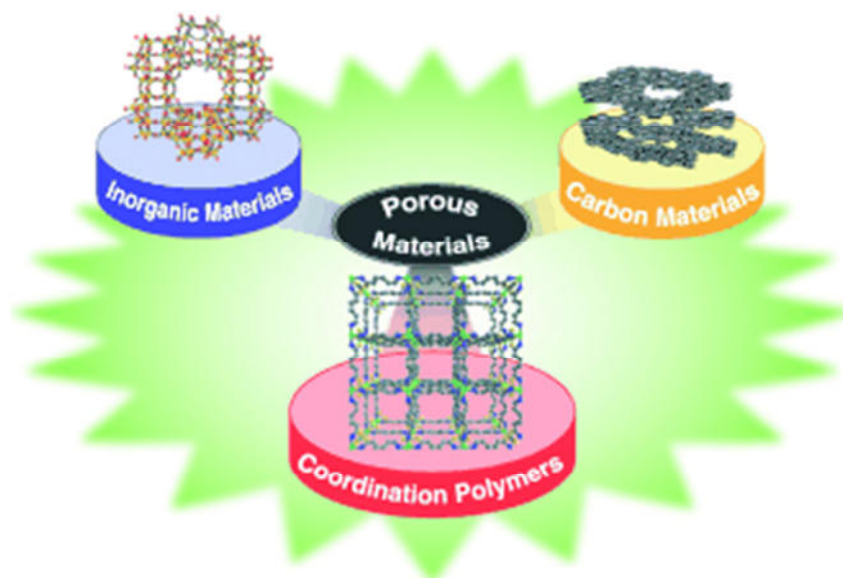
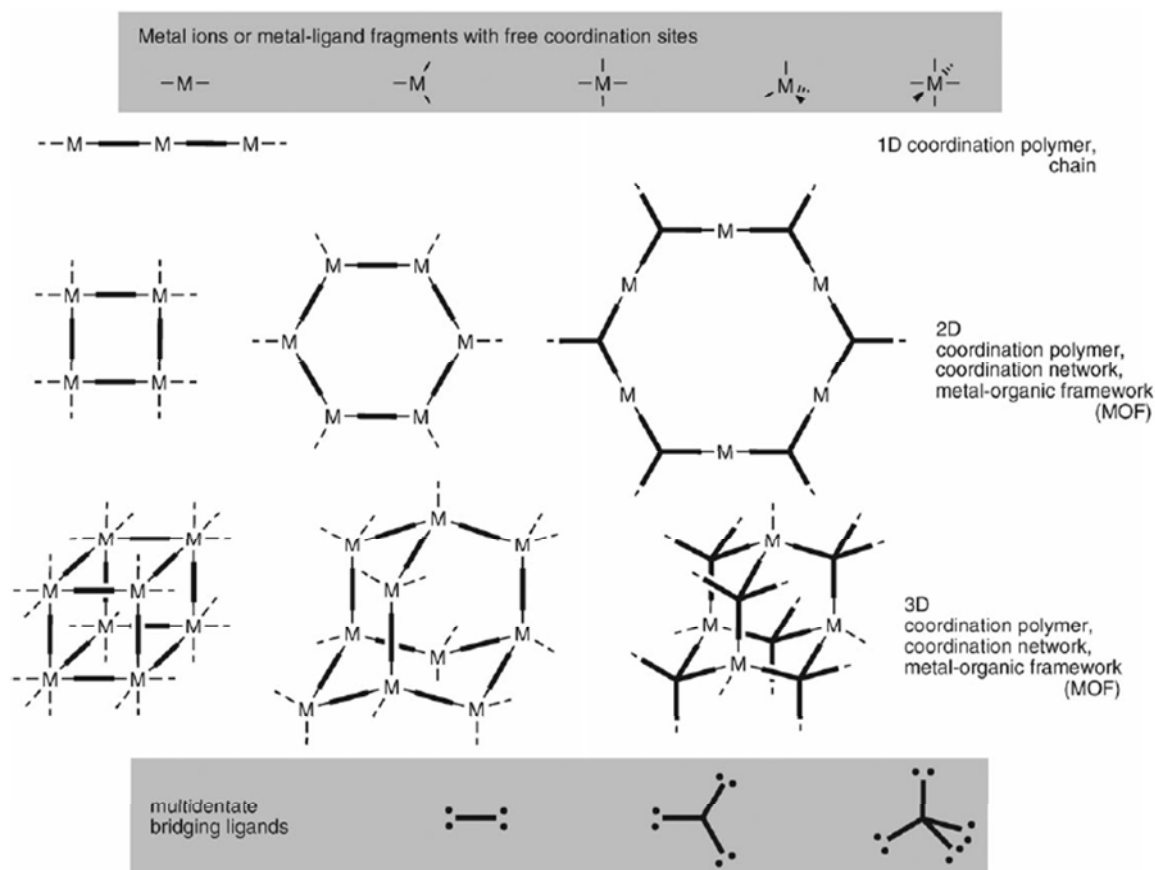


**Fig. 7.** Classes of porous materials (inorganic materials, carbon materials and coordination polymers). Reprinted from ref. 77, Copyright 2004, with permission from John Wiley and Sons.

MOFs are potentially porous, crystalline, three-dimensional coordination networks consisting of metal ions or metal clusters (nodes), connected by multidentate organic ligands, which can feature different geometries (Scheme 2).<sup>78</sup> Coordination polymers, which are known since the 1960s, are the predecessors of MOFs. Hoskins and Robson and also others published several works of porous coordination polymers in the early 1990s, which accelerated the interest in this new topic.<sup>79,80</sup> The term metal-organic framework was popularized by Yaghi et al. around 1995 for a layered Co-trimesate that showed reversible sorption properties.<sup>81,82</sup> Metal organic frameworks have uniform micro-/mesopore structures with high surface areas, which can reach more than  $6000 \text{ m}^2\cdot\text{g}^{-1}$  for MOF-210 or NU-100.<sup>83,84</sup> MOFs exhibit permanent or flexible porosity and/or guest exchange properties and tunable pore sizes and topologies.



**Scheme 2.** Schematic presentation for the construction of coordination polymers and MOFs from molecular building blocks. Reproduced (in part) from ref. 85 with permission of The Royal Society of Chemistry (RSC) on behalf of the European Society for Photobiology, the European Photochemistry Association and the RSC.

MOFs are traditionally synthesized from multidentate ligands and metal salts in solution by hydro/solvothermal treatment (Figure 8). New synthetic approaches such as electrochemistry, microwave-assisted heating, mechanochemistry and sonochemistry extended the synthetic diversity of metal-organic framework structures yielding different crystal sizes, morphologies and properties of MOFs.<sup>85</sup>

Metal-organic frameworks do not have to contain only one type of linker. There are several examples where two or more linkers are used to synthesize porous coordination polymers.<sup>86</sup> The organic ligands can be either rigid or flexible and the usage of flexible ligands can lead to so-called 'breathing MOFs' with applications such as drug-storage and- delivery.<sup>87</sup>

The possibility to post-synthetically modify metal-organic frameworks either by linker modifications or by other techniques can tune the pore sizes and geometries and therefore the properties of MOFs in a very sensitive way (see section 1.3.2).<sup>88</sup>

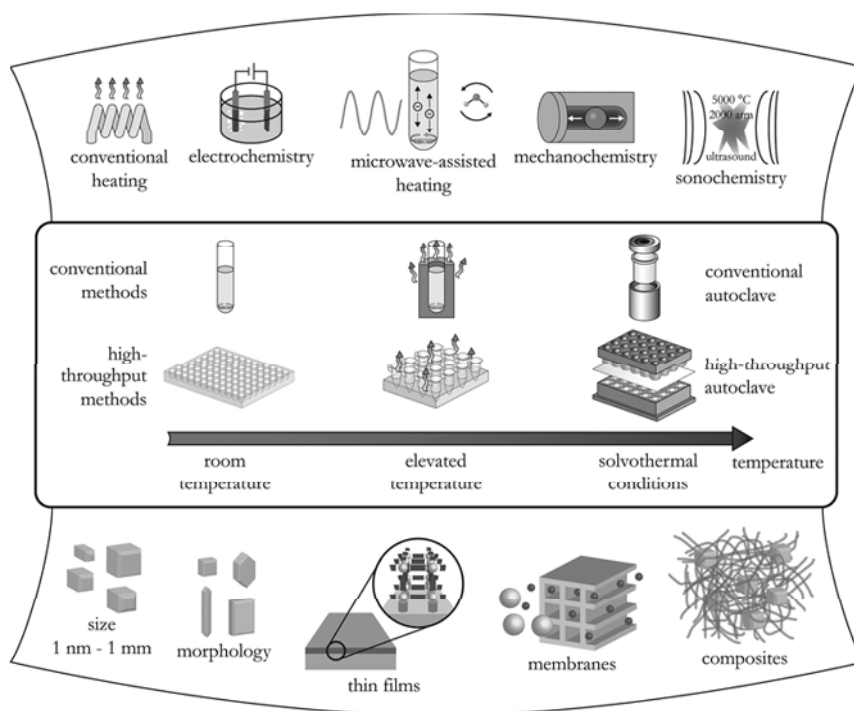


**Fig. 8.** Overview of synthesis methods at various temperatures yielding different final MOF products. Reprinted with permission from ref. 89. Copyright 2011 American Chemical Society.

Research tries to advance MOFs towards applications,<sup>90–92</sup> such as catalysis,<sup>93–97</sup> gas storage,<sup>98–101</sup> gas separation and other industrially relevant areas (Figure 9).<sup>102–106</sup> Many review articles indicate the increasing interest in MOF chemistry over the last years.<sup>77,85,89,107–109</sup>

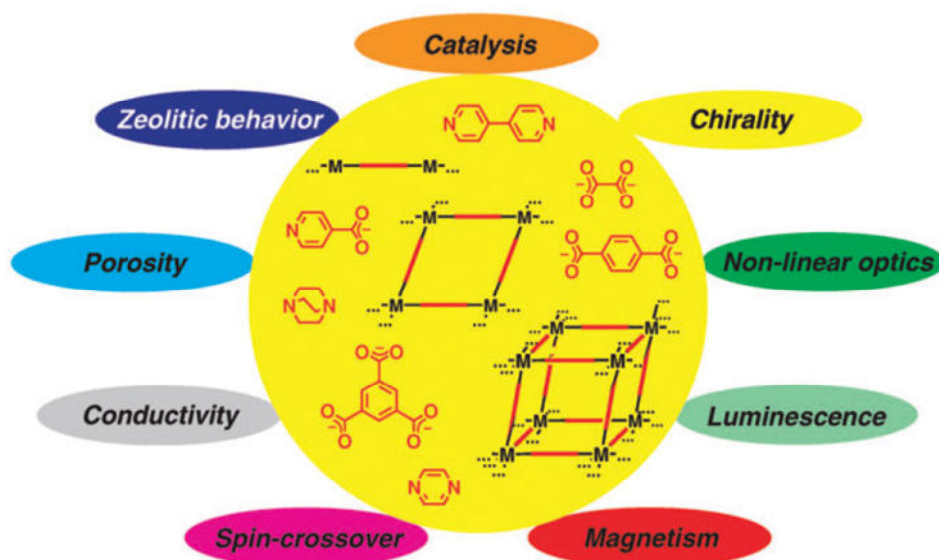


**Fig. 9.** Schematic presentation of application-oriented properties of MOFs with prototypical linkers. Reproduced (in part) from ref. 85 with permission of The Royal Society of Chemistry (RSC) on behalf of the European Society for Photobiology, the European Photochemistry Association and the RSC.

### 1.3.2 Post-synthetic modification in metal-organic frameworks

The introduction of different functional groups into metal-organic frameworks is an essential point to develop new materials with active sites for e.g. catalysis, storage or separation applications. In principle, the preparation of highly functionalized MOFs is limited by the solvothermal synthesis conditions, in which high temperature and pressure are used to obtain MOF structures. Under these conditions, ligands cannot possess functional groups, which are thermally labile or create bonds towards metals during the solvothermal treatment. Fortunately, there are alternative routes to circumvent these limitations for the introduction of functional groups into MOFs. Post-synthetic modifications (PSM) describe chemical modifications of metal-organic frameworks after the crystalline materials have been formed. The concept of PSM was developed more than two decades ago by Hoskins and Robson.<sup>79c</sup> In a paper in 1990 the following prophetic suggestion was made: 'Relatively unimpeded migration of species throughout the lattice may allow chemical functionalization of the rods subsequent to construction of the framework'. Therefore it should be possible to modify a MOF after the framework is formed.

The most common and simplest forms of PSMs are 'non-covalent modifications' of MOFs such as guest removal/exchange and ion exchange.<sup>88</sup> Whereas ion exchange is restricted to charged frameworks, guest removal and exchange can in principle occur in all robust, porous MOFs. Yaghi and co-workers observed a Co(II)BTC based MOF, which was stable upon reversible loss and uptake of pyridine guests.<sup>82</sup> Guest exchange with more volatile liquids followed by removal under temperature and vacuum treatment has now been developed as a standard practice for MOF activation.<sup>110</sup>

Besides non-covalent modifications, Cohen and co-workers describe three different post-synthetic methods (Figure 10).<sup>88,111</sup> The type of chemical bond, which is broken or formed during the PSM distinguishes each of the three methods. The aim of a 'covalent PSM' (Figure 10, top) is the organic linker of the metal-organic framework, in which new covalent bonds are created. Covalent PSMs are the most investigated modifications. During a 'dative PSM' (Figure 10, middle), dative (or coordinative) metal-ligand bonds are formed either by coordination of an external ligand to the SBU of the MOF through ligand substitution or by adding a metal source to the metal-organic framework, which then coordinates to the functional groups of the MOF ligand. The 'post-synthetic deprotection' (PSD) (Figure 10, bottom), which describes the cleavage of chemical bonds within the framework, has been less widely explored as a post-synthetic method.

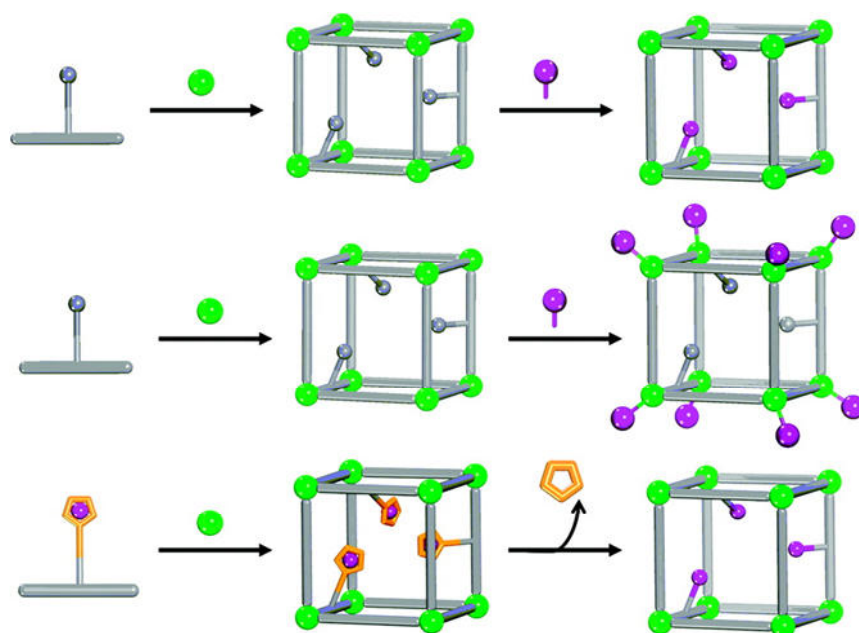


**Fig. 10.** Three types of post-synthetic modifications (PSM) in MOFs. Covalent PSM (top), dative PSM (middle) and post-synthetic deprotection (PSD) (bottom). Reprinted with permission from ref. 88. Copyright 2011 American Chemical Society.

The earliest example of a PSM was published by Lee and co-workers in 1999.<sup>112</sup> A metal-organic framework consisting of Ag(I) ions and a 3-fold symmetric 1,3,5-tri(4-ethynylbenzotrile)benzene ligand, which is substituted with a pendant alcohol group on the 2-position, could be successfully modified with trifluoroacetic anhydride under acetylation without destroying the crystalline topology. Another example was reported by Kim et al. in 2000. A crystalline homochiral metal-organic framework 'POST-1' consisting of a pyridine derivate of D-tartaric acid and Zn(II) was post-synthetically modified at the free and basic pyridyl groups with iodomethane and iodohexane.<sup>113</sup> The PSM reaction converts POST-1 from a neutral (pyridyl) to a cationic (pyridinium) framework. *N*-Alkylation was performed without collapse of the porous structure.

The principle behind post-synthetic deprotection PSD is that a protected functional group bonded to an organic ligand is introduced into a metal-organic framework under solvothermal conditions followed by removal of the protected groups to obtain the desired functional groups. Telfer et al. protected 2-aminobiphenyl-4,4'-dicarboxylate with a bulky *tert*-butylcarbamate (Boc) at the amino group. An IRMOF-10 analogue was then obtained through solvothermal treatment with Zn(II). By thermolysis of the Boc-protected IRMOF-10 analogue carbon dioxide and isobutylene were released accompanied by maintaining of the free amino groups and preservation of the crystallinity.<sup>114</sup>

Post-synthetic modifications under breaking and reforming of covalent bonds feature the most powerful tool in modern synthetic chemistry. Different types of covalent PSM such as amide coupling,<sup>115</sup> imine condensation,<sup>116</sup> introduction of urea functionalities,<sup>117</sup> *N*-alkylation,<sup>113</sup> bromination,<sup>118</sup> reduction,<sup>119</sup> click reactions<sup>120</sup> and protonations<sup>121</sup> have been widely carried out in post-synthetic MOF modifications.

Cohen and co-workers have undertaken covalent PSM reactions with IRMOF-3, which is the amino-substituted analogue of IRMOF-1 (MOF-5) consisting of non-coordinating amino groups. An acetylation of IRMOF-3 was performed with acetic anhydride (Figure 11).<sup>122</sup> Larger acid anhydrides with the general formula O[CO(CH<sub>2</sub>)<sub>n</sub>CH<sub>3</sub>]<sub>2</sub> (*n* = 1–18) were also used in covalent PSM reactions of IRMOF-3.<sup>115</sup> Figure 11 displays the synthetic diversity of non-coordinating amino groups, in which cyclic and chiral anhydrides were used as chemical reagents.<sup>123</sup>

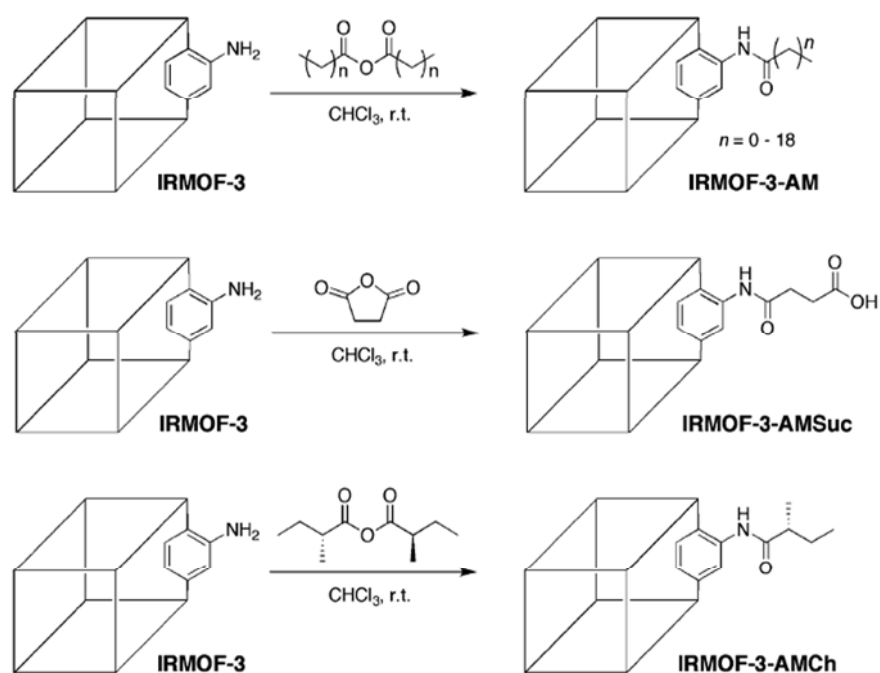


**Fig. 11.** Covalent PSM on free amino groups in IRMOF-3 with different anhydrides. Reproduced from ref. 111 with permission of The Royal Society of Chemistry.

Farrusseng and co-workers used several amino-derived MOFs and converted them into MOFs with azido functionalities (N<sub>3</sub>) followed by ‘Click Chemistry’ with different alkynes.<sup>124</sup> Not only amino groups are amenable to covalent PSM. Yaghi et al. prepared a sodalite-like zeolitic imidazolate framework (ZIF), which is composed of Zn(II) and imidazole-2-carboxyaldehyde (ZIF-90).<sup>119</sup> The existence of free aldehyde functionalities allows an imine condensation with ethanolamine.

As mentioned before, dative or coordinative PSM can be executed via two approaches to generate a metal-ligand interaction. The first method targets the metal sites in metal-organic frameworks, the second explores the coordination chemistry of the organic ligand.

In 1999, Williams et al. published the well-known copper based MOF HKUST-1, which is a porous 3D coordination polymer with dimeric Cu(II) paddle-wheel SBUs and BTC<sup>3-</sup> ligands.<sup>125</sup> The dehydrated HKUST-1 possesses coordinatively unsaturated metal centers (CUS), which are required for coordinative PSM reactions. The axial water molecules, bound to Cu(II), can be removed by temperature treatment and exchanged by other molecules, such as pyridine, while the 3D lattice remained intact. Two further studies are reported on the coordination of electron-rich reagents onto unsaturated metal sites in MOFs. In the first report, MIL-101(Cr) was treated under vacuum and heat to generate the free chromium(III) sites, which were then modified with ethylenediamine in the next step (Figure 12, top).<sup>126</sup> Also, other amines, such as diethylenetriamine or (3-aminopropyl)trialkoxysilane, were used as reagents. The coordination of nucleophilic molecules onto unsaturated metal sites in MOFs is called 'Grafting'. In the second study, ethylenediamine was successfully grafted via a dative PSM on a MOF consisting of copper(II) and triazole ligands (Figure 12, bottom).<sup>127</sup>

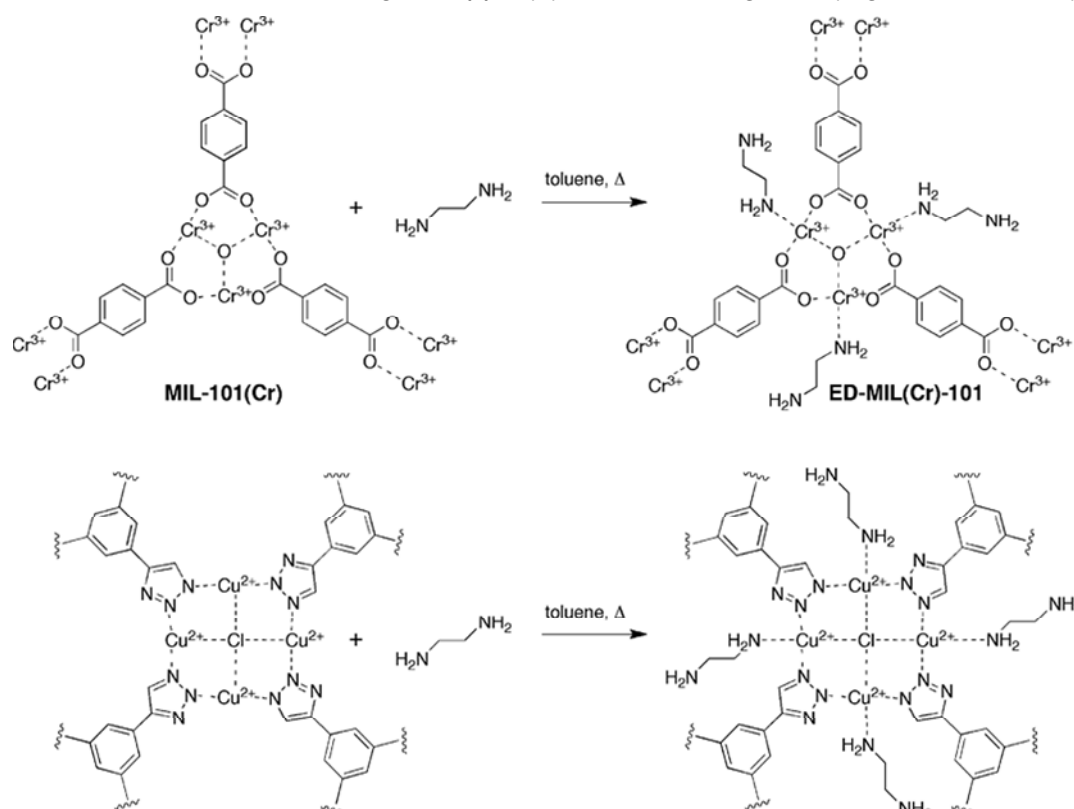


**Fig. 12.** Dative PSM on the SBUs of two MOFs with ethylenediamine. Reprinted with permission from ref. 88. Copyright 2011 American Chemical Society.



In section 3.1 of this work, grafting of small, hydrophilic glycols and ethylenediamine on coordinatively unsaturated metal sites in MIL-100(Cr) was successfully performed for improved water adsorption characteristics in heat transformation applications.<sup>128</sup>

Lin et al. synthesized a 3D homochiral porous metal-organic framework with Gd(III) and a BINOL (BINOL = 1,1'-bi-2-naphthol) type chiral bridging ligand, which contains pyridyl and dihydroxy functional groups. These dihydroxyl functionalities are not coordinated to Gd(III) and are therefore accessible for a dative PSM, which has been shown by metalation of the MOF with titanium isopropoxide  $\text{Ti}(\text{O}^i\text{Pr})_4$ .<sup>129</sup>

### 1.3.3 Water adsorption in MOFs for heat pump applications

The interest in efficient and environmentally friendly heating and cooling technologies is quickly growing and there is an increasing energy demand for air-conditioning. Energy consumption produced by electric air-conditioning features 30 to 50 % of total electric energy consumed during hot seasons in the most cities.<sup>130</sup> Traditional air-conditioning techniques are based on vapor-compression processes, which entirely use electrical power or fossil fuels. Sorption-based heat transformations do not require electrical power and make use of low temperature waste heat or solar collectors as primary energy sources, which explains the growing interest during the last years.<sup>131,132</sup> Thermally driven adsorption chillers (TDC) or adsorption heat pumps (AHP) represent promising alternatives for traditional cooling or heating devices in terms of saving energy and reducing greenhouse gases.

The basic principle of a vapor sorption based chiller or heat pump is illustrated in figure 13.<sup>30e</sup> In principle it consists of a vessel containing the dehydrated, porous adsorbent (e.g. MOF) and another vessel, which includes the working fluid (e.g. water). The whole set-up is under vacuum and both vessels are connected by a manual valve. Water is often used as working fluid due to its non-toxicity, low costs and high evaporation enthalpy ( $2440 \text{ kJ}\cdot\text{mol}^{-1}$  at  $25 \text{ }^\circ\text{C}$ ). During the production cycle, the working fluid is evaporated, which generates useful cold in a cooling case and the heat of adsorption is released to the environment, unless this heat is required in a heating case. For regeneration of the wet, porous adsorbent, heat from an external source such as a solar collector or waste heat is used to desorb the working fluid, which then starts to condensate releasing heat of condensation. In the heat pump mode, this heat is used or it is simple rejected to the environment in a cooling application. Water vapor is exchanged reversibly within the production/regeneration cycle.

Figure 14 shows the temperature changes during the adsorption step in the porous adsorbent, recorded by a thermal camera.<sup>133</sup> While water evaporation takes place in the left vessel, cold is produced. Simultaneously adsorption heat is generated in the porous material in the right vessel. The thermodynamics of this system follow a 'Carnot cycle' consisting of two isosteres and two isobars with three relevant temperature levels: (i) high temperature level (desorption heat), (ii) medium temperature level (adsorption and condensation heat) and (iii) low temperature level (evaporation heat).<sup>134</sup>

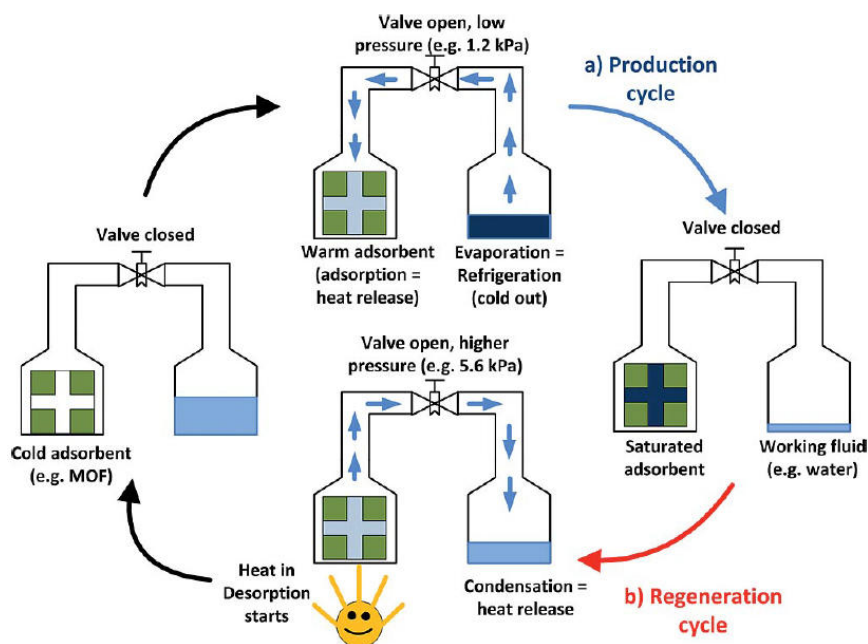


**Fig. 13.** Basic principle of heat transformation. Reprinted from ref. 30e, Copyright 2012, with permission from John Wiley and Sons.

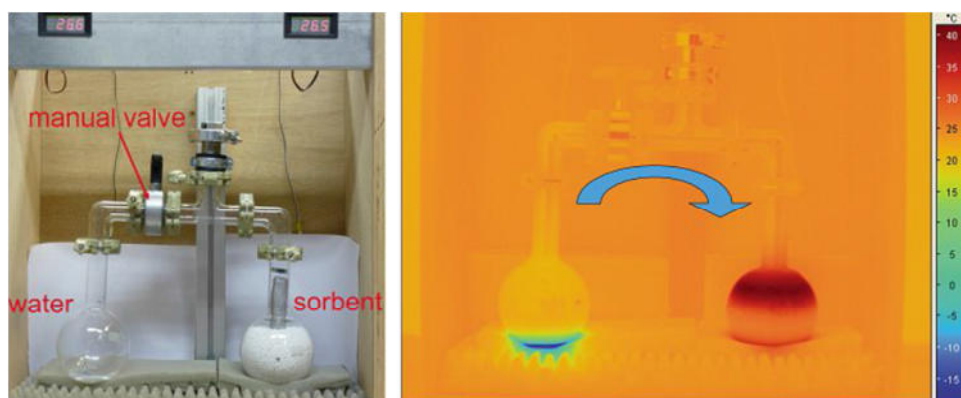


**Fig. 14.** Experimental setup for the illustration of the working cycle (adsorption step) in a TDC or AHP. Left: Before opening the manual valve. Right: Thermal camera picture a couple of minutes after opening the valve. The left water flask shows ice formation ( $\approx -5$  °C), the right one achieves a temperature of approximately 40 °C. Reprinted from ref. 133, Copyright 2013 with permission from Schweizerische Chemische Gesellschaft.

Several criteria for achieving high performing porous materials for water adsorption have to be fulfilled.<sup>30e,135</sup> First, the pore filling of the adsorbent should occur within a narrow pressure range of  $0.05 < P \cdot P_0^{-1} < 0.35$  with a steep uptake behavior. The second criterion refers to the loading spread or working capacity, i.e. the mass of adsorbed water per mass of adsorbent, which has to be as high as possible within the aforementioned narrow pressure range (at least  $0.3 \text{ g} \cdot \text{g}^{-1}$ ).<sup>30e,136</sup> The first and second criterion describe a water adsorbent, which features an s-shaped water adsorption isotherm with high water uptake within the narrow pressure range. Third, a high cycling performance and water stability of the adsorbent are

absolutely required for the intended applications. Furthermore, the wet adsorbent should be regenerated at low-costs below 80 °C.<sup>137</sup>

The inorganic materials silica gels and zeolites are currently employed in commercial TDCs or AHPs, but they have several disadvantages.<sup>23,138</sup> Highly hydrophilic zeolites exhibit moderate loading capacities with a high affinity towards water, which is connected with a water uptake at very low relative humidity ( $0.001 < P/P_0 < 0.01$ ) (Figure 15a). However, the high hydrophilicity of zeolites leads to a high desorption temperature ( $>200$  °C), which is often higher than the temperature provided by the external source (solar collector/waste heat). In comparison to zeolites, silica gels are less hydrophilic than zeolites with lower desorption temperatures of approximately 100 °C and poor water uptakes within the relevant pressure range. Zeolites and silica gels typically feature surface areas not exceeding 1000  $\text{m}^2\cdot\text{g}^{-1}$ . Zeolite-like crystalline aluminophosphates (AIPOs) and silica-aluminophosphates (SAPOs) can have higher water loading lifts than zeolites. Both classes of materials have the desired s-shaped water adsorption isotherms. However, the broader use of AIPOs and SAPOs for intended heat transformation applications is limited by the high costs of the solvothermal syntheses and the use of expensive template molecules.

Research is trying to develop new porous materials to find the ‘ideal adsorbent’ for heat transformation applications, which fulfill the desired criteria. Metal-organic frameworks are very promising materials due to their tunable pore sizes, high surface areas of several thousand  $\text{m}^2\cdot\text{g}^{-1}$  and high water loading lifts, exceeding 1  $\text{g}\cdot\text{g}^{-1}$  in some cases, which is much higher compared to traditional water adsorbents presented in Figure 15b. Furthermore, MOFs often exhibit the desired s-shaped adsorption isotherm with high water loading lifts within a narrow window of low to medium humidity. Unfortunately, there is a lack of hydrothermal stability of metal-organic frameworks, especially for zinc-carboxylate MOFs such as MOF-5.<sup>139</sup> As discussed before in section 1.3.2, MOFs can be post-synthetically modified to improve their water sorption characteristics. Purely inorganic, traditional materials such as silica gels or zeolites are also not too versatile in terms of their chemical composition, tunable pore size and topology compared to MOFs.<sup>64</sup>

Comparative studies of water adsorption processes in traditional materials and metal-organic frameworks investigated their advantages and disadvantages. Henninger and co-workers tested the cycling stability and water sorption behavior of silica gels, zeolites, AIPOs, SAPOs and MOFs.<sup>30d,136,140</sup> Water adsorption of two types of MOFs has been compared with that of silica gels.<sup>141</sup> Aristov et al. investigated porous water adsorbents such as aluminophosphates, metal-organic frameworks, porous carbons, mesoporous silicas and

different composites as potential heat pumps.<sup>142</sup> For further studies concerning adsorbents for heating and cooling applications, the reader is referred to other literature.<sup>49,54,143–145</sup>

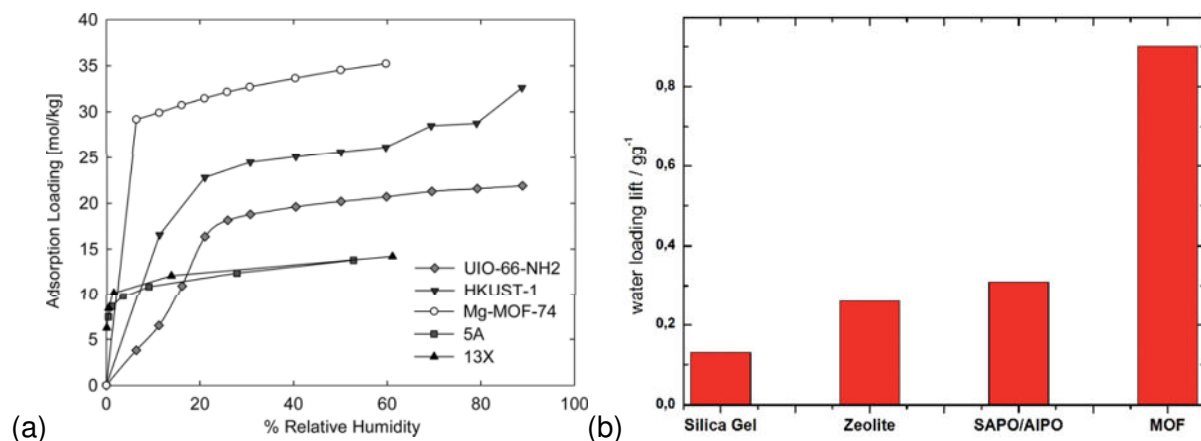


**Fig. 15.** (a) Water adsorption isotherms of UiO-66-NH<sub>2</sub>, HKUST-1 and Mg-MOF-74 compared to the zeolites 5A and 13X recorded at 298 K from the work of Wang et al.<sup>146</sup> Reprinted with permission from ref. 147. Copyright 2012 American Chemical Society. (b) Comparison of typical water loading capacities within an adsorption/desorption cycle for traditional porous materials and MOFs. Reprinted from ref. 30e, Copyright 2012, with permission from John Wiley and Sons.

Nevertheless, some metal-organic frameworks show good water cycling stability behavior and have been examined for their potential application as TDCs or AHPs in the last few years with promising results. A selection of well-examined MOF candidates with good (or at least moderate) hydrothermal stabilities are now presented.

One of the first metal-organic frameworks which was examined for water sorption was the mixed-ligand MOF ISE-1 3D-[Ni<sub>3</sub>(μ<sub>3</sub>-BTC)<sub>2</sub>(μ<sub>4</sub>-BTRE)<sub>2</sub>(μ-H<sub>2</sub>O)<sub>2</sub>]·~22H<sub>2</sub>O, BTRE = 1,2-bis(1,2,4-triazol-4-yl)ethane with a potential solvent volume of 1621 Å<sup>3</sup> (52 % of the unit cell volume) (Figure 16a). The crystal water content of 30 wt% could be reversibly exchanged over at least 10 water cycles and the maximum water loading lift is 0.21 g·g<sup>-1</sup>.<sup>148</sup>

HKUST-1 or Cu-BTC (Hongkong University of Science and Technology) with the empirical formula [Cu<sub>3</sub>(BTC)<sub>2</sub>(H<sub>2</sub>O)<sub>3</sub>] · 10H<sub>2</sub>O was published by Williams and co-workers in 1999 and is one of the widely investigated MOFs, which is commercially available as Basolite™ C300, produced by BASF.<sup>125</sup> It is constructed from Cu<sup>2+</sup>-Cu<sup>2+</sup> handles, which are coordinated by four benzene-tricarboxylate molecules to a paddle-wheel structure (Figure 16b). A cubic structure can be realized with a bimodal pore size distribution of pores with 6 and 9 Å in diameter. It shows a water loading lift of 0.3–0.55 g·g<sup>-1</sup> and poor hydrothermal stability with a loss of water uptake of about 37 % after 30 water cycles.<sup>30d,149</sup> Water adsorption isotherms of different HKUST-1 samples are presented in figure 16c. The steep rise at low relative

pressure reflects the highly hydrophilic nature of Cu-BTC. Discussion of the adsorption shape was done in detail by Kaskel and co-workers.<sup>149</sup>

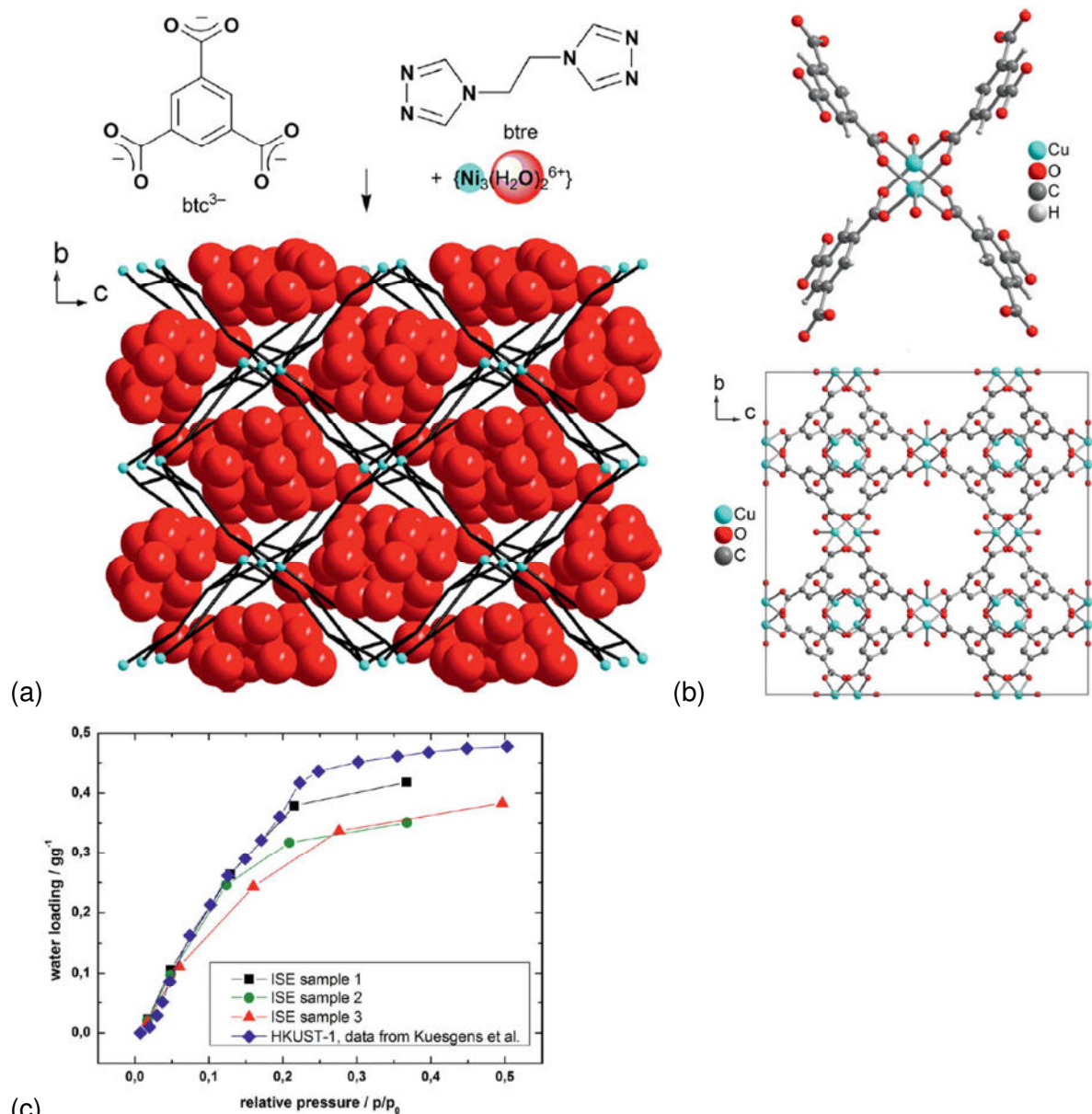


**Fig. 16.** (a) Schematic drawing of ISE-1 and the organic ligands. Both ligands are shown as black lines, nickel atoms as light blue spheres and oxygen atoms of the water molecules as red spheres. (b)  $[\text{Cu}_2(\text{BTC})_4]$  secondary building block of HKUST-1 and cubic unit cell of 3D- $[\text{Cu}_3(\text{BTC})_2(\text{H}_2\text{O})_3] \cdot \sim 10\text{H}_2\text{O}$ . (c) Water adsorption isotherms of different HKUST-1 samples. Sample 1 was synthesized in ethanol of high purity, sample 2 and 3 were synthesized in technical ethanol. Reprinted from ref. 30e, Copyright 2012, with permission from John Wiley and Sons.

The group of Férey developed a series of porous materials, known as MILs (**M**aterial **I**nstitute **L**avoisier), which consist of three- and four-valent metal ions ( $\text{Cr}^{3+}$ ,  $\text{Fe}^{3+}$ ,  $\text{Al}^{3+}$ ,  $\text{Ti}^{4+}$ ) and aromatic di- and tri-carboxylate organic linkers with large surface areas and pore volumes.<sup>87</sup>

MILs are synthesized under harsh conditions in aqueous solutions so that hydrothermal stability can be expected.

The crystalline, micro/mesoporous MIL-101(Cr) is based on a chromium(III)-terephthalate framework and has turned out to be a promising candidate for heat transformation applications with surface areas of approximately  $4000 \text{ m}^2\cdot\text{g}^{-1}$ .<sup>150</sup> The secondary building units (chromium trimers) are connected to pentagonal (12 Å) and hexagonal windows (15–16 Å), respectively, which form free cages of 29 Å and 34 Å in diameter (Figure 17a). The material shows the desired s-shaped water adsorption isotherm with loading lifts of  $1.0\text{--}1.5 \text{ g}\cdot\text{g}^{-1}$  depending on the synthesis and purification conditions (Figure 17b).<sup>138,151</sup> A large loading lift can be achieved within a narrow range of relative pressure. Water cycling tests have only shown a slight degradation of approximately 3 % after 40 ad-/desorption cycles.<sup>151</sup> A covalent post-synthetic modification of MIL-101(Cr) at the organic linker leads to the introduction of  $\text{NH}_2$ -,  $\text{NO}_2$ - or  $\text{SO}_3\text{H}$ -groups.<sup>152–154</sup> Through a time-controlled PSM, about 78 mol% of partially amino- and nitro-functionalized terephthalate linker was obtained.<sup>154</sup> The introduction of hydrophilic  $\text{NH}_2$ -,  $\text{NO}_2$ - and  $\text{SO}_3\text{H}$ -groups was done to shift the water adsorption isotherm of native MIL-101 to lower relative pressures for a potential heat pump application. Fully and partially amino-modified MIL-101(Cr) feature unchanged water loading lifts but only, a very slightly earlier water uptake together with a high water stability over 40 water cycles.<sup>154</sup> Hydrophilic sulfonic acid ( $\text{SO}_3\text{H}$ ) groups, bonded at the terephthalate linker, also lead to water uptakes at lower partial pressures compared to the pure MIL.<sup>153</sup>

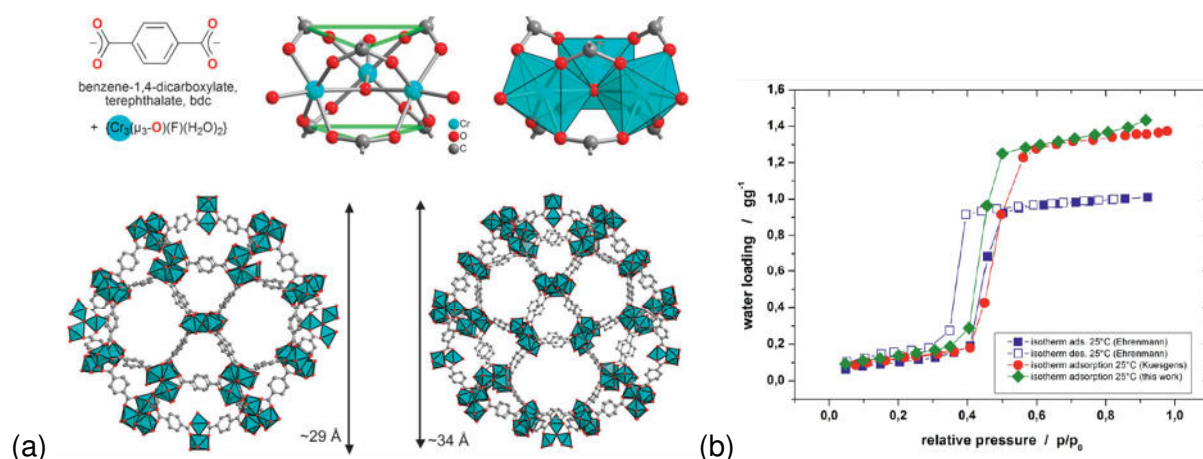


**Fig. 17.** (a) Secondary building unit for MIL-101(Cr),  $3\text{D}\text{-}[\text{Cr}_3(\mu_3\text{-O})(\text{BDC})_3(\text{OH},\text{F})(\text{H}_2\text{O})_2]\cdot\sim 25\text{H}_2\text{O}$  (top) and the small and large cages (bottom). Hydrogen atoms and solvent molecules of crystallization are not shown. Reproduced (Adapted) from ref. 85 with permission of The Royal Society of Chemistry (RSC) on behalf of the European Society for Photobiology, the European Photochemistry Association and the RSC. (b) Water adsorption isotherms at 25 °C of different MIL-101(Cr) samples: Henninger and Janiak et al. (blue)<sup>151</sup>; Kaskel et al. (red)<sup>149</sup>; Henninger et al. (green).<sup>30e</sup> Reprinted from ref. 30e, Copyright 2012, with permission from John Wiley and Sons.

Metal-organic frameworks of the MIL-100 type,  $[M_3(\mu_3-O)(OH,F)(H_2O)_2(BTC)_2] \cdot nH_2O$  ( $M = Cr^{3+},^{155} Fe^{3+},^{156} Al^{3+},^{157}$ ) are further potential adsorbents for AHP and TDC applications, consisting of  $M^{3+}$  cations and tricarboxylate linkers. Herein, the molecular building units or metal-clusters/trimers build up two types of mesopores with cages of 25 Å and 29 Å in diameter consisting of hexagonal (8.6 Å) and pentagonal windows (4.7–5.5 Å), respectively, with surface areas of 1500–2000  $m^2 \cdot g^{-1}$  (Figure 18a). The desired s-shaped adsorption isotherms feature loading lifts of 0.6–0.7  $g \cdot g^{-1}$  for MIL-100(Cr), 0.65–0.75  $g \cdot g^{-1}$  for MIL-100(Fe) and 0.5  $g \cdot g^{-1}$  for MIL-100(Al) with a stepwise adsorption shape and promising cycling stabilities (Figure 18b).<sup>149,158,159</sup> Akiyama and co-workers performed a stability test of MIL-100(Cr) with two thousand cycles with satisfying results.<sup>159</sup>

Tuning of the adsorption property of MIL-100(Cr) by grafting short polyols and ethylenediamine on coordinative unsaturated metal sites was performed in this work. Although post-synthetic grafting leads to a decrease in the surface areas, water adsorption isotherms of the modified materials MIL-100(Cr)-EG, MIL-100(Cr)-DEG and MIL-100(Cr)-EN show an increased water uptake at lower partial pressures and no loss of total water uptake capacity in comparison to pure MIL-100(Cr).<sup>128</sup>

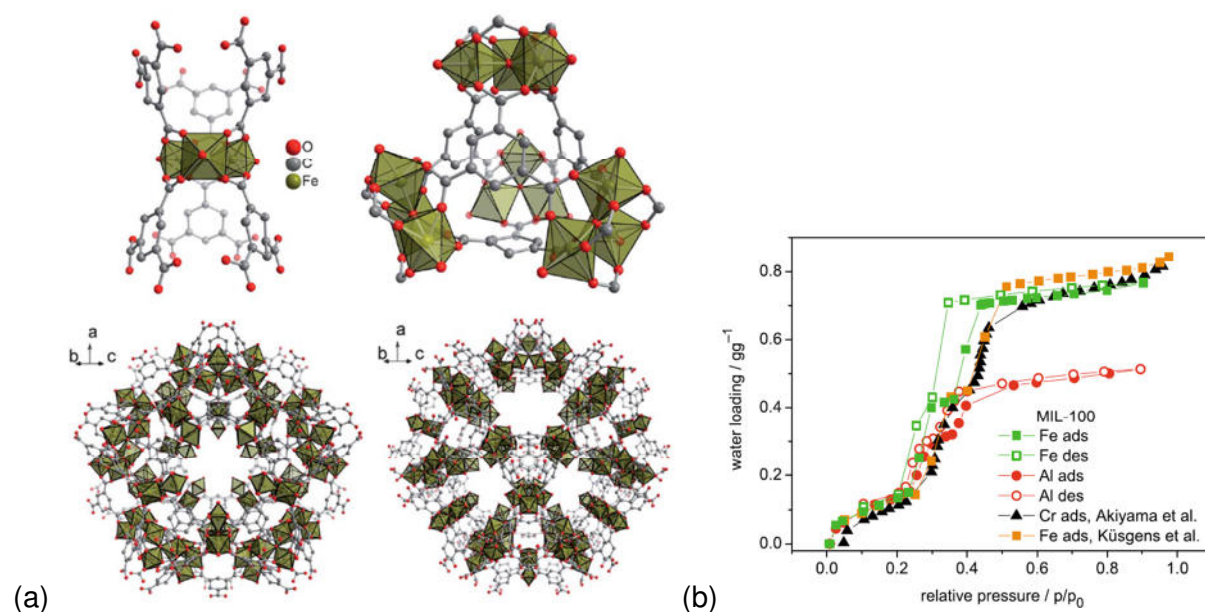


**Fig. 18.** (a) SBU and supertetrahedra (top), small and large cage (bottom) in MIL-100(Fe),  $[Fe_3(\mu_3-O)(OH,F)(H_2O)_2(BTC)_2] \cdot 14.5H_2O$ . Hydrogen atoms and solvent molecules of crystallization are not shown. MIL-100(Fe,Cr,Al) are isostructural. Reproduced (Adapted) from ref. 158 with permission of The Royal Society of Chemistry. (b) Water sorption isotherms of MIL-100(Fe,Cr,Al) at 25 °C from different sources. MIL-100(Fe,Cr) in green and red from Henninger and Janiak et al.<sup>158</sup>; MIL-100(Cr) in black from Akiyama et al.<sup>159</sup>; MIL-100(Fe) in orange from Kaskel et al.<sup>149</sup> Reprinted from ref. 133, Copyright 2013 with permission from Schweizerische Chemische Gesellschaft.



Henninger and Janiak et al. investigated microporous UiO-66(Zr), UiO-67(Zr), H<sub>2</sub>N-UiO-66(Zr) and H<sub>2</sub>N-MIL-125(Ti) as potential sorption materials for adsorption chillers or heat pumps (UiO = **U**niversity of **O**slo).<sup>160</sup> UiO-66 is based on zirconium(IV) cations and 1,4-benzenedicarboxylate linkers, which is isorecticular to UiO-67, consisting of 4,4'-biphenyldicarboxylate (BPDC) (Figure 19a, top).<sup>161</sup> UiO-66 can be modified with 2-aminoterephthalate (H<sub>2</sub>N-BDC) forming H<sub>2</sub>N-UiO-66.<sup>161–163</sup> Herein, chemically stable [Zr<sub>6</sub>O<sub>4</sub>(OH)<sub>4</sub>]<sup>12+</sup> SBUs are formed. H<sub>2</sub>N-MIL-125(Ti) consists of Ti<sup>4+</sup> and H<sub>2</sub>N-BDC linkers, which build up [Ti<sub>8</sub>O<sub>8</sub>(OH)<sub>4</sub>]<sup>12+</sup> secondary building units (Figure 19a, bottom).<sup>163,164</sup> The amino-modified MOFs H<sub>2</sub>N-UiO-66 and H<sub>2</sub>N-MIL-125(Ti) show a high heat of adsorption and satisfying water sorption properties (Figure 19b). While H<sub>2</sub>N-UiO-66 features a limited water cycling stability during a hydrothermal stress test, the water uptake of H<sub>2</sub>N-MIL-125(Ti) remains almost unchanged after 40 cycles. H<sub>2</sub>N-MIL-125(Ti) shows a steep rise in the pressure range of 0.1 < P·P<sub>0</sub><sup>-1</sup> < 0.2, which is advantageous for heat transformation applications. As already discussed before, the introduction of hydrophilic amino groups lead to an early water uptake and good sorption properties.<sup>128,153,154</sup> The promising water sorption characteristics of zirconium based MOFs were discussed by Yaghi and co-workers.<sup>135</sup>

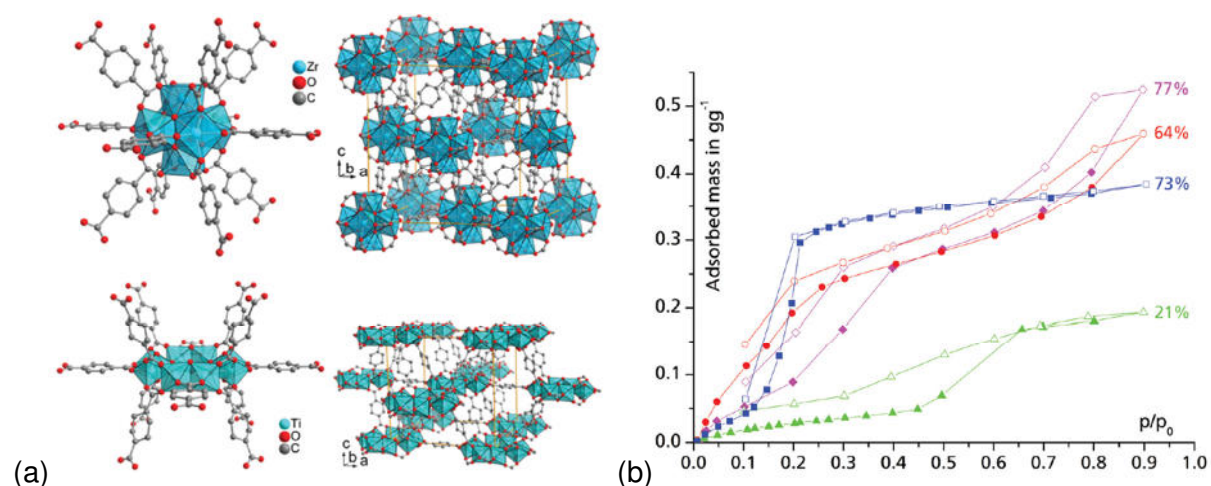


**Fig. 19.** (a) Structure of zirconium terephthalate (top). The SBU is an octahedral cluster of six vertex-sharing ZrO<sub>8</sub> square-antiprism, which is connected to 12 neighboring SBUs in a fcc packing arrangement. Structure of titanium terephthalate MIL-125 (bottom). The SBU is an eight-membered ring of edge- and vertex-sharing TiO<sub>6</sub> octahedra, which is connected to 12 neighboring SBUs in a body-centered cubic packing arrangement. (b) Water sorption isotherms of UiO-66 (purple), H<sub>2</sub>N-UiO-66 (red), UiO-67 (green) and H<sub>2</sub>N-MIL-125(Ti) (blue) at 25 °C. Reproduced (Adapted) from ref. 160 with permission of The Royal Society of Chemistry.

Several Al-based MOFs of the CAU family have been investigated for heat transformation applications so far (CAU = **C**hristian-**A**lbrechts-**U**niversitat Kiel). Stock and co-workers have reported interesting aluminum-based MOFs since 2009 with special water sorption characteristics.<sup>165</sup> Besides strongly hydrophobic CAUs, such as CAU-3 and CAU-6, CAUs such as CAU-1, CAU-1-(OH)<sub>2</sub>, CAU-8, CAU-10-H, CAU-10-NH<sub>2</sub> and CAU-10-OH show a moderate or high hydrophilic behavior (Figure 20b). CAU-1 consists of octahedral [Al<sub>8</sub>(OH)<sub>4</sub>(OCH<sub>3</sub>)<sub>8</sub>]<sup>12+</sup> clusters connected with 2-aminoterephthalate ligands. It shows the beneficial s-shaped isotherm but unfortunately water adsorption does not start until a relative pressure of  $P/P_0 = 0.4$  is reached (black curve). When the linker is changed to 2,5-hydroxyterephthalate in CAU-1-(OH)<sub>2</sub>, the hydrophilic nature is enhanced compared to CAU-1 (red curve). CAU-8 is consisting of [Al-OH]<sup>2+</sup> chains, which are bonded to 4,4'-benzophenonedicarboxylate ligands, but the water uptake capacities are low (light blue curve). CAU-10-H is the most promising candidate for TDC or AHP applications. Herein, the [Al-OH]<sup>2+</sup> chains are linked together by isophthalate ligands (Figure 20a). The corresponding water adsorption isotherm shows the desired s-shape with a high water uptake within a narrow window of relative pressure and good cycling stability (purple curve).<sup>166</sup> Unfortunately, amino- (CAU-10-NH<sub>2</sub>) or hydroxyl (CAU-10-OH) modification leads to a less desired adsorption behavior (green and dark blue curve).<sup>167</sup>

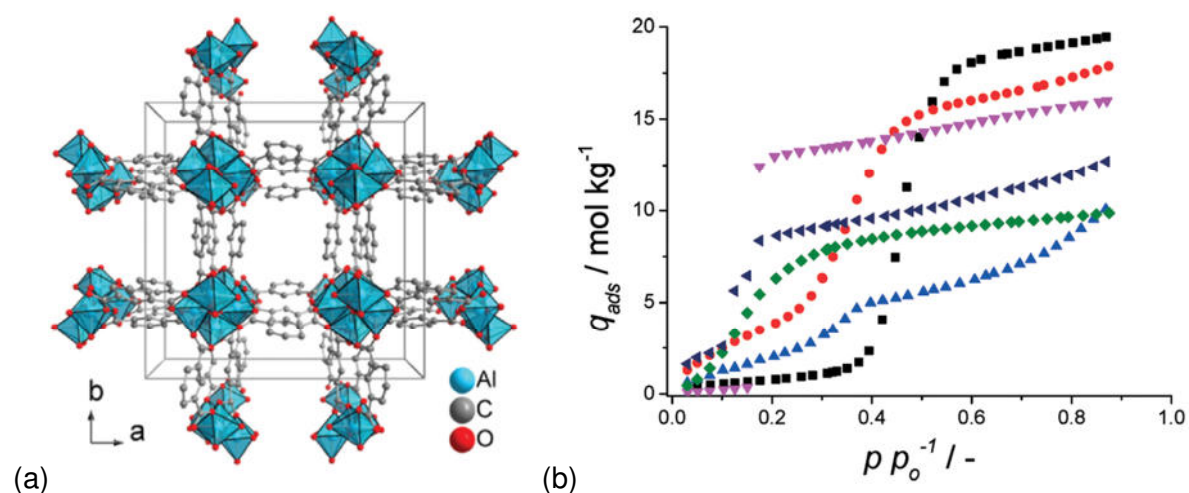


**Fig. 20.** (a) Section of the packing diagram of CAU-10-H. (b) Water adsorption isotherms of CAU-1 (black), CAU-1-(OH)<sub>2</sub> (red), CAU-8 (light blue), CAU-10-H (purple), CAU-10-NH<sub>2</sub> (green) and CAU-10-OH (dark blue). Published by The Royal Society of Chemistry, ref. 166, 167.

The pros and cons of using alcohols instead of water, such as methanol and ethanol as working fluids in TDCs and AHPs, are discussed by Saha and Janiak/Henninger et al.<sup>64,168</sup> For further analyses of water adsorption processes in metal-organic frameworks, in which topics such as 'water stability' and 'water interaction' are discussed, the reader is referred to other literature.<sup>169–172</sup>

## 1.4 Metal-organic framework composites for various applications

Metal-organic frameworks, with their wide range of possible applications, are generally obtained as fine (micro)crystalline powders. For any material to find practical utilization there is a need for processing and formulation into specific configurations. An appropriate shaping and immobilization of MOF powders is an indispensable requirement for any intended application to avoid e.g. dust problems due to the powdery appearance. The great challenge is ideal shaping of porous MOF powders without diminishing their chemical or physical properties and simultaneously guarantees mechanical stability according to the utilization process. The usage of additives or binding agents can help to efficiently shape the powdery appearance of MOFs, which leads to MOF composites. This is a rapidly growing research topic and this work is not intended to give the reader a thorough overview about metal-organic framework composites. This interesting research topic has been recently reviewed by Bradshaw and co-workers and Xu et al.<sup>173,174</sup>

In the focus of this section, the reader is first given an introduction into the chemistry of two types of binding agents, which play a key role in this work. The chemical diversity and properties of high internal phase emulsions (in short HIPEs) and aero-/xerogels based on resorcinol and formaldehyde are briefly discussed. At the end of this section several exemplars for polymeric organic/inorganic MOF composite materials in different macroscopic shapes, such as monoliths, beads or fibers are presented. Synthetic techniques, properties and potential utilization of these materials are introduced. For a discussion of metal-organic framework immobilization in membranes, the reader is referred to other literature.<sup>175</sup>

## 1.4.1 Pure binding agents

### 1.4.1.1 High internal phase emulsions (HIPEs)

High internal phase emulsion (HIPE) polymerization is one synthetic technique to obtain macroporous polymers. In 1982, researchers at Unilever patented a technique for the synthesis of a highly porous, cross-linked polymer from a HIPE.<sup>176</sup> In a conventional emulsion the internal/dispersed phase is insoluble in the continuous phase (Figure 21a). When the volume fraction is increased to 74 %, which is the maximum packing fraction, the dispersed phase is surrounded by a thin film of the external/continuous phase. This specific state is named 'HIPE'.<sup>177</sup> Usually, non-ionic surfactants were used to stabilize the high internal phase emulsion. After polymerization of the monomers and cross-linkers in the continuous phase and removing of the internal phase by washing steps, a monolithic macroporous polyHIPE material of low density ( $<0.1 \text{ g}\cdot\text{cm}^{-3}$ ) can be obtained (Figure 21b). Different polymerization methods can be applied, such as radical polymerization, ATRP,<sup>178</sup> thiolene/-yne click chemistry,<sup>179</sup> ROMP<sup>180</sup> and polycondensation.<sup>181</sup> PolyHIPEs possess a special open cell structure with two kinds of macropores. The larger voids of approximately 0.5–600  $\mu\text{m}$  in diameter, induced by the droplets of the internal phase, are connected by the smaller windows of approximately 0.1–300  $\mu\text{m}$  in diameter (Figure 21c).<sup>177a</sup> Due to their macroporous nature, polyHIPEs show BET surface areas of  $<50 \text{ m}^2\cdot\text{g}^{-1}$ . An increasing of the surface area and introduction of additional micro- and mesopores is possible by a post-synthetic hyper-cross-linking treatment or addition of porogenic solvents to the continuous phase. Hyper-cross-linking can enhance the BET surface area to  $1210 \text{ m}^2\cdot\text{g}^{-1}$ .<sup>182</sup>

The unique open cellular macroporous structure of polyHIPEs yields to a wide range of possible applications such as separation,<sup>183</sup> template for tissue engineering,<sup>184</sup> catalysis<sup>185</sup> and sensor technology.<sup>186</sup> PolyHIPEs based on styrene, cross-linked with divinylbenzene (DVB), are the most investigated systems. Herein, radical polymerization of the monomers in the oily, continuous phase of the water/oil (w/o) emulsion occurs. The aqueous droplets in the HIPE refer to the initial phase and both phases are stabilized by sorbitan monooleate surfactant molecules. Not only styrene-based monomers are used in polyHIPEs. (Meth)acrylic monomers as well as other vinyl monomers such as acrylonitrile<sup>187</sup> and *N*-isopropyl acrylamide<sup>188</sup> have been utilized to synthesize monolithic polyHIPE bodies. The monomers, used in w/o HIPE systems, are hydrophobic and the polymerization of the continuous, oily phase also leads to hydrophobic products. Hydrophilic polyHIPEs are obtained by polymerization of hydrophilic monomers in the aqueous phase of oil/water (o/w) HIPEs. Unfortunately, these polyHIPEs lead to a large amount of waste organic solvent and

this disadvantage was overcome by designing of supercritical CO<sub>2</sub> in water (c/w) HIPEs,<sup>189</sup> or surfactant-free methods ('Pickering HIPE').<sup>177,190</sup>

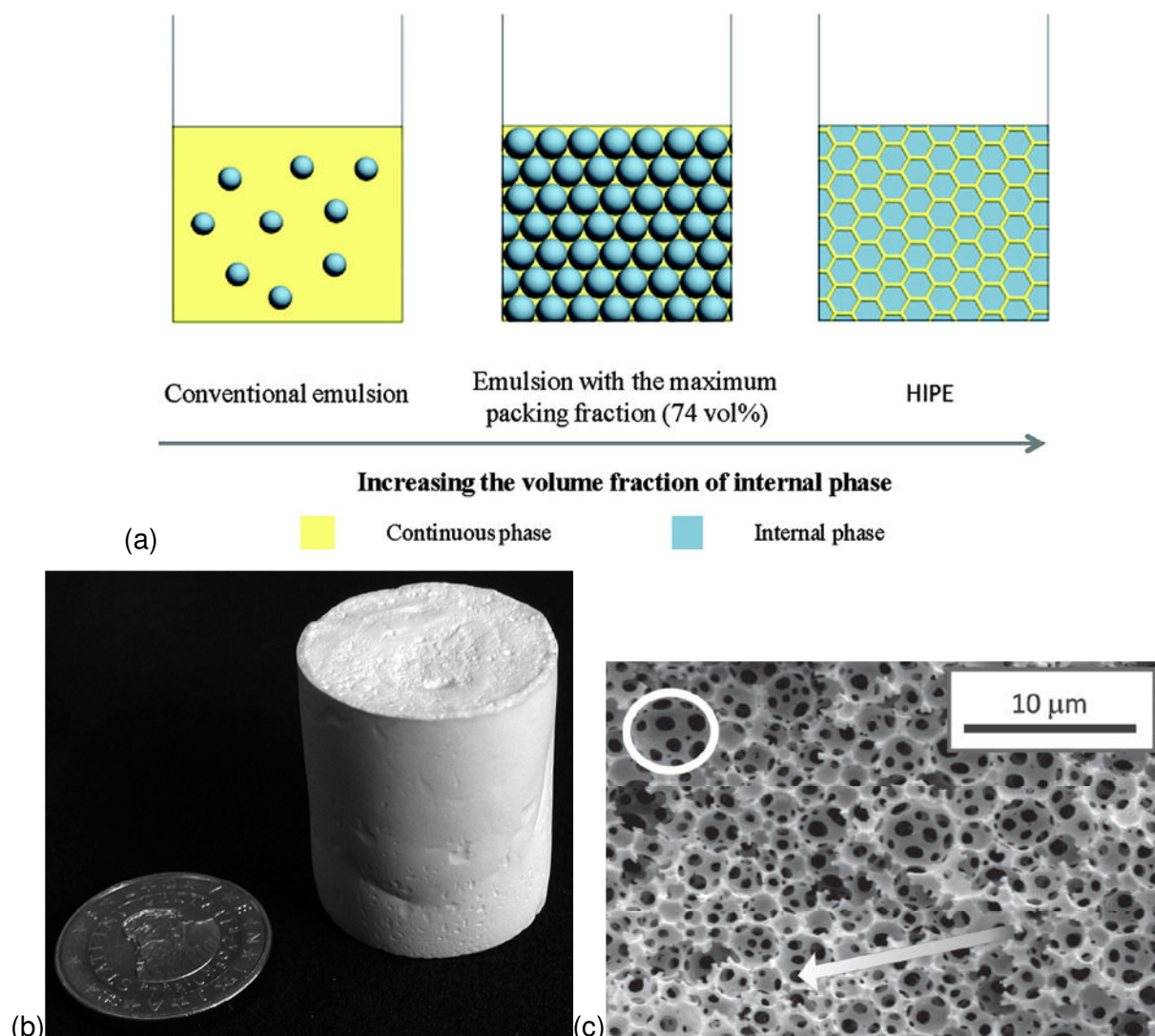


**Fig. 21.** (a) Schematic representation for the change from conventional emulsion, through emulsion with the maximum packing fraction of 74 vol%, to HIPE when enhancing the volume fraction of the internal phase. Reprinted (Adapted) with permission from ref. 191. Copyright 2012 American Chemical Society. (b) Photograph of a HIPE monolith based on cross-linked 2-hydroxyethyl methacrylate (HEMA). Reprinted with permission from ref. 192. Copyright 2007 American Chemical Society. (c) Microcellular structure of PolyHIPE (SEM image; circle denotes cavity, arrow points to interconnecting pore). Reprinted with permission from ref. 193. Copyright 2012 John Wiley and Sons.

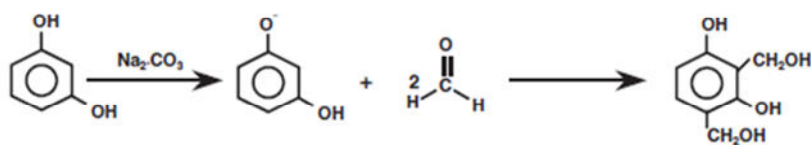
An accurate control over the porous structures can be obtained by fine-tuning of the different experimental parameters such as the ratio of both phases, choice of monomers and surfactants, degree of cross-linking, temperature, curing time and several others.<sup>178,183,184,190a,194,195</sup>

### 1.4.1.2 Aero-/Xerogels based on resorcinol and formaldehyde

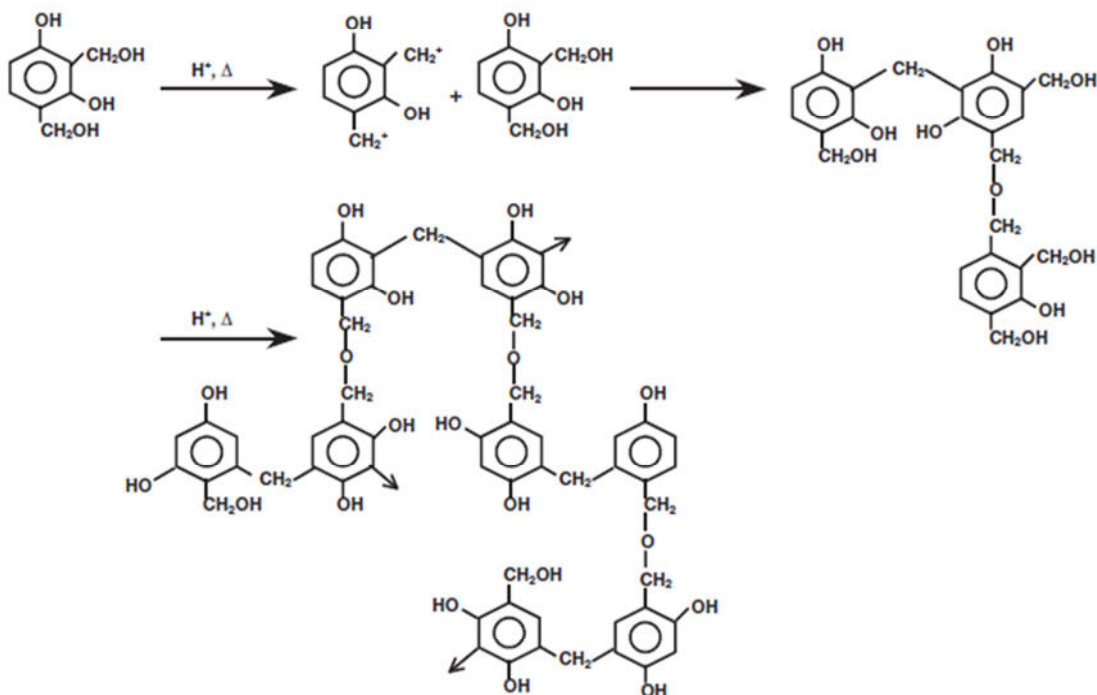
Porous aerogels are interesting compounds with attractive properties such as high porosity (>80 %), large surface areas (up to  $1000 \text{ m}^2 \cdot \text{g}^{-1}$ ), low density ( $0.03\text{--}0.5 \text{ g} \cdot \text{cm}^{-3}$ ) and low thermal conductivity.<sup>42,196</sup> Therefore, aerogels are applied as thermal or acoustic insulation materials and porous filters in aerospace, automotive engineering and buildings.<sup>197</sup> Furthermore, carbon aerogels, which are synthesized by pyrolysis of organic aerogels, find application as electrode materials due to their high electrical conductivity.<sup>198</sup>

The best-known organic aerogel is based on resorcinol and formaldehyde, invented by Pekala and co-workers in 1989.<sup>199</sup> These materials are synthesized by a sol-gel process of resorcinol (1,3-dihydroxybenzene) and formaldehyde in an aqueous medium.<sup>200</sup> After deprotonation of the acidic phenol groups, resorcinol molecules undergo an electrophilic aromatic substitution with formaldehyde molecules under formation of hydroxymethyl resorcinol derivatives ( $-\text{CH}_2\text{OH}$ ) with up to three times of substitution at positions 2, 4 and 6 of the aromatic ring. The next step is the condensation reaction to a methylene ( $-\text{CH}_2-$ ) and methylene ether ( $-\text{CH}_2\text{OCH}_2-$ ) cross-linked porous polymer (Figure 22a). The sol-gel step can be either base-catalyzed (activation of resorcinol) or acid-catalyzed (activation of formaldehyde).<sup>200a</sup> The catalyst influences the time of gelation and the porous nature of the material. Furthermore, the molar ratios of resorcinol to formaldehyde (R/F), resorcinol to water (R/W), resorcinol to catalyst (R/C), curing time and temperature and washing/drying procedures determine the latter properties of the aerogels such as density, surface area, thermal conductivity, particle- and pore size in a sensitive way.<sup>201</sup> In spite of these several parameters, pore sizes of R,F-aerogels are typically in the mesoporous range ( $\leq 500 \text{ \AA}$ ).<sup>42</sup> R,F-aerogels are typically dried via supercritical  $\text{CO}_2$  drying techniques, but subcritical drying of the wet aerogels at ambient pressure is also a common method, which was firstly described by Fischer and co-workers in 1997.<sup>198b</sup> Through decreasing the catalyst concentration to  $\text{R/C} = 1000\text{--}1500$  (typical values:  $50 < \text{R/C} < 300$ ), the mechanical stability of the final monoliths are enhanced in the same way, which are strong enough to resist the capillary forces during subcritical drying (evaporation of the solvent) (Figure 22b). Materials, which are obtained from a supercritical drying process are named ‘aerogels’, whereas subcritical drying leads to ‘xerogels’. These xerogels have higher thermal conductivity, lower surface area and denser structures compared to aerogels.<sup>202</sup>

### 1. Addition Reaction



### 2. Condensation Reaction



(a)



(b)

**Fig. 22.** (a) Molecular presentation of the polymerization mechanism of resorcinol and formaldehyde. Reprinted from ref. 203, Copyright 1997, with permission from Elsevier. (b) Photograph of a subcritically dried resorcinol-formaldehyde aerogel. Reprinted from ref. 204, Copyright 2014, with permission from Elsevier.

## 1.4.2 Polymeric MOF composites

There are currently two types of polymeric MOF composite materials. The first type describes the *in situ* growth of a metal-organic framework at a pre-formed polymer using precursor solutions and the second one is characterized by a direct synthesis of pre-formed MOF particles into a polymeric solution/emulsion before curing of the polymer.

The fabrication of a monolithic HKUST-1 body was performed by Kaskel and co-workers in 2010 in a two-step process (Figure 23a).<sup>205</sup> In the first step, pre-formed HKUST-1 particles were mixed in a laboratory-scale kneader with a liquid binding agent (methoxy functionalized siloxane ether) and a plasticization additive (methyl cellulose) until the molding batch appeared as homogeneous. In the second step, the mixture was extruded in a ram-extruder at elevated temperatures yielding a blue-colored monolith, which showed reasonable mechanical stability and was able to be cut into 20 cm pieces. The monolith showed a BET surface area of  $480 \text{ m}^2\cdot\text{g}^{-1}$ , which decreased after several months to  $287 \text{ m}^2\cdot\text{g}^{-1}$ , possibly due to moisture-induced degradation. Unfortunately, neither MOF quantification was given nor possible application was tested for this compound.

The first report of a MOF-polymer composite through the *in situ* growth of a MOF in a pre-formed polymer was published in 2008.<sup>206</sup> Cu-BTC crystals were formed and embedded within the interconnected voids of a monolithic, macroporous polyHIPE, which was obtained via polymerization of 4-vinylbenzyl chloride and divinylbenzene. An initial hydrophilization step of the polyHIPE by introducing of hydroxyl groups was necessary to obtain a homogeneous distribution of embedded MOF crystals. The HKUST-1@polyHIPE composite was synthesized by soaking of the pure polyHIPE with MOF precursor solutions, followed by solvothermal treatment. Figure 23b displays a scanning electron image of octahedral HKUST-1 crystal in the macropores of the polyHIPE system. The MOF loading was tunable depending on the number of impregnation steps. 62.3 wt% of Cu-BTC loading could be achieved after the third impregnation step with a maximum surface area of  $570 \text{ m}^2\cdot\text{g}^{-1}$ .

In this thesis work, similar monolithic composites were synthesized via a direct route, based on MIL-101(Cr) crystals and poly(2-hydroxyethyl methacrylate)HIPE.<sup>207</sup> Micro- and mesoporous MIL-101 was incorporated into the macropores of the HIPE and the resulting stable monolithic composites MIL-101(Cr)@HIPE with up to 59 wt% of MIL loading showed high methanol and water uptake capacities. These composites could be applied for adsorption chiller (TDC) or heat pump (AHP) applications.



Similar observations were published by Bradshaw et al. through an *in situ* growth of HKUST-1 into pre-formed, macroporous, mm-sized PAM-HIPE beads (PAM = polyacrylamide), which were prepared using an emulsion-templated oil/water/oil (o/w/o) sedimentation polymerization technique (Figure 23c).<sup>208</sup> The ratio of HKUST:PAM could be finely adjusted by changing of the concentration of the precursors in the solution leading to different HKUST-1@PAM composites with a maximum Cu-BTC loading of 62 wt% and a BET surface areas of  $654 \text{ m}^2\cdot\text{g}^{-1}$  (pure HKUST-1:  $1075 \text{ m}^2\cdot\text{g}^{-1}$ ). Pre-swelling of the native beads in pure solvent (without MOF precursors), prior to the MOF formation exclusively led to crystal growth on the external surface of the beads through prevention of diffusion into the bead interior.

The fabrication of ZIF-8@PS (PS = polysulfone) composite beads were obtained from a dispersion containing ZIF-8 nanocrystals and the dissolved polymer using a single orifice spinneret.<sup>209</sup> Different amounts of ZIF-8 were stirred together with the polymer solution, which further contained a surface pore forming surfactant. A loading of 80 wt% was obtained with a BET surface area of  $761 \text{ m}^2\cdot\text{g}^{-1}$  (pure ZIF-8:  $1023 \text{ m}^2\cdot\text{g}^{-1}$ ). The dispersions were injected through a syringe tip into an aqueous solution to generate the composite spheres via solvent/water exchange.

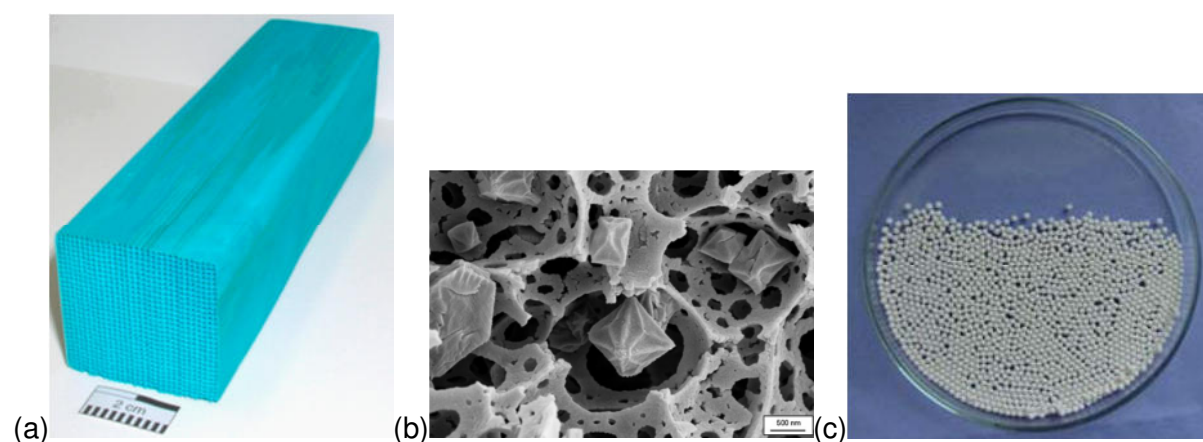


**Fig. 23.** (a) Photograph of HKUST-1 monolith, obtained via extrusion. Reprinted from ref. 205, Copyright 2010, with permission from John Wiley and Sons. (b) SEM image of HKUST-loaded poly(HIPE). Reprinted from ref. 206, Copyright 2008, with permission from John Wiley and Sons. (c) Photograph of HKUST@PAM (PAM = polyacrylamide) beads. Reproduced (adapted) from ref. 208, Copyright 2010, with permission of The Royal Society of Chemistry.

The incorporation of UiO-66 crystals into macroporous polyurethane (PU) foams was done by Pinto et al.<sup>210</sup> *In situ* crystallization techniques led to monolithic UiO-66@PU composites, which were applied as adsorbents for adsorption of organic vapors such as benzene and *n*-hexane. A loading of 71 wt% was obtained with a BET surface area of  $511 \text{ m}^2\cdot\text{g}^{-1}$  (pure UiO-66:  $1175 \text{ m}^2\cdot\text{g}^{-1}$ ).

Erkey and co-workers synthesized novel composites of mesoporous silica aerogels and microporous HKUST-1 in monolithic shape by using a modified version of the conventional sol-gel method involving hydrolysis, condensation, gelation, curing, solvent exchange and supercritical drying steps (Figure 24a).<sup>211</sup> Supercritical drying prevented the collapse of the pores. The ratio of micro- to mesoporosity could be tuned by changing the Cu-BTC amount and the blue-colored HKUST-1@silica aerogels showed MOF loadings in the range of 5 to 30 wt% with BET surface areas varying from 1025 to 1138 m<sup>2</sup>·g<sup>-1</sup> (pure HKUST-1: 1352 m<sup>2</sup>·g<sup>-1</sup>). The amount of free and accessible micropores increased with the amount of Cu-BTC. These composite materials were expected to find application in gas storage or gas separation, but no further studies were carried out. Similar composites were manufactured by Galarneau et al. through an *in situ* deposit of HKUST-1 in macro-/mesoporous silica.<sup>212</sup> HKUST-1@macro-/mesoporous silica could be loaded with up to 25 wt% of Cu-BTC and the monolithic composite of high porosity (971 m<sup>2</sup>·g<sup>-1</sup>) could be successfully applied as catalyst for the Friedländer reaction (pure HKUST-1: 1812 m<sup>2</sup>·g<sup>-1</sup>).

A further report of MOF@aero-/xerogel composites was published by Lu et al. in 2012, who synthesized HKUST-1@porous carbon monoliths.<sup>213</sup> HKUST-1 crystals were *in situ* grown into the porous carbon materials through a multiple step-by-step impregnation. Porous carbon monoliths were prepared by pyrolysis of a resorcinol and formaldehyde based xerogel under nitrogen atmosphere at 800 °C. The MOF loading could be increased to 68 wt% after the third impregnation step (516 m<sup>2</sup>·g<sup>-1</sup>; pure HKUST-1: 1448 m<sup>2</sup>·g<sup>-1</sup>) and the monolithic composites were investigated as potential materials for CO<sub>2</sub> storage and gas separation (CO<sub>2</sub>/N<sub>2</sub>) applications.

Monolithic MOF@xerogel composites were also synthesized in this thesis work using a mesoporous resorcinol, formaldehyde based xerogel as matrix for the embedding of MIL-100(M) and MIL-101(Cr) (M = Fe, Cr) crystals.<sup>214</sup> Embedding up to 77 wt% of MOF powder was possible, with high mechanical stability of the monolithic composites. Pore blocking effects through polymerization of the binding agent in the MIL pores could be largely avoided by pre-polymerization of the xerogel solution before addition of the MIL powders. These MOF@xerogel composites showed the expected high water vapor uptakes, which are advantageous for a potential application in heat transformation processes.

Synthetic polymer fibers were also used as substrates and MOF@polymeric fiber composites could be obtained by electrospinning techniques. Electrospinning is typically used for the synthesis of thin uniform polymer fibers in which an electrified jet of polymer solution is rapidly stretched because of electrostatic repulsions between surface charges and

evaporation of the solvent.<sup>215</sup> In the first report, ZIF-8@PVP (PVP = polyvinylpyrrolidone) fiber composites were obtained starting from a dispersion of ZIF-8 nanocrystals in a solution containing the dissolved polymer (Figure 24b).<sup>216</sup> The width of the fibers with 150–300 nm could be adjusted by varying the polymer concentration and MOF loadings of up to 56 wt% were possible ( $530 \text{ m}^2\cdot\text{g}^{-1}$ ; pure ZIF-8:  $960 \text{ m}^2\cdot\text{g}^{-1}$ ). Another report discussed the preparation of MOF@polymer composite fibers with different mechanical stabilities (MOF: HKUST-1, MIL-100; polymer: polysulfone, polyvinylpyrrolidone, polyacrylonitrile, polypropylene).<sup>217</sup>

Another novel field of research is the synthesis of monolithic MOF-like structures without any binding agent. Phase pure monolithic iron-BTC bodies were manufactured by Kaskel and co-workers (Figure 24c).<sup>218,219</sup> Iron(III)nitrate and 1,3,5-tricarboxylic acid were simply mixed in an ethanolic solution under vigorous stirring. Gelation occurred within a few seconds and after washing and drying, either air-dried (Figure 24c, top) or supercritically (Figure 24c, bottom), phase pure, amorphous MOF-like metallogel materials were obtained with high permanent porosity ( $1618 \text{ m}^2\cdot\text{g}^{-1}$ ) consisting of micro- and macropores.



**Fig. 24.** (a) Photograph of monolith silica aerogel Cu-BTC composite. Reprinted from ref. 211, Copyright 2012, with permission from Elsevier. (b) Photograph of ZIF-8@PVP (PVP = polyvinylpyrrolidone) fibers. Reproduced from ref. 215, Copyright 2011, with permission of The Royal Society of Chemistry. (c) Photograph of phase, pure 'MIL-100(Fe)-like' monoliths, which were air-dried (top) and supercritically dried with  $\text{CO}_2$  (bottom). Reproduced from ref. 218, Copyright 2009, with permission of The Royal Society of Chemistry.

## 2. Assignment of tasks

Several metal-organic frameworks have been well investigated as water adsorbents for potential applications in heat transformation processes over the last 5–10 years. These relative new members of porous materials exhibit advantages over traditional water adsorbents (silica gels, zeolites) like the variety of their chemical composition, tunable pore sizes and high water uptakes. Nevertheless, water loading lifts of the most MOFs in the region of low to medium humidity still remain comparably low. For intended applications, water uptakes in a relative pressure window of  $0.05 < P \cdot P_0^{-1} < 0.35$  have to be maximized.

In this work post-synthetic modifications should be done on pure, water stable MIL frameworks in order to increase their hydrophilicity for a more effective, potential usage in heat transformation applications. Small glycols and amines shall be attached directly onto the metal oxidoclusters. Therefore, the terminal water molecules can be removed in advance, thus creating the coordinatively unsaturated metal sites (CUS), which are then available and usable for post-synthetic modifications. Creating a coordinative metal-ligand interaction in this context is called 'grafting'. The newly introduced O-H- and N-H groups should increase the hydrophilicity of the MOFs through more pronounced hydrogen bonds between hydroxyl-/amine groups and water molecules. The supposable rise of the hydrophilicity of these modified MOFs is probably accompanied by a favored water uptake, which shall shift the water adsorption isotherms to lower relative pressures in comparison to the non-modified MOFs. The hydrothermal stabilities of these grafted MOFs should be investigated by water cycling stability tests, if the modified MOFs show increased hydrophilicity.

Post-synthetic modifications of MOFs to enhance their hydrophilicity, which should lead to higher water loading lifts in the region of low to medium humidity, is only one step to obtain the favored adsorbents over traditional materials.

Another challenge, which has to be accepted, concerns the shaping of metal-organic frameworks, normally obtained as powders or microcrystals. Due to e.g. dust problems, MOFs have to be shaped into a more utilizable form, regardless of the kind of application. A mechanically stable and manageable shape is an indispensable requirement for any kind of application. Possible shapes could be manufactured in membrane-, fiber-, bead- or monolithic form. In this work we focused on the synthesis and characterization of monolithic MOF shaping. One approach to solve this problem could be realized by using organic and inorganic polymers (so-called binding agents), which have the ability to be manufactured in

monolithic bodies. Such porous polymers can either be synthesized by high internal phase emulsions, so-called HIPEs, or by xerogels.

The embedding of three different MOFs of the MIL-family (MIL-100(Fe,Cr) and MIL-101(Cr)) into porous Si(HIPE), poly(HEMA)HIPE, poly(NIPAM)HIPE and a xerogel, based on resorcinol and formaldehyde should be investigated. An effective incorporation of powdery MIL into these polymers shall be achieved with retention of the monolithic shape and a high MOF loading. Pore blocking effects of the MIL pores through the polymer precursors shall be avoided or at least minimized. Different strategic methods for the synthesis of MIL@Polymer composites can be carried out in order to achieve highly porous, monolithic composite materials with high vapor (water, alcohols) uptakes as potential adsorbents for heat transformation applications. In principle, two different synthetic routes are envisioned: first, one direct method, in which the pre-formed MIL powders can be added to the polymer during its synthesis (Route A) and secondly an *in situ* route, at which the pre-formed polymer (HIPE or R,F-Xerogel) can be used as a template for *in situ* MIL crystal growing in the pores of the porous polymer (Route B). Evaluations of efficiency of the resulting composites shall be performed by gas- and vapor sorption studies.

Nitrogen sorption isotherms should be measured to evaluate BET surface areas and pore size distribution curves of the modified, grafted MOFs and MIL@Polymer composite materials. In order to classify changes of the hydrophilic/hydrophobic behavior, measurements of water and methanol sorption isotherms are crucial for the evaluation of the new materials, which should find applications as AHPs or TDCs.

### **3. Cumulative part**

Sections 3.1–3.3 present the published/submitted work of this thesis in a chronological order.

Each of the published or submitted work is self-contained with a discrete and short introductory part and a separate list of references. Before each section of this cumulative part, a short overview is given to integrate the results into the further context of this thesis. A short summary of the obtained results and a statement about the author's share of work is presented. Further unpublished work is illustrated in section 4.

### 3.1 Grafting of hydrophilic ethylene glycols or ethylenediamine on coordinatively unsaturated metal sites in MIL-100(Cr) for improved water adsorption characteristics

M. Wickenheisser, F. Jeremias, S. K. Henninger, C. Janiak

*Inorg. Chim. Acta* **2013**, *407*, 145–152. Reference 128.

<http://dx.doi.org/10.1016/j.ica.2013.07.024>

Impact factor 2013: 2.041

MIL-100(Cr) with the empirical formula  $\{\text{Cr}_3(\mu_3\text{-O})(\text{X})(\text{H}_2\text{O})_2(\text{BTC})_2\} \cdot \sim 28\text{H}_2\text{O}$  (X = OH, F) possesses two types of mesoporous cages of 25 and 29 Å in diameter.<sup>155</sup> Isostructural compounds containing  $\text{Fe}^{3+}$  or  $\text{Al}^{3+}$  instead of  $\text{Cr}^{3+}$  can also be obtained.<sup>156,157</sup> MIL-100(Cr) has attracted attention as a promising adsorbent for cyclic heat transformation due to the interesting water sorption characteristics, which have been well investigated with a high water uptake of  $0.60 \text{ g}\cdot\text{g}^{-1}$  at a moderate humidity ( $P\cdot P_0^{-1} < 0.6$ ).<sup>159</sup> Furthermore, MIL-100(Cr) shows a high BET surface area and a good hydrothermal stability over 2000 water adsorption/desorption cycles. However, for realistic applications the water loading lift in a region of low to medium humidity is comparatively low and has therefore to be maximized. Increasing the water uptake in a specific pressure range can be obtained by increasing the hydrophilic nature of the MOF. This can be manufactured by linker modifications through implementation of hydrophilic  $-\text{NO}_2$ ,  $\text{NH}_2$  or  $-\text{SO}_3\text{H}$  groups, already done for MIL-101(Cr).<sup>153,154</sup> If linker modifications are not done post-synthetically, the process is time- and energy-consuming. Another easier possibility for increasing the hydrophilicity of MOFs was needed. Therefore, the post-synthetic modification reaction, so-called 'Grafting', was applied on MIL-100(Cr).<sup>88,111</sup> Amine grafting of MIL-101(Cr) and grafting of MIL-100(M) (M =  $\text{Fe}^{3+}$ ,  $\text{Cr}^{3+}$ ,  $\text{Al}^{3+}$ ) with small, polar molecules such as CO,  $\text{CD}_3\text{OH}$ ,  $\text{CF}_3\text{CH}_2\text{OH}$  and  $(\text{CF}_3)\text{CH}_2\text{OH}$  have been investigated so far.<sup>126,220–222</sup> A coordinative metal-ligand interaction is created by substitution of terminal Cr(III)- $\text{H}_2\text{O}$  molecules by small glycols and ethylenediamine directly at the chromium oxidoclusters. Hydrophilic  $-\text{OH}$  and  $-\text{NH}_2$  could be successfully introduced into the porous metal-organic MIL framework and water sorption characteristics of modified MIL-100(Cr) materials were investigated. It could be shown that slight shifting of water adsorption isotherms to lower partial pressures of these modified MOFs compared to the non-modified MOF is possible through this simple grafting method.

Author's share of work:

- Designing, performing of the synthetic work and evaluation of the results except for the water cycling stability test of MIL-100(Cr)-EN (done by Mr. Jeremias and Mr. Henninger).
- Writing of the manuscript and drawing of the figures, graphs and tables except for figures 2 and 8 (done by Mr. Janiak).
- Editing of the manuscript regarding the reviewers' comments.

Reprinted from ref. 128, Copyright 2013, with permission from Elsevier.





# Grafting of hydrophilic ethylene glycols or ethylenediamine on coordinatively unsaturated metal sites in MIL-100(Cr) for improved water adsorption characteristics



Martin Wickenheisser<sup>a</sup>, Felix Jeremias<sup>b</sup>, Stefan K. Henninger<sup>b</sup>, Christoph Janiak<sup>a,\*</sup>

<sup>a</sup> Institut für Anorganische Chemie und Strukturchemie, Universität Düsseldorf, 40204 Düsseldorf, Germany

<sup>b</sup> Dept. Thermally Active Materials and Solar Cooling, Fraunhofer Institute for Solar Energy Systems ISE, Heidenhofstr. 2, 79110 Freiburg, Germany

## ARTICLE INFO

### Article history:

Received 25 April 2013

Received in revised form 4 July 2013

Accepted 10 July 2013

Available online 23 July 2013

### Keywords:

Metal–organic framework

Grafting

Ethylene glycols

Ethylenediamine

Water adsorption

Heat transformation

## ABSTRACT

Grafting of activated MIL-100(Cr) with EG (ethylene glycol), DEG (diethylene glycol), TEG (triethylene glycol) and EN (ethylenediamine) leads to a decrease of the BET surface area and pore volume. Yet, water adsorption isotherms of the modified compounds MIL-100(Cr)-EG, MIL-100(Cr)-DEG and MIL-100(Cr)-EN show a favored uptake of water at lower partial pressures and no loss of total water uptake capacity compared to non-modified MIL-100(Cr). The reduction in surface area is offset by an increased hydrophilicity and an advantageous smaller pore size for the adsorption of water. MIL-100(Cr) is therefore very promising as a water sorption material, e.g., for heat-transformation applications.

© 2013 Elsevier B.V. All rights reserved.

## 1. Introduction

Since the past decade, tremendous research progress has been made in the utilization of metal organic frameworks (MOFs) [1–7], e.g., in gas storage [8–14], gas separation [8–10,15–20] and catalysis [21–26]. This class of compounds is based on metal clusters or metal ions linked by organic ligands forming a three-dimensional network possessing unique properties like huge surface areas and large pore volumes due to their tunable compositions. In recent years several groups have proposed that MOFs can be used as materials for reversible adsorption and desorption of water for possible use in heat transformation processes [27–36]. The basic principle for thermally driven adsorption chillers or heat pumps is shown in Fig. 1 [37,38]. The working fluid, e.g., water, is exchanged reversibly between the evaporator/condenser and the adsorbent, e.g., a MOF-material. The whole process can be split into a production and a regeneration cycle. During the production cycle (Fig. 1b) water is evaporated taking up evaporation enthalpy at a low temperature level. The evaporation enthalpy is useful cold in the cooling case, or taken from the environment during heat pump mode. The water vapor is then adsorbed in the porous material,

releasing heat at a medium temperature level. The heat is used in the heat-pump case, or rejected to the environment during cooling mode. In the regeneration cycle (Fig. 1a) the saturated porous material is simply heated to release the adsorbed water. The required driving heat can be obtained at low cost, e.g., by a solar thermal facility, district heating, or excess heat from power-heat cogeneration plants. The water vapor is condensed at a medium temperature level and the heat of condensation is used or simply released to the environment in a cooling application [29].

Inorganic porous compounds like silica gels, aluminophosphates or zeolites have already been studied as water adsorbents for thermally driven adsorptions chillers or heat pump applications [39], but they have several disadvantages [40,41]. Zeolites have a high affinity to water and already adsorb at a low relative pressure of  $P/P_0^{-1} = 0.001–0.01$ , but they require high desorption temperatures (typically over 300 °C) and have a low water loading lift [34]. Silica gels are less hydrophilic than zeolites which lead to lower desorption temperatures (typically approx. 100 °C) but also to a low water loading within the cycle [34]. Therefore, the development of new porous materials for water adsorption/desorption processes is an active research topic [37,38,41–43]. Purely inorganic materials like silica gels or zeolites are also not too versatile in terms of their chemical composition and tunable pore sizes compared to MOFs. Several MOFs have already shown higher water uptake capacities

\* Corresponding author. Tel.: +49 2118112286.

E-mail addresses: [stefan.henninger@ise.fraunhofer.de](mailto:stefan.henninger@ise.fraunhofer.de) (S.K. Henninger), [janjak@uni-duesseldorf.de](mailto:janjak@uni-duesseldorf.de) (C. Janiak).

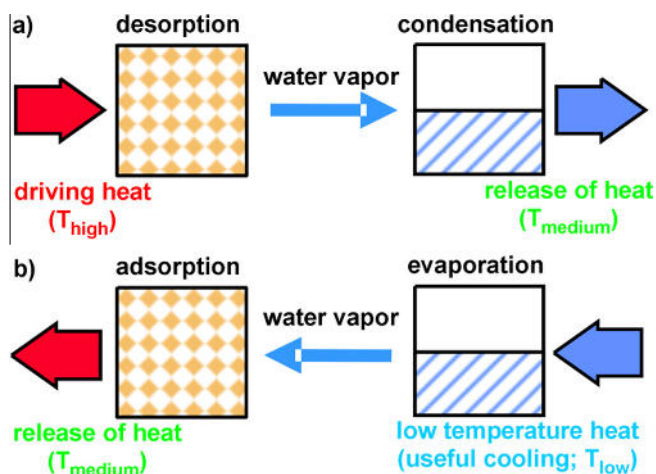


Fig. 1. Basic principle for thermally driven adsorption chillers or heat pumps [29].

with very promising water sorption characteristics like the MIL-100 [30,32,44] and MIL-101 [31,35,36,45] compounds (MIL stands for Materials of Institute Lavoisier [46,47]) [29,34,48]. MIL-100 has the empirical formula  $\{M_3(\mu_3-O)(X)(H_2O)_2(BTC)_2 \cdot nH_2O\}_n$  ( $M = Cr$  [49], Fe [50], Al [51];  $X = OH, F$ ;  $BTC = 1,3,5$ -benzene tricarboxylate) (Fig. 2). These three isostructural compounds possess two types of mesopores with cages of 25 and 29 Å in diameter (Fig. 2c).

The water sorption characteristics of native MIL-100(Cr) have been investigated by Kitagawa et al. with a water uptake of  $0.60 \text{ g g}^{-1}$  at a moderate humidity ( $P \cdot P_0^{-1} < 0.6$ ) [30]. The high internal surface area and a good hydrothermal stability (stable over 2000 water ad-/desorption cycles) make MIL-100(Cr) a promising material for heat transformation processes [30]. For the intended application however, the water uptake in a relative pressure window of  $0.05 < P \cdot P_0^{-1} < 0.32$  has to be maximized [34,37]. Shifting the water adsorption curves of porous, hydrophilic compounds to lower relative pressure is connected with increasing the hydrophilicity of this material. Stock et al. realized a post-synthetic modification of MIL-101(Cr) by introducing hydrophilic groups like  $-NO_2$  or  $-NH_2$  directly at the linker molecule [36,52,53]. Both compounds and another “ $-SO_3H$  modified” version of MIL-101(Cr) were investigated by Kitagawa and co-workers in terms of their water sorption behavior [35]. Two of these modified materials have shown an increased hydrophilicity, which means that the loading step of the corresponding adsorption isotherms were shifted by  $P \cdot P_0^{-1} = 0.05$  to lower relative pressure compared to the native MIL-101(Cr) compound [35,36].

A second possibility to increase the hydrophilicity of MOFs can be realized by creating a coordinative metal–ligand interaction, as described by Cohen and Wang [52]. The group of Feréy et al. modified MIL-101(Cr) by grafting with ethylenediamine, diethylenetriamine and 3-aminopropyltrialkoxysilane directly at the chromium oxidocluster. Cr(III) octahedral clusters of MIL-100(Cr) possess terminal water molecules (Fig. 2a, Fig. 2b), which can be removed by vacuum treatment of the material at 473 K, generating the coordinatively unsaturated metal sites (CUS) available and usable for post-synthetic modifications [54]. In the case of MIL-101(Cr) and MIL-100(Fe) approximately 3 and 2  $\text{mmol g}^{-1}$  of free CUS, respectively, can be generated [54]. Successful grafting experiments are reported for MIL-100(Cr) (in which the CUS have been grafted with  $CO$ ,  $CD_3OH$ ,  $CF_3CH_2OH$  and  $(CF_3)_2CHOH$ ) [55] for MIL-100(Fe) [56] MIL-100(Al) [57] and MIL-101(Cr) [54].

In this work we present the grafting of MIL-100(Cr) (Fig. 2) with hydrophilic ethylene glycol (EG), diethylene glycol (DEG), triethylene glycol (TEG) and ethylenediamine (EN) (Scheme 1) to study their water sorption characteristics.

## 2. Experimental

### 2.1. Materials and methods

All chemicals were obtained commercially and were used without further purification: 1,3,5-benzenetricarboxylic acid ( $H_3BTC$ ) (Alfa Aesar, 98%); hydrofluoric acid (Acros Organics, 48–51% in water);  $CrO_3$  (Alfa Aesar, 99%); ethylene glycol (EG) (Janssen Chimica, >99%); diethylene glycol (DEG) (Sigma–Aldrich, >99%); triethylene glycol (TEG) (J.T. Baker, 99%); ethylenediamine (EN) (Alfa Aesar, 99%);  $D_2O/NaOD$  (40 wt.% NaOD in  $D_2O$ ) (Sigma–Aldrich, 99.9%); toluene (VWR, p.a.); DMF (VWR, p.a.), ethanol (VWR, p.a.). Toluene was additionally dried over molecular sieve (4 Å) before usage leading to a water content of 0.015 wt.% (determined by Karl Fischer titration). Post-synthetic modification reactions were carried out under nitrogen atmosphere. Filtration, centrifugation and washing of the crude products were performed with exposure to air.

### 2.2. Physical measurements

Powder X-ray diffraction (PXRD) patterns of all the samples were measured at ambient temperature on a Bruker D2 Phaser using a flat sample holder and  $Cu K\alpha$  radiation ( $\lambda = 1.54182 \text{ \AA}$ ). Diffractograms were obtained on flat layer sample holders where at low angle the beam spot is strongly broadened so that only a fraction of the reflected radiation reaches the detector which leads to the low relative intensities measured at  $2\theta < 7^\circ$ . FT-IR measurements were carried out on a Bruker TENSOR 37 IR spectrometer at ambient temperature in a range of  $4000$ – $500 \text{ cm}^{-1}$  either in a KBr disk or on a diamond ATR unit. Nitrogen physisorption isotherms were measured on a Quantachrome Nova 4000e at 77 K. Water physisorption isotherms were measured volumetrically on a Quantachrome Autosorb iQ MP at 293 K. All samples were activated and vacuum-degassed before nitrogen and water sorption measurements for 2–4 h at 473 K. The samples were transferred to a pre-weighed sample tubes capped with a septum. Then the sample tube was connected to the preparation port of the sorption analyzer and degassed under vacuum for the specified time and temperature. After weighing, the sample tube was then transferred to the analysis port of the sorption analyzer. Helium gas was used for the determination of the cold and warm free space of the sample tubes. DFT calculations for the pore size distribution curves were carried out with the native *ASIQWIN* 1.2 software employing the ‘ $N_2$  at 77 K on carbon, slit pore, NLDFT equilibrium’ model [58–60]. The water cycling measurement was performed in a Setaram TG-DSC 111, where samples were exposed to an Ar flow humidified by a Setaram WetSys. Solution NMR spectra were recorded on a Bruker Avance DRX200 operating at 200 MHz for  $^1H$  (see Supplementary data for details).

### 2.3. Synthesis of MIL-100(Cr)

MIL-100(Cr) was hydrothermally synthesized according to the literature [44]. Typical batch sizes of 1.20 g (12.0 mmol)  $CrO_3$ , 2.52 g (12.0 mmol)  $H_3BTC$  and 0.42 mL hydrofluoric acid (12 mmol; 48–51% HF in  $H_2O$ ) in water (58 mL) at 473 K for 4 days yielded MIL-100(Cr)-as synthesized. For activation the as-synthesized material was purified through stepwise washing procedures with DMF, EtOH and deionized water (see Supplementary data for details). An amount of 2.65 g of the purified MIL-100 was obtained (60% yield based on Cr) as a light green powder with a BET surface of  $1330 \text{ m}^2 \text{ g}^{-1}$  and a pore volume of  $0.77 \text{ cm}^3 \text{ g}^{-1}$  (measured at  $P \cdot P_0^{-1} = 0.95$ ) (cf. Table 2).

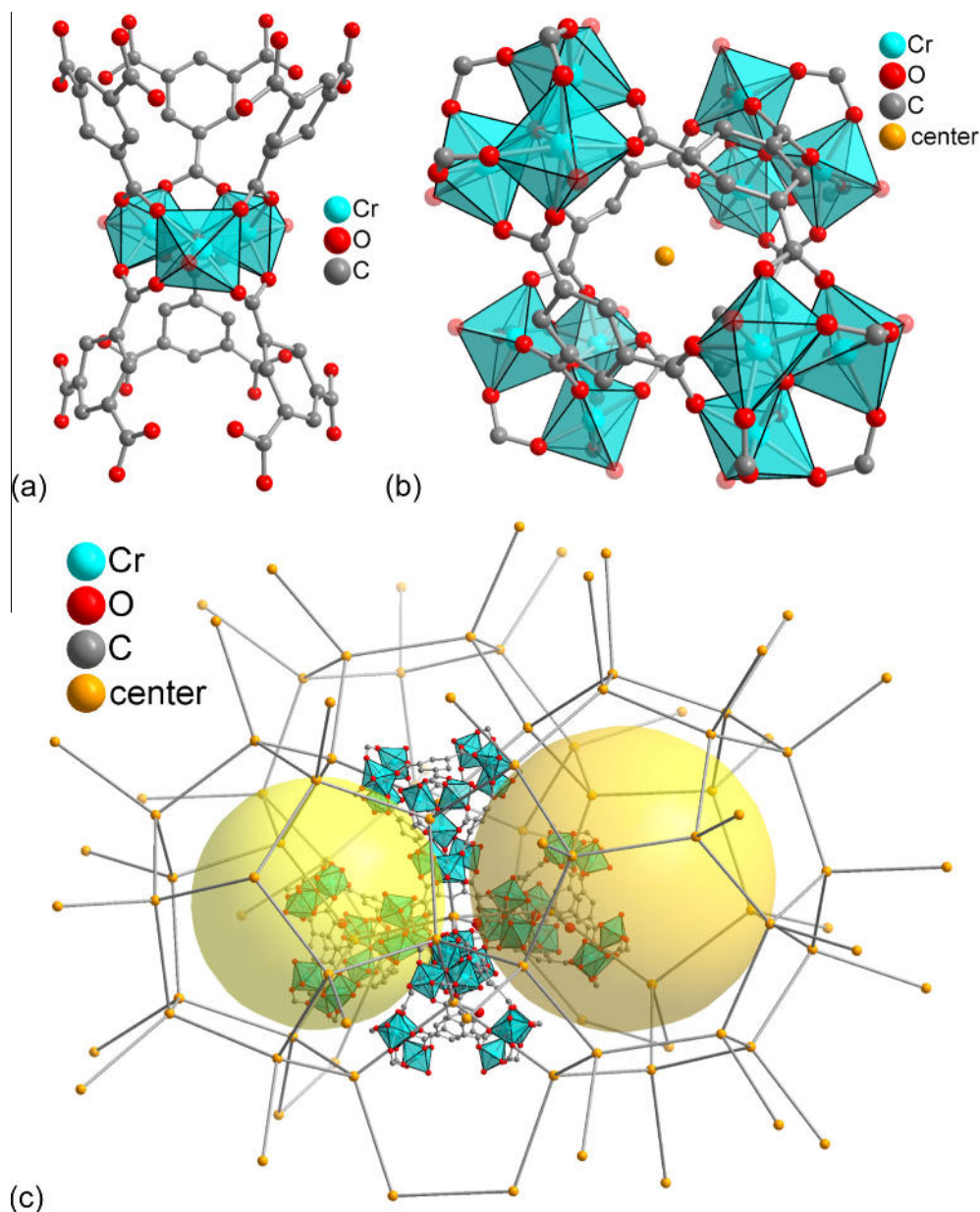


**Fig. 2.** (a) Secondary building unit, (b) single supertetrahedra with indicated center, (c) polygons for small S cage and large L cage in MIL-100(Cr) formed by connecting the centers of the corner-sharing supertetrahedra (different objects are not drawn to scale). The transparent yellow spheres of diameter 25 Å (left) and 29 Å (right) depict the void space in the cages. In (a) and (b) the O-atoms of the removable aqua ligands at the Cr octahedra are shown semi-transparent. Hydrogen atoms and solvent molecules of crystallization are not shown (redrawn from deposited cif-file to CCDC number 648835).

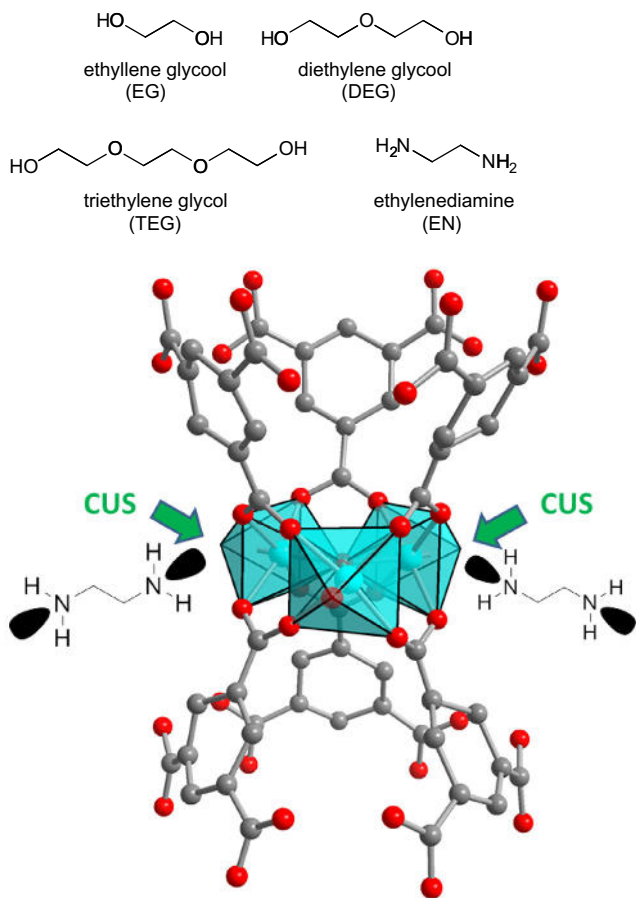
#### 2.4. Reactions of EG, DEG, TEG and EN with activated MIL-100(Cr)

The purified, solid MIL-100(Cr) material (100 mg) was placed in a two-necked flask and degassed for at least 1 h in vacuum at 473 K to remove any adsorbed water or solvent from the metal sites, thus generating the coordinatively unsaturated sites (CUS) according to the literature [44]. After cooling to r.t., dry toluene was added to the activated solid. Then pure, neat (mono, di- or tri-)ethylene glycol or ethylenediamine was added dropwise to the suspensions. The reaction mixtures were stirred for at least 16 h at r.t. (EN) or at 373 K (EG, DEG, TEG). The crude products were isolated by filtration and purified by removing the excessive glycols or amines by washing with acetone (see [Supplementary data](#) for details).

### 3. Results and discussion

#### 3.1. Syntheses of ethylene glycol and ethylenediamine grafted MIL-100(Cr)

The synthesis of the EG-, DEG-, TEG- and EN-grafted MIL-100(Cr) materials with (mono, di- or tri-)ethylene glycol and ethylenediamine, respectively, was carried out by stirring activated MIL-100(Cr) with the substrate molecules in dry toluene for at least 16 h at r.t. (EN) or at 373 K (EG, DEG, TEG). The unchanged X-ray diffraction patterns of the isolated, modified compounds MIL-100(Cr)-EG, MIL-100(Cr)-DEG, MIL-100(Cr)-TEG and MIL-100(Cr)-EN show no loss of crystallinity compared to native MIL-100(Cr) (Fig. 3).



**Scheme 1.** Molecules used for grafting of MIL-100(Cr) and schematic illustration of addition (grafting) of EN to coordinatively unsaturated metal sites (CUS) at the secondary building unit of MIL-100(Cr) (cf. Fig. 2).

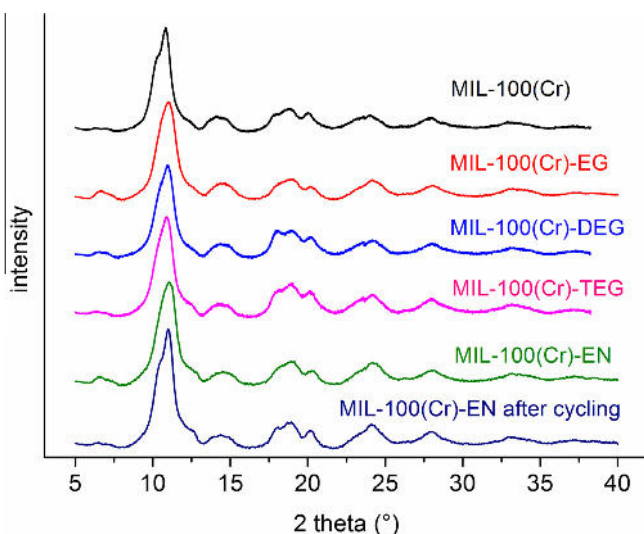


**Fig. 3.** PXRD patterns of native MIL-100(Cr) and EG-, DEG-, TEG- and EN-modified MIL-100(Cr). The PXRD for MIL-100(Cr)-EN is given before and after water sorption cycling (bottom-two curves).

Infrared spectra of ethylene glycol-modified MIL-100(Cr) prove the presence of the glycols EG, DEG and TEG by the new  $\nu(\text{C-H})$ - and  $\nu(\text{C-O})$ -stretching vibrations at  $2959\text{--}2877\text{ cm}^{-1}$  ( $\nu(\text{C-H})$ ) and  $1123\text{--}1042\text{ cm}^{-1}$  ( $\nu(\text{C-O})$ ), respectively (Fig. 4a). The  $\nu(\text{C-H})$ -stretching vibrations are shifted to larger wavenumbers by

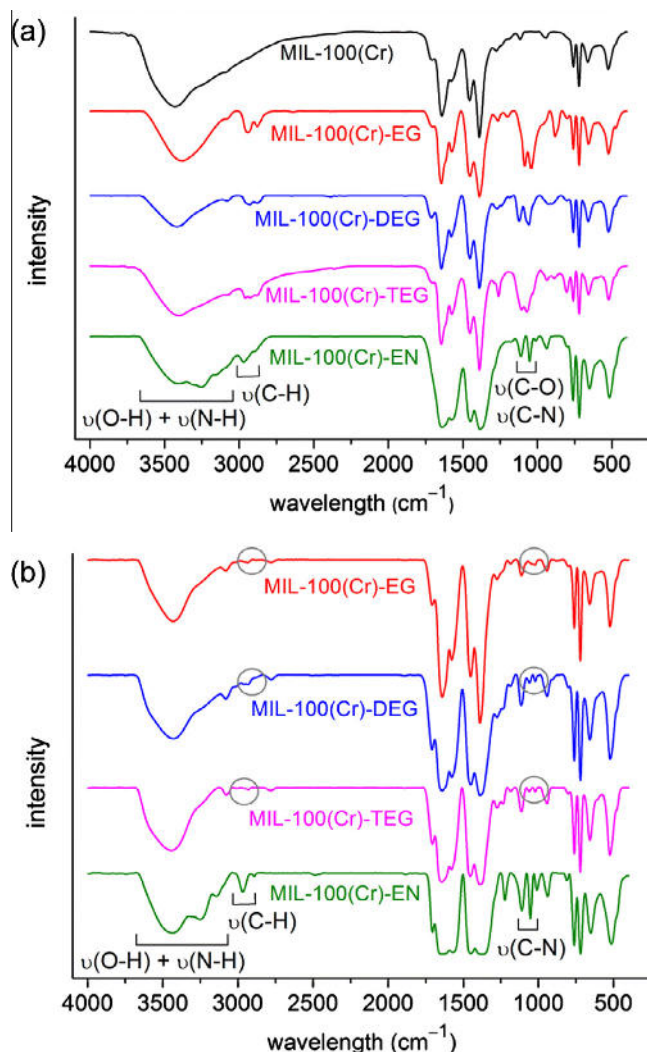


**Fig. 4.** (a) IR-spectra (KBr) of activated native MIL-100(Cr) and EG-, DEG-, TEG- and EN-modified MIL-100(Cr) obtained by reaction of activated MIL-100(Cr) with the glycols and EN in toluene. (b) IR-spectra (KBr) of isolated reaction products of MIL-100(Cr) treated first with water, then with the grafting reagents (EG, DEG, TEG, EN). The grey circles highlight the areas of the missing aliphatic  $\nu(\text{C-H})$ - and  $\nu(\text{C-O})$ -stretching vibrations for the glycols (cf. Fig. 4a).

$3\text{--}9\text{ cm}^{-1}$  compared to the free ligands (see Table S1 in Supplementary data for details). This shift can be observed when a ligand is coordinated to a Lewis acidic center [61,62], therefore indicating the successful grafting of EG, DEG and TEG onto chromium(III) sites. The presence of EN in MIL-100(Cr) is proven by the IR-spectrum (Fig. 4a), showing shoulders in the area of  $3700\text{--}2600\text{ cm}^{-1}$ , which can be assigned to  $\nu(\text{N-H})$ -valence vibrations. Aliphatic  $\nu(\text{C-H})$ -vibration bands of coordinated EN are shifted to larger wavenumbers compared to the free EN ligand ( $44\text{--}47\text{ cm}^{-1}$ ) (see Table S1 for details), indicating a coordination onto the Lewis acid chromium centers [61,62]. The band at  $1053\text{ cm}^{-1}$  can be assigned to a  $\nu(\text{C-N})$ -stretching vibration of coordinated EN.

To further verify coordination of glycols and ethylenediamine to the chromium center, the activated MIL-100(Cr) compound was first soaked with water to ensure that the coordinative unsaturated metal sites were occupied by water molecules, followed by an intensive treatment with EG, DEG, TEG or EN (see Supplementary data for details). IR-spectra of the compounds treated this way show only almost invisible, that is, barely detectable bands of low intensity for aliphatic  $\nu(\text{C-H})$ - and  $\nu(\text{C-O})$ -stretching vibrations in the region of  $2900\text{--}3000\text{ cm}^{-1}$  and  $1150\text{--}1000\text{ cm}^{-1}$ ,

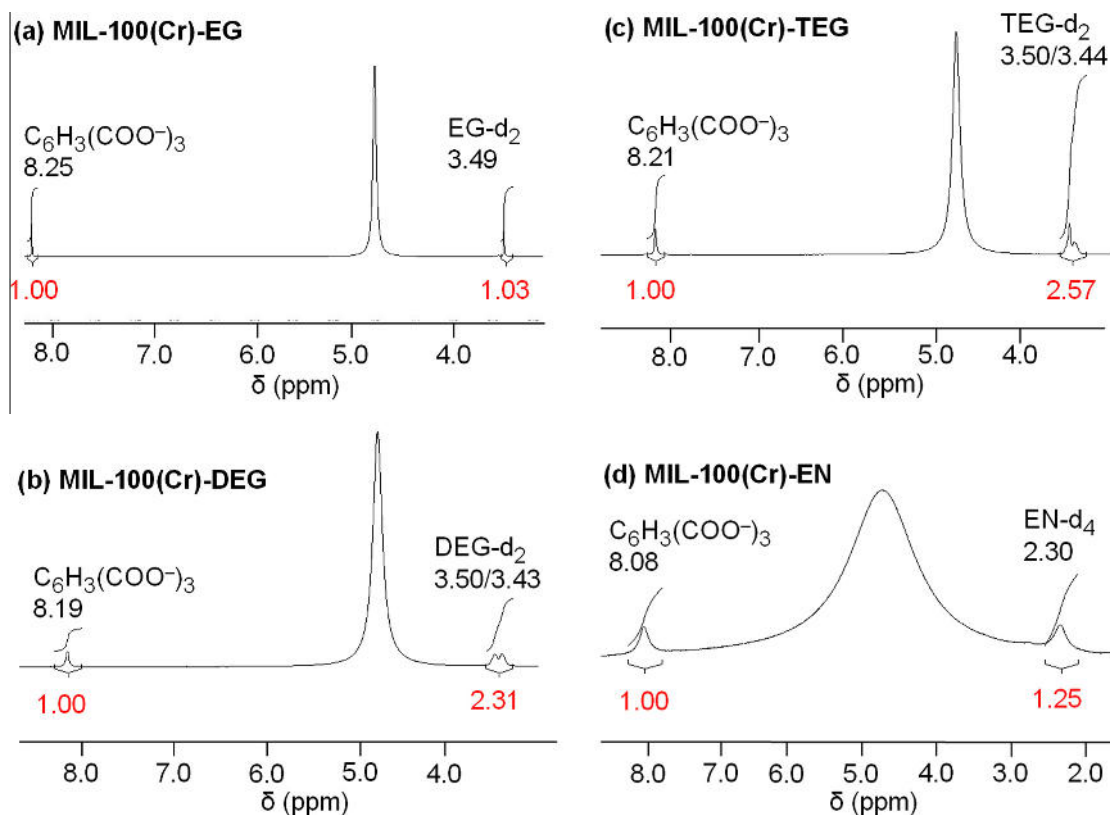


**Fig. 5.**  $^1\text{H}$  NMR spectra (200 MHz) of the organic components in  $\text{D}_2\text{O}/\text{NaOD}$  solution after decomposition of (a) MIL-100(Cr)-EG, (b) MIL-100(Cr)-DEG, (c) MIL-100(Cr)-TEG and (d) MIL-100(Cr)-EN in  $\text{D}_2\text{O}/\text{NaOD}$  (40 wt.% of NaOD in  $\text{D}_2\text{O}$ ) with the relative intensities (in red) and assignments of individual (pH dependent) resonances. The solvent signals  $\text{D}_2\text{O}$  were set to  $\delta = 4.79$  ppm. (For interpretation of the references to colour in this figure legend, the reader is referred to the web version of this article.)

respectively (Fig. 4b). This indicates that a possible exchange of aqua ligands by glycol ligands occurs only to an insignificant extent. As a result it can be stated that grafting of MIL-100(Cr) with glycols requires vacant Cr(III) sites for coordination. However, the IR-spectrum of the EN-modified compound, obtained after water treatment, shows bands for aliphatic  $\nu(\text{C-H})$ -stretching vibrations at 2968 and 2892  $\text{cm}^{-1}$  (Fig. 4b) as before in Fig. 4a. This indicates that aqua ligands were exchanged by EN due to the larger nucleophilicity of the latter.

### 3.2. Quantification of grafting reagents by NMR-spectroscopy

To determine quantitatively the amount of grafted EG, DEG, TEG and EN, the modified MILs were hydrolyzed in  $\text{D}_2\text{O}/\text{NaOD}$  (see Supplementary data for details).  $^1\text{H}$  NMR spectra were recorded of the supernatant solution after hydrolysis and show signals of the deprotonated and deuterium exchanged ligand  $\text{C}_6\text{H}_3(\text{COO}^-)_3$  ligand ( $\text{BTC}^{3-}$ ) and the grafting reagents (EG- $\text{d}_2$ , DEG- $\text{d}_2$ , TEG- $\text{d}_2$ , EN- $\text{d}_4$ ) (Fig. 5).

The amounts of grafted EG, DEG, TEG and EN in MIL-100(Cr) range from 0.64 to 0.94 for the molar BTC to graft molecule ratio and 0.43 to 0.63 for the molar Cr: graft ratio (Table 1).

### 3.3. $\text{N}_2$ -sorption studies

Successful grafting explains the decrease in BET surface from  $\text{N}_2$ -sorption measurements. The BET surfaces of the modified compounds MIL-100(Cr)-EG, MIL-100(Cr)-DEG, MIL-100(Cr)-TEG and MIL-100(Cr)-EN are reduced to approximately 50% compared to the BET surface area of non-modified MIL-100(Cr). With the BET surface also the available pore volume is reduced (Table 2).

**Table 1**

Amount of graft reagent in modified MIL-100(Cr).

Graft reagent	MIL-100(Cr)			
	-EG	-DEG	-TEG	-EN
Molar ratio <sup>a</sup> BTC:graft reagent	1:0.77	1:0.87	1:0.64	1:0.94
Molar ratio <sup>b</sup> Cr:graft reagent	1:0.51	1:0.58	1:0.43	1:0.63
wt.% Graft reagent <sup>c</sup>	13.6%	23.4%	24.1%	15.7%

<sup>a</sup> Determined from  $^1\text{H}$  NMR integrals of aromatic H atoms of  $\text{C}_6\text{H}_3(\text{COO}^-)_3$  ligand and aliphatic  $\text{CH}_2$  groups of grafting reagents (EG- $\text{d}_2$ , DEG- $\text{d}_2$ , TEG- $\text{d}_2$ , EN- $\text{d}_4$ ), see Fig. 5. The NMR proton ratio takes into account the different proton number of the  $\text{C}_6\text{H}_3(\text{COO}^-)_3$  linker (3 H atoms), EG (4), DEG (8), TEG (12) and EN (4 H atoms).

<sup>b</sup> Calculated based on the molar ratio of 3:2 for Cr and BTC ligand in  $(\text{Cr}_3(\mu_3\text{-O})(\text{F})(\text{BTC})_2)$  ( $\text{C}_{18}\text{H}_6\text{Cr}_3\text{FO}_{13}$ , 605.231  $\text{g mol}^{-1}$ ).

<sup>c</sup>  $w(x) = \frac{m(\text{graft})}{m(\text{graft}) + m(\text{MIL-100})}$ . Calculated based on the molar masses ( $\text{g mol}^{-1}$ ) of EG (62.07), DEG (106.12), TEG (150.17) and EN (60.10).

The pore size distribution curves indicate that non-modified MIL-100(Cr) possesses two different kinds of pores with average pore diameters of 15 and 26 Å, respectively (Fig. 6). Possibly due to retained impurities the average diameters of both pores are smaller than expected (25 and 29 Å, cf. Fig. 2) [49,50]. Grafting of MIL-100(Cr) with EG, DEG and TEG leads to at least three different kinds of pores with diameters varying around 12, 15 and 19 Å. In the case of MIL-100(Cr)-DEG, a small fraction of the pores seems to remain unaltered with a pore diameter of 26 Å. Filling of the larger pores of 26 Å probably leads to the reduced pore size of about 19 Å. The smaller pores of MIL-100(Cr) (15 Å diameter) are mostly transformed to pores with a diameter of about 12 Å in all three cases. Grafting of MIL-100(Cr) with EN leads to five type of pores with diameters of 12, 15, 19, 23 and 26 Å (Fig. 6). Filling of the

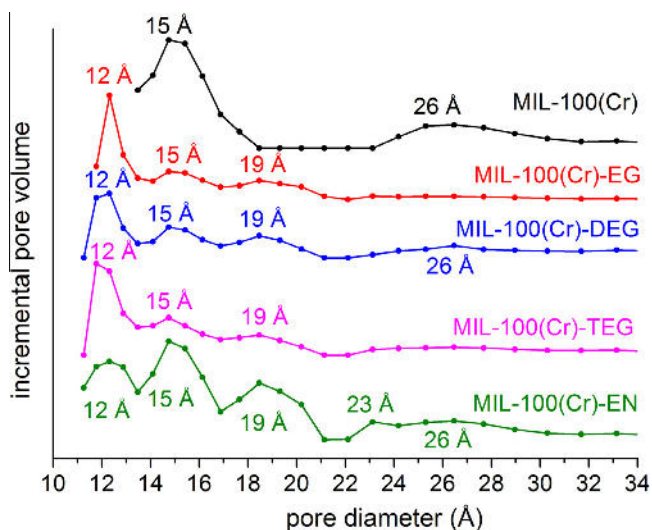


Fig. 6. Pore size distribution curves of non-modified MIL-100(Cr) and EG-, DEG-, TEG- and EN-modified MIL-100(Cr).

larger pores (26 Å) with EN mostly leads to the reduced pore sizes of 19 and 23 Å with a residual amount of original pores (26 Å). The smaller pores of MIL-100(Cr) (15 Å) are again partially transformed into pores with a diameter of ~12 Å.

### 3.4. Water sorption studies

Water adsorption isotherms of MIL-100(Cr)-EG, MIL-100(Cr)-DEG, MIL-100(Cr)-TEG and MIL-100(Cr)-EN are shown in comparison to the adsorption isotherm of the native MIL-100(Cr) (Fig. 7). Water loading values are included in Table 2. The water sorption isotherm of MIL-100(Cr) has been investigated in detail before [30].

Despite the reduction of the BET surfaces of grafted MIL-100(Cr) by about or more than 50% compared to non-modified MIL-100(Cr) (see Table 2), the water loadings remain comparatively high (Fig. 7, Table 2). The EG- and DEG-modified samples even have slightly higher water uptake capacities, compared to native MIL-100(Cr). However, the increase in the water adsorption isotherm near  $P \cdot P_0^{-1} = 1$  may be due to a water condensation effect, which can occur close to the dew point of water [63,64]. The water uptake capacity is not only determined by the available porosity, but also by the hydrophobicity/hydrophilicity of the ligand, the hydrogen-bonding capabilities, directing and interference effects of functional groups, site preference and a possible degradation or struc-

Table 2  
Nitrogen and water adsorption measurements.

Compound	BET surface area ( $\text{m}^2 \text{g}^{-1}$ ) of activated material <sup>a</sup>	Total pore volume ( $\text{cm}^3 \text{g}^{-1}$ ) <sup>b</sup>	max. water loading ( $\text{g g}^{-1}$ ) at 20 °C <sup>c</sup>	BET surface area ( $\text{m}^2 \text{g}^{-1}$ ) after water sorption <sup>d</sup>
MIL-100(Cr)	1330	0.77	0.40	–
MIL-100(Cr)-EG	710	0.47	0.43	800
MIL-100(Cr)-DEG	580	0.50	0.42	720
MIL-100(Cr)-TEG	680	0.53	0.33	700
MIL-100(Cr)-EN	640	0.42	0.37	690 <sup>d</sup> , 700 <sup>e</sup>

<sup>a</sup> BET surface area calculated at  $0.05 < P \cdot P_0^{-1} < 0.2$  from  $\text{N}_2$  sorption isotherm at 77 K with a standard deviation of  $\pm 20 \text{ m}^2/\text{g}$ .

<sup>b</sup> Calculated from  $\text{N}_2$  sorption isotherm at 77 K ( $P \cdot P_0^{-1} = 0.95$ ) for pores  $\leq 20 \text{ nm}$ .

<sup>c</sup> Calculated from water sorption isotherm at 293 K ( $P \cdot P_0^{-1} = 0.9$ ).

<sup>d</sup> After single water sorption experiment.

<sup>e</sup> After 20 water sorption cycle experiments.

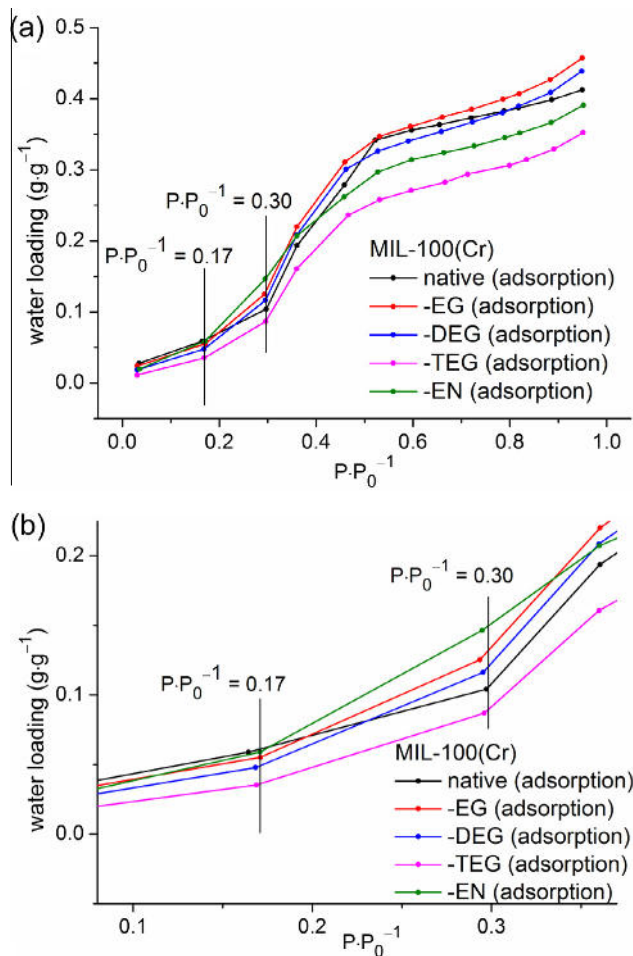
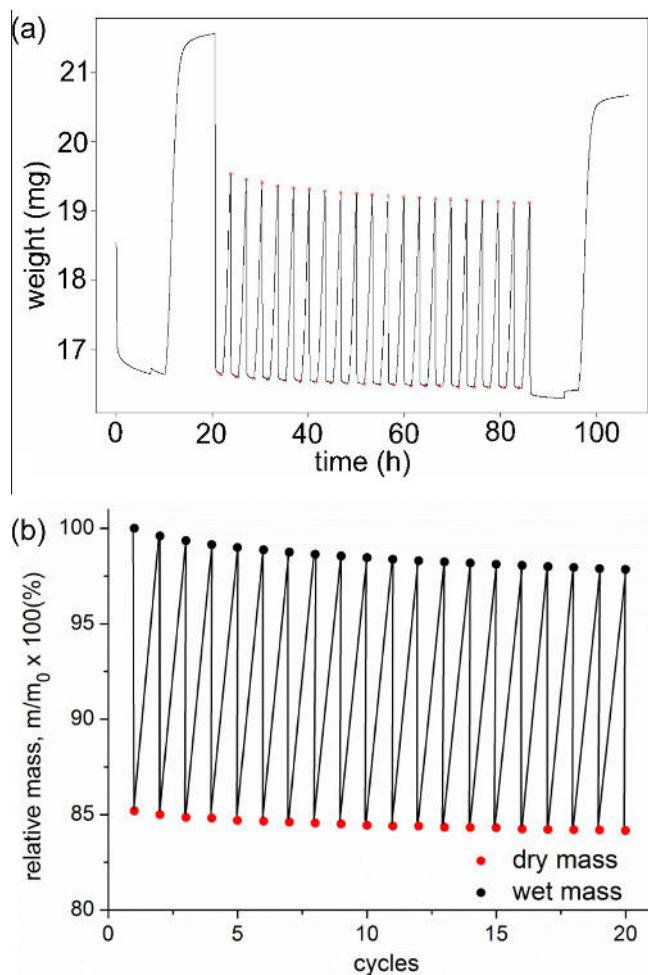


Fig. 7. (a) Water adsorption isotherms of non-modified MIL-100(Cr) and EG-, DEG-, TEG- and EN-modified MIL-100(Cr) at 293 K. (b) Enlargement for region  $0.10 < P \cdot P_0^{-1} < 0.35$ .

ture transition of the adsorbent material [65]. The inverse relation of the pore size distribution and the water adsorption capacity was tried to understand by infrared spectroscopy and  $\text{N}_2$ -sorption studies of the compounds after water sorption measurements. The IR-spectra of the four grafted samples show that MIL-100(Cr)-EG loses part of the coordinated EG. Coordinated DEG, TEG and EN is still visible in the IR-spectra and their  $\nu(\text{C-H})$ - and  $\nu(\text{C-O})$ - or  $\nu(\text{C-N})$ -bands show only a slight decrease in their intensities (Fig. S4b, Fig. S7). The BET surface areas of the grafted samples, recorded after water sorption measurements, are only slightly increased compared to the surface areas measured before (Table 2). Both studies agree that only a small part of EG, DEG, TEG and EN is removed through the water sorption measurements. The high water uptakes together with the reduction of the surface areas can only be explained by the fact that the sizes of the pores are not the crucial factor for a high amount of adsorbed water. The chemical alteration of the MOF material after modification seems to dominate the water uptake capacities.

The samples MIL-100(Cr)-EG, MIL-100(Cr)-DEG and MIL-100(Cr)-EN exhibit even a slightly favored water uptake compared to MIL-100(Cr) due to the higher slope of the adsorption isotherms of the modified compounds in comparison to MIL-100(Cr) in a region of  $0.17 < P \cdot P_0^{-1} < 0.30$  (Fig. 7a and b). This proof of concept demonstrates that it is possible to shift the water adsorption isotherms to lower relative pressure by grafting hydrophilic groups onto coordinatively unsaturated metal sites.



**Fig. 8.** (a) Water load signal and (b) relative mass variation of MIL-100(Cr)-EN during water desorption and adsorption over 20 cycles acquired at  $p_{\text{H}_2\text{O}} = 5.6$  kPa. In (b) the initial mass  $m_0$  with adsorbed water is set to 100% and the subsequent masses related thereupon as  $m/m_0 \times 100\%$

A porous sorption material for thermally driven adsorptions chillers or heat pump applications should show a high water uptake capacity in between  $0.05 < P \cdot P_0^{-1} < 0.32$  relative pressure range, that is, at low to medium humidity. With regard to the performance at low to medium water partial pressure, an adsorption/desorption cycle stability test of the promising MIL-100(Cr)-EN was performed, monitoring the loading of the sample by thermogravimetry (Fig. 8). The EN-grafted MIL-100(Cr) was chosen for the cycle stability test due to the higher stability of the Cr-EN coordinative bond compared to the Cr-glycol bond. The sample has been exposed to a humidified gas flow in a short cycle test consisting of a continuous cycling between 140 and 40 °C over 20 cycles under a constant partial water vapor pressure of 5.6 kPa using argon as a carrier and 4 h per cycle. As the heat of adsorption is poorly dissipated in the cycling experiments, kinetics is slow and absolute equilibrium is reached only in the long analytic cycles at the beginning and in the end of the experiment (Fig. 8a). The change of total mass variation during water desorption and adsorption is shown in Fig. 8, which indicates a total (dry) mass loss of 1.7%. Compared to non-grafted MOFs like MIL-100(Fe) and MIL-100(Al) ( $\Delta$  dry mass loss = 0.6% (Fe), 1.4% (Al)) the mass loss of EN-grafted MIL-100(Cr) is only slightly increased [33]. Water loading capacities were measured before and after the cycles. The total water loading loss of 10.8% the long analytic cycles at the beginning and in the end of the experiment (Fig. 8a) indicates

**Table 3**  
Results of water cycling stability test of MIL-100(Cr)-EN.

	Before cycling	After cycling	$\Delta$ (%)
Dry mass (mg)	16.64	16.35	-1.7
Water loading ( $\text{g g}^{-1}$ )	0.296	0.264	-10.8
BET surface ( $\text{m}^2 \text{g}^{-1}$ )	640	700	+9.4

some sort of degradation. This degradation of MIL-100(Cr)-EN is higher than in MIL-101(Cr) (-1.9%) [31], MIL-100(Fe) (-3.0%) and MIL-100(Al) (-4.5%) [33]. The increased mass and water loading loss could be explained due to a partial loss of grafted ethylenediamine. The partial loss of EN is supported by the loss in dry mass. The results of the cycling stability test are summarized in Table 3.

Powder X-ray diffraction, infrared-spectroscopy and BET measurements were carried out after 20 cycles. There is no significant change in crystallinity (Fig. 3). The IR-spectrum appears almost unchanged (Fig. S7) and the BET-surface increases from  $640 \text{ m}^2 \text{g}^{-1}$  before to  $700 \text{ m}^2 \text{g}^{-1}$  after 20 water cycles (Table 2). This BET surface increase of 9.4% may be due to a partial loss of coordinated ethylenediamine, concomitant with the decrease in dry mass. Long-time measurements will have to prove the stability of MIL-100(Cr)-EN after a large number of cycles. Regarding possible practical applications, the use of EN-grafted MIL-100 has to be critically evaluated due to the partial loss of EN as evidenced by BET- and water loading measurements before and after 20 water adsorption-desorption cycles. Cycling experiments with an even larger number of water cycles still have to evaluate the practical use of this new compound.

#### 4. Conclusions

We presented the grafting of coordinatively unsaturated metal sites (CUS) in MIL-100(Cr) with EG, DEG, TEG and EN characterized by IR-spectroscopy and  $\text{N}_2$ -sorption measurements. The slope of the water adsorption isotherms of MIL-100(Cr)-EG, MIL-100(Cr)-DEG and MIL-100(Cr)-EN in the  $0.17 < P \cdot P_0^{-1} < 0.30$  is increased, compared to native MIL-100(Cr). This means that water uptake in the modified materials is favored in this partial pressure region for thermally driven adsorptions chillers or heat pump applications which should show a high water uptake capacity in between  $0.05 < P \cdot P_0^{-1} < 0.32$  relative pressure range, that is, at low to medium humidity. In spite of the fact that the modifications of MIL-100(Cr) lead to materials with reduced pore sizes, the total water uptake capacities remain high. Water adsorption capacity correlates with the available pore volume and the hydrophobicity/hydrophilicity of the ligand, the hydrogen-bonding capabilities and directing effects of functional groups, site preference and a possible degradation or structure transition. The increased hydrophilicity of the MOF material after modification seems to dominate the water uptake capacities. Further, smaller pores can be advantageous for earlier water adsorption and condensation [30,33]. Despite the different interaction between MOFs and active carbon or AlPOs with water smaller pores in the range of 6–10 Å known from active carbon and AlPOs might be preferable also in case of MOFs for earlier water adsorption [66].

This proof-of-concept illustrates and opens the possibility to fine-tune the water adsorption characteristics based on well-investigated stable MOFs without linker or post-synthetic linker modification by simple addition (grafting) of terminal ligands to free metal sites or exchange of terminal aqua ligands at the metal sites. An amine ligand has shown more stable binding to Cr(III) over alcohol ligands and more amine ligands will be investigated in more detail for the grafting of MIL-100(Cr) and MIL-101(Cr).

## Acknowledgement

Funding by the Federal of Economics (BMW) under Grant 0327851A/B is gratefully acknowledged.

## Appendix A. Supplementary material

Supplementary data associated with this article can be found, in the online version, at <http://dx.doi.org/10.1016/j.ica.2013.07.024>.

## References

- [1] J.R. Long, O.M. Yaghi, *Chem. Soc. Rev.* 38 (2009) 1213.
- [2] K. Biradha, M.J. Zaworotko, *New J. Chem.* 34 (2010) 2353.
- [3] S. Kitagawa, S. Natarajan, *Eur. J. Inorg. Chem.* 24 (2010) 3685.
- [4] C. Janiak, *Dalton Trans.* 14 (2003) 2781.
- [5] C. Janiak, J.K. Vieth, *New J. Chem.* 34 (2010) 2366.
- [6] A.U. Czaja, N. Trukhan, U. Müller, *Chem. Soc. Rev.* 38 (2009) 1284.
- [7] U. Müller, M. Schubert, F. Teich, H. Pütter, K. Schierle-Arndt, J. Pastré, *J. Mater. Chem.* 16 (2006) 626.
- [8] (a) H. Wu, Q. Gong, D.H. Olson, J. Li, *Chem. Rev.* 112 (2012) 836;  
(b) K. Li, D.H. Olson, J. Li, *Inorg. Chem.* 12 (2010) 13.
- [9] (a) L.J. Murray, M. Dinca, J.R. Long, *Chem. Soc. Rev.* 38 (2009) 1294;  
(b) R.E. Morris, P.S. Wheatley, *Angew. Chem., Int. Ed.* 47 (2008) 4966.
- [10] J.-R. Li, R.J. Kuppler, H.-C. Zhou, *Chem. Soc. Rev.* 38 (2009) 1477.
- [11] (a) M. Paik Suh, Y.E. Cheon, E.Y. Lee, *Coord. Chem. Rev.* 252 (2008) 1007;  
(b) C.J. Kepert, *Chem. Commun.* 7 (2006) 695.
- [12] M. Paik Suh, H.J. Park, T.K. Prasad, D.-W. Lim, *Chem. Rev.* 112 (2012) 782.
- [13] (a) T. Düren, Y.-S. Bae, R.Q. Snurr, *Chem. Soc. Rev.* 38 (2009) 1237;  
(b) S.S. Han, J.L. Mendoza-Cortés, W.A. Goddard, *Chem. Soc. Rev.* 38 (2009) 1460;  
(c) R.B. Getman, Y.-S. Bae, C.E. Wilmer, R.Q. Snurr, *Chem. Rev.* 112 (2012) 703.
- [14] (a) Z. Chen, S. Xiang, H.D. Arman, P. Li, S. Tidrow, D. Zhao, B. Chen, *Eur. J. Inorg. Chem.* 24 (2010) 3745;  
(b) F. Ma, S. Liu, D. Liang, G. Ren, C. Zhang, F. Wei, Z. Su, *Eur. J. Inorg. Chem.* 24 (2010) 3756.
- [15] Z. Zhang, Y. Zhao, Q. Gong, Z. Li, J. Li, *Chem. Commun.* 49 (2013) 653.
- [16] (a) J.-R. Li, Y. Ma, M.C. McCarthy, J. Sculley, J. Yu, H.-K. Jeong, P.B. Balbuena, H.-C. Zhou, *Coord. Chem. Rev.* 255 (2011) 1791;  
(b) J.-R. Li, J. Sculley, H.-C. Zhou, *Chem. Rev.* 112 (2012) 869.
- [17] D. Liu, C. Zhong, *J. Mater. Chem.* 20 (2010) 10308.
- [18] G. Férey, C. Serre, T. Devic, G. Maurin, H. Jobic, P.L. Llewellyn, G. De Weireld, A. Vimont, M. Daturi, J.-S. Chang, *Chem. Soc. Rev.* 40 (2011) 550.
- [19] (a) S.K. Nune, P.K. Thallapally, B.P. McGrail, *J. Mater. Chem.* 20 (2010) 7623;  
(b) G.-P. Hao, W.-C. Li, A.-H. Lu, *J. Mater. Chem.* 21 (2011) 6447.
- [20] (a) H.B. Tanh Jeazet, C. Staudt, C. Janiak, *Dalton Trans.* 41 (2012) 14003;  
(b) B. Zornoza, C. Tellez, J. Coronas, J. Gascon, F. Kapteijn, *Microporous Mesoporous Mater.* 166 (2013) 67;  
(c) D. Bastani, N. Esmaili, M. Asadollahi, *J. Ind. Eng. Chem.* 19 (2013) 375;  
(d) G. Dong, H. Li, V. Chen, *J. Mater. Chem. A* 1 (2013) 4610.
- [21] M. Yoon, R. Srirambalaji, K. Kim, *Chem. Rev.* 112 (2012) 1196.
- [22] D. Farrusseng, S. Aguado, C. Pinel, *Angew. Chem., Int. Ed.* 48 (2009) 7502.
- [23] J. Lee, O.K. Farha, J. Roberts, K.A. Scheidt, S.T. Nguyen, J.T. Hupp, *Chem. Soc. Rev.* 38 (2009) 1450.
- [24] L. Ma, C. Abney, W. Lin, *Chem. Soc. Rev.* 38 (2009) 1248.
- [25] T. Ladrak, S. Smulders, O. Roubeau, S.J. Teat, P. Gamez, J. Reedijk, *Eur. J. Inorg. Chem.* 24 (2010) 3804.
- [26] W. Kleist, F. Jutz, M. Maciejewski, A. Baiker, *Eur. J. Inorg. Chem.* 24 (2009) 3552.
- [27] Yu.I. Aristov, *J. Chem. Eng. Jpn.* 40 (2007) 1241.
- [28] E. Biemmi, A. Darga, N. Stock, T. Bein, *Microporous Mesoporous Mater.* 114 (2008) 380.
- [29] S.K. Henninger, H.A. Habib, C. Janiak, *J. Am. Chem. Soc.* 131 (2009) 2776.
- [30] G. Akiyama, R. Matsuda, S. Kitagawa, *Chem. Lett.* 39 (2010) 360.
- [31] J. Ehrenmann, S.K. Henninger, C. Janiak, *Eur. J. Inorg. Chem.* 4 (2011) 471.
- [32] J.-P. Zhang, A.-X. Zhu, R.-B. Lin, X.-L. Qi, X.-M. Chen, *Adv. Mater.* 23 (2011) 1268.
- [33] F. Jeremias, A. Khutia, S.K. Henninger, C. Janiak, *J. Mater. Chem.* 22 (2012) 10148.
- [34] (a) C. Janiak, S.K. Henninger, *Chimia* 67 (2013) 754;  
(b) S.K. Henninger, F. Jeremias, H. Kummer, C. Janiak, *Eur. J. Inorg. Chem.* 16 (2012) 2625.
- [35] G. Akiyama, R. Matsuda, H. Sato, A. Hori, M. Takata, S. Kitagawa, *Microporous Mesoporous Mater.* 157 (2012) 89.
- [36] (a) A. Khutia, H.U. Rammelberg, T. Schmidt, S. Henninger, C. Janiak, *Chem. Mater.* 25 (2013) 1235;  
(b) F. Jeremias, V. Lozan, S. Henninger, C. Janiak, *Dalton Trans.* (2013) in press, Doi: <http://dx.doi.org/10.1039/C3DT51471D>.
- [37] (a) Yu.I. Aristov, *Appl. Therm. Eng.* 50 (2013) 1610;  
(b) A. Hauer, *Adsorption* 13 (2007) 399;  
(c) T. Núñez, W. Mittelbach, H.-M. Henning, *Appl. Therm. Eng.* 27 (2007) 2205.
- [38] (a) S.K. Henninger, F. Jeremias, H. Kummer, P. Schossig, H.-M. Henning, *Energy Procedia* 30 (2012) 279;  
(b) H. Demira, M. Mobedi, S. Ülkü, *Renewable Sustainable Energy Rev.* 12 (2008) 2381;  
(c) Yu.I. Aristov, B. Dawoud, I.S. Glaznev, A. Elyas, *Int. J. Heat Mass Transfer* 51 (2008) 4966;  
(d) H.-M. Henning, *Appl. Therm. Eng.* 27 (2007) 1734.
- [39] (a) Yu.I. Aristov, *Int. J. Refrig.* 32 (2009) 675;  
(b) B.B. Saha, A. Chakraborty, S. Koyama, Yu.I. Aristov, *Int. J. Heat Mass Transfer* 52 (2009) 516;  
(c) R.E. Critoph, Z. Tamainot-Telto, S.J. Metcalf, *Int. J. Refrig.* 32 (2009) 1212;  
(d) J.V. Veselovskaya, R.E. Critoph, R.N. Thorpe, S. Metcalf, M.M. Tokarev, Yu.I. Aristov, *Appl. Therm. Eng.* 30 (2010) 1188.
- [40] Y.-K. Seo, J.W. Yoon, J.S. Lee, Y.K. Hwang, C.-H. Jun, J.-S. Chang, S. Wuttke, P. Bazin, A. Vimont, M. Daturi, S. Bourrelly, P.L. Llewellyn, P. Horcajada, C. Serre, G. Férey, *Adv. Mater.* 24 (2012) 806.
- [41] J. Jänchen, D. Ackermann, H. Stach, W. Brösicke, *Sol. Energy* 76 (2004) 339.
- [42] E. Ng, S. Mintova, *Microporous Mesoporous Mater.* 114 (2008) 1.
- [43] S.K. Henninger, F.P. Schmidt, H.-M. Henning, *Appl. Therm. Eng.* 30 (2010) 1692.
- [44] (a) L. Hamon, C. Serre, T. Devic, T. Loiseau, F. Millange, G. Férey, G. De Weireld, *J. Am. Chem. Soc.* 131 (2009) 8775;  
(b) P.L. Llewellyn, S. Bourrelly, C. Serre, A. Vimont, M. Daturi, L. Hamon, G. De Weireld, J.-S. Chang, D.-Y. Hong, Y.K. Hwang, S.H. Jhung, G. Férey, *Langmuir* 24 (2008) 7245;  
(c) A. Vimont, J.-M. Goupil, J.-C. Lavalley, M. Daturi, S. Surblé, C. Serre, F. Millange, G. Férey, N. Audebrand, *J. Am. Chem. Soc.* 128 (2006) 3218.
- [45] G. Férey, C. Mellot-Draznieks, C. Serre, F. Millange, J. Dutour, S. Surblé, I. Margiolaki, *Science* 309 (2005) 2040.
- [46] G. Férey, *Dalton Trans.* 23 (2009) 4400.
- [47] G. Férey, C. Serre, *Chem. Soc. Rev.* 38 (2009) 1380.
- [48] P. Küsgens, M. Rose, I. Senkowska, H. Fröde, A. Henschel, S. Siegle, S. Kaskel, *Microporous Mesoporous Mater.* 120 (2009) 325.
- [49] G. Férey, C. Serre, C. Mellot-Draznieks, F. Millange, S. Surblé, J. Dutour, I. Margiolaki, *Angew. Chem., Int. Ed.* 43 (2004) 6296.
- [50] P. Horcajada, S. Surblé, C. Serre, D.-Y. Hong, Y.-K. Seo, J.-S. Chang, J.-M. Grenèche, I. Margiolaki, G. Férey, *Chem. Commun.* 27 (2007) 2820.
- [51] C. Volkringer, D. Popov, T. Loiseau, G. Férey, M. Burghammer, C. Riekel, M. Haouas, F. Taulelle, *Chem. Mater.* 21 (2009) 5695.
- [52] Z. Wang, S.M. Cohen, *Chem. Soc. Rev.* 38 (2009) 1315.
- [53] S. Bernt, V. Guillermin, C. Serre, N. Stock, *Chem. Commun.* 47 (2011) 2838.
- [54] Y.K. Hwang, D.-Y. Hong, J.-S. Chang, S.H. Jhung, Y.-K. Seo, J. Kim, A. Vimont, M. Daturi, C. Serre, G. Férey, *Angew. Chem.* 120 (2008) 4212.
- [55] A. Vimont, H. Leclerc, F. Maugé, M. Daturi, J.-C. Lavalley, S. Surblé, C. Serre, G. Férey, *J. Phys. Chem. C* 111 (2007) 383.
- [56] H. Leclerc, A. Vimont, J.-C. Lavalley, M. Daturi, A.D. Wiersum, P.L. Llewellyn, P. Horcajada, G. Férey, C. Serre, *Phys. Chem. Chem. Phys.* 13 (2011) 11748.
- [57] C. Volkringer, H. Leclerc, J.-C. Lavalley, T. Loiseau, G. Férey, M. Daturi, A. Vimont, *J. Phys. Chem. C* 116 (2012) 5710.
- [58] L. D. Gelb, K.E. Gubbins, R. Radhakrishnan, M. Sliwinski-Bartowiak, *Rep. Prog. Phys.* 62 (1999) 1573.
- [59] N.A. Sedron, J.P.R.B. Walton, N. Quirk, *Carbon* 27 (1989) 853.
- [60] A. Vishnyakov, P. Ravikovitch, A.V. Neimark, *Langmuir* 16 (2000) 2311.
- [61] K. Krishnan, R.A. Plane, *Inorg. Chem.* 5 (1966) 852.
- [62] D.A. Young, T.B. Freedman, E.D. Lipp, L.A. Nafie, *J. Am. Chem. Soc.* 108 (1986) 7255.
- [63] A.L. Buck, *J. Appl. Meteorol.* 20 (1981) 1527.
- [64] D. Bolton, *Mon. Weather Rev.* 180 (1980) 1046.
- [65] (a) P.M. Schoenecker, C.G. Carson, H. Jasuja, C.J.J. Flemming, K.S. Walton, *Ind. Eng. Chem. Res.* 51 (2012) 6513;  
(b) G.E. Cmarik, M. Kim, S.M. Cohen, K.S. Walton, *Langmuir* 28 (2012) 15606;  
(c) H. Jasuja, J. Zang, D.S. Sholl, K.S. Walton, *J. Phys. Chem. C* 116 (2012) 23526.
- [66] A. Ristić, N.Z. Logar, S.K. Henninger, V. Kaučić, *Adv. Funct. Mater.* 22 (2012) 1952.



## Supplementary data

### Grafting of hydrophilic ethylene glycols or ethylenediamine on coordinatively unsaturated metal sites in MIL-100(Cr) for improved water adsorption characteristics

Martin Wickenheisser<sup>a</sup>, Felix Jeremias<sup>b</sup>, Stefan Henninger<sup>b</sup>, Christoph Janiak<sup>\*a</sup>

<sup>a</sup> *Institut für Anorganische Chemie und Strukturchemie, Universität Düsseldorf, 40204 Düsseldorf, Germany. E-mail: janiak@uni-duesseldorf.de*

<sup>b</sup> *Dept. Thermally Active Materials and Solar Cooling, Fraunhofer Institute for Solar Energy Systems ISE, Heidenhofstr. 2, 79110 Freiburg, Germany. E-mail: stefan.henninger@ise.fraunhofer.de*

## Experimental Section

### Synthesis of the starting materials

MIL-100(Cr)  $\{Cr_3(O)(F)(H_2O)_2(BTC)_2 \cdot \sim 28H_2O\}$ : MIL-100(Cr) was prepared according to the literature.<sup>1</sup> 1.200 g CrO<sub>3</sub> (12.00 mmol), 2.520 g H<sub>3</sub>BTC (11.99 mmol), 0.42 mL HF (12 mmol; 48-51 % in H<sub>2</sub>O) and 58 mL of deionized water were placed in a 90 mL Teflon-liner. The Teflon-liner was placed in an autoclave and heated to 473 K within 2 h. After 96 h the autoclave was cooled to r.t. within 2 h. The green powder was filtered, washed with deionized water (2 x 30 mL) and dried in air for 20 h. The IR-spectrum of the as-material showed impurities of unreacted H<sub>3</sub>BTC. For activation the powder was first stirred for 4 h in 140 mL DMF at 383 K, then additional 16 h at r.t.. After filtration and stirring for 5 h in 100 mL EtOH at 333 K, the green powder was centrifuged and stirred again for 20 h in 200 mL of deionized water at 363 K. After centrifugation the solid was dried in air. 2.650 g of light green powder was isolated (2.39 mmol, 60 % for  $\{Cr_3(\mu_3-O)(F)(BTC)_2 \cdot \sim 28H_2O\}$  (C<sub>18</sub>H<sub>6</sub>Cr<sub>3</sub>FO<sub>13</sub>·H<sub>56</sub>O<sub>28</sub>, 1109.65 g·mol<sup>-1</sup>)).<sup>2</sup>

<sup>1</sup> A. Vimont, J.-M. Goupil, J.-C. Lavalley, M. Daturi, S. Surblé, C. Serre, F. Millange, G. Férey, N. Audebrand, J. Am. Chem. Soc. 128 (2006), 3218–3227.

<sup>2</sup> The washing procedure above differed from the procedure described in the literature due to impurities of unreacted H<sub>3</sub>BTC.

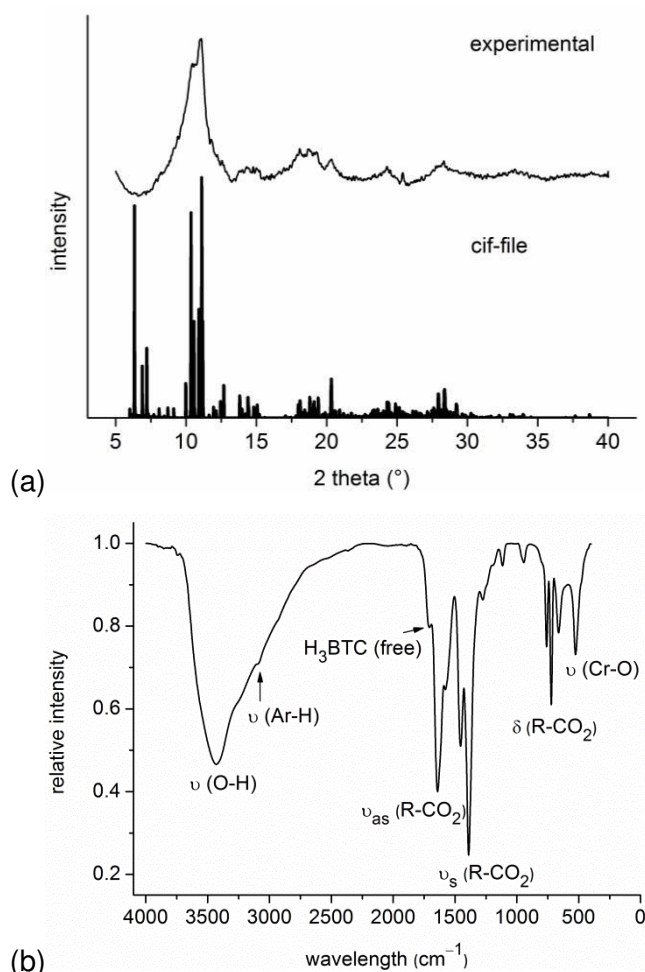


**Fig. S1.** (a) Experimental powder X-ray diffraction pattern of activated MIL-100(Cr) and theoretical XRD pattern simulated from the cif-file of MIL-100(Cr). The diffractogram was obtained with Cu-K $\alpha$ -radiation on flat layer sample holders where at low angle the beam spot is strongly broadened so that only a fraction of the reflected radiation reaches the detector, hence, the low relative intensities measured at  $2\theta < 7^\circ$ . (b) IR-spectrum (KBr) of activated MIL-100(Cr).

The PXRD pattern proves the successful synthesis of the MIL material due to the positions of the reflections, which are in good agreement with the simulated diffraction patterns (Fig. S1a). The IR-spectrum of the starting material MIL-100(Cr) (Fig. S1b), measured in air without previous degasing, shows broad bands between 3700 – 2700 cm<sup>-1</sup>, which can be assigned to  $\nu(\text{O-H})$ -vibrations of coordinated and free water in the pores. IR spectroscopic data exhibits the characteristic asymmetric and symmetric valence-vibrations of the carboxyl groups of the coordinated BTC-ligand between 1650 and 1370 cm<sup>-1</sup>. The region of 770 and 710 cm<sup>-1</sup> shows deformation-vibrations, coming from the carboxyl groups. Cr-O-valence-vibrations of CrO<sub>6</sub>-octahedrons can be found at 663 cm<sup>-1</sup>. The vibration band of low intensity at 1707 cm<sup>-1</sup> indicates small impurities of non-coordinated H<sub>3</sub>BTC, which could not be

removed through the washing procedure.  $N_2$ -sorption isotherm and the water sorption isotherm of activated MIL-100(Cr) are shown in Figure S2.

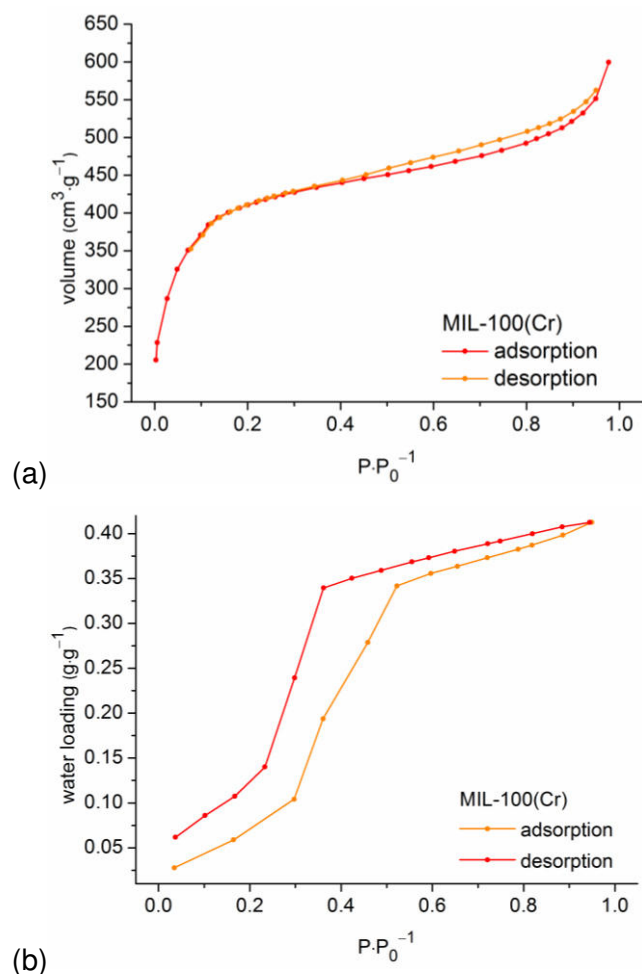


**Fig. S2.** (a)  $N_2$ -sorption isotherms of activated MIL-100(Cr) (degasing conditions: 19 h, 473 K). (b) water sorption isotherms of activated MIL-100(Cr) (degasing conditions: 3 h, 473 K).

### Synthesis of MIL-100(Cr)-EG, MIL-100(Cr)-DEG and MIL-100(Cr)-TEG

The activated, solid MIL-100(Cr) materials (100 mg) were placed in 50 mL two-necked flasks and degased for 1.5 h (MIL-100(Cr)-EG) and 1 h (MIL-100(Fe)-DEG, MIL-100(Fe)-TEG) in vacuo at 473 K to remove any adsorbed water or solvent from the metal sites, thus giving the coordinatively unsaturated sites (CUS). After cooling to r.t., 10 mL of dry toluene (water content of 0.015 %, determined by Karl Fischer titration) and 1.0 mL of EG ( $\rho = 1.11 \text{ g} \cdot \text{mL}^{-1}$ ; 18 mmol), 1.0 mL of DEG ( $\rho = 1.12 \text{ g} \cdot \text{mL}^{-1}$ ; 11 mmol) and 1.0 mL of TEG ( $\rho = 1.12 \text{ g} \cdot \text{mL}^{-1}$ ; 7.5 mmol) were added dropwise. The suspensions were stirred for 17.5 h at 373 K and the green solids were filtered from the clear supernatants. The crude products were washed with acetone (2 x 5 mL) and dried for 18 h at 373 K. In all three cases powders were isolated with the same colors compared to the starting material.

**Table S1.**  $\nu(\text{C-H})$ - and  $\nu(\text{C-O})$ -vibration bands (in  $\text{cm}^{-1}$ ) of neat EG, DEG and TEG and corresponding bands in MIL-100(Cr)-EG, MIL-100(Cr)-DEG and MIL-100(Cr)-TEG.

	EG <sup>a</sup>	DEG <sup>a</sup>	TEG <sup>a</sup>
$\nu(\text{C-H})$	2937, 2875	2924, 2871	2915, 2869
$\nu(\text{C-O})$	1083, 1033	1126, 1052	1116, 1058
	MIL-100(Cr)-EG <sup>b</sup>	MIL-100(Cr)-DEG <sup>b</sup>	MIL-100(Cr)-TEG <sup>b</sup>
$\nu(\text{C-H})$	2943, 2878	2928, 2879	2959, 2924, 2877
$\nu(\text{C-O})$	1086, 1042	1123, 1058	1106, 1072

<sup>a</sup> measured on ATR unit

<sup>b</sup> measured in KBr disk

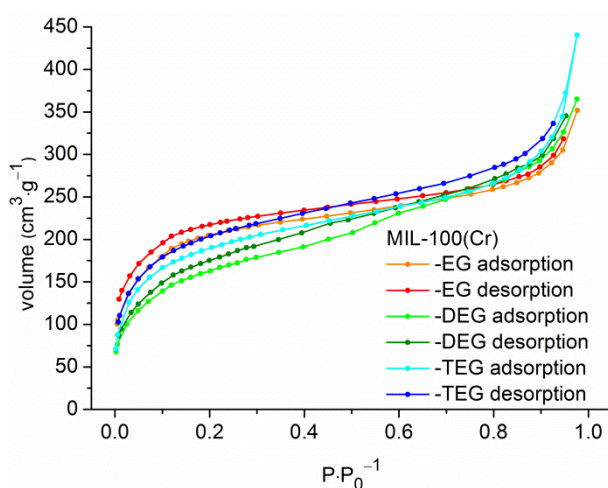


**Fig. S3.**  $\text{N}_2$ -sorption isotherms of EG-, DEG- and TEG-modified MIL-100(Cr) (degassing conditions: MIL-100(Cr)-EG: 3.5 h, 473 K; MIL-100(Cr)-DEG: 3.5 h, 473 K; MIL-100(Cr)-TEG: 2 h, 473 K).

In all three cases the colors of the powders did not change after  $\text{N}_2$ -sorption and after water sorption measurements.

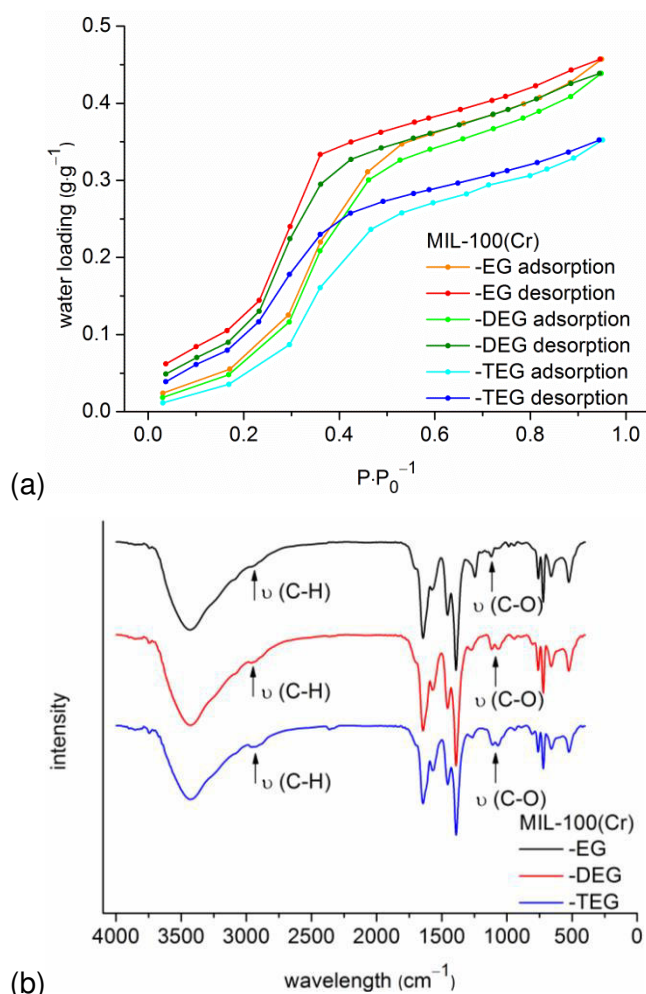


**Fig. S4.** (a) Water sorption isotherms of EG-, DEG- and TEG-modified MIL-100(Cr) (degassing conditions: MIL-100(Cr)-EG: 3.5 h, 473 K; MIL-100(Cr)-DEG: 3.5 h, 473 K; MIL-100(Cr)-TEG: 2 h, 473 K). (b) IR-spectra (KBr) of EG-, DEG- and TEG-modified MIL-100(Cr) **after** water sorption measurements.

IR-spectra of these three samples, recorded after water sorption measurements, show that MIL-100(Cr)-EG loses part of coordinated EG. Coordinated DEG and TEG are still visible in the IR-spectra and their  $\nu(\text{C-H})$ - and  $\nu(\text{C-O})$ -bands show only a slight decrease in their intensities (Fig. S4b).  $\text{N}_2$ -sorption measurements were done on the same three samples, which were measured for water sorption before (Fig. S5).

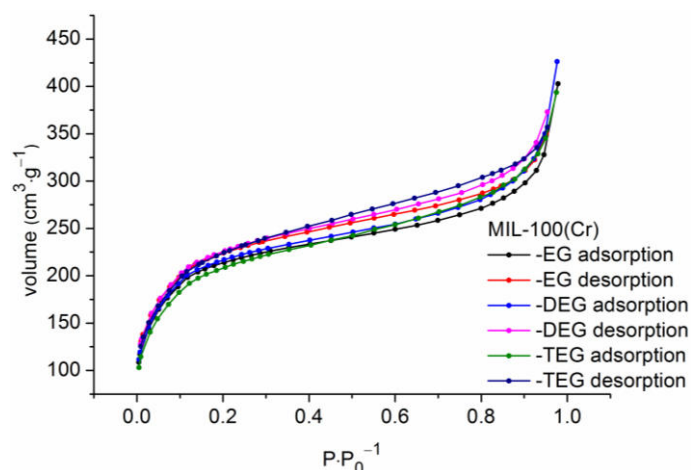


**Fig. S5.**  $N_2$ -sorption isotherms of EG-, DEG- and TEG-modified MIL-100(Cr) **after** water sorption measurements (degassing conditions: MIL-100(Cr)-EG: 2.5 h, 473 K; MIL-100(Cr)-DEG: 2.5 h, 473 K; MIL-100(Cr)-TEG: 2.5 h, 473 K).

### Synthesis of MIL-100(Cr)-EN

The activated, solid MIL-100(Cr) material (100 mg) was placed in a 50 mL two-necked flask and degased for 1 h 45 min in vacuo at 473 K to remove any adsorbed water or solvent from the metal sites, thus giving the coordinatively unsaturated sites (CUS). After cooling to r.t., 10 mL of dry toluene (water content of 0.015 %, determined by Karl Fischer titration) and 1.0 mL of EN ( $\rho = 0.90 \text{ g}\cdot\text{mL}^{-1}$ ; 15 mmol) was added dropwise. The suspension was stirred for 16 h at r.t. and the green solid was filtered from the clear supernatant. The product was washed with acetone (2 x 5 mL) and dried for 18 h at 373 K. A gray, greenish powder was isolated.

**Table S2.**  $\nu(\text{C-H})$ -vibration bands of neat EN and corresponding bands in MIL-100(Cr)-EN.

	EN <sup>a</sup>	MIL-100(Cr)-EN <sup>b</sup>	[ $\text{cm}^{-1}$ ]
$\nu(\text{C-H})$	2922, 2850	2969, 2894	

<sup>a</sup> measured on ATR unit

<sup>b</sup> measured in KBr disk

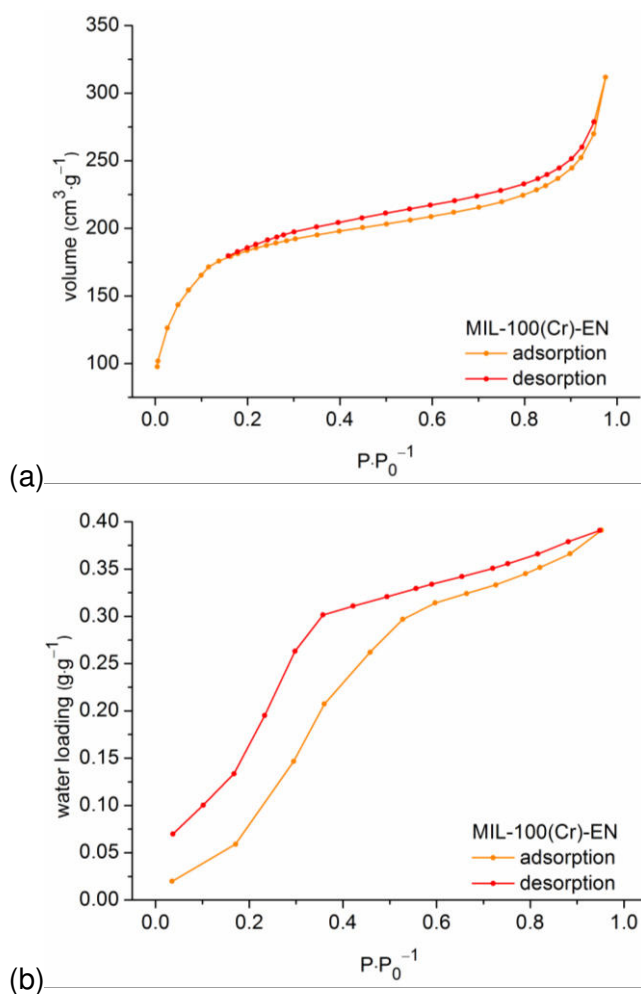


**Fig. S6.** (a)  $N_2$ -sorption isotherm of EN-modified MIL-100(Cr) (degassing conditions: 3 h, 473 K). (b) Water sorption isotherm of EN-modified MIL-100(Cr) (degassing conditions: 3 h, 473 K).

IR-spectra of MIL-100(Cr)-EN were measured after water sorption measurement and the cycling experiment, which proved that the coordination of EN was almost unchanged (Fig. S7).

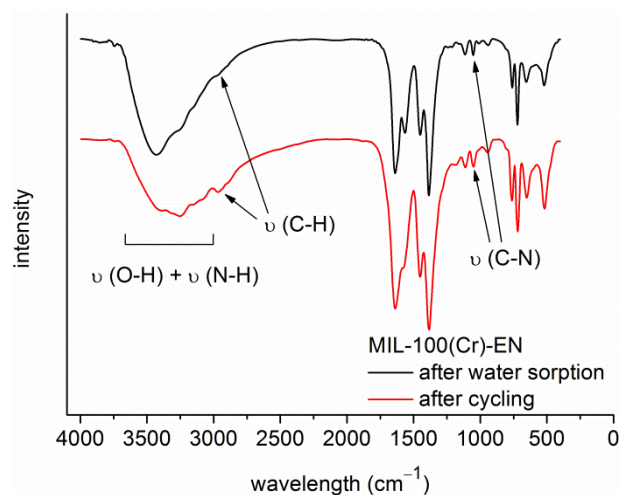


**Fig. S7.** IR-spectra of MIL-100(Cr)-EN **after** water sorption measurement and cycling experiment.

N<sub>2</sub>-sorption measurements were done on the samples after water sorption measurement and the cycling experiment (Fig. S8).

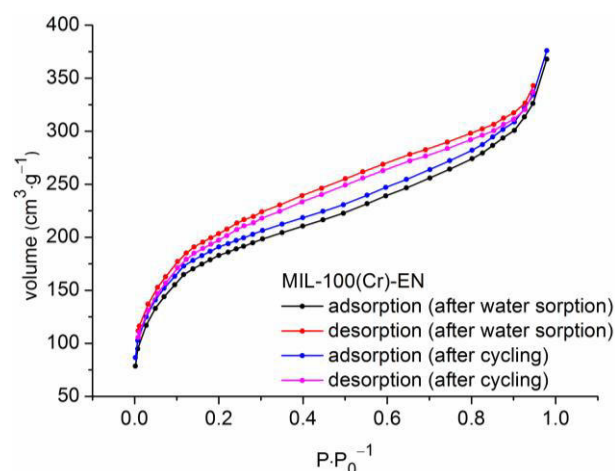


**Fig. S8.** N<sub>2</sub>-sorption isotherms of MIL-100(Cr)-EN **after** water sorption measurement and cycling experiment (degassing conditions: 3 h, 473 K).

### Reaction of MIL-100(Cr) with EG, DEG, TEG and EN without previous degassing of MIL-100(Cr)

The activated, solid MIL-100(Cr) materials (25 mg) were placed in 25 mL beakers and stirred for 10 min in 0.5 mL of deionized water to block the CUSs with water molecules. After adding 3 mL of DMF to the aqueous suspensions 0.25 mL of EG ( $\rho = 1.11 \text{ g}\cdot\text{mL}^{-1}$ ; 5 mmol), DEG ( $\rho = 1.12 \text{ g}\cdot\text{mL}^{-1}$ ; 2.8 mmol), TEG ( $\rho = 1.12 \text{ g}\cdot\text{mL}^{-1}$ ; 1.9 mmol) and EN ( $\rho = 0.90 \text{ g}\cdot\text{mL}^{-1}$ ; 3.8 mmol) were added dropwise. The reaction mixtures were stirred for 20 h at 373 K (EG, DEG, TEG) or at r.t. (EN). The solids were centrifuged from the clear supernatants, washed with acetone (2 x 4 mL) and dried for 20 min at 373 K. A gray, greenish powder was isolated



(MIL-100(Cr) + EN). Reactions of MIL-100(Cr) with EG, DEG and TEG led to powders with the same color like the starting material.

### Basic hydrolyses of EG-, DEG-, TEG- and EN-modified MIL-100(Cr) with D<sub>2</sub>O/NaOD

To quantify the amount of grafted EG, DEG, TEG and EN, 45 mg of MIL-100(Cr)-EG, MIL-100(Cr)-DEG, MIL-100(Cr)-TEG and MIL-100(Cr)-EN were stirred in 1.5 mL of a D<sub>2</sub>O/NaOD (40 wt % of NaOD in D<sub>2</sub>O) solution for 22 h at r.t.. The green supernatants were separated from the green precipitates (Cr(OD)<sub>3</sub>) by centrifugation and the alkaline solutions were measured by <sup>1</sup>H-NMR spectroscopy.

**Table S3.** Proton ratio (C-H bonds) of deprotonated ligand C<sub>6</sub>H<sub>3</sub>(COO<sup>-</sup>)<sub>3</sub> (BTC<sup>3-</sup>) and grafting reagents (EG-d<sub>2</sub>, DEG-d<sub>2</sub>, TEG-d<sub>2</sub>, EN-d<sub>4</sub>) determined by <sup>1</sup>H-NMR spectra.

BTC : EG-d <sub>2</sub>	BTC : DEG-d <sub>2</sub>	BTC : TEG-d <sub>2</sub>	D <sub>3</sub> BTC : EN-d <sub>4</sub>
1.00 : 1.03	1.00 : 2.31	1.00 : 2.57	1.00 : 1.25

### 3.2 Hierarchical embedding of micro-mesoporous MIL-101(Cr) in macroporous poly(2-hydroxyethyl methacrylate) for high internal phase emulsions with monolithic shape for vapor adsorption applications

M. Wickenheisser, C. Janiak

*Microporous Mesoporous Mater.* **2015**, *204*, 242–250. Reference 207.

<http://dx.doi.org/10.1016/j.micromeso.2014.11.025>

Impact factor 2013: 3.209

The usage of MOFs as potential thermally driven adsorption chiller or heat pumps is a fast growing research topic. Chemical modifications, either on a direct route before solvo-/hydrothermal treatment or post-synthetically, can influence the pore size or vapor uptake capacities in a very sensitive way, but one important factor is often neglected, when it should come to intended applications. Shaping of powdery metal-organic frameworks is an indispensable requirement for any kind of application. Therefore, MOFs can either be coated on surfaces or shaped e.g. into monoliths.<sup>223,224</sup>

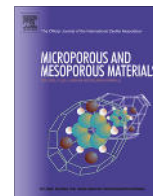
For monolithic MOF-shaping a further component, a so-called binding agent, is necessary, which possesses the ability to be manufactured in a monolithic shape. In case of heat transformation applications, these polymerized binding agents should further have the ability to be combined with powdery MOF particles without preventing vapor adsorption in the MOF pores.

In this work we obtained and analyzed different mechanically stable, monolithic MIL@Polymer composite materials, in which micro- and mesoporous MIL-101(Cr) was embedded into a macroporous HIPE foam based on cross-linked poly(2-hydroxyethyl methacrylate). MIL-101(Cr) is a promising material for potential heat transformation processes, due to its good chemical and thermal stability, high surface area, large vapor uptake capacities and good cycling stability.<sup>150</sup> Reports on water adsorption in pure HIPE materials are scarce.<sup>182,225,226</sup> The only MOF@HIPE reports, published so far, deal with the embedding of HKUST-1 into porous styrene- and polyacrylamide based HIPEs, but no potential applications were investigated.<sup>182,206</sup> Porosity characterization and vapor adsorption measurements have been carried out of the hierarchical MIL-101(Cr)@HIPE composites, possessing pores in the micro-meso-macro sized range.

Author's share of work:

- Designing, performing of the synthetic work and evaluation of the results except for measuring of the SEM images (done by Mr. Köhler).
- Writing of the manuscript and drawing of the figures except for figure A.9 (done by Mr. Janiak).
- Editing of the manuscript regarding the reviewers' comments.

Reprinted from ref. 207, Copyright 2014, with permission from Elsevier.



# Hierarchical embedding of micro-mesoporous MIL-101(Cr) in macroporous poly(2-hydroxyethyl methacrylate) high internal phase emulsions with monolithic shape for vapor adsorption applications



Martin Wickenheisser, Christoph Janiak\*

Institut für Anorganische Chemie und Strukturchemie I, Universitätsstraße 1, 40225 Düsseldorf, Germany

## ARTICLE INFO

### Article history:

Received 3 September 2014  
Received in revised form 14 October 2014  
Accepted 22 November 2014  
Available online 4 December 2014

### Keywords:

Metal-organic framework  
Hierarchical porosity  
High internal phase emulsion (HIPE)  
Monoliths  
Heat transformation

## ABSTRACT

Shaping metal-organic frameworks (MOFs), normally obtained as powders or microcrystals, e.g., into monoliths is one indispensable factor for potential applications of MOFs. MIL-101(Cr) as a water stable micro- and mesoporous network was successfully embedded into a macroporous and monolithic oil-water (o/w) high internal phase emulsion (HIPE) foam, based on crosslinked poly(2-hydroxyethyl methacrylate). These hierarchical and mechanically stable monolithic composite materials with up to 59 wt% of MIL-101(Cr) show higher methanol and water vapor uptake capacities compared to the pure HIPE.

© 2014 Elsevier Inc. All rights reserved.

## 1. Introduction

MOFs (metal-organic framework) are three-dimensional permanently porous networks based on metal ions or metal clusters, connected by organic ligands [1,2]. Metal organic frameworks have uniform micropore structures with high surface areas and large pore volumes. An immense research advancement has been made in the utilization of MOFs since the past 10–15 years [3–5], such as catalysis [6–9], gas storage [10–13] and gas separation [14–18]. Numerous overview or review articles has been published in the last years indicating the increasing interest in MOF chemistry [19–24].

Microporous materials with a high vapor uptake capacity are of increasing interest for low temperature heat transformation applications in thermally driven adsorption chillers (TDCs) or adsorption heat pumps (AHPs). TDCs or AHPs could be an alternative to traditional compressor air conditioners or heat pumps run by electricity or fossil fuels. The use of solar or waste heat as the driving energy in TDCs or AHPs can minimize primary energy consumption. In Fig. A.8 the thermodynamic principle for adsorption chillers or heat pumps is displayed [25–31]. In the case of a cooling application  $Q_{\text{evap}}$  is used as useful cold and  $Q_{\text{ads}}$  and  $Q_{\text{cond}}$  are released to

the environment. During a heat pump application  $Q_{\text{evap}}$  can be delivered from the environment at low temperature and  $Q_{\text{ads}}$  and  $Q_{\text{cond}}$  will be useful higher temperature heat. The working fluid is exchanged reversibly between the evaporation/condensation vessel and the porous material where ad- and desorption takes place. Alcohols like methanol or water are suitable, vaporizable working fluids due to their high evaporation enthalpies. Water is often the working fluid of choice because of its high evaporation enthalpy ( $2440 \text{ kJ kg}^{-1}$  at  $25^\circ\text{C}$ ) and non-toxicity despite the need to work under vacuum because of the low vapor pressure of only  $3.17 \text{ kPa}$  at  $25^\circ\text{C}$ . Alcohols like methanol and ethanol are interesting alternatives because of the lower boiling points so that evaporator temperatures below  $0^\circ\text{C}$  are possible [32].

New research developments aim for new porous materials as adsorbents due to disadvantages of classical adsorbents (silica gels, zeolites, aluminophosphates) [33–38]. Zeolites have a high affinity to water and therefore require high desorption temperatures with a not too high water uptake capacity. Silica gels have a lower hydrophilic character than zeolites which leads to lower desorption temperatures but a low water loading lift in the ideal interval  $0.05 < P \cdot P_0^{-1} < 0.35$ . Hence, MOFs have been studied as adsorbents for cycling vapor sorption (mostly water and methanol) over the last years [33–35,39–50]. MIL-101(Cr) (Fig. A.9) [51–53] is a promising material for potential heat transformation processes with its high BET surface ( $>3000 \text{ m}^2 \text{ g}^{-1}$ ), the large water and methanol

\* Corresponding author. Tel.: +49 2118112286.

E-mail address: [janiak@uni-duesseldorf.de](mailto:janiak@uni-duesseldorf.de) (C. Janiak).

uptake capacity ( $>1 \text{ g g}^{-1}$ ) and good cycling stability [40,49]. Besides vapor sorption applications MIL-101(Cr) has been investigated for drug delivery [54], catalysis [55–57] and gas storage [58,59], sometimes in connection with post-synthetic modifications [55,56,59,60].

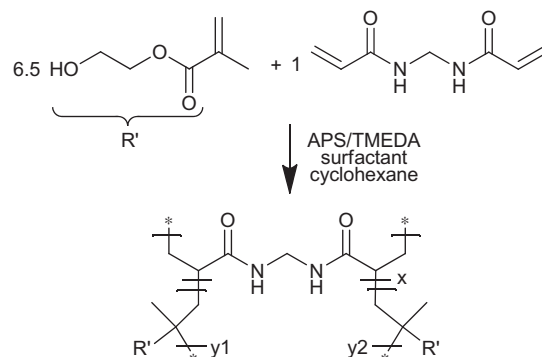
MOFs are generally obtained as (micro)crystalline powders, which is disadvantageous for potential applications, e.g., due to dust problems. Therefore shaping of MOFs into a mechanically manageable form is an indispensable requirement. Composite materials containing MOFs and an organic component (mostly polymers) can be named “shaped MOFs” and possess the chemical and physical properties of each component. MOF-organic matrix composites are well known as membranes [61–65], fibers [66–68] and as beads [69]. Küsgens and coworkers manufactured a MOF in a monolithic shape in a two-step process: pre-synthesized HKUST-1 crystals were mixed together with a liquid binding agent and a plasticizer followed by extrusion to a monolithic structure [70]. Monolithic HKUST-1@Aerogel composites were synthesized by in-situ HKUST-1 formation in the macropores of a pre-synthesized porous carbon monolith [71–73], or by adding HKUST-1 powder during silica aerogel synthesis [74]. Hierarchical composites of HKUST-1 in macroporous polyacrylamide (PAM) beads, HKUST-1 in macro-/mesoporous silica and UiO-66 in polyurethane (PU) foams were synthesized by Bradshaw, Galarneau and Pinto et al. [69,75,76]. Monolithic structures can also be manufactured based on polymerized high internal phase emulsions, so called poly(HIPEs) [77–79]. Hydrophilic, macroporous poly(HIPEs) are synthesized by concentrated o/w emulsions, where an oily phase (o) is added dropwise to an aqueous solution (w) consisting of a hydrophilic monomer and a crosslinker. The internal, oily phase occupies more than 74% of the volume of the emulsion, kinetically stabilized by a surfactant. After polymerization of the monomer in the aqueous, continuous phase, the organic phase can be removed by washing steps and drying, and a monolithic structure can be obtained. The only MOF@HIPE composite reported, so far, is HKUST-1 which was synthesized in-situ into a pre-formed macroporous HIPE based on 4-vinylbenzyl chloride crosslinked with divinylbenzene [80]. A three-step synthetic route was used to obtain a monolithic HKUST-1@HIPE hybrid material with a maximal BET surface area of  $570 \text{ m}^2 \text{ g}^{-1}$  and a pore volume of  $0.38 \text{ cm}^3 \text{ g}^{-1}$ . The HIPE material then contained 62.3 wt% of HKUST-1 after the third impregnation step. Taking into account the MOF loading and BET surface areas of pure HKUST-1 and HIPE with  $1340 \text{ m}^2 \text{ g}^{-1}$  and  $30 \text{ m}^2 \text{ g}^{-1}$ , respectively, the estimated BET surface area of  $846 \text{ m}^2 \text{ g}^{-1}$  could not be achieved. No potential applications, e.g., as gas storage material, were investigated with HKUST-1@HIPE.

In this work we present the embedding of pre-synthesized MIL-101(Cr) crystals into a poly(HIPE) material based on polymerized 2-hydroxyethylmethacrylate (HEMA), crosslinked with *N,N'*-methylenebisacrylamide (MBA) (see Scheme 1) [81,82]. The methanol and water uptake capacities of the MIL-101(Cr)@poly(HEMA)HIPE or in short MIL-101@HIPE composites were investigated.

## 2. Experimental

### 2.1. Materials and methods

All chemicals were obtained commercially and used without further purification except *N,N'*-methylenebisacrylamide (MBA), which was recrystallized from methanol: 2-hydroxyethyl methacrylate (HEMA) (Alfa Aesar 97% stabilized with approx. 500 ppm 4-methoxyphenol), *N,N'*-methylenebisacrylamide (MBA) (Sigma-Aldrich 99%), ammonium persulfate (APS) (Roth  $\geq 98\%$ ), Kolliphor® P188 (Sigma), *N,N,N',N'*-tetramethylethylenediamine (TMEDA) (Merck  $> 99\%$ ),  $\text{Cr}(\text{NO}_3)_3 \cdot 9\text{H}_2\text{O}$  (Acros Organics 99%),



**Scheme 1.** Radical polymerization of 2-hydroxyethyl methacrylate (HEMA) and *N,N'*-methylenebisacrylamide (MBA) initiated by ammonium persulfate (APS) ( $x = 13 \text{ mol}\%$ ,  $y_1 + y_2 = 87 \text{ mol}\%$ ).

1,4-benzenedicarboxylic acid ( $\text{H}_2\text{BDC}$ ) (Acros Organics  $> 99\%$ ), tetramethylammonium hydroxide (TMAOH) (25 wt% in water), cyclohexane (AppliChem. p.a.), DMF (VWR, p.a.), ethanol (VWR, p.a.). All experimental work was performed with exposure to air.

### 2.2. Physical measurements

Powder X-ray diffraction (PXRD) patterns were done at ambient temperature on a Bruker D2 Phaser using a flat sample holder and  $\text{Cu-K}\alpha$  radiation ( $\lambda = 1.54182 \text{ \AA}$ ). FT-Infrared spectra were measured on a Bruker TENSOR 37 IR spectrometer at ambient temperature as KBr disk in the range of  $4000\text{--}500 \text{ cm}^{-1}$ . Nitrogen physisorption isotherms were carried out on a Quantachrome Nova 4000e at 77 K. Water and methanol physisorption isotherms were measured volumetrically on a Quantachrome Autosorb iQ MP at 293 K. The materials were put into sample tubes capped with septa. The weighed sample tubes were attached to the preparation port of the sorption analyzer, degassed under vacuum (3–4 h at 373–473 K), weighed out again and then transferred to the analysis port of the sorption analyzer. For determination of the cold and warm free space of the sample tubes helium gas was used. DFT calculations for the pore size distribution curves were done with the native NovaWin 11.03 software using the ‘ $\text{N}_2$  at 77 K on carbon, slit pore, NLDFT equilibrium’ model [83–85]. Scanning electron microscopy images of poly(HEMA)HIPE and pre-polymerized MIL-101@HIPE composites were obtained with a LEO 1430 VP SEM after coating with Au for 180 s at 30 mA by an AGAR sputter coater. MIL-101(Cr) and standard MIL-101@HIPE composites (without pre-polymerization) were imaged on a FEI Quanta 400 FEG (ESEM). Before imaging the materials were coated with Au/Pd (80: 20) using an Emitech K550 sputter for 1 min at 15 mA. The thermogravimetric analysis (TGA) curve of poly(HEMA)HIPE was measured on a TG 209 F3 Tarsus from Netzsch.

### 2.3. Synthesis of MIL-101(Cr)

MIL-101(Cr) was hydrothermally synthesized according to the literature [58]. Typical batch sizes of 4.80 g (12.0 mmol)  $\text{Cr}(\text{NO}_3)_3 \cdot 9\text{H}_2\text{O}$ , 1.98 g (11.9 mmol)  $\text{H}_2\text{BDC}$ , 1.1 mL TMAOH (3.1 mmol;  $\rho = 1.014 \text{ g mL}^{-1}$ ; 25 wt% in  $\text{H}_2\text{O}$ ) and 60 mL of deionized water at 453 K for 24 h yielded MIL-101(Cr)-as synthesized. For activation the as-synthesized MIL-101 was purified through a consecutive washing procedure with DMF, EtOH and deionized water (see Supplementary data for details). 2.34 g of purified MIL-101 was obtained (50% yield based on Cr) as a green powder with a BET surface of  $3060 \text{ m}^2 \text{ g}^{-1}$  and a pore volume of  $1.45 \text{ cm}^3 \text{ g}^{-1}$  (measured at  $P \cdot P_0^{-1} = 0.95$ ), which was calculated from the type-I

$N_2$  sorption isotherm (Fig. A.2a, Table A.1). Experimental, theoretical powder X-ray patterns and the IR-spectrum are shown in Fig. A.1.

#### 2.4. Synthesis of poly(HEMA)HIPE

The synthesis of native poly(HEMA)HIPE, from 2-hydroxyethyl methacrylate copolymerized with 13 mol% *N,N'*-methylenebisacrylamide, was carried out according to the literature [81,82]. The reaction equation for the radical polymerization is displayed in Scheme 1. An aqueous solution of the monomer 2-hydroxyethyl methacrylate and copolymer *N,N'*-methylenebisacrylamide was prepared. After adding ammonium persulfate, as the radical initiator and the surfactant Kolliphor® P188 (poly(ethylene glycol)-*block*-poly(propylene glycol)-*block*-poly(ethylene glycol)), cyclohexane as the internal organic phase of the *o/w* emulsion was slowly added dropwise into the aqueous solution. Addition of *N,N,N',N'*-tetramethylethylenediamine, which acts together with APS as a redox initiator pair, was necessary for a successful curing of the emulsion. Curing for 3 days at room temperature, followed by washing and drying steps led to a mechanically stable, white monolith (Fig. 3a) (see Supplementary data for details).

#### 2.5. Synthesis of MIL-101@HIPE composites

MIL-101@HIPE composites (in short for MIL-101(Cr)@poly(HEMA)HIPEs) with different weight percentages of MIL-101(Cr) were synthesized by a modified synthetic procedure of the pure poly(HEMA)HIPE material. Various amounts of well ground MIL-101 powders were filled in 5 mL plastic syringes, which were cut off from one side (side where the cannula is normally attached). Then specific amounts of pure emulsions were added to each syringe and after homogenization, curing, washing and drying green monoliths were obtained (Fig. 3b). The composites were synthesized in three different ways: (i) standard without and (ii) with additional pre-polymerization (pp) of the HIPE emulsion and (iii) with impregnation of the MIL with cyclohexane ( $cC_6$ ). Modifications (ii) and (iii) are indicated by the prefix pp- and  $cC_6$ -, respectively, to MIL-101@HIPE. The weight percentages of MIL-101(Cr) in the composites were calculated by simply dividing the amount of MIL added to the HIPE by the final mass of the composites supposing no MOF was lost during the synthesis (see Formula A.1).

### 3. Results and discussion

#### 3.1. Pure poly(HEMA)HIPE

Infrared spectroscopic analysis of the HIPE materials supports their purity due to the absence of bands for starting materials like monomers or surfactant (Fig. 1). The region between 3720 and 3140  $cm^{-1}$  shows a broad band which can be assigned to the O–H and N–H stretching vibrations of free water in the pores of the HIPE material and the bonded MBA copolymer respectively. Beside the  $\nu(C-H)$  stretching vibrations at around 2950  $cm^{-1}$ , infrared data shows typical carbonyl stretching vibrations in the region of 1740 and 1640  $cm^{-1}$ . Compared to the infrared spectrum of pure poly(HEMA) material without the presence of bonded MBA, the band at 1539  $cm^{-1}$  can be assigned to deformation vibrations of the N–H bond [86,87]. Other characteristic vibration bands like  $\delta(C-H)$  (1470–1380  $cm^{-1}$ ),  $\nu(C-O)$  (1263  $cm^{-1}$ ),  $\nu(C-N)$  (1161  $cm^{-1}$ ),  $\nu(C-O-C)$  (1078  $cm^{-1}$ ) and  $\gamma_{oop}(C-O)$  (748  $cm^{-1}$ ) display the presence of the anticipated functional groups.

The porosity of the macroporous poly(HEMA)HIPE material was assessed by  $N_2$  sorption experiments (Fig. A.3b) and scanning electron microscopy (Fig. 2). Multi-point BET calculations from the  $N_2$

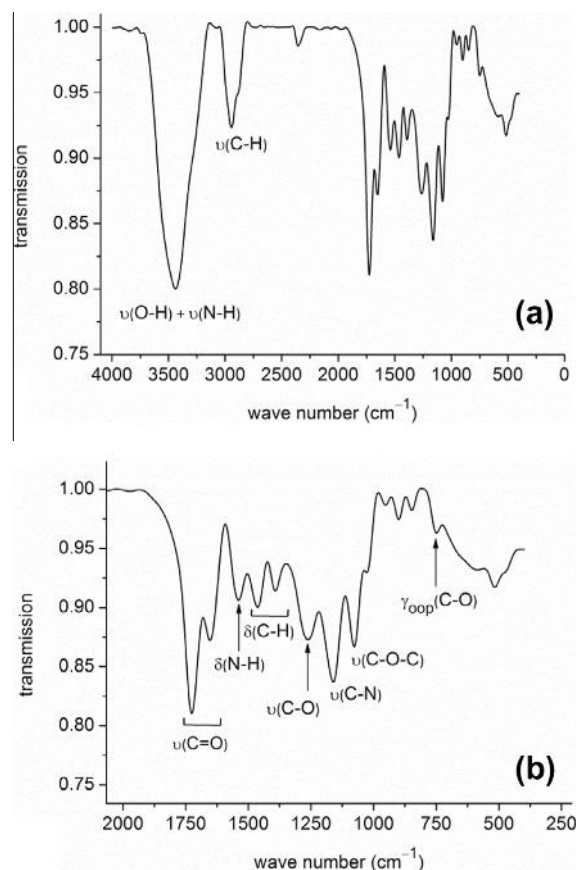


Fig. 1. (a) IR-spectrum (KBr) of poly(HEMA)HIPE. (b) Enlargement for region 250–2000  $cm^{-1}$ .

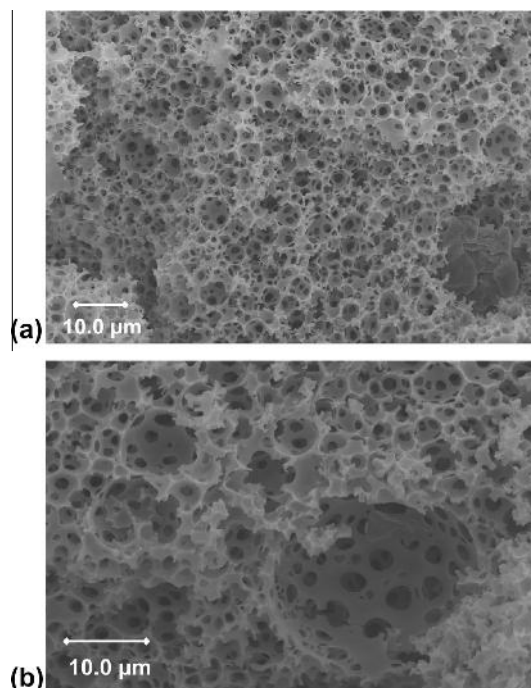
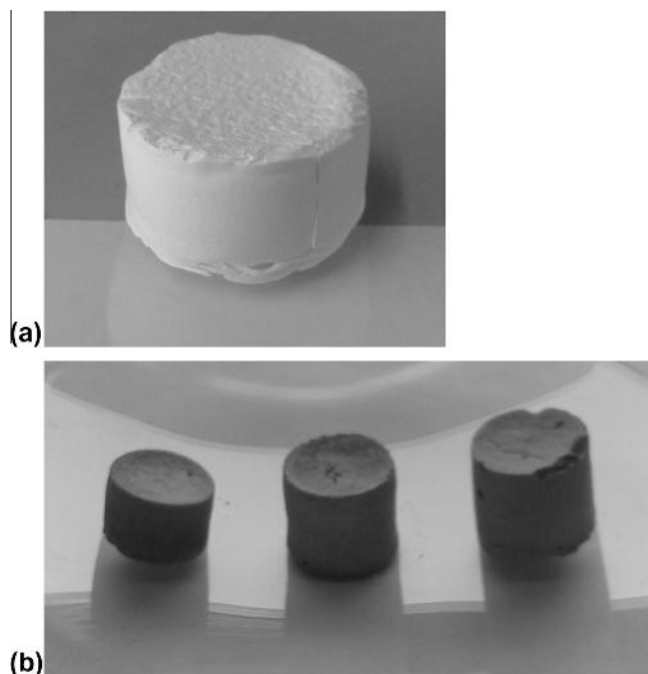


Fig. 2. (a)–(b) Scanning electron microscopic (SEM) images of poly(HEMA)HIPE (average pore size diameter 2–6  $\mu m$ ).

sorption isotherm show a BET surface area of 50  $m^2 g^{-1}$  (Table A.1). The typical macroporous morphology, which is known for HIPE systems is shown in Fig. 2 [77–79]. The diameters of the voids



**Fig. 3.** (a) Pure poly(HEMA)HIPE material. (b) pp-MIL-101@HIPE composites with 38, 59 and 67 wt% of MIL-101. Dimensions are for (a)  $22 \times 15$  mm, and for (b)  $13 \times 11$ ,  $13 \times 14$ ,  $13 \times 17$  mm. The first values stand for the diameter, the second for the height.

and the connecting pores of 2–6  $\mu\text{m}$  and 1–2  $\mu\text{m}$  are consistent with other literature data [81,82]. It has to be mentioned that porosity analysis of such macroporous systems should better be evaluated from mercury intrusion porosimetry experiments, which is the favored method for the analysis of macropores between 3 nm and 950  $\mu\text{m}$ . Porosity analysis based on gas physisorption is limited to pore sizes with diameter of 400 nm and below. The pore size distribution curve of poly(HEMA)HIPE, calculated from mercury intrusion measurements, was taken from the literature and displayed in Fig. A.4d. The only pore size of approximately  $1.0(\pm 0.1)$   $\mu\text{m}$ , found by mercury porosimetry, is consistent with the SEM image reflecting the size of the connecting pores [81].

### 3.2. Embedding MIL-101(Cr) into poly(2-hydroxyethyl methacrylate) monoliths

By modifying the synthetic procedure for crosslinked poly(HEMA)HIPEs through addition of specific amounts of emulsion to selected amounts of MIL powders, green monoliths with 38, 59 and 67 wt% of MIL-101(Cr) can be obtained (Fig. 3b, see Formula S1 for definition of wt%). MIL-101@HIPE with 67 wt% of MIL turned out to be mechanically not stable enough, which means that it crumbled easily due to the high amount of MIL-101 powder. The monolithic composites were synthesized in three different ways: (i) as standard the HIPE emulsions were added to the MILs after a short period of stirring, that is, without pre-polymerization (38, 59 and 67 wt% MIL in MIL-101@HIPE), (ii) after a longer pre-stirring time, that is, with pre-polymerization (38 and 59 wt% MIL in pp-MIL-101@HIPE) and (iii) with impregnation of the MIL with cyclohexane before adding the HIPE emulsions (38 and 59 wt% MIL in  $\text{cC}_6$ -MIL-101@HIPE). The last two ways of synthesis have been carried out in order to avoid pore blocking by HIPE-monomer polymerization in the MIL pores. The stirring time of the HIPE emulsion was elongated in (ii), which is equivalent to a HIPE

pre-polymerization. This should lower the diffusion rate of HIPE-monomers/oligomers into the MIL pores. Another way of protecting the MIL pores utilized the insolubility of HEMA and MBA

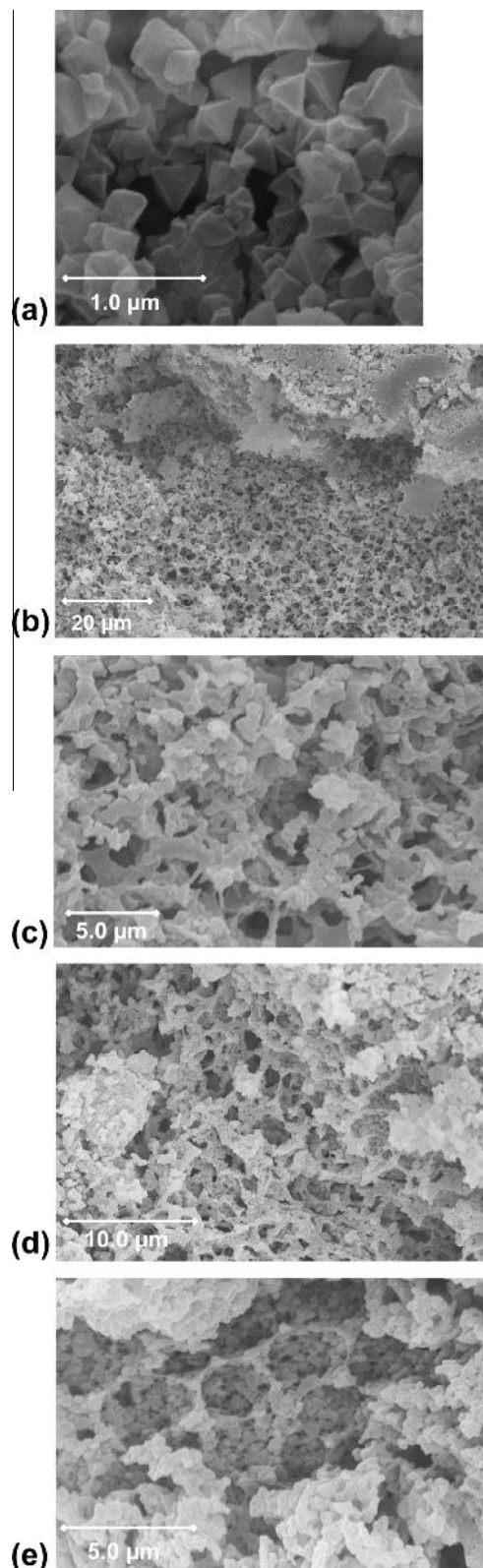


**Fig. 4.** Scanning electron microscopic (SEM) images of (a) MIL-101(Cr) and pp-MIL-101@HIPE composites with (b)–(c) 38 wt% and (d)–(e) 59 wt% of MIL-101.

monomers in cyclohexane. Therefore, in (iii) the MIL powders were impregnated with cyclohexane before adding HIPE emulsions to protect the pores from intrusion by HEMA/MBA-monomers (see [Supplementary data for details](#)).

Scanning electron images of pure MIL-101(Cr) show the typical octahedral morphology with a particle size varying between 300 and 500 nm, typical for hydrothermally synthesized MIL-101(Cr) (Fig. 4a) [58]. Fig. 4b–e shows the composite materials with 38 and 59 wt% loading of MIL-101(Cr) (pp-MIL-101@HIPE). Fig. 4b shows HIPE voids with an almost unchanged diameter. The MIL particles adhere on the HIPE walls mostly as agglomerates. MIL octahedrons, which seem to have an unchanged particle size, can be found in the agglomerates (Fig. 4c). The higher loading of MIL-101(Cr) is apparent in the SEM images by simply comparing Fig. 4b, c with 6d, e. Even at a high MIL loading of 59 wt% the original HIPE morphology with its macroscopic voids is still evident (Fig. 4d–e). The adherence of particles to the HIPE walls and not occupying the voids was also shown for a polystyrene coated poly(NIPAM)HIPE (NIPAM: *N*-isopropylacrylamide) [88]. Similar SEM images with 38 and 67 wt% of MIL-101(Cr) in MIL-101(Cr)@poly(HEMA)HIPE (standard procedure) are displayed in Fig. A.5b–f.

The powder X-ray diffraction patterns of the composite compounds standard- and pp-MIL-101@HIPE with 38, 59 and 67 wt% of MIL show that the crystallinity remains unchanged compared to pure MIL-101(Cr) (Fig. 5a).

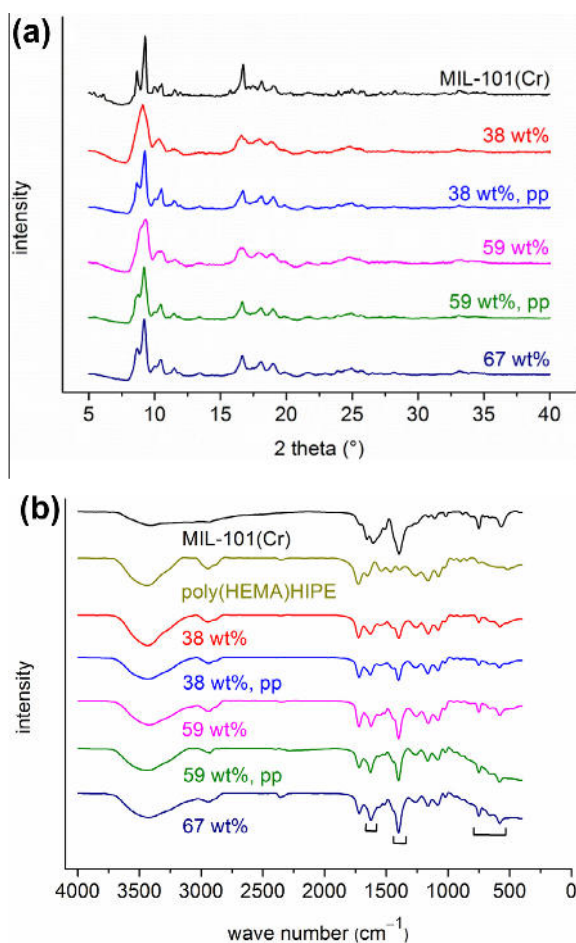


**Fig. 5.** (a) Experimental powder X-ray diffraction pattern of activated MIL-101(Cr) standard- and pp-MIL-101@HIPE composites with 38, 59 and 67 wt% of MIL. (b) IR-spectra (KBr) of activated MIL-101(Cr), poly(HEMA)HIPE, standard- and pp-MIL-101@HIPE composites with 38, 59 and 67 wt% of MIL-101. Square brackets highlight the bands of MIL-101 in the composite materials.

Infrared spectra of the composites can be seen as an overlap of the individual spectra of MIL-101(Cr) and poly(HEMA)HIPE (Fig. 5b). With increasing loading of the MIL the intensities of the characteristic vibration bands for MIL-101 in the composite materials are enhanced (see regions highlighted by square brackets in Fig. 5b).

### 3.3. N<sub>2</sub>, methanol and water sorption studies

Fig. 6a shows the N<sub>2</sub> sorption isotherms of the standard- and pp-MIL-101@HIPE composites in comparison to the pure poly(HEMA)HIPE. As expected an increasing amount of MIL-101 in MIL-101@HIPE leads to higher nitrogen adsorption and BET surface areas (Table 1). Importantly, the N<sub>2</sub> uptake and BET surface area increase significantly for the same MIL wt% upon pre-polymerization (pp) of the poly(HEMA)HIPE compared to the standard procedure without pre-polymerization. For example, for 59 wt% the BET surface is 990 m<sup>2</sup> g<sup>-1</sup> for the pre-polymerized pp- and only 450 m<sup>2</sup> g<sup>-1</sup> for standard MIL-101@HIPE (Table 1). The N<sub>2</sub> sorption isotherms are consistent with type-I isotherms therefore proving the accessibility of nitrogen to the micropores of MIL-101 (Fig. A.2c). Yet, the characteristic shape of the N<sub>2</sub> sorption isotherm of pure MIL-101(Cr) with defined steps between 0.1 < P · P<sub>0</sub><sup>-1</sup> < 0.2 (Fig. A.2a), which are attributed to two kinds of mesopores (Fig. A.9), is not well developed in the MIL@HIPE composites [51]. The almost negligible steps between 0.1 < P · P<sub>0</sub><sup>-1</sup> < 0.2 in the composites are explained by the overall lower N<sub>2</sub> uptake of 1/3 and less due to the decrease in surface area in the composites.

Pore size distribution curves show that pure MIL-101(Cr) possesses different pores in the micro- and mesoporous area

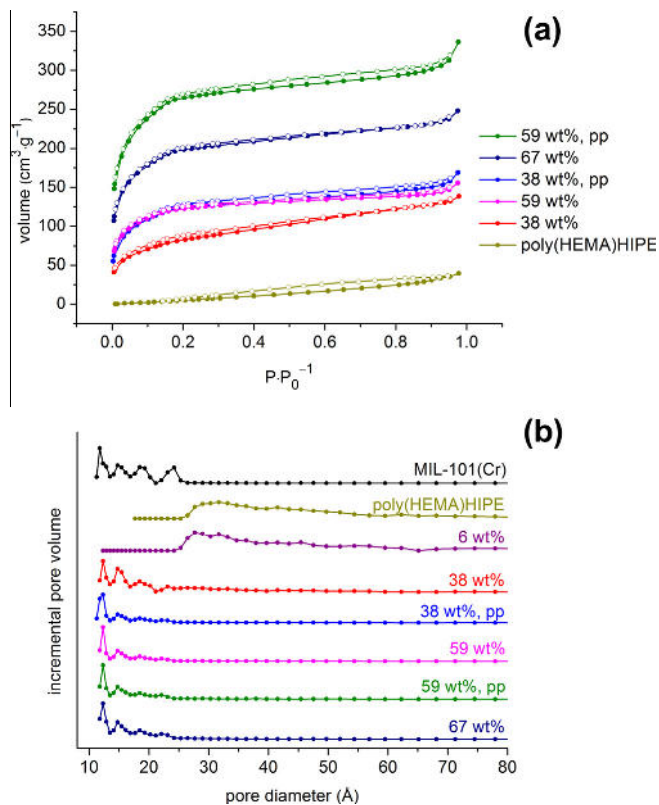


**Fig. 6.** (a) N<sub>2</sub>-sorption isotherms of standard- and pp-MIL-101@HIPE composites with 38, 59 and 67 wt% MIL-101(Cr). (b) Pore size distribution curves of activated MIL-101(Cr), poly(HEMA)HIPE, standard- and pp-MIL-101@HIPE composites with 6, 38, 59 and 67 wt% MIL-101(Cr). Adsorption is depicted with filled, desorption with empty symbols (degassing conditions: 4 h, 373 K).



**Table 1**  
Nitrogen, methanol and water sorption measurements of poly(HEMA)HIPE and composite materials.

Materials	BET surface area <sup>a</sup> ; (Estimated) <sup>b</sup> (m <sup>2</sup> ·g <sup>-1</sup> )	Water loading <sup>c</sup> ; (Estimated) <sup>d</sup> (g·g <sup>-1</sup> )	Methanol loading <sup>c</sup> ; (Estimated) <sup>d</sup> (g·g <sup>-1</sup> )
poly(HEMA)HIPE	50	0.16	0.30
MIL-101(Cr)	3060	1.06	1.08
Composites: <sup>e</sup>			
6 wt%	30 (230)	n.d.	n.d.
38 wt%	300 (1190)	n.d.	n.d.
38 wt%, pp	460 (1190)	0.21 (0.50)	0.33 (0.60)
38 wt%, cC <sub>6</sub>	290 (1190)	n.d.	n.d.
59 wt%	450 (1830)	n.d.	n.d.
59 wt%, pp	990 (1830)	0.29 (0.69)	0.37 (0.76)
59 wt%, cC <sub>6</sub>	450 (1830)	n.d.	n.d.
67 wt%	540 (2050)	n.d.	n.d.

<sup>a</sup>BET surface area calculated at  $0.05 < P \cdot P_0^{-1} < 0.2$  from N<sub>2</sub> sorption isotherm 77 K with a standard deviation  $\pm 20$  m<sup>2</sup> g<sup>-1</sup>.

<sup>b</sup>BET surface area as the sum of the mass-weighted surface areas of MIL-101(Cr) (3060 m<sup>2</sup> g<sup>-1</sup>) and HIPE (50 m<sup>2</sup> g<sup>-1</sup>) calculated from the following formula:

$$\text{BET(estimated)} = \frac{\text{wt\% of MIL-101(Cr)}}{100} \times 3060 \text{ m}^2 \text{ g}^{-1} + \frac{\text{wt\% of MIL}}{100} \times 50 \text{ m}^2 \text{ g}^{-1}$$

<sup>c</sup>Calculated from water sorption isotherm at 293 K ( $P \cdot P_0^{-1} = 0.9$ ). n.d. = not determined.

<sup>d</sup>Water and methanol loading estimated as the sum of the mass-weighted vapor uptakes at  $P \cdot P_0^{-1} = 0.9$  of MIL-101(Cr) (1.06 g g<sup>-1</sup> for water; 1.08 g g<sup>-1</sup> for methanol) and HIPE (0.16 g g<sup>-1</sup> for water; 0.30 g g<sup>-1</sup> for methanol) calculated from the following formula:

$$\text{Vapor loading(estimated)} = \frac{\text{wt\% of MIL-101(Cr)}}{100} \times 1.06 \text{ (water) or } 1.08 \text{ (methanol) g g}^{-1} + \frac{\text{wt\% of HIPE}}{100} \times 0.16 \text{ (water) or } 0.30 \text{ (methanol) g g}^{-1}$$

<sup>e</sup>wt% refers to MIL-101(Cr) amount.

(Fig. 6b). The two maxima at diameters 12 and 15 Å could be assigned to the regions of the pentagonal and hexagonal windows, which surround the actual pores with 19 and 24 Å in diameter (see Fig. A.9). Compared to literature data these two pores are smaller than expected (29 and 34 Å) possibly due to retained impurities of unreacted H<sub>2</sub>BDC ligand located in the pores [20]. The pore size distribution curves of the composites show that the micro- and mesopores, especially the pores with 12 and 15 Å in diameter, remain unchanged therefore proofing the accessibility for nitrogen (Fig. 6b).

From the wt% of MIL-101(Cr) in the composite the BET surface areas could be estimated (expected) as the sum of the mass-weighted surface areas of pure MIL and HIPE (see Table 1 for further explanation). Synthesizing the composites by the standard procedure (MIL-101@HIPE) led to BET surface areas, which are approximately four times lower compared to the expected BETs (Table 1). A possible explanation would be that 75% of the pores of MIL-101(Cr) in the composites are fully blocked by HIPE material and only 25% of pores are still accessible. To confirm the assumption that the HIPE material is able to fully block the pores of MIL-101(Cr) a composite material was synthesized with only 6 wt% of MIL-101 (see Supplementary data for details). Offering a large excess of HIPE over the MIL amount could be expected to result in full blockage of the pores of MIL-101(Cr). The BET surface

area and pore size distribution of the 6 wt% MIL loaded composite material match those of the pure HIPE material. Hence, it is apparent that a sufficient excess of poly(HEMA)HIPE material is indeed able to block all MIL pores (Table 1, Fig. 6b).

In order to avoid or minimize pore blocking by HIPE polymerization in the pores of MIL-101, which occurs to a great extent in the standard procedure (i), the monolithic composites were also synthesized in two other ways; (ii) after a longer pre-stirring time, that is, with pre-polymerization and (iii) with impregnation of the MIL with cyclohexane before adding the HIPE emulsions. (ii) Increasing the stirring time of the HIPE emulsion is equivalent to a higher degree of HIPE polymerization. HEMA and MBA monomers were pre-polymerized to create longer oligomers and polymer chains, which are more hindered to diffuse into the MIL-101 pores. The BET surface areas could indeed be increased from 300 to 460 m<sup>2</sup> g<sup>-1</sup> for 38 wt% MIL-101@HIPE and from 450 to 990 m<sup>2</sup> g<sup>-1</sup> for 59 wt% MIL-101@HIPE upon pre-polymerization (Table 1). This shows that pre-polymerization is an indispensable step for MIL-101@poly(HEMA)HIPE syntheses to create monoliths with maximized porosities (see Supplementary data for details). Still, the expected BET surface areas of 1190 m<sup>2</sup> g<sup>-1</sup> (38 wt%) and 1830 m<sup>2</sup> g<sup>-1</sup> (59 wt%) could not be achieved showing that total protection of the MIL micro- and mesopores by pre-polymerization is not possible (Table 1). (iii) Impregnating the MIL-101(Cr) pow-

ders with cyclohexane before adding the HIPE emulsion should fill and protect the MIL pores from HIPE polymerization due to the insolubility of HEMA and MBA monomers in cyclohexane. Unfortunately this approach did not lead to increased BET surface areas compared to the standard procedure (Table 1, Fig. A.6).

This phenomenon of not achieving the estimated BET surface areas is literature-known. Similar hierarchical composites like HKUST-1 embedded in porous carbon monoliths only reach approx. 40% of the calculated BET surface areas [73]. Other composites like UiO-66@polyurethane or HKUST-1@HIPE reach about 60% of the theoretically estimated values [76,80]. Our 38 wt% and 59 wt% loaded pp-MIL-101@HIPE composites lie also in this range. MOFs in inorganic templates, like HKUST-1 embedded in silica aerogels [74] or HKUST-1@macro-/mesoporous silica [75] match or even exceed the estimated BET values (Table A.3). We note that the MOF wt% determination in the composite HKUST-1@PAM was based on a BET surface area determination under the assumption that 100% of the native MOF surface area will be retained and still accessible in the composite [69]. However, from other and our study of MOF composites with organic polymers it is evident that the organic matrix leads to partial pore blocking.

For investigation of the hydrophilicity of the pure poly(HEMA)-HIPE and interactions between vapor and native adsorbent, methanol and water vapor were tested as possible working fluids. It has been shown that methanol is the more suitable working vapor showing almost twice the amount of total vapor uptake toward pure poly(HEMA)HIPE.  $0.30 \text{ g g}^{-1}$  of methanol and  $0.16 \text{ g g}^{-1}$  of water vapor are adsorbed at  $P \cdot P_0^{-1} = 0.9$  (Fig. 7, Table 1). Therefore pure poly(HEMA)HIPE is rather hydrophobic.

Water and methanol sorption isotherms of pp-MIL-101@HIPE with 38 and 59 wt% loading are shown in comparison to the sorption isotherm of the pure MIL and poly(HEMA)HIPE in Fig. 8. The higher uptake capacities (Table 1) compared to the pure HIPE is apparent for both vapors. The maximum water loadings of the 38 and 59 wt% composite materials are 0.21 and  $0.29 \text{ g g}^{-1}$ , respectively, at  $P \cdot P_0^{-1} = 0.9$  and higher than the loading of pure poly(HEMA)HIPE with  $0.16 \text{ g g}^{-1}$ . Methanol sorption measurements outperform the water uptake capacities with loadings of 0.33 and  $0.37 \text{ g g}^{-1}$  for both composites together with a steeper adsorption rise up to  $P \cdot P_0^{-1} = 0.35$ . Gravimetric vapor loading capacities of the composites are comparable to commercial adsorbents like zeolites [34]. Zeolite-like crystalline aluminophosphates (AIPO) and silica-aluminophosphates (SAPO) can provide a higher maximum water uptake capacity than zeolites. For zeolites the strong hydrophilicity significantly reduces the fluid exchange within the cycle for desorption temperatures below  $140 \text{ }^\circ\text{C}$  [28]. AIPOs and SAPOs

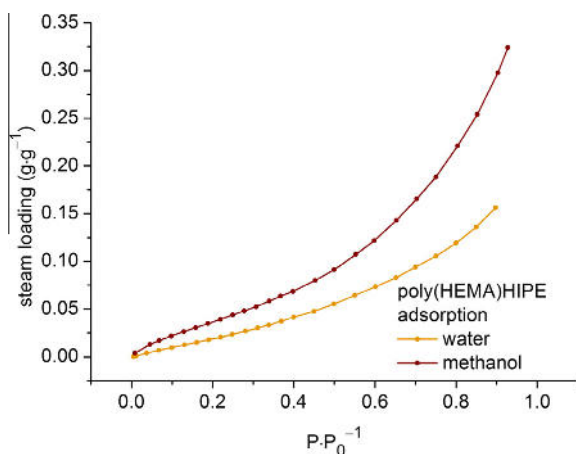


Fig. 7. Water and methanol adsorption isotherms of poly(HEMA)HIPE.

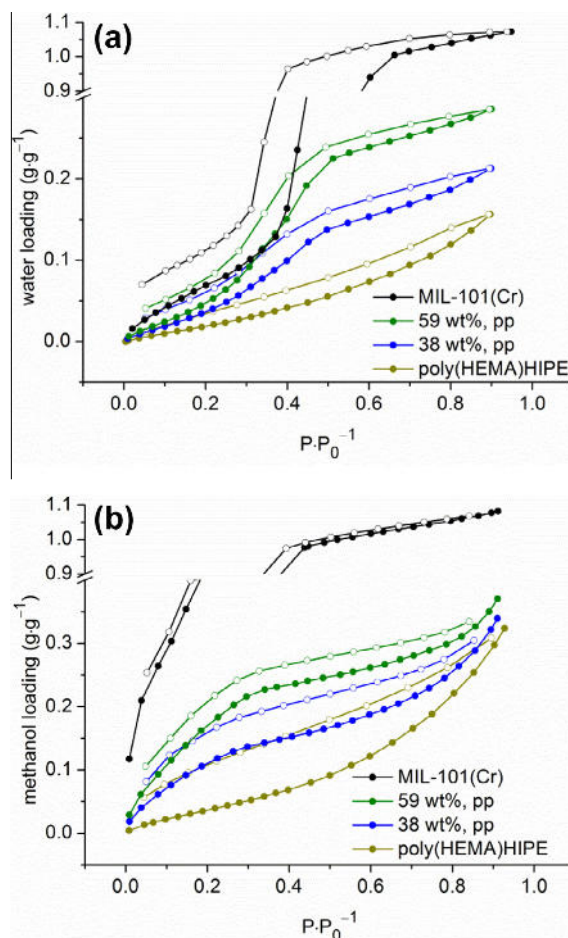


Fig. 8. (a) Water and (b) methanol sorption isotherms of poly(HEMA)HIPE, MIL-101(Cr) and pp-MIL-101@HIPE composites with 38 and 59 wt% MIL-101(Cr). Adsorption is depicted with filled, desorption with empty symbols.

have the desired s-shape adsorption isotherms for water uptake. Yet, the broader use of AIPOs and SAPOs for heat transformations is hampered by the high costs of the solvothermal/hydrothermal syntheses which requires the use of (expensive) template molecules or salts, such as morpholine or tetramethylammonium hydroxide [49].

The expected vapor loading at  $P \cdot P_0^{-1} = 0.9$  can be estimated from maximum vapor loadings of poly(HEMA)HIPE and MIL-101(Cr) taking into account their wt% in the composite material (Table 1). The lower than estimated vapor uptake correlates with the lower than estimated BET surface area of the composites. Again, methanol is the more suitable working fluid because the experimental vapor uptake capacities are closer to the estimated values (Table 1). The lower fraction of water uptake of MIL-101@HIPE to pure MIL-101 corresponds rather well to the lower surface fraction. For example, 59% MIL-101@HIPE has about one third of the BET surface of MIL-101 ( $990/3060$ ) and exhibits about one third of the water uptake capacity ( $0.29/1.06$ ).

A sorption material for TDCs or AHPs should show a high water uptake capacity at low to medium humidity and desorb the vapor at low temperature (below  $80 \text{ }^\circ\text{C}$ ) [89]. Ideally, a porous material should perform in between  $0.05 < P \cdot P_0^{-1} < 0.35$  relative pressure range with a sharp, s-shaped loading step and should have a desorption temperature at or below  $80 \text{ }^\circ\text{C}$  [33,90].

To check if longer diffusion paths through the monolith could have influenced the gas adsorption the MIL-101@HIPE monoliths

were measured again as well ground powders and with a longer equilibration time for the adsorption points of the isotherms. However, almost unchanged BET surface areas were obtained from nitrogen adsorption (Table A.2). Thus, the accessibility of nitrogen to the pores of the composite materials seems to be independent from the shape or diffusion path length.

#### 4. Conclusion

We presented the successfully embedding of the micro- and mesoporous metal-organic framework MIL-101(Cr) into a macroporous, high internal phase emulsion (HIPE) foam based on cross-linked poly(2-hydroxyethyl methacrylate) by simply adding the high internal phase emulsion to the MOF before curing. The MIL-101(Cr)/poly(HEMA)HIPE composites (in short MIL-101@HIPEs) were characterized by X-ray powder diffraction, IR-spectroscopy, scanning electron microscopy, nitrogen- methanol and water sorption studies. A maximal loading of 59 wt% MIL was achieved with a mechanically stable monolithic shape. Pre-polymerization of the HIPE emulsions was shown to be an indispensable factor for synthesizing highly porous composites where the micro- and mesopores of MIL-101(Cr) remain partially unblocked. As seen before for HKUST-1@porous carbon [73], UiO-66@polyurethane [76] and HKUST-1@HIPE [80] the BET surfaces of MIL-101@HIPE composites are lower than expected from the MOF weight percentage. Still, the MIL-101@HIPE monoliths show higher methanol and water uptake capacities compared to the pure HIPE. The maximum vapor exchange of  $0.29 \text{ g g}^{-1}$  (for water) and  $0.37 \text{ g g}^{-1}$  (for methanol) of the MIL-101@HIPE composite is certainly lower than in pure MIL-101(Cr) but most of it can be utilized under realistic working conditions up to  $P \cdot P_0^{-1} = 0.4$ . Embedding of other water-stable MOFs like MIL-100(Fe) and MIL-100(Cr) will be investigated.

#### Acknowledgements

Support by the University of Düsseldorf through its strategic research fund (SFF) is gratefully acknowledged. We thank Mr. Steffen Köhler for help with the SEM images.

#### Appendix A. Supplementary data

Supplementary data associated with this article can be found, in the online version, at <http://dx.doi.org/10.1016/j.micromeso.2014.11.025>.

#### References

- [1] O.M. Yaghi, H. Li, *J. Am. Chem. Soc.* 117 (1995) 10401–10402.
- [2] O.M. Yaghi, G. Li, H. Li, *Nature* 378 (1995) 703–705.
- [3] J.R. Long, O.M. Yaghi, *Chem. Soc. Rev.* 38 (2009) 1213–1214.
- [4] S. Kitagawa, S. Natarajan, *Eur. J. Inorg. Chem.* 24 (2010) 3685.
- [5] C. Serre, S. Kitagawa, P.D.C. Dietzel, *Micropor. Mesopor. Mater.* 157 (2012) 1–2.
- [6] M. Yoon, R. Srirambalaji, K. Kim, *Chem. Rev.* 112 (2012) 1196–1231.
- [7] D. Farrusseng, S. Aguado, C. Pinel, *Angew. Chem. Int. Ed.* 48 (2009) 7502–7513.
- [8] J. Lee, O.K. Farha, J. Roberts, K.A. Scheidt, S.T. Nguyen, J.T. Hupp, *Chem. Soc. Rev.* 38 (2009) 1450–1459.
- [9] F.X. Llabrés i Xamena, F.G. Cirujano, A. Corma, *Micropor. Mesopor. Mater.* 157 (2012) 112–117.
- [10] R.B. Getman, Y.-S. Bae, C.E. Wilmer, R.Q. Snurr, *Chem. Rev.* 112 (2012) 703–723.
- [11] Z. Chen, S. Xiang, H.D. Arman, P. Li, S. Tidrow, D. Zhao, B. Chen, *Eur. J. Inorg. Chem.* 24 (2010) 3745–3749.
- [12] F. Ma, S. Liu, D. Liang, G. Ren, C. Zhang, F. Wei, Z. Su, *Eur. J. Inorg. Chem.* 24 (2010) 3756–3761.
- [13] L. Wu, M. Xue, S.-L. Qiu, G. Chaplais, A. Simon-Masseron, J. Patarin, *Micropor. Mesopor. Mater.* 157 (2012) 75–81.
- [14] Z. Zhang, Y. Zhao, Q. Gong, Z. Li, J. Li, *Chem. Commun.* 49 (2013) 653–661.
- [15] J.-R. Li, Y. Ma, M.C. McCarthy, J. Sculley, J. Yu, H.-K. Jeong, P.B. Balbuena, H.-C. Zhou, *Coord. Chem. Rev.* 155 (2011) 1791–1823.
- [16] J.-R. Li, J. Sculley, H.-C. Zhou, *Chem. Rev.* 112 (2012) 869–932.
- [17] Z.R. Herm, R. Krishna, J.R. Long, *Micropor. Mesopor. Mater.* 157 (2012) 94–100.
- [18] M.G. Plaza, A.F.P. Ferreira, J.C. Santos, A.M. Ribeiro, U. Müller, N. Trukhan, J.M. Loureiro, A.E. Rodrigues, *Micropor. Mesopor. Mater.* 157 (2012) 101–111.
- [19] C. Janiak, *Dalton Trans.* 14 (2003) 2781–2804.
- [20] C. Janiak, J.K. Vieth, *New J. Chem.* 34 (2010) 2366–2388.
- [21] G. Férey, *Chem. Soc. Rev.* 37 (2008) 191–214.
- [22] N. Stock, S. Biswas, *Chem. Rev.* 112 (2012) 933–969.
- [23] (a) S. Kitagawa, R. Kitaura, S. Noro, *Angew. Chem. Int. Ed.* 43 (2004) 2334–2375;  
(b) S. Kitagawa, R. Kitaura, S. Noro, *Angew. Chem.* 116 (2004) 2388–2430.
- [24] M. Gaab, N. Trukhan, S. Maurer, R. Gummaraju, U. Müller, *Micropor. Mesopor. Mater.* 157 (2012) 131–136.
- [25] Yu.I. Aristov, *Appl. Therm. Eng.* 42 (2012) 18–24.
- [26] Yu.I. Aristov, *J. Chem. Eng. Jpn.* 40 (2007) 1242–1251.
- [27] A. Hauer, *Adsorption* 13 (2007) 399–405.
- [28] S.K. Henninger, F. Jeremias, H. Kummer, P. Schossig, H.-M. Henning, *Energy Procedia* 30 (2012) 279–288.
- [29] H. Demira, M. Mobedi, S. Ülkü, *Renewable Sustainable Energy Rev.* 12 (2008) 2381–2403.
- [30] Yu.I. Aristov, B. Dawoud, I.S. Glaznev, A. Elyas, *Int. J. Heat Mass Transfer* 51 (2008) 4966–4972.
- [31] H.-M. Henning, *Appl. Therm. Eng.* 27 (2007) 1734–1749.
- [32] L.W. Wang, R.Z. Wang, R.G. Oliveira, *Renewable Sustainable Energy Rev.* 13 (2009) 518–534.
- [33] S.K. Henninger, F. Jeremias, H. Kummer, C. Janiak, *Eur. J. Inorg. Chem.* 16 (2012) 2625–2634.
- [34] C. Janiak, S.K. Henninger, *Chimia* 67 (2013) 419–424.
- [35] Y.-K. Seo, J.W. Yoon, J.S. Lee, Y.K. Hwang, C.-H. Jun, J.-S. Chang, S. Wuttke, P. Bazin, A. Vimont, M. Daturi, S. Bourrelly, P.L. Llewellyn, P. Horcajada, *Adv. Mater.* 24 (2012) 806–810.
- [36] T. Núñez, W. Mittelbach, H.-M. Henning, *Appl. Therm. Eng.* 27 (2007) 2205–2212.
- [37] J. Jänchen, D. Ackermann, H. Stach, W. Brösicke, *Sol. Energy* 76 (2004) 339–344.
- [38] E.-P. Ng, S. Mintova, *Micropor. Mesopor. Mater.* 114 (2008) 1–26.
- [39] P. Küsgens, M. Rose, I. Senkovska, H. Fröde, A. Henschel, S. Siegle, S. Kaskel, *Micropor. Mesopor. Mater.* 120 (2009) 325–330.
- [40] J. Ehrenmann, S.K. Henninger, C. Janiak, *Eur. J. Inorg. Chem.* 4 (2011) 471–474.
- [41] F. Jeremias, A. Khutia, S.K. Henninger, C. Janiak, *J. Mater. Chem.* 22 (2012) 10148–10151.
- [42] S.K. Henninger, H.A. Habib, C. Janiak, *J. Am. Chem. Soc.* 131 (2009) 2776–2777.
- [43] G. Akiyama, R. Matsuda, S. Kitagawa, *Chem. Lett.* 39 (2010) 360–361.
- [44] G. Akiyama, R. Matsuda, H. Sato, A. Hori, M. Takata, *Micropor. Mesopor. Mater.* 157 (2012) 89–93.
- [45] C. Janiak, S.K. Henninger, *Nachr. Chem.* 61 (2013) 520–523.
- [46] A. Khutia, H.U. Rammelberg, T. Schmidt, S. Henninger, C. Janiak, *Chem. Mater.* 25 (2013) 790–798.
- [47] F. Jeremias, V. Lozan, S.K. Henninger, C. Janiak, *Dalton Trans.* 42 (2013) 15967–15973.
- [48] M. Wickenheisser, F. Jeremias, S.K. Henninger, C. Janiak, *Inorg. Chim. Acta* 407 (2013) 145–152.
- [49] F. Jeremias, D. Fröhlich, C. Janiak, S. Henninger, *New J. Chem.* 38 (2014) 1846–1852.
- [50] F. Jeremias, D. Fröhlich, C. Janiak, S.K. Henninger, *RSC Adv.* 4 (2014) 24073–24082.
- [51] G. Férey, C. Mellot-Draznieks, C. Serre, F. Millange, J. Dutour, *Science* 309 (2005) 2040–2042.
- [52] G. Férey, *Dalton Trans.* 23 (2009) 4400–4415.
- [53] G. Férey, C. Serre, *Chem. Soc. Rev.* 38 (2009) 1380–1399.
- [54] P. Horcajada, C. Serre, M. Vallet-Regi, M. Sebban, F. Taulelle, G. Férey, *Angew. Chem.* 118 (2006) 6120–6124.
- [55] Y.K. Hwang, D.Y. Hong, J.-S. Chang, S.H. Jhung, *Angew. Chem.* 120 (2008) 4212–4216.
- [56] D.Y. Hong, Y.K. Hwang, C. Serre, G. Férey, J.-S. Chang, *Adv. Funct. Mater.* 19 (2009) 1537–1552.
- [57] A. Herbst, A. Khutia, C. Janiak, *Inorg. Chem.* 53 (2014) 7319–7333.
- [58] J. Yang, Q. Zhao, J. Li, J. Dong, *Micropor. Mesopor. Mater.* 130 (2010) 174–179.
- [59] A. Khutia, C. Janiak, *Dalton Trans.* 43 (2014) 1338–1347.
- [60] S. Berni, V. Guillermin, C. Serre, N. Stock, *Chem. Commun.* 47 (2011) 2838–2840.
- [61] E.V. Perez, K.J. Jr., *J. Membr. Sci.* 328 (2009) 165–173.
- [62] S. Basu, A. Cano-Odena, I.F.J. Vankelecom, *J. Membr. Sci.* 362 (2010) 478–487.
- [63] S. Basu, M. Maes, A. Cano-Odena, L. Alearts, D.E. De Vos, I.F.J. Vankelecom, *J. Membr. Sci.* 344 (2009) 190–198.
- [64] H.B. Tanh Jeazet, C. Staudt, C. Janiak, *Chem. Commun.* 48 (2012) 2140–2142.
- [65] H.B. Tanh Jeazet, T. Koschine, C. Staudt, K. Raetzke, C. Janiak, *Membranes* 3 (2013) 331–353.
- [66] R. Ostermann, J. Cravillon, C. Weidmann, M. Wiebcke, B.M. Smarsly, *Chem. Commun.* 47 (2011) 442–444.
- [67] M. Rose, B. Bohringer, M. Jolly, R. Fischer, S. Kaskel, *Adv. Eng. Mater.* 13 (2011) 356–360.
- [68] P. Küsgens, S. Siegle, S. Kaskel, *Adv. Eng. Mater.* 11 (2009) 93–95.
- [69] L.D. O'Neill, H. Zhang, D.J. Bradshaw, *J. Mater. Chem.* 20 (2010) 5720–5726.
- [70] P. Küsgens, A. Zgaverdea, H.-G. Fritz, S. Siegle, S. Kaskel, *J. Am. Ceram. Soc.* 93 (2010) 2476–2479.
- [71] N. Hüsing, U. Schubert, *Angew. Chem.* 110 (1998) 22–47.
- [72] S.A. Al-Muhtaseb, J.A. Ritter, *Adv. Mater.* 15 (2003) 101–114.

- [73] D. Qian, C. Lei, G.-P. Hao, W.-C. Li, A.-H. Lu, *Appl. Mater. Interfaces* 4 (2012) 6125–6132.
- [74] Z. Ulker, I. Erucar, S. Keskin, C. Erkey, *Micropor. Mesopor. Mater.* 170 (2013) 352–358.
- [75] A. Sachse, R. Ameloot, B. Coq, F. Fajula, B. Coasne, D. De Vos, A. Galarneau, *Chem. Commun.* 48 (2012) 4749–4751.
- [76] M.L. Pinto, S. Dias, J. Pires, *Appl. Mater. Interfaces* 5 (2013) 2360–2363.
- [77] N.R. Cameron, *Polymer* 46 (2005) 1439–1449.
- [78] H. Zhang, A.I. Cooper, *Soft Matter* 1 (2005) 107–113.
- [79] N. Brun, S. Ungureanu, H. Deleuze, R. Backov, *Chem. Soc. Rev.* 40 (2011) 771–788.
- [80] M.G. Schwab, I. Senkovska, M. Rose, M. Koch, J. Pahnke, G. Jonschker, S. Kaskel, *Adv. Eng. Mater.* 10 (2008) 1151–1155.
- [81] S. Kovačič, D. Štefanec, P. Krajnc, *Macromolecules* 40 (2007) 8056–8060.
- [82] O. Kulygin, M.S. Silverstein, *Soft Matter* 3 (2007) 1525–1529.
- [83] L.D. Gelb, K.E. Gubbins, R. Radhakrishnan, M. Sliwinski-Bartowiak, *Rep. Prog. Phys.* 62 (1999) 1573–1659.
- [84] N.A. Sedron, J.P.R.B. Walton, N. Quirke, *Carbon* 27 (1989) 853–861.
- [85] A. Vishnyakov, P. Ravikovitch, A.V. Neimark, *Langmuir* 16 (2000) 2311–2320.
- [86] S. Morita, K. Kitagawa, Y. Ozaki, *Vib. Spectrosc.* 51 (2009) 28–33.
- [87] T.S. Perova, J.K. Vij, H. Xu, *Colloid Polym. Sci.* 275 (1997) 323–332.
- [88] N.C. Grant, A.I. Cooper, H. Zhang, *Appl. Mater. Interfaces* 2 (2010) 1400–1406.
- [89] S.K. Henninger, G. Munz, K.-F. Ratzsch, P. Schossig, *Adsorption* 17 (2011) 833–843.
- [90] Yu.I. Aristov, *Appl. Phys. Lett.* 91 (2007) 111902-1–111902-3.

## Supplementary data

### Hierarchical embedding of micro-mesoporous MIL-101(Cr) in macroporous poly(2-hydroxyethyl methacrylate) high internal phase emulsions with monolithic shape for vapor adsorption applications

Martin Wickenheisser<sup>a</sup> and Christoph Janiak<sup>\*a</sup>

<sup>a</sup> *Institut für Anorganische Chemie und Strukturchemie I, Universitätsstraße 1, 40225 Düsseldorf, Germany. E-mail: janiak@uni-duesseldorf.de*

## Experimental

### *Synthesis of the starting materials*

**MIL-101(Cr)**  $\{Cr_3(\mu_3-O)(F)(H_2O)_2(BDC)_3\} \cdot \sim 25H_2O$  was prepared according to the literature [1].  $Cr(NO_3)_3 \cdot 9H_2O$  (4.80 g, 12.0 mmol) and  $H_2BDC$  (terephthalic acid) (1.98 g, 11.9 mmol) were stirred in 60 mL of deionized  $H_2O$  for 5 min. Then 1.1 mL TMAOH (tetramethylammonium hydroxide) (3.1 mmol;  $\rho = 1.014 \text{ g} \cdot \text{mL}^{-1}$ ; 25 wt% in  $H_2O$ ) was dropped slowly to the mixture and the suspension was stirred for 20 min. The mixture was placed in a 90 mL Teflon-lined autoclave and heated to 453 K within 10 h. After 24 h the autoclave was cooled to room temperature over 18 h. The green powder was centrifuged off and washed consecutively with DMF (1 x 240 mL), EtOH (1 x 240 mL) and deionized  $H_2O$  (1 x 240 mL). Between each washing step the powder was centrifuged off and finally dried for 22 h at 373 K. The IR-spectrum of this material showed impurities of unreacted  $H_2BDC$ . For further activation the powder was first stirred for 20 h in 400 mL DMF at 383 K. After centrifugation and stirring for 19 h in 400 mL EtOH at 333 K, the green powder was centrifuged off and stirred again for 19 h in 400 mL of deionized water at 353 K. After centrifugation the solid was dried for 24 h at

---

[1] J. Yang, Q. Zhao, J. Li, J. Dong, *Microporous Mesoporous Mater.* 130 (2010) 174–179.

373 K. The IR spectrum of the final product (Fig. A.1b) shows no characteristic bands for unreacted H<sub>2</sub>BDC anymore. 2.34 g of a green powder was isolated (2.00 mmol, 50 % for {Cr<sub>3</sub>(μ<sub>3</sub>-O)(F)(H<sub>2</sub>O)<sub>2</sub>(BDC)<sub>3</sub>}·~25H<sub>2</sub>O} (C<sub>24</sub>H<sub>16</sub>Cr<sub>3</sub>FO<sub>15</sub>·H<sub>50</sub>O<sub>25</sub>, 1169.74 g·mol<sup>-1</sup>)).

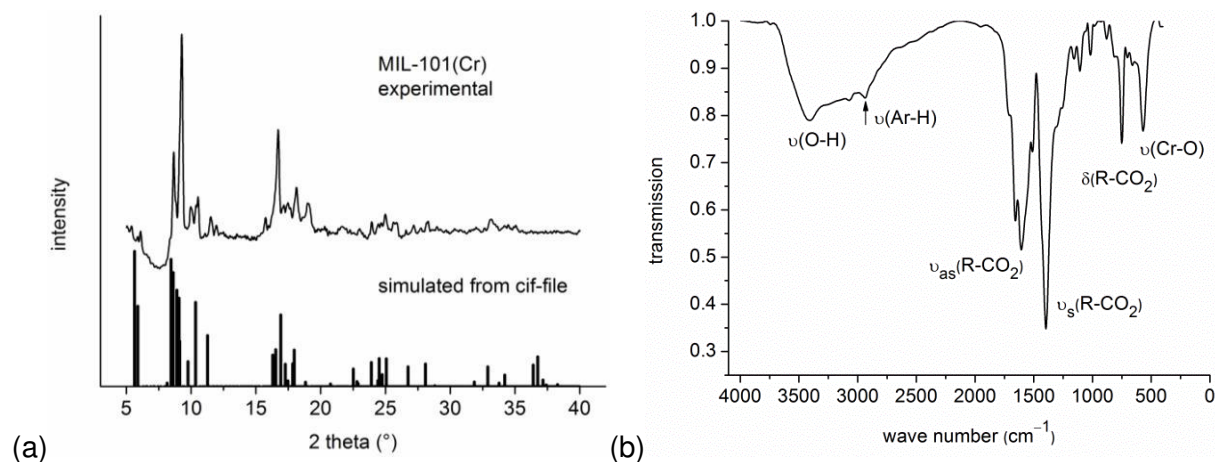


**Fig. A.1.** (a) Experimental powder X-ray diffraction pattern of activated MIL-101(Cr) and theoretical XRD pattern simulated from the cif-file of MIL-101(Cr) CSD-Refcode OCUNAK [2]. (b) IR-spectrum (KBr) of activated MIL-101(Cr).

The PXRD pattern gives evidence for the successful synthesis of the MIL due to the positions of the reflections, which are in good agreement with the simulated diffraction pattern, created from the cif-file (Fig. A.1a). The IR-spectrum (Fig. A.1b), measured in air, shows a broad band between 3700 – 2700 cm<sup>-1</sup>, which can be assigned to ν(O-H)-vibrations of coordinated and free water in the pores of MIL-101(Cr). Infrared data shows the characteristic asymmetric and symmetric valence-vibrations of the carboxyl groups of the coordinated BDC-ligand between 1670 and 1370 cm<sup>-1</sup>. The band located at 750 cm<sup>-1</sup> shows deformation-vibrations, coming from the carboxyl groups. Cr-O-valence-vibrations of CrO<sub>6</sub>-octahedrons can be found at 569 cm<sup>-1</sup>. N<sub>2</sub>-sorption isotherm, water sorption isotherm and the pore size distribution curve of activated MIL-101(Cr) are shown in Figure S2 (a)-(c).

[2] G. Férey, C. Mellot-Draznieks, C. Serre, F. Millange, J. Dutour, S. Surblé, I. Margiolaki, Science 309 (2005) 2040–2042.

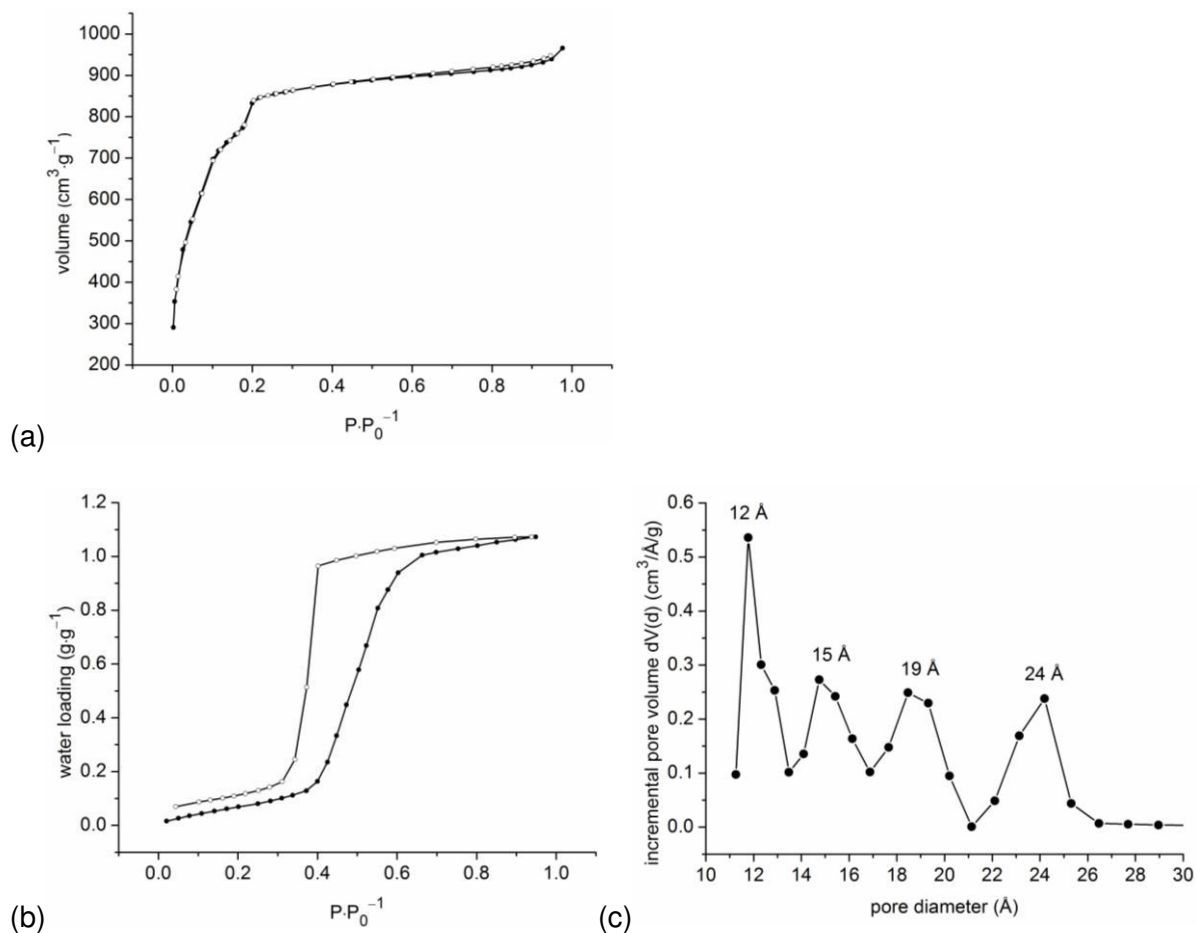


**Fig. A.2.** (a) N<sub>2</sub>-sorption isotherms of activated MIL-101(Cr) (degassing conditions: 2.5 h, 473 K, BET = 3060 m<sup>2</sup>·g<sup>-1</sup>). (b) Water sorption isotherm of activated MIL-101(Cr) (degassing conditions: 3 h, 473 K). Adsorption is depicted with filled, desorption with empty symbols. (c) Pore size distribution curve of activated MIL-101(Cr) from 'N<sub>2</sub> at 77 K on carbon, slit pore, NLDFT equilibrium' model [3,4,5].

[3] L.D Gelb, K.E. Gubbins, R. Radhakrishnan, M. Sliwinski-Bartowiak, Rep. Prog. Phys. 62 (1999) 1573–1659.

[4] N.A. Sedron, J.P.R.B. Walton, N. Quirke, Carbon 27 (1989) 853–861.

[5] A. Vishnyakov, P. Ravikovitch, A.V. Neimark, Langmuir 16 (2000) 2311–2320.

**poly(HEMA)HIPE:** poly(HEMA)HIPE was prepared according to the literature [6]. 1.03 mL of 2-hydroxyethyl methacrylate (HEMA) ( $\rho = 1.071 \text{ g}\cdot\text{mL}^{-1}$ ; 8.48 mmol) was added dropwise to 2.60 g of deionized water. After adding 200 mg of *N,N'*-methylenebisacrylamide (MBA) (1.30 mmol), 35 mg of ammonium persulfate (APS) (0.15 mmol) and 750 mg of the surfactant Kolliphor® P188 to the aqueous solution, the mixture was stirred for 10 min. Then 11.0 mL of cyclohexane was added to the clear solution via a dropping funnel. After that the mixture was further stirred for 30 min. An aqueous solution of *N,N,N',N'*-tetramethylethylenediamine (TMEDA) (0.15 mL with 20 vol% TMEDA; TMEDA : deionized water: 1 : 4;  $c = 1.3 \text{ mmol}\cdot\text{mL}^{-1}$ ; 0.20 mmol) was then added dropwise to the emulsion and the mixture was further stirred for 3 min. The white, viscous crude product was filled into a Teflon-liner and cured for 3 days at r.t.. A washing procedure with deionized water (6 x 150 mL, min. 14 h for each washing step) was followed by drying the monolith for 23 h at 353 K. 1.61 g of a mechanically stable white monolith was isolated.

---

[6] S. Kovačič, D. Štefanec, P. Krajnc, *Macromolecules* 40 (2007) 8056–8060.



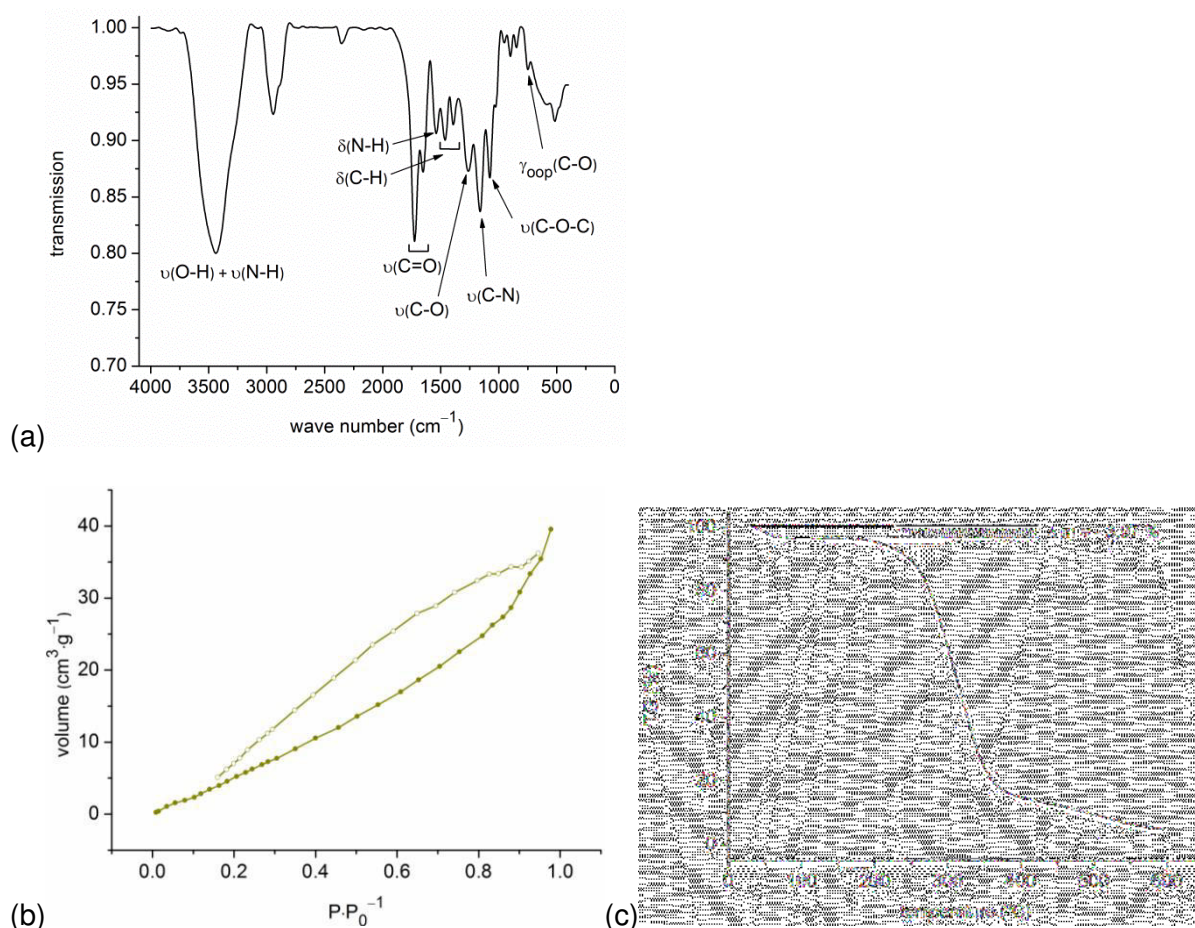


**Fig. A.3.** (a) IR-spectrum (KBr) of poly(HEMA)HIPE. (b)  $N_2$ -sorption isotherm of poly(HEMA)HIPE (degassing conditions: 4 h, 373 K, BET =  $50 \text{ m}^2\cdot\text{g}^{-1}$ ). Adsorption is depicted with filled, desorption with empty symbols. (c) Thermogravimetric analysis of poly(HEMA)HIPE shows a first mass loss of approximately 4 wt% due to loss of physisorbed water. A more hydrophilic compound like water-filled MIL-101(Cr) loses around 40 wt% of water in the first step [7].

[7] G. Férey, C. Mellot-Draznieks, C. Serre, F. Millange, J. Dutour, S. Surblé, I. Margiolaki, *Science* 309 (2005) 2040–2042.

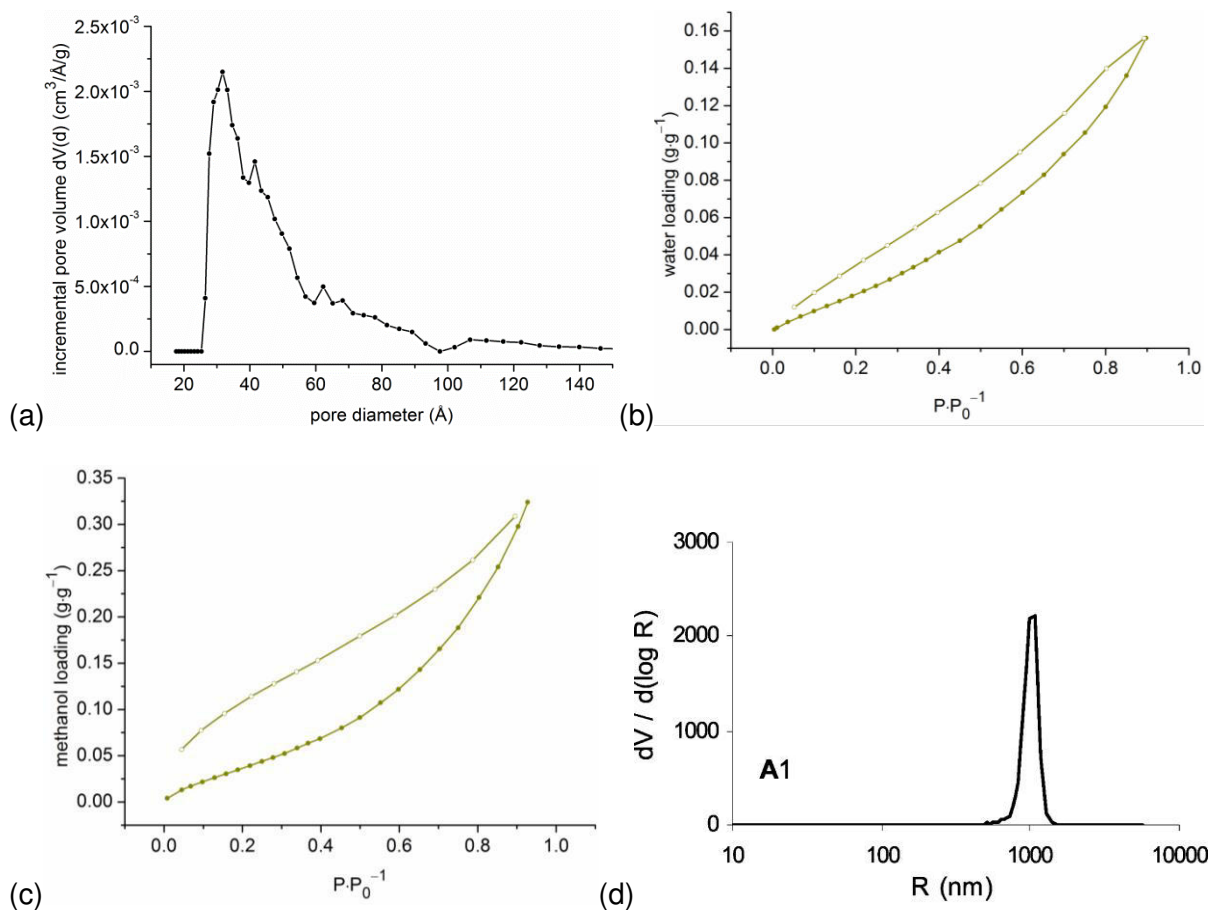


**Fig. A.4.** Characterization of poly(HEMA)HIPE by (a) pore size distribution curve from nitrogen adsorption isotherm with from N<sub>2</sub> at 77 K on carbon, slit pore, NLDFT equilibrium' model. (b) water sorption isotherm (degassing conditions: 4 h, 373 K). (c) Methanol sorption isotherm (degassing conditions: 4 h, 373 K). Adsorption is depicted with filled, desorption with empty symbols. (d) Pore size distribution from mercury porosimetry published in: S. Kovačič, D. Štefanec, P. Krajnc *Macromolecules* 40 (2007) 8056–8060. DOI: 10.1021/ma071380c. Copyright © 2007 American Chemical Society).

**Table A.1**

Nitrogen and water sorption measurements of activated MIL-101(Cr) and poly(HEMA)HIPE.

	BET surface area ( $\text{m}^2 \cdot \text{g}^{-1}$ ) <sup>a</sup>	Total pore volume ( $\text{cm}^3 \cdot \text{g}^{-1}$ ) <sup>b</sup>	Max. water loading ( $\text{g} \cdot \text{g}^{-1}$ ) <sup>c</sup>
MIL-101(Cr)	3060	1.45	1.06
poly(HEMA)HIPE	50	0.05	0.16

<sup>a</sup> BET surface area calculated at  $0.05 < P \cdot P_0^{-1} < 0.2$  from  $\text{N}_2$  sorption isotherm 77 K with a standard deviation  $\pm 20 \text{ m}^2 \cdot \text{g}^{-1}$ .

<sup>b</sup> calculated from  $\text{N}_2$  sorption isotherm at 77 K and  $P \cdot P_0^{-1} = 0.95$  for pores  $\leq 20 \text{ nm}$ .

<sup>c</sup> calculated from water sorption isotherm at 293 K and  $P \cdot P_0^{-1} = 0.9$ .

**Synthesis of the composite materials MIL-101(Cr)@poly(HEMA)HIPE with different wt% of MIL-101(Cr) (standard procedure, without pre-polymerization of the HIPE emulsion)**

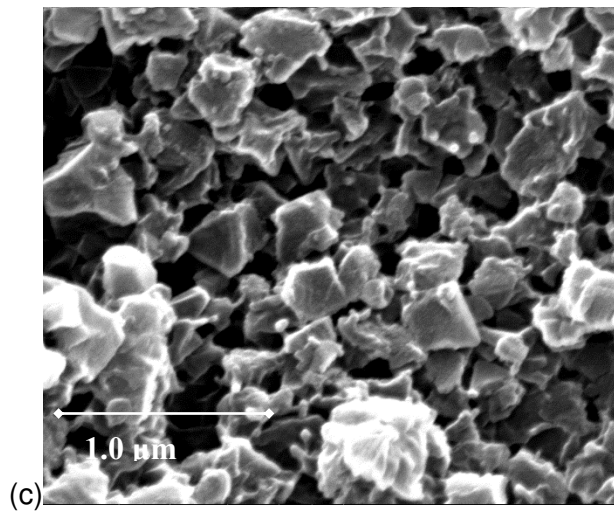
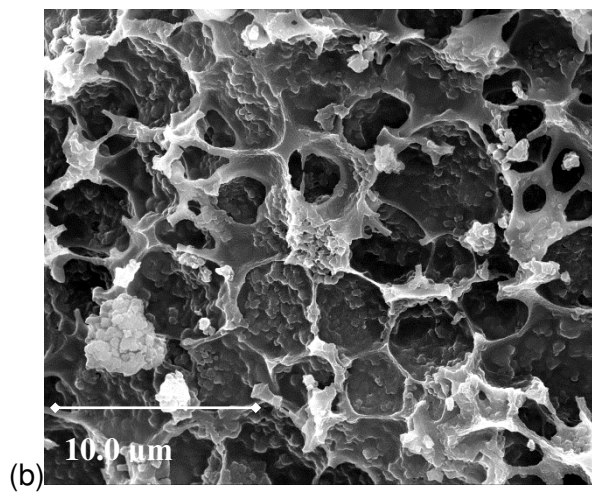
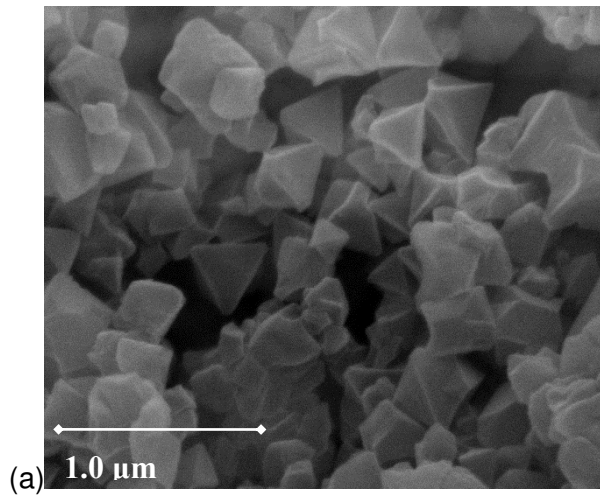
1.03 mL of 2-hydroxyethyl methacrylate (HEMA) ( $\rho = 1.071 \text{ g}\cdot\text{mL}^{-1}$ ; 8.48 mmol) was added dropwise to 2.60 g of deionized water. After adding 200 mg of *N,N'*-methylenebisacrylamide (MBA) (1.30 mmol), 35 mg of ammonium persulfate (APS) (0.15 mmol) and 750 mg of the surfactant Kolliphor® P188 to the aqueous solution, the mixture was stirred for 10 min. Cyclohexane (11.0 mL) was added to the clear solution via a dropping funnel. After that the mixture was further stirred for 30 min. For preparing the composite materials, plastic syringes (5 mL) were cut off from one side and filled with a specific mass of well ground MIL-101(Cr) and the just prepared emulsion (syringe 1: 50 mg MIL + 1005 mg emulsion, syringe 2: 100 mg MIL + 1022 mg emulsion, syringe 3: 150 mg MIL + 1000 mg emulsion, syringe 4: 200 mg MIL + 1019 mg emulsion). Each syringe was stirred well with a spatula until homogeneous appearance was reached. Then each syringe was filled with 0.05 mL of aqueous *N,N,N',N'*-tetramethylethylenediamine solution (TMEDA) (20 vol%; TMEDA : deionized water: 1 : 4;  $c = 1.3 \text{ mmol}\cdot\text{mL}^{-1}$ ; 0.07 mmol) and stirred again by a spatula. The green, viscous crude products were compressed and cured for 3 days at room temperature. A washing procedure with deionized water (6 x 100 mL for each monolith, min. 14 h for each washing step) was followed by drying the monoliths (first 16 h at 333 K, then 97 h at 353 K). The green monolith from syringe 4 crumbled immediately by contact with water. 132 mg (**38 wt%**, syringe 1), 170 mg (**59 wt%**, syringe 2) and 224 mg (**67 wt%**, syringe 3) of green monoliths were isolated. The loading of MIL-101(Cr) in MIL-101(Cr)@poly(HEMA)HIPE was calculated from formula S1.

MIL-101(Cr)@poly(HEMA)HIPE with **6 wt%** of MIL-101(Cr) was synthesized by the same procedure, which is described above for the composite materials by using 100 mg of MIL-101(Cr) and the entire emulsion [1.03 mL HEMA, 2.60 g deionized water, 200 mg MBA, 35

mg APS, 750 mg Kolliphor® P188, 11.0 mL cyclohexane, 0.15 mL TMEDA, (20 vol% in deionized water,  $c = 1.3 \text{ mmol}\cdot\text{mL}^{-1}$ ]. 1.67 g of a light green monolith was isolated.

**Formula A.1.** Used for calculations of wt% MIL-101(Cr) in MIL-101(Cr)@poly(HEMA)HIPEs.

$$\begin{aligned} & \text{wt\% (MIL-101(Cr) in MIL-101(Cr)@poly(HEMA)HIPE} \\ &= \frac{m(\text{weighted MIL-101(Cr)})}{m(\text{MIL-101(Cr)@poly(HEMA)HIPE})} \times 100 \end{aligned}$$



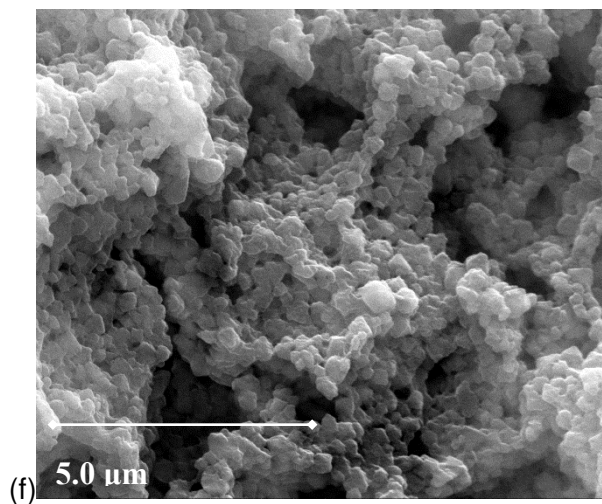
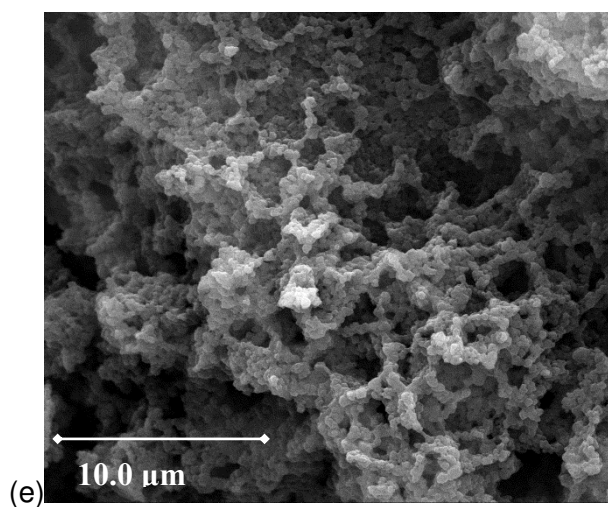
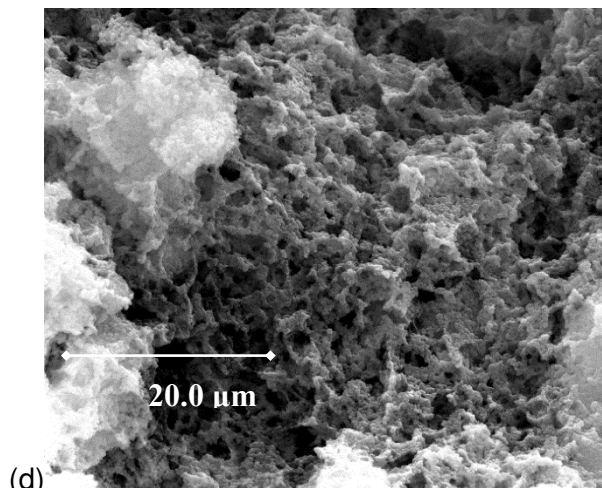


**Fig. A.5.** Scanning electron microscopic (SEM) images of (a) native MIL-101(Cr) and MIL-101(Cr)@poly(HEMA)HIPE (standard procedure) composites with (b)-(c) 38 wt% and (d)-(f) 67 wt% of MIL-101(Cr).

### **Synthesis of the composite materials pp-MIL-101(Cr)@poly(HEMA)HIPE with 38 and 59 wt% of MIL-101(Cr) with pre-polymerization (pp) of the HIPE emulsion**

The synthetic procedure of the MIL-101(Cr)@poly(HEMA)HIPEs with 38 and 59 wt% MIL-101(Cr) with pre-polymerization of the HIPE emulsion was done on the same scale as the standard procedure described before. After adding cyclohexane the emulsion was stirred for 22 h (instead of 30 min in the standard procedure) at r.t.. 60  $\mu\text{L}$  of aqueous TMEDA solution (20 vol%; TMEDA : deionized water: 1 : 4;  $c = 1.3 \text{ mmol}\cdot\text{mL}^{-1}$ ; 0.08 mmol) was then added to the entire emulsion continued by further stirred for 3 min. The longer stirring time of the HIPE emulsion is equivalent to a pronounced degree of HIPE polymerization. The composite materials were prepared in plastic syringes as described before (syringe 1: 50 mg MIL + 1005 mg emulsion, syringe 2: 100 mg MIL + 1022 mg emulsion). Each syringe was stirred well with a spatula until homogeneous appearance was reached. Then each syringe was filled additionally with 30  $\mu\text{L}$  of aqueous TMEDA solution (20 vol%; TMEDA : deionized water: 1 : 4;  $c = 1.3 \text{ mmol}\cdot\text{mL}^{-1}$ ; 0.04 mmol) and stirred again by a spatula. The green, viscous crude products were compressed and cured for 3 days at r.t.. The crude monoliths were washed and dried in the same way as described before. 130 mg (**38 wt%**, syringe 1) and 169 mg (**59 wt%**, syringe 2) of green monoliths were isolated.



## Synthesis of the composite materials $cC_6$ -MIL-101(Cr)@poly(HEMA)HIPE with 38 and 59 wt% of MIL-101(Cr) with impregnation of the MIL with cyclohexane ( $cC_6$ ) before curing

The synthetic procedure of the MIL-101(Cr)@poly(HEMA)HIPEs with 38 and 59 wt% MIL-101(Cr) with impregnation of the MIL with cyclohexane was done on the same scale and in the same way as the standard procedure described before. The pure MILs were impregnated with 0.27 mL (syringe 1: 50 mg MIL + 1005 mg emulsion) and 0.50 mL (syringe 2: 100 mg MIL + 1022 mg emulsion) of cyclohexane for 75 min before adding the HIPE emulsion containing 10.0 mL of cyclohexane (instead of 11.0 mL). After curing, washing and drying 131 mg (**38 wt%**, syringe 1) and 170 mg (**59 wt%**, syringe 2) of green monoliths were isolated.

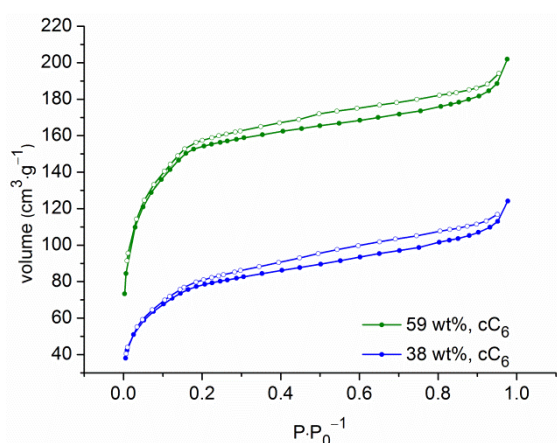


**Fig. A.6.**  $N_2$ -sorption isotherms of  $cC_6$ -MIL-101(Cr)@poly(HEMA)HIPE composites with 38 and 59 wt% MIL-101(Cr) (degassing conditions: 4 h, 373 K). Adsorption is depicted with filled, desorption with empty symbols.

**Nitrogen experiments of the 38 and 67 wt% MIL loaded composites MIL-101(Cr)@poly(HEMA)HIPE as powder and monoliths**

Nitrogen sorption experiments of the 38 and 67 wt% standard composites were carried out on powdered monoliths with longer equilibration time. The results in Table A.2 show that the BET surface areas for both materials are the same in all three cases (540, 540 and 550 m<sup>2</sup>·g<sup>-1</sup> for 67 wt%) or nearly the same (300, 270 and 250 m<sup>2</sup>·g<sup>-1</sup> for 38 wt%). Therefore, the accessibility of nitrogen for the pores of the composite materials does not seem to depend on the shape of the composites or the time, which is given for the equilibration during adsorption.

**Table A.2**

Nitrogen measurements of MIL-101(Cr)@poly(HEMA)HIPE.

MIL-101(Cr)@poly (HEMA)HIPE	BET surface areas of monoliths (m <sup>2</sup> ·g <sup>-1</sup> ) a,b	BET surface areas of powders (m <sup>2</sup> ·g <sup>-1</sup> ) a,b	BET surface areas of powders measured with longer equilibration time for adsorption points (m <sup>2</sup> ·g <sup>-1</sup> ) <sup>a,c</sup>
38 wt%	300	270	250
67 wt%	540	540	550

<sup>a</sup> BET surface area calculated at  $0.05 < P/P_0 < 0.2$  from N<sub>2</sub> sorption isotherm 77 K with a standard deviation  $\pm 20$  m<sup>2</sup>·g<sup>-1</sup>.

<sup>b</sup> parameters for adsorption points: Equilibration time 180 sec. Equilibration timeout 720 sec.

<sup>c</sup> parameters for adsorption points: Equilibration time 1200 sec. Equilibration timeout 2400 sec.

## Infrared spectra of monomers and surfactant

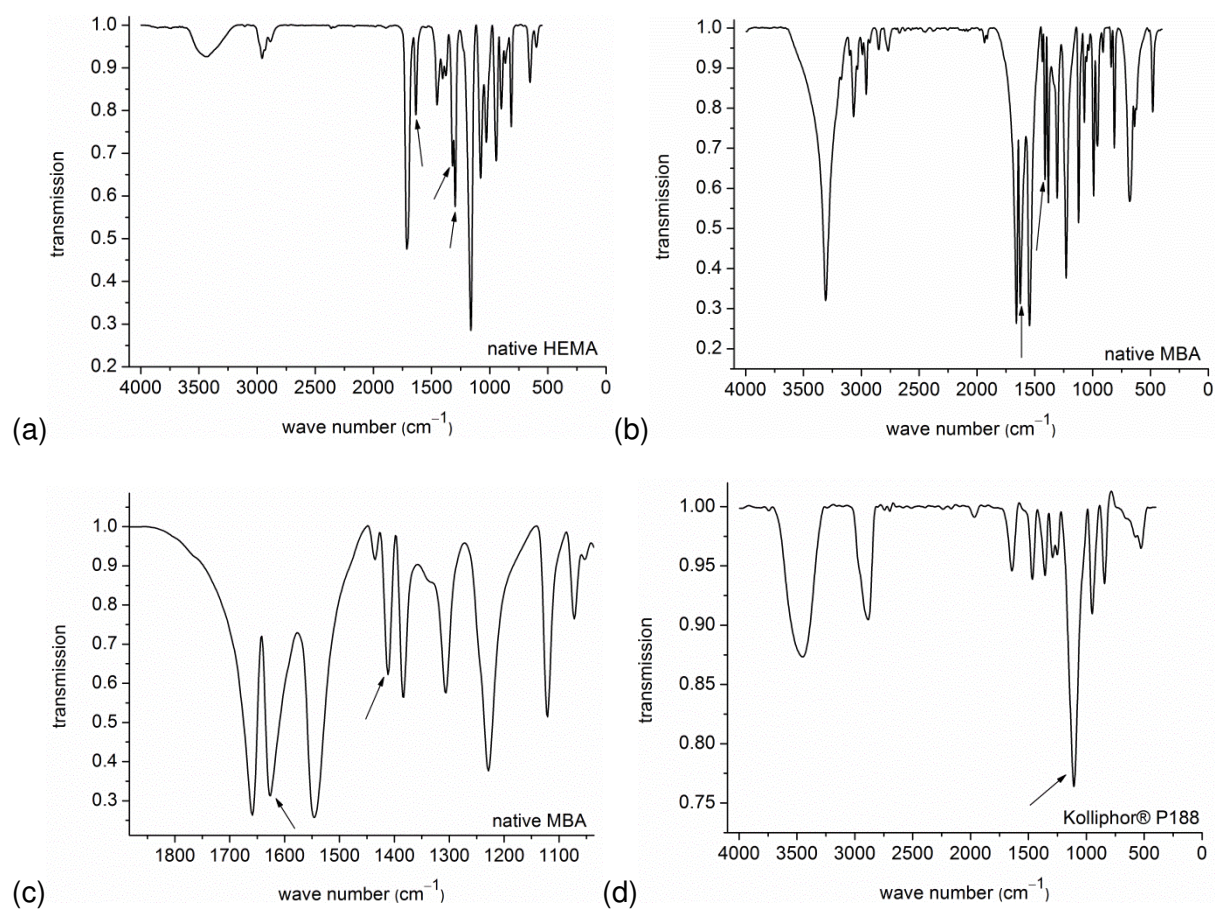


**Fig. A.7.** IR-spectra of (a) HEMA, (b) MBA, (c) MBA (enlargement for region 1850–1050 cm<sup>-1</sup>) and (d) Kolliphor® P188. The black arrows show representative bands, which do not occur in the poly(HEMA)HIPE material.

## Thermodynamic principle for adsorption chillers or heat pumps

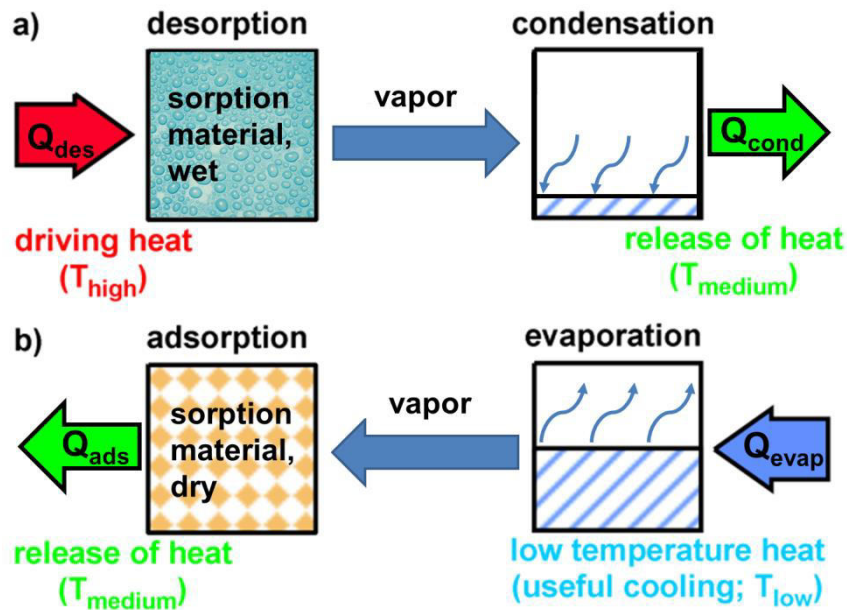


**Fig. A.8.** Thermodynamic principle for adsorption chillers or heat pumps [8]. The working cycle (b) describes the evaporation of the working fluid at a low temperature level, which creates useful cold due to  $Q_{\text{evap}}$ . The vapor is then adsorbed in the dry sorption material, releasing useful heat  $Q_{\text{ads}}$  at a medium temperature level. In the regeneration cycle (a) the vapor is desorbed from the saturated sorption material applying  $Q_{\text{des}}$  (driving heat) and condensed at a medium heat temperature level, releasing heat of condensation  $Q_{\text{cond}}$ .

[8] S.K. Henninger, H.A. Habib, C. Janiak, J. Am. Chem. Soc. 131 (2009) 2776–2777.

## Porous structure of MIL-101(Cr)

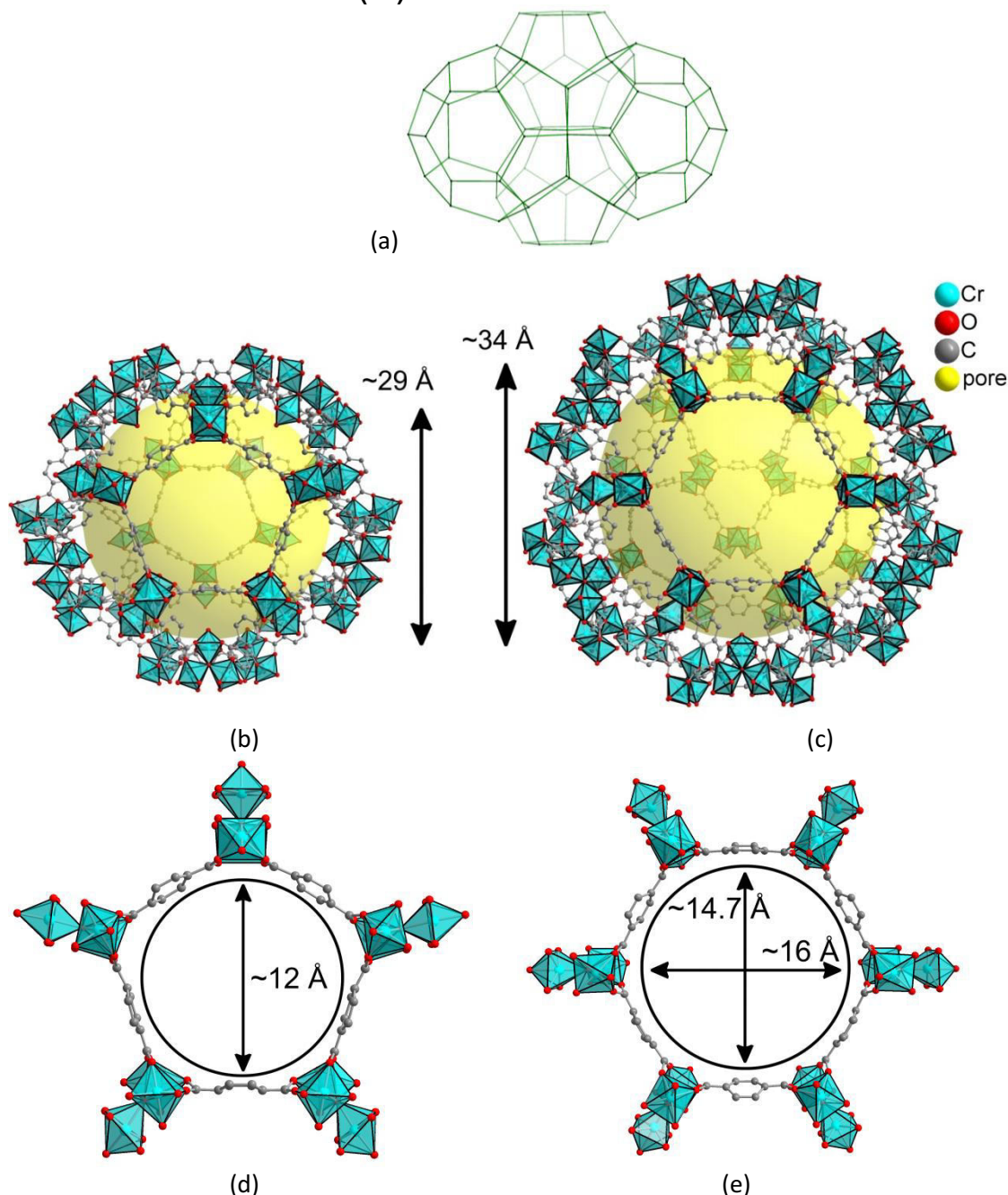


**Fig. A.9.** MIL-101(Cr) of formula  $\{\text{Cr}_3(\mu_3\text{-O})(\text{F})(\text{H}_2\text{O})_2(\text{BDC})_3\} \cdot \sim 25\text{H}_2\text{O}$  (BDC = 1,4-benzene dicarboxylate) presents a 3D framework constructed by two mesopores (in a 2:1 ratio) with diameter of 29 and 34 Å (a-c). The small cage (b) has an inner diameter 29 Å and only pentagonal windows (d). The large cage (c) has an inner diameter of 34 Å and both pentagonal and hexagonal windows (e). The MIL-101(Cr) structure is redrawn from the deposited cif file at the Cambridge Structure Database (CSD-Refcode OCUNAK [9]) using the software DIAMOND [10].

[9] G. Férey, C. Mellot-Draznieks, C. Serre, F. Millange, J. Dutour, S. Surblé, I. Margiolaki, *Science* 309 (2005) 2040–2042.

[10] K. Brandenburg, *Diamond (Version 3.2), crystal and molecular structure visualization*, Crystal Impact. K. Brandenburg & H. Putz Gbr, Bonn, Germany, 2007–2012.

**Table A.3**Comparison of N<sub>2</sub> sorption data of similar composite materials from the literature.

Composites [Reference]	Experimental BET surface area (m <sup>2</sup> ·g <sup>-1</sup> )	Estimated BET surface area (m <sup>2</sup> ·g <sup>-1</sup> ) <sup>e</sup>	wt% of MOFs and quantification method	Possible application
HKUST-1@PAM <sup>a</sup> [11]	654 <sup>c</sup>	667	62 wt%; N <sub>2</sub> sorption data + TGA	No application investigated
HKUST-1 monolith <sup>b</sup> [12]	484 <sup>d</sup>	-	No wt% given	No application investigated
HKUST-1@porous carbon monoliths [13]	270; 455; 516	816; 988; 1198	19 wt%; 41 wt%; 68 wt%; Weighing method	CO <sub>2</sub> storage; Gas separation (CO <sub>2</sub> / N <sub>2</sub> )
HKUST-1@silica aerogel [14]	1025; 1036; 1138	944; 955; 1056	4.2 wt%; 16.3 wt%; 30.5 wt%; Weighing method	No application investigated
HKUST-1@macro-/mesoporous silica [15]	971	907	25 wt%; TGA	catalysis
UiO-66@polyurethane [16]	511 <sup>c</sup> ; 427 <sup>c</sup>	834; 752	71 wt%; 64 wt%; TGA	Adsorption of organic vapors
HKUST-1@HIPE [17]	570	846	62.3 wt%; TGA	No application investigated

<sup>a</sup> PAM stands for polyacrylamide.<sup>b</sup> binding agent: methoxy functionalized siloxane ether; plasticizer: methyl hydroxyl propyl cellulose.<sup>c</sup> BET surface areas of pure binding agents are not considered in calculations due to their absence in the corresponding literature.<sup>d</sup> Values decreased after several months to 287 m<sup>2</sup>·g<sup>-1</sup>.<sup>e</sup> BET surface area as the sum of the mass-weighted surface areas of MOFs and porous binding agents calculated from the following formula:

$$\text{BET (estimated)} = \frac{\text{wt\% of MOF}}{100} \times \text{BET of pure MOF} + \frac{\text{wt\% of binding agent}}{100} \times \text{BET of pure binding agent}$$

[11] L.D. O'Neill, H. Zhang, D.J. Bradshaw, *J. Mater. Chem.* 20 (2010) 5720–5726.[12] P. Küsgens, A. Zgaverdea, H.-G. Fritz, S. Siegle, S. Kaskel, *J. Am. Ceram. Soc.* 93 (2010) 2476–2479.[13] D. Qian, C. Lei, G.-P. Hao, W.-C. Li, A.-H. Lu, *Appl. Mater. Interfaces* 4 (2012) 6125–6132.[14] Z. Ulker, I. Erucar, S. Keskin, C. Erkey, *Microporous Mesoporous Mater.* 170 (2013) 352–358.[15] A. Sachse, R. Ameloot, B. Coq, F. Fajula, B. Coasne, D. De Vos, A. Galarneau, *Chem. Commun.* 48 (2012) 4749–4751.[16] M.L. Pinto, S. Dias, J. Pires, *Appl. Mater. Interfaces* 5 (2013) 2360–2363.[17] M.G. Schwab, I. Senkovska, M. Rose, M. Koch, J. Pahnke, G. Jonschker, S. Kaskel, *Adv. Eng. Mater.* 10 (2008) 1151–1155.

### 3.3 Hierarchical MOF-xerogel monolith composites from embedding MIL-100(Fe,Cr) and MIL-101(Cr) in resorcinol-formaldehyde based xerogels for water adsorption applications

M. Wickenheisser, A. Herbst, R. Tannert, B. Milow, C. Janiak  
*submitted*. Reference 214.

Shaping of metal-organic frameworks into monolithic structures is of high importance due to their powdery appearance. Binding agents such as poly(HIPes) can be used to obtain monolithic MOF@Polymer composite materials with maximized porosities and high vapor uptake capacities due to the pre-polymerization method of the binding agent. As seen before for MIL-101(Cr)@HIPE materials, methanol adsorption is clearly favored over water adsorption (section 3.2) due to the hydrophobic nature of the pure poly(HEMA)HIPE. For realistic application as adsorption chillers (TDCs) or heat pumps (AHPs), the use of water as working fluid is economically advantageous compared to alcohols like methanol. Water is non-toxic and has more than twice the amount of the evaporation enthalpy in comparison to methanol. Therefore, the usage of water as working fluid is an essential requirement for highly efficient TDCs or AHPs.

A new binding agent was found for the incorporation of MOFs, which exhibits a more hydrophilic behavior compared to poly(HEMA)HIPE. A porous xerogel, based on resorcinol and formaldehyde, was found to be a suitable candidate with an almost linear rise of the water adsorption isotherm. Water sorption properties of the pure material have been already published before, but reports on MOF@xero-/aerogels composites are scarce.<sup>227</sup> In one of these reports, HKUST-1 was embedded into a porous carbon monolith and into a silica aerogel.<sup>211,213</sup>

Three MOFs of the MIL family with good water sorption properties and cycling stabilities (MIL-100(Fe,Cr) and MIL-101(Cr)) were successfully embedded into the porous R,F-xerogel and the resulting mechanically stable MIL@R,F-xerogels exhibited accessible and free MIL pores together with high water loading lifts. Pore blocking effects of the MIL pores could be mostly avoided through the pre-polymerization method. A possible industrial utilization as water adsorbents becomes realizable due to the monolithic shape and almost no loss of BET surface area, porosity and water uptake capacity especially for MIL-101(Cr)@R,F-xerogel composites are observed.

Author's share of work:<sup>iii</sup>

- Designing, performing of the synthetic work and evaluation of the results except for the pre-polymerized-MIL-101(Cr)@R,F-xerogel composites and method of additional usage of water (done by Mrs. Herbst) and the SEM images (done by Mr. Köhler and Mrs. Herbst).
- Writing of the manuscript except for the introduction and drawing of the figures except for figures 1 and 2 (done by Mrs. Herbst) and figure S16 and S17 (done by Mr. Janiak).
- Editing of the manuscript regarding the reviewers' comments.

Reproduced with permission from Chemistry of Materials, submitted for publication. Unpublished work copyright 2015 American Chemical Society. Manuscript ID cm-2015-01325j, ref. 214.

---

<sup>iii</sup> The xerogel project was worked out in cooperation with Annika Herbst, Sebastian Glomb, Tian Zhao and co-workers of the DLR in Cologne. We thank Marina Schwan and Jessica Laskowski from DLR for the kind introduction to xerogel syntheses. Pre-polymerization experiments, performing of pure xerogel syntheses with different parameters (variation of R/C, R/F and R/W ratios) and initial MIL@R,F-xerogel syntheses were done together with Annika Herbst (MIL-101(Cr)), Sebastian Glomb (HKUST-1) and Tian Zhao (NH<sub>2</sub>-MIL-101(Al)).



# Hierarchical MOF-xerogel monolith composites from embedding MIL-100(Fe,Cr) and MIL-101(Cr) in resorcinol-formaldehyde xerogels for water adsorption applications

Martin Wickenheisser,<sup>†</sup> Annika Herbst,<sup>†</sup> René Tannert<sup>‡</sup>, Barbara Milow<sup>‡</sup> and Christoph Janiak<sup>\*,†</sup>

<sup>†</sup> *Institut für Anorganische Chemie und Strukturchemie I, Universitätsstraße 1, 40225 Düsseldorf, Germany*

<sup>‡</sup> *Deutsches Zentrum für Luft- und Raumfahrt (DLR), Institut für Werkstoff-Forschung, Aerogele, Linder Höhe, 51147 Köln, Germany*

*Keywords:* Metal-organic framework, Resorcinol-formaldehyde xerogels, Monoliths, Water adsorption, Heat transformation.

## Abstract

Shaping of otherwise powdery metal-organic frameworks is recognized as a more-and-more important issue to advance them to the application stage. Monolithic MOF composites were synthesized using micro-to-mesoporous MIL-100(Fe,Cr) and MIL-101(Cr) as thermally and chemically stable MOFs together with a mesoporous resorcinol-formaldehyde based xerogel as binding agent. The monolithic bodies could be loaded with up to 77 wt% of powdery MIL material under retention of the MIL surface area and porosities (from N<sub>2</sub> adsorption) by pre-polymerization of the xerogel solution. The obtained monoliths are mechanically stable and adsorb close to the expected water vapor amount according to the MIL weight percentage. There is no loss of BET surface area, porosity and water uptake capacity especially for the MIL-101(Cr) composites. Water vapor adsorption isotherms show that the 77 wt% MIL-101(Cr) loaded composite even features a slightly increased water vapor uptake compared to pure MIL-101(Cr) up to a relative vapor pressure of  $P/P_0^{-1} = 0.5$ . These hydrophilic

monolithic composites could be applied for heat transformation application such as thermally driven adsorption chillers or adsorption heat pumps.

## 1. Introduction

MOFs (metal-organic framework) are potentially porous coordination networks<sup>1</sup> based on metal ions or metal clusters, connected by organic ligands.<sup>2,3</sup> Metal organic frameworks are often three-dimensional networks and have uniform micropore structures with high surface areas and large pore volumes. Research tries to advance MOFs towards applications,<sup>4,5-6</sup> such as catalysis,<sup>7,8,9,10-11</sup> gas storage,<sup>12,13,14-15</sup> and gas separation.<sup>16,17,18,19-20</sup> Many review articles are evidence to the increasing interest in MOF chemistry over the last years.<sup>21,22,23,24,25-26</sup>

Recently, MOFs are investigated as microporous materials for cycling water sorption for heat transformation: During hot seasons in large part of cities energy consumption caused by electric air-conditioning represents 30 to 50 % of total electric energy consumed.<sup>27</sup> Therefore it would be beneficial to use a cooling system based on adsorption chilling running on solar thermal energy. In this context sorption-based heat transformations attracted growing interest during the last years.<sup>28,29,30,31</sup>

A schematic diagram of a thermally driven adsorption chiller or adsorption heat pump is depicted in Figure 1. Bed 1 and Bed 2 contain the porous (MOF-) material in combination with a heat exchange device and are switched between the working and regeneration cycle. During the working cycle, adsorption of the working fluid (e.g. water) takes place in the bed until the desired loading is reached. At the same time the other bed is regenerated by applying heat to desorb the working fluid. The desorbed vapor is liquefied in the condenser and the liquid working fluid then flows back to the evaporator, where again evaporation takes place. The heat of condensation ( $Q_{out}^{cond}$ ) and the heat of adsorption ( $Q_{out}^{ads}$ ) can be used in a heating application or are dissipated to the environment. From the heat of evaporation ( $Q_{in}^{evap}$ ) either useful cold is generated for the cooling application or it is the low-temperature

heat (blue) which is converted to medium temperature levels (green) by means of the driving heat of desorption  $Q_{in}^{drive,des}$  (red). When the water loadings in bed 1 and 2 reach the same level, the two beds are interchanged with respect to regeneration and working cycle by closing and opening the respective valves.<sup>32</sup>

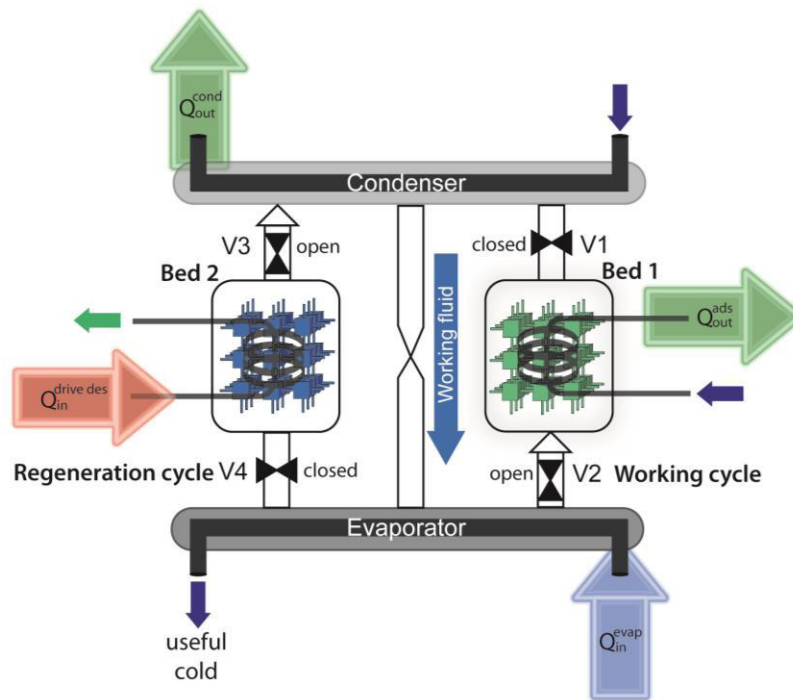


**Figure. 1.** Thermodynamic principle for adsorption chillers or heat pumps. Bed 1 (here in working cycle) and bed 2 (here in regeneration cycle) contain the porous adsorbent.<sup>32</sup>  $Q_{in}^{drive,des}$  driving heat of desorption at a high temperature level (red),  $Q_{out}^{cond}$  and  $Q_{out}^{ads}$ , heat of condensation and heat of adsorption at a medium temperature level (green),  $Q_{in}^{evap}$  heat of evaporation at a low temperature level (blue).

The key part of the system is the sorption material which should have a high water loading lift in the ideal interval  $0.05 < P \cdot P_0^{-1} < 0.35$ . Water is the working fluid of choice because of its high evaporation enthalpy ( $2440 \text{ kJ} \cdot \text{kg}^{-1}$  at  $25 \text{ }^\circ\text{C}$ ) and non-toxicity despite the need to work under vacuum because of the low vapor pressure of only  $3.17 \text{ kPa}$  at  $25 \text{ }^\circ\text{C}$ .<sup>22,33,34</sup> During the last years significant progress has been made in the development of MOF-based sorption materials.<sup>35</sup> Various materials, predominately of the MIL (Materials of Institute Lavoisier) family, have been investigated for water adsorption<sup>36,37</sup> and also different strategies of tuning

prototypical MOFs to enhance the water uptake have been examined.<sup>38,39</sup> Long term and cycle measurements have been performed to ensure the required water stability.<sup>40,41,42</sup> Three of these MOFs, namely MIL-100(Fe,Cr) and MIL-101(Cr), were selected for the present study due their good water sorption properties and stability.<sup>39,43</sup>

MIL-100  $\{M_3(\mu_3-O)(X)(H_2O)_2(BTC)_2 \cdot nH_2O\}_n$  ( $M = Cr^{44}, Fe^{45}; X = OH, F; BTC = 1,3,5$ -benzene tricarboxylate) possesses two types of mesopores with cages of 25 Å and 29 Å in diameter consisting of hexagonal (8.6 Å) and pentagonal windows (4.7–5.5 Å) (Fig. 2, Fig. S17).<sup>45</sup> MIL-101(Cr)<sup>46</sup>  $\{Cr_3(\mu_3-O)(F,OH)(H_2O)_2(BDC)_3 \cdot \sim 25H_2O\}_n$  is a micro- and mesoporous material, having 1,4-benzene dicarboxylate (BDC) as linker, with hexagonal (15–16 Å) and pentagonal windows (12 Å) and inner free cages of 29 Å and 34 Å in diameter (Fig. 2, Fig. S16). The water uptake of MIL-100(Cr), MIL-100(Fe) and MIL-101(Cr) are in the range of 0.6–0.7 g g<sup>-1</sup>, 0.65–0.75 g g<sup>-1</sup> and 1.0–1.5 g g<sup>-1</sup>, respectively.<sup>42</sup>

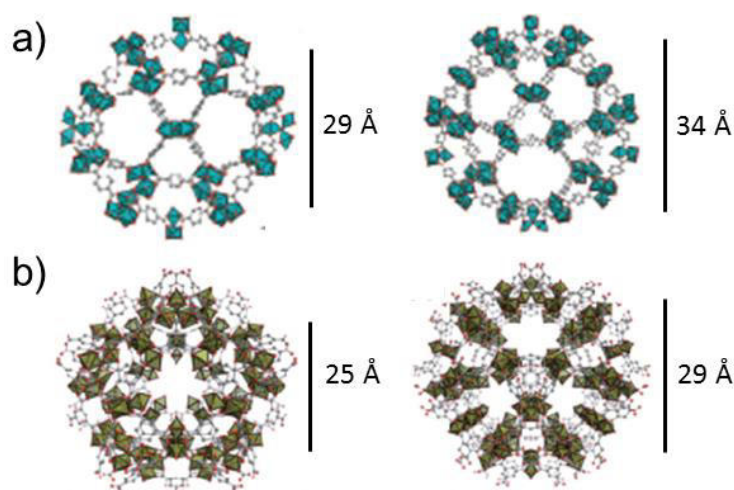


**Figure 2.** a) MIL-101(Cr) small and large cages (CSD-Refcode OCUNAK<sup>46</sup>). b) Small cage and large cage in MIL-100(Fe) (CSD-Refcode CIGXIA<sup>45</sup>) (different objects are not drawn to scale). Hydrogen atoms and solvent molecules of crystallization are not shown. MIL-100(Cr) is isostructural to MIL-100(Fe).

MOFs are typically obtained as crystalline fine powders, yet almost every application requires an appropriate shaping, *e.g.*, monolithic structures, of the used materials without diminishing its useful properties.<sup>47,48</sup>

Different strategies of shaping MOFs have been investigated so far:<sup>47,49,50</sup> One possibility is to press the material into tablets or pellets.<sup>51</sup> MOF-177 has been mechanical compressed to a monolithic structure, resulting in enhanced hydrogen storage capacity, but also leading to an amorphous material.<sup>52</sup> An alternative strategy is the preparation of pure MOF monoliths, although there are often difficulties in obtaining phase pure MOFs and retaining porosity.<sup>53,54</sup> More studies have been performed on MOF composites where an organic or inorganic additive acts as binder to shape the material.<sup>24,55,56,57,58</sup> The resulting monoliths or membranes were tested for example in separation processes.<sup>59,60,61,62,63</sup> Aerogels are characterized by high porosity and high surface area as well as a low density and low thermal conductivity.<sup>64,65</sup> To obtain an aerogel with these properties supercritical drying with CO<sub>2</sub> is a necessary step.<sup>64,66</sup> Resorcinol-formaldehyde based gels can be dried under atmospheric conditions, if the ratio of resorcinol to basic catalyst is high enough leading to mechanically stable xerogels with negligible shrinking during the drying procedure.<sup>67</sup> In the following, the term xerogel is defined as subcritically dried and aerogel is used for supercritical dried materials. Easily obtainable resorcinol-formaldehyde aero- and xerogels are well investigated and can be tuned by several parameters. For example, the ratio of resorcinol and catalyst as well as the pH of the solution influences the properties of the gel material.<sup>68,69,70,71</sup> A major advantage, in terms of embedding porous materials, is the possibility of pre-polymerizing the polymer, which was reported first by Czakkel et al.<sup>72</sup> By applying this method to MOF polymer composites, pore-blocking effects, which often occur in composite syntheses, could be avoided in order to retain the porous properties of the MOFs.<sup>47,50,58</sup>

In this work, we present for the first time the embedding of three different metal-organic frameworks (MIL-100(Fe, Cr) and MIL-101(Cr)) in resorcinol-formaldehyde xerogels and investigate the resulting monoliths for their porosity and water-sorption behavior.

## 2. Experimental section

### 2.1 Materials and methods

All chemicals were obtained commercially and were used without further purification: Fe<sup>0</sup> powder (Riedel-de Haën, > 99 %), CrO<sub>3</sub> (Alfa Aesar, 99 %), Cr(NO<sub>3</sub>)<sub>3</sub>·9H<sub>2</sub>O (Acros Organics, 99 %), hydrofluoric acid (Acros Organics, 48-51 wt% in H<sub>2</sub>O), HNO<sub>3</sub> (Grüssing, 65 wt%), 1,3,5-benzenetricarboxylic acid (H<sub>3</sub>BTC) (Alfa Aesar, 98 %), 1,4-benzenedicarboxylic acid (H<sub>2</sub>BDC) (Acros Organics, > 99 %), tetramethylammonium hydroxide (TMAOH) (Alfa Aesar, 25 wt% in water), resorcinol (Acros Organics, 98 %), Na<sub>2</sub>CO<sub>3</sub> (Riedel-de Haën, > 99.8 %), formaldehyde (VWR, 24 wt% in water), acetic acid (VWR, 99.9 %), DMF (VWR, p.a.), ethanol (VWR, p.a.). All experimental work was performed in air.

### 2.2 Physical measurements

Powder X-ray diffraction (PXRD) diffractograms were obtained at ambient temperature on a Bruker D2 Phaser with a flat sample holder using Cu-K $\alpha$  radiation ( $\lambda = 1.54182 \text{ \AA}$ ). Fourier transform infrared spectra were done on a Bruker TENSOR 37 IR spectrometer at ambient temperature in a KBr disk in a range of 4000 to 500 cm<sup>-1</sup>. Nitrogen physisorption isotherms were carried out on a Nova 4000e from Quantachrome at 77 K. Water physisorption isotherms were measured volumetrically on a Quantachrome Autosorb iQ MP at 293 K. For measuring the isotherms the materials were loaded into glass tubes capped with septa. The weighted tubes were attached to the corresponding degassing port of the sorption analyzer, degased under vacuum at elevated temperature, weighted out again and then transferred to the analysis port of the sorption analyzer. BET surface areas were calculated from the nitrogen physisorption isotherms. DFT calculations for the pore size distribution curves were done with the native NovaWin 11.03 software using the 'N<sub>2</sub> at 77 K on carbon, slit pore, nonlinear density functional theory (NLDFT) equilibrium' model.<sup>73,74,75</sup> Scanning electron microscopic images were done on a LEO 1430 VP (native xerogel, MIL-100(Fe)@xerogel),

on a LEO 982 (77 wt%, MIL-101(Cr)@xerogel-H<sub>2</sub>O) both from Zeiss and on a JSM-6510 (MIL-100(Cr)@xerogel; 35 wt%, MIL-101(Cr)@xerogel) from Jeol. The samples were coated with Au for 180 sec at 30 mA by an AGAR sputter coater (LEO 1430 VP), sputtered with chromium (approx. 10 nm thickness, LEO 982) or with Au for 20 sec at 35 mA by an Jeol JFC-1200 sputter (JSM-6510). The thermogravimetric analysis (TGA) curve of native R,F-xerogel was measured on a TG 209 F3 Tarsus from Netzsch in the temperature range between 303 and 873 K, with heating rate of 3 K·min<sup>-1</sup>.

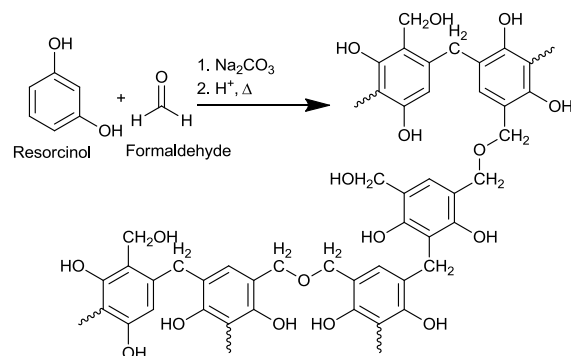
### 2.3 Synthesis of MIL-100(Fe,Cr) and MIL-101(Cr)

MIL-100(Fe), MIL-100(Cr) and MIL-101(Cr) were hydrothermally synthesized according to the literature.<sup>76,77,78</sup> Typical batch sizes of 665 mg Fe<sup>0</sup> powder (11.9 mmol), 1.65 g H<sub>3</sub>BTC (7.85 mmol), 0.83 mL hydrofluoric acid (24 mmol; 48-51 wt% in H<sub>2</sub>O), 0.5 mL HNO<sub>3</sub> (7 mmol; 65 wt%) and 60 mL of deionized H<sub>2</sub>O (for *MIL-100(Fe)*), 1.20 g CrO<sub>3</sub> (12.0 mmol), 2.52 g H<sub>3</sub>BTC (12.0 mmol), 0.42 mL hydrofluoric acid (12 mmol; 48-51 wt% in H<sub>2</sub>O) and 58 mL of deionized H<sub>2</sub>O (for *MIL-100(Cr)*) and 4.80 g (12.0 mmol) Cr(NO<sub>3</sub>)<sub>3</sub>·9H<sub>2</sub>O, 1.98 g (11.9 mmol) H<sub>2</sub>BDC, 1.1 mL TMAOH (3.1 mmol; ρ = 1.014 g·mL<sup>-1</sup>; 25 wt% in H<sub>2</sub>O) and 60 mL of deionized water (for *MIL-101(Cr)*) yielded the raw MILs. For further activation the MILs were purified through a consecutive washing procedure with DMF, EtOH and deionized water (see Supporting Information for details). 1.50, 3.18 and 2.34 g of purified MIL-100(Fe), MIL-100(Cr) and MIL-101(Cr) were isolated (41, 69 and 50 % yield based on Fe or Cr), as orange-brown (MIL-100(Fe)) and green powders (MIL-100/101(Cr)) with BET surface areas and pore volumes shown in Table 1. Pore volumes (measured at P/P<sub>0</sub><sup>-1</sup> = 0.95) and BET surface areas were calculated from the type I N<sub>2</sub> sorption isotherms (Fig. S2a, S4a, S6a, Table 1). Experimental, theoretical powder X-ray patterns and the IR-spectra are shown in Figures S1, S3, S5.

## 2.4 Synthesis of native R,F-xerogel

The polycondensation reaction of resorcinol and formaldehyde is initiated by the basic catalyst  $\text{Na}_2\text{CO}_3$ , which first leads to deprotonation of the acidic phenol groups followed by addition of formaldehyde to the phenol ring. The formed hydroxymethyl functionalities ( $-\text{CH}_2\text{OH}$ ) undergo a condensation reaction forming a methylene ( $-\text{CH}_2-$ )- and methylene ether ( $-\text{CH}_2\text{OCH}_2-$ )-bridged polymer illustrated in Scheme 1. For gelation (polymerization) typically resorcinol (R) and formaldehyde (F) are dissolved in a basic, aqueous  $\text{Na}_2\text{CO}_3$  solution (C,  $c = 2.1 \cdot 10^{-3} \text{ mol} \cdot \text{L}^{-1}$ ). The base C is essential for the formation of the R anions, which are more active towards the addition of F compared to uncharged, neutral R. After a short period of stirring (5 min), the so-called sol mixture, is transferred into an appropriate mold and cured for 7 days at 333 K. The curing of the sol leads to a monolithic product, which is then placed for 1 day in dilute acetic acid solution to increase the crosslinking of the residual hydroxymethyl groups. The monolithic resorcinol-formaldehyde polymers are washed in ethanol several times and finally dried subcritically by conventional evaporation of the solvent at atmospheric pressure (see Supporting Information for details). The obtained brown-colored polymers are called “xerogels”. Supercritical drying with  $\text{CO}_2$  would lead to so-called “aerogels”. The choice of the catalyst concentration, the initial gel pH, the concentration of R and F in the sol, dilution effects and the way of drying the monoliths all influence the particle size, density, surface area and mechanical strength of the final monoliths. For a detailed analysis of these factors the reader is referred to other literature.<sup>64,68,69,71</sup>





**Scheme 1.** Schematic presentation of the polymerization reaction of resorcinol (R) with formaldehyde (F) in the presence of a base (C).

## 2.5 Syntheses of MIL-100(Fe,Cr)@xerogel and MIL-101(Cr)@xerogel

MIL@xerogel with different wt% of MILs were synthesized by homogenization of the MIL powders with the pre-polymerized R,F-xerogel solution. The prepared R,F-xerogel solution was filled into syringes (approx. 1 g per syringe), which were cut off from the cannula side, properly sealed by several layers of polyethylene- and aluminum foil and pre-polymerized for 5 h at 343 K. During this step the native R,F-xerogel changed from a clear, almost colorless solution to a honey-like, viscous material (Fig. S8). Various amounts of well-ground MIL-100(Fe), MIL-100(Cr) and MIL-101(Cr) powders (100, 150 and 180 mg) were added to the pre-polymerized R,F-xerogel. After homogenization of the mixtures directly in the syringes by a spatula, curing, washing and drying brown monoliths with MIL contents between 35 and 58 wt% were isolated. To maximize the amount of MOF powder in the composites, one MIL-101(Cr)@xerogel-H<sub>2</sub>O with 77 wt% of MIL was synthesized by additional usage of water to the pre-polymerized xerogel for proper homogenization of the MIL@xerogel mixture yielding a green monolith (Fig. 5). The suffix -H<sub>2</sub>O is added to MIL@xerogel, when additional water was used in the composite syntheses. MIL-101(Cr)@xerogel-H<sub>2</sub>O (35, 46, 50 wt%) were also obtained using additional water during the synthetic procedure (see Supporting Information for details). If no additional water was used, the term ‘standard synthesis’ was used.

### 3. Results and discussion

#### 3.1 Native R,F-xerogel

Infrared data (Fig. 3a) of the native or bulk resorcinol-formaldehyde based xerogel reveal the expected organic functional groups (*cf.* R,F-xerogel structure in Scheme 1). The broad band between 3700 and 3000  $\text{cm}^{-1}$  is associated with the  $\nu(\text{O-H})$  stretching vibrations, originating from the phenol groups and water molecules in the hydrophilic xerogel. Aliphatic stretching vibrations  $\nu(\text{CH}_2)$  can be assigned to the band at 2931  $\text{cm}^{-1}$ . The corresponding  $\delta(\text{CH}_2)$  deformation vibration is located at 1474  $\text{cm}^{-1}$ . The band at 1613  $\text{cm}^{-1}$  corresponds to the aromatic ring stretching vibration  $\nu(\text{C}=\text{C})$  and valence vibration bands at 1217 and 1092  $\text{cm}^{-1}$  reveal the presence of the methylene ether bridges  $\nu(\text{C-O-C})$ . The IR-spectrum is consistent with other literature data.<sup>79,80</sup>

The porous nature of the xerogel is verified by  $\text{N}_2$  sorption experiments (Fig. 3b). The  $\text{N}_2$  sorption isotherm exhibits a mixture of type II (macroporous) shape together with type IV (mesoporous) shape, due to the hysteresis between adsorption and desorption isotherm.<sup>81</sup> The pore volume of 0.16  $\text{cm}^3\text{g}^{-1}$  and the BET surface area of 100  $\text{m}^2\text{g}^{-1}$ , both calculated from the  $\text{N}_2$  adsorption isotherm, are typical values for subcritically dried R,F-xerogels with the following molar ratios of the starting materials: resorcinol/formaldehyde = 0.73, resorcinol/ $\text{Na}_2\text{CO}_3$  = 1000, resorcinol/water = 0.031 (Table 1).<sup>82,68,79</sup>

Scanning electron microscopy (SEM) images displays the typical morphological surface known for resorcinol-formaldehyde xerogels with low catalytic  $\text{Na}_2\text{CO}_3$  concentrations (high resorcinol/ $\text{Na}_2\text{CO}_3$  molar ratios of R/C = 1000) (Fig. 3c). The morphology can be described as interconnected colloidal-like particles, which do not possess porosity themselves, but generate porosity between the gaps of the particles.<sup>68,79</sup>

Thermogravimetric analysis of the native xerogel shows a first mass loss of approximately 10 wt% up to temperature of 473 K, which can be assigned to the loss of physisorbed water (Fig. S7a). The R,F-xerogel is thermally stable up to 493 K. The first mass loss of 10 wt% of water together with the shape of its water adsorption isotherm, showing an almost linear rise of water vapor with a total water uptake of  $0.10 \text{ g}\cdot\text{g}^{-1}$  at  $P\cdot P_0^{-1} = 0.9$ , indicates a hydrophilic character, which is comparable to silica gels (Fig. 3d, Table 1).

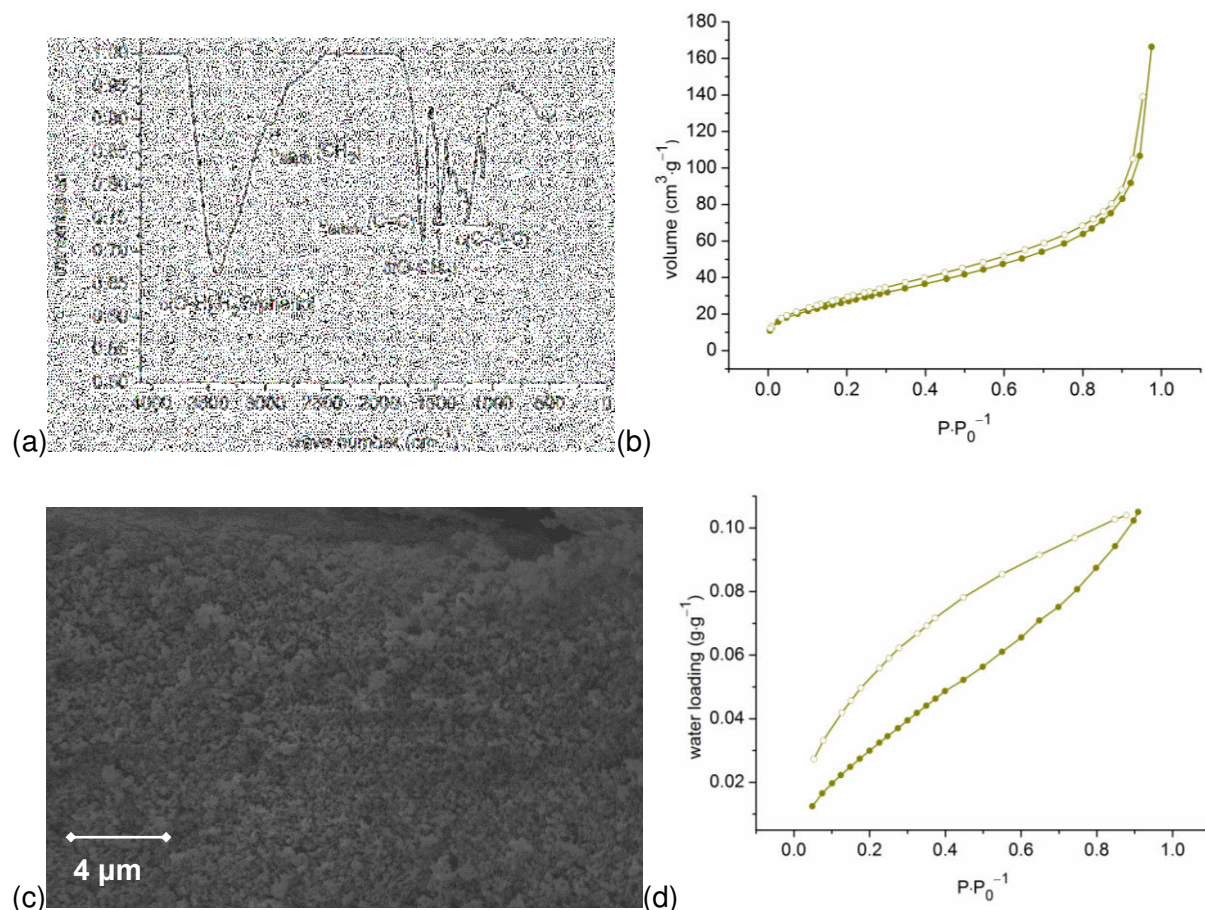


**Figure 3.** Native or bulk R,F-xerogel (a) IR-spectrum (KBr), (b)  $\text{N}_2$ -sorption isotherm (degassing conditions: 3 h, 423 K), (c) scanning electron microscopy (SEM) image, (d) water vapor sorption isotherm (degassing conditions: 3 h, 423 K). Adsorption is depicted with filled, desorption with empty symbols.

### 3.2 Embedding MIL-100(Fe,Cr) and MIL-101(Cr) into R,F-xerogel monoliths

Monolithic composites, consisting of a metal-organic framework (*e.g.* MILs) and an organic polymer (*e.g.* R,F-xerogel), can be synthesized in two different ways: (i) The synthesized MIL powder can either be mixed together with the just prepared xerogel solution, followed by curing, washing and drying steps ('direct route'). (ii) The MIL can be synthesized *in situ* into the already cured, porous system of a R,F-xerogel monolith by impregnating it with the corresponding starting materials (metal source and linker) followed by an appropriate temperature program ('in-situ route'). Through the direct route the ratio of MIL and R,F-xerogel in the final monolithic product can easily be predetermined by varying the amount of MIL powder and xerogel solution, which is not that realizable in the in-situ route. A disadvantage of the direct route is that the micro- and mesopores of the MOF can be blocked by the monomers or oligomers of the xerogel precursors. This pore blocking is accompanied by a pronounced decrease of the total surface area of the monolith. In this paper, we describe how to avoid pore blocking by pre-polymerization of the xerogel solution, resulting in highly porous and therefore active monolithic MIL@xerogel composites through the direct route.

In a first experiment aimed to synthesize a highly porous composite, MIL-100(Cr) powder was mixed together with an excess of the just prepared R,F-xerogel solution without any pre-polymerization. To maximize the amount of MIL in the monolithic composite, the powder was sedimented for one day followed by curing. After washing and drying steps the resulting monolith consisted of a brown bottom layer containing MIL and xerogel and a top brown layer, which represents the pure xerogel (Fig. S8a). Powder X-ray diffraction pattern and infrared spectrum reveal the unchanged presence of the MIL-100(Cr) phase in the composite material (Fig. S8b-c), but the N<sub>2</sub>-sorption isotherm and the corresponding pore size distribution curve showed only a small residual porosity of 20 m<sup>2</sup>·g<sup>-1</sup>, indicative of complete blockade of the micro- and mesopores of MIL-100(Cr) in the monolithic composite (Fig. S9a-

b) (see Supporting Information for details). The disappearance of the MIL pores in the composites occurs through the initial filling of the micro- and mesopores or at least the pore mouths by resorcinol and formaldehyde molecules followed by polycondensation inside these MIL pores or pore mouths.

For the synthesis of highly porous monolithic MOF@xerogel composites the MIL pores have to be protected during the synthesis. To avoid, or at least minimize polymerization reactions of resorcinol and formaldehyde inside the MIL pores, the xerogel solution has to be pre-polymerized before adding the MIL powder to create larger resorcinol-formaldehyde oligomers or small polymer strands. Those larger oligomers should be less prone to diffuse into and block the MIL pores.

Similar experiments were carried out here on MIL-100(Fe)@xerogel composites. Identical amounts of just prepared xerogel solution were placed for 3, 4 and 5 h into an oven at 343 K. After 3, 4 and 5 h of pre-polymerization time the viscous solutions were mixed together with 100 mg of MIL-100(Fe) powder, respectively. Homogenization, curing, washing and drying were done according to the native R,F-xerogel synthesis yielding brown monoliths each with 11 wt% of MIL-100(Fe) (see Supporting Information for details). X-ray diffraction patterns and infrared spectra prove the existence of MIL-100(Fe) in all three composites (Fig. S12a-b). The weight-averaged estimated BET surface area of the composite would be  $= \frac{\text{wt\% of xerogel}}{100} \times 100 \text{ m}^2 \cdot \text{g}^{-1} + \frac{\text{wt\% of MIL}}{100} \times 2200 \text{ (MIL-100Fe) m}^2 \cdot \text{g}^{-1}$ . For 11 wt% of MIL-100(Fe) the estimated BET surface of the composite would then be  $\sim 330 \text{ m}^2 \cdot \text{g}^{-1}$ . The corresponding N<sub>2</sub>-sorption isotherms yield increased BET surface areas by elongation of the pre-polymerization time of the xerogel solution:  $180 \text{ m}^2 \cdot \text{g}^{-1}$  for 3 h,  $210 \text{ m}^2 \cdot \text{g}^{-1}$  for 4 h,  $220 \text{ m}^2 \cdot \text{g}^{-1}$  for 5 h (Fig. 4a). Pore size distribution curves also confirm the increasing fraction of the MIL-100(Fe) micropores with elongation the pre-polymerization rate (Fig. 4b). After 3 h the MIL-100(Fe) pores between 12–21 Å are hardly visible in the composite material,

whereas 4 and 5 h of pre-polymerization time leads to more accessible, clearly observable micropores.

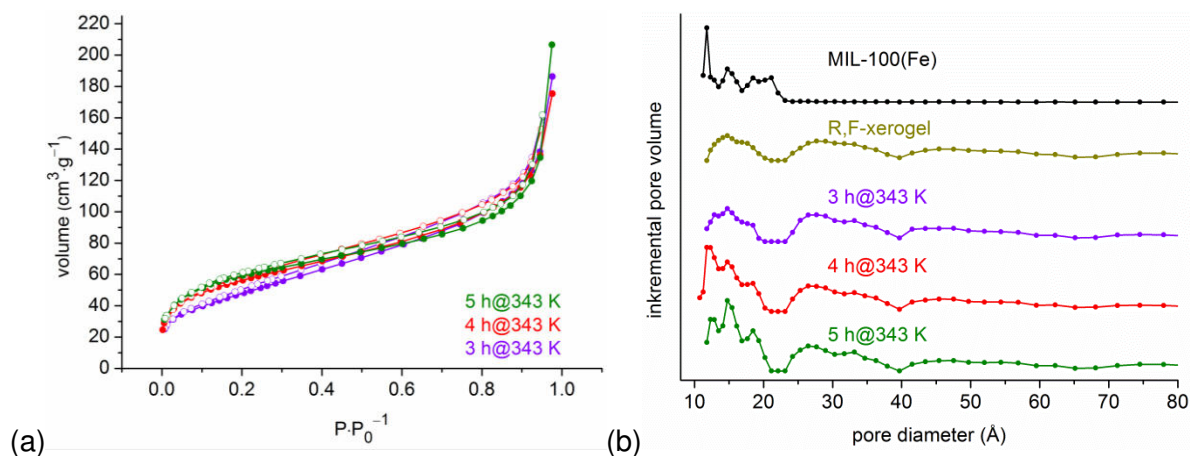


**Figure 4.** (a)  $N_2$ -sorption isotherms of MIL-100(Fe)@xerogel with 11 wt% MIL-100(Fe). MIL-100(Fe) powders were added to the R,F-xerogel solutions after 3, 4 and 5 h of pre-polymerization time at 343 K, respectively (degassing conditions: 3 h, 423 K,  $S(BET) = 180 \text{ m}^2 \cdot \text{g}^{-1}$  (3 h),  $210 \text{ m}^2 \cdot \text{g}^{-1}$  (4 h),  $220 \text{ m}^2 \cdot \text{g}^{-1}$  (5 h)). (b) Pore size distribution curves of native MIL-100(Fe), native R,F-xerogel and MIL-100(Fe)@xerogel with 11 wt% MIL-100(Fe) (3, 4 and 5 h of polymerization at 343 K). Adsorption is depicted with filled, desorption with empty symbols.

The pre-polymerization rate is not only controllable by temperature and time. Also the amount of xerogel solution at a given concentration is an important parameter. A larger amount of a xerogel solution needs more time for curing at a given temperature. It has been found that the maximum pre-polymerization time for 1 g of xerogel solution at 343 K is 5 h. With a longer temperature treatment the MIL powder and pre-polymerized xerogel solution cannot be homogenized properly any more.

Different, mechanically stable, monolithic MIL@xerogel composite materials were synthesized using well-ground MIL-100(Fe), MIL-100(Cr) and MIL-101(Cr) powder (100–460 mg) respectively and 1 g of pre-polymerized (5 h, 343 K) xerogel solution for each monolith. Figure 5 shows the pure R,F-xerogel monolith together with MIL-100(Fe)@xerogel (43 wt%),

MIL-100(Cr)@xerogel (41 wt%) MIL-101(Cr)@xerogel (50 wt%) and MIL-101(Cr)@xerogel-H<sub>2</sub>O (77 wt%) (from left to right). To maximize the amount of MOF in the composite, a small amount of water was added to the pre-polymerized xerogel to reach a proper homogenization with 77 wt% MIL-101(Cr) in the composite material (see Supporting Information for details). Increasing the amount of MIL-101(Cr) powder up to 77 wt% yielded green monolith with the typical green color of MIL-101(Cr). Other monolithic composites using lower weight percentages of orange-brown MIL-100(Fe) or green MIL-100/101(Cr) powders yielded brown monoliths. Mechanical stability tests have been carried out on the pure R,F-xerogel and three representative composites in a shaking incubator for 3 hours to determine the abrasion under mechanical treatment (see Supporting Information for details, Figure S18). Pure R,F-xerogel shows the lowest degree of abrasion with only 1.1 wt% of mass loss. The composites feature more abrasion (6.8–19.5 wt% mass loss) due to the MIL content, but fortunately none of the tested monoliths did break into granules through shaking for 3 hours.

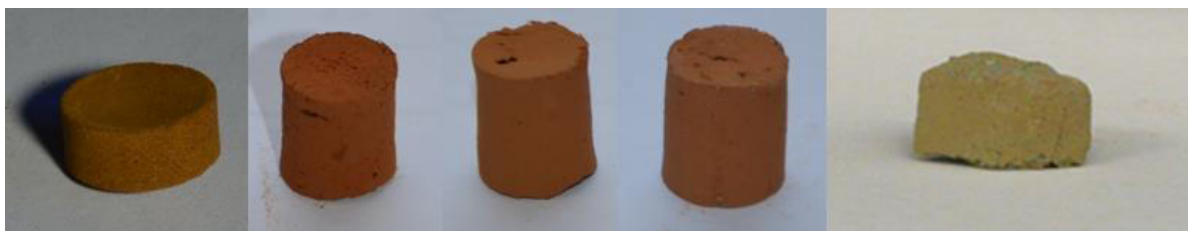


**Figure 5.** From left to right: Pure R,F-xerogel, MIL@xerogel composites with 58 wt% MIL-100(Fe), 41 wt% MIL-100(Cr), 50 wt% MIL-101(Cr) and 77 wt% MIL-101(Cr) (77 wt%, MIL-101(Cr)@xerogel-H<sub>2</sub>O). Dimensions (diameter x height) are 13 x 8 mm for pure R-F-xerogel; 10 x 13 mm for both MIL-100@xerogel; 10 x 14 mm for MIL-101(Cr)@xerogel (50 wt%) and 15 x 10 mm for MIL-101(Cr)@xerogel-H<sub>2</sub>O (77 wt%). MIL-101(Cr)@xerogel-H<sub>2</sub>O was cut to show the MIL distribution inside the monolith.

Representative scanning electron microscopy images of MIL-100(Fe)@xerogel (43 wt%) and MIL-101(Cr)@xerogel-H<sub>2</sub>O (77 wt%) (Fig. 6a-d) show the typical octahedral MIL morphologies with particle sizes between 2–5  $\mu\text{m}$  for MIL-100(Fe) and 300–500 nm for

MIL-101(Cr) in the composites.<sup>78,83</sup> MIL octahedrons and xerogel substrate are well grown together showing a reasonable adherence between both components. The increasing amount of MIL octahedrons in the composites is obvious by comparing Figure 6a-b (43 wt% MIL) with Figure 6c-d (77 wt% MIL).

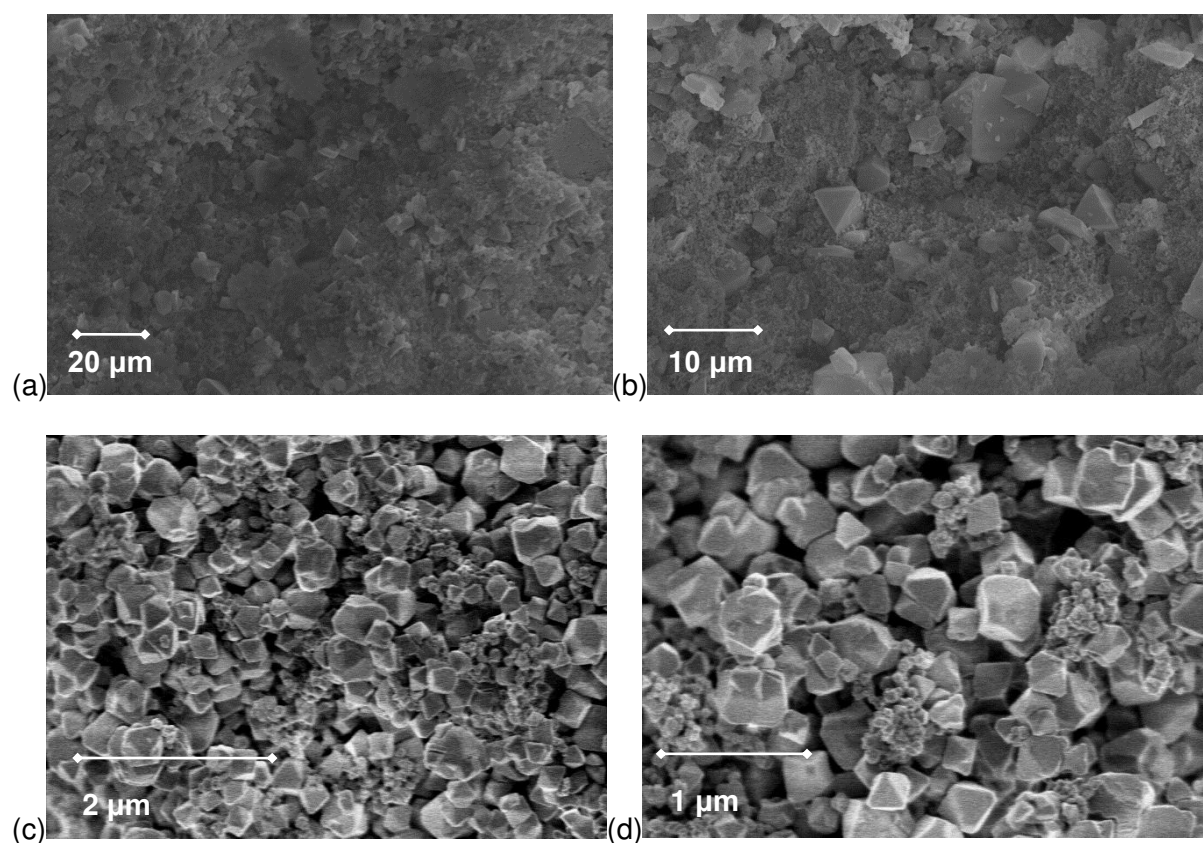


**Figure 6.** Scanning electron microscopy (SEM) images of (a)-(b) MIL-100(Fe)@xerogel (43 wt% MIL-100(Fe)) and (c)-(d) MIL-101(Cr)@xerogel-H<sub>2</sub>O (77 wt% MIL-101(Cr)) composites.

Powder X-ray diffraction patterns of MIL@xerogel compounds demonstrate the unchanged, crystalline phase of the respective MILs in the composites (Fig. 7a-c) although the reflections of MIL-101(Cr) composites are slightly broadened compared to bulk MIL-101.



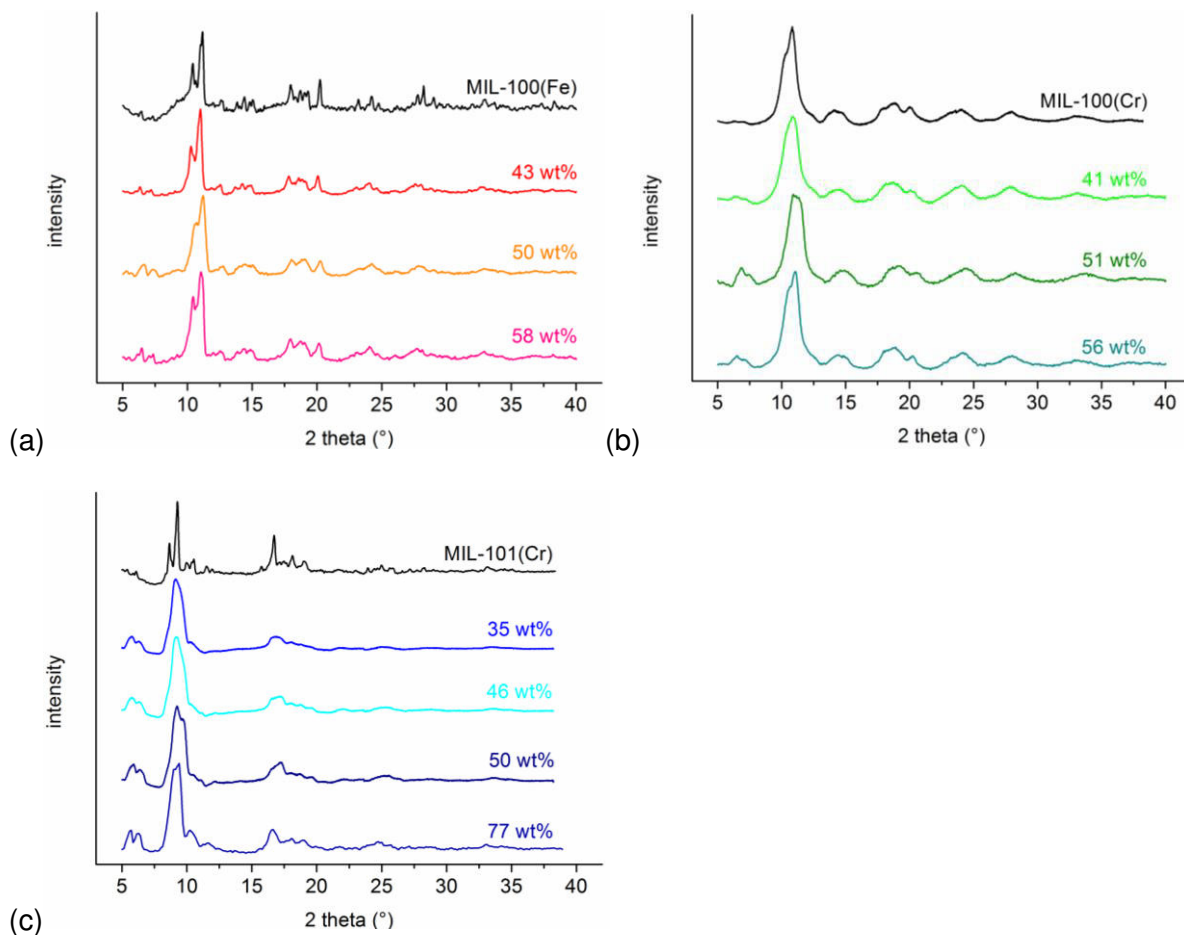


**Figure 7.** Experimental powder X-ray diffraction patterns of (a) MIL-100(Fe) and MIL-100(Fe)@xerogel with 43, 50 and 58 wt% MIL-100(Fe). (b) MIL-100(Cr) and MIL-100(Cr)@xerogel with 41, 51 and 56 wt% MIL-100(Cr). (c) MIL-101(Cr) and MIL-101(Cr)@xerogel with 35, 46, 50 and 77 wt% MIL-101(Cr). 77 wt% MIL containing MIL-101(Cr)@xerogel-H<sub>2</sub>O was obtained using additional water in the synthesis.

Infrared spectra of the composite materials represent an additive overlap of the individual spectra of the corresponding components (MILs and xerogel) (Fig. 8a-c). With increasing loading of MIL in the MIL@xerogel composites, the intensities of bands, coming from the MIL components are enhanced. The regions highlighted by square brackets in Figure 8 show the increasing bands for the asymmetric [ $\nu_{as}(\text{R-CO}_2)$ , region 1] and symmetric [ $\nu_s(\text{R-CO}_2)$ , region 2] valence-vibrations of the coordinated BDC- or BTC-ligand of the MILs. Region 3 displays the deformation-vibration of the carboxyl groups [ $\delta(\text{R-CO}_2)$ ].

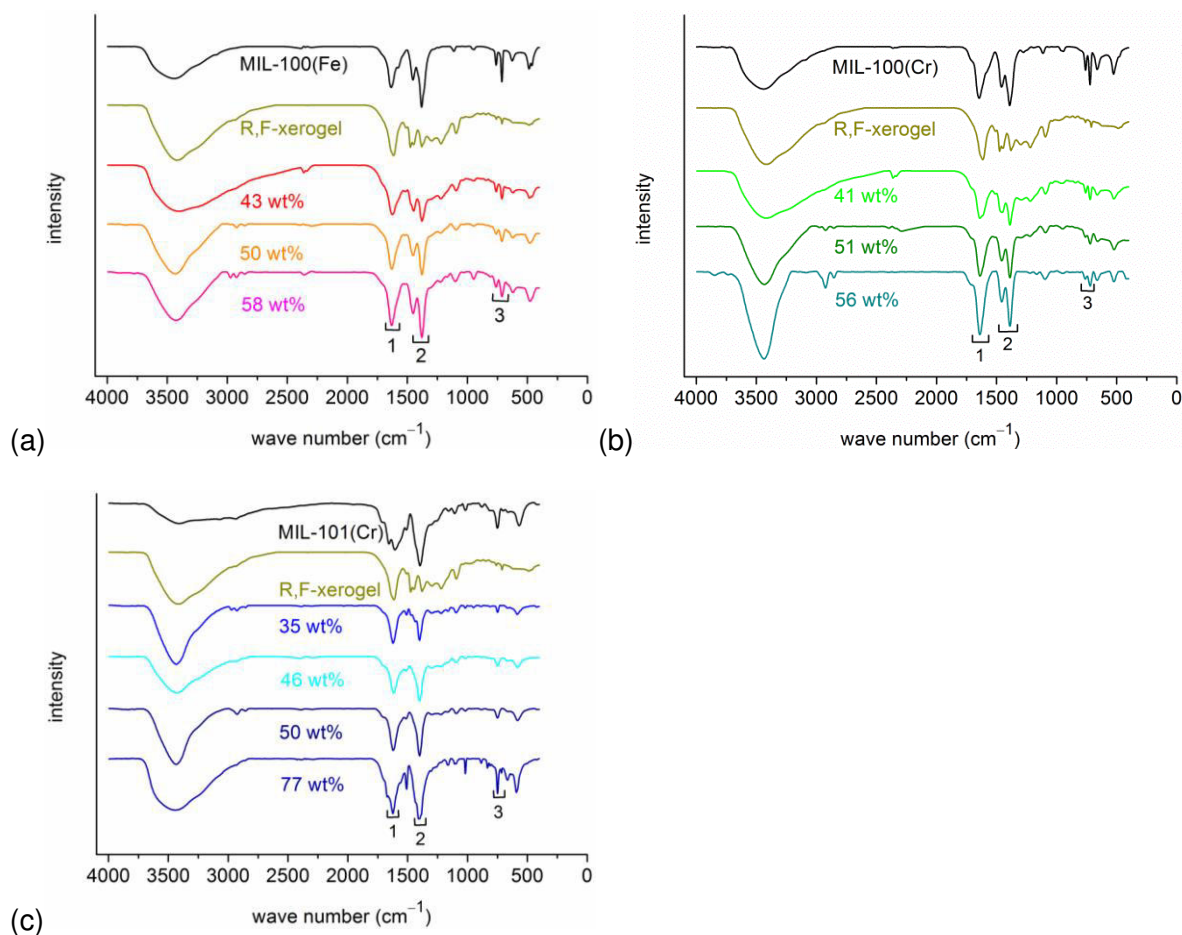


**Figure 8.** IR-spectra (KBr) of (a) MIL-100(Fe), R,F-xerogel and MIL-100(Fe)@xerogel with 43, 50 and 58 wt% MIL-100(Fe). (b) MIL-100(Cr), R,F-xerogel and MIL-100(Cr)@xerogel with 41, 51 and 56 wt% MIL-100(Cr). (c) MIL-101(Cr), R,F-xerogel and MIL-101(Cr)@xerogel with 35, 46, 50 and 77 wt% MIL-101(Cr). Square brackets (1, 2, 3) indicate the bands of the MILs in the composite materials. 77 wt% MIL containing MIL-101(Cr)@xerogel-H<sub>2</sub>O was obtained using additional water in the synthesis.

### 3.3 N<sub>2</sub>- and water sorption studies

N<sub>2</sub> sorption measurements have been carried out for all pre-polymerized MIL@xerogel composites (Fig. 9a, c, e). The nitrogen adsorption capacities increase continuously with increasing the MIL content. The composites feature a transition from type II/IV for the bulk R,F-xerogel to type I shaped N<sub>2</sub> isotherms with the MIL additive and its free and accessible micropores. The step rise at low relative pressures, typical for type I isotherms, becomes

more pronounced with increasing MIL ratios. BET surface areas increase with the amount of MIL in the monolithic composites (Table 1). The relevant comparison is to the estimated mass-weighted surface areas of bulk MIL and xerogel using Formula (I) from Table 1. MIL-100(M)@xerogel (M = Fe, Cr) composites reach approximately 60 % of the estimated surface areas. MIL-101(Cr)@xerogel composites with MIL loading between 35 and 50 wt% achieve nearly 83 % of the expected values. The higher BET surface areas for MIL-101 composites, compared to the MIL-100 composites, can be explained by pronounced pore blocking effects in the MIL-100 containing composites. The xerogel binding agent can more easily diffuse and therefore block the smaller MIL-100 pores due to the smaller windows size of MIL-100 (4.7–5.5 Å, 8.6 Å) compared to the windows of MIL-101 (12 Å, 15–16 Å) (Fig. S16, Fig. S17). In other words: Smaller pores are more difficult to protect than larger pores.

As stated above, to maximize the amount of MIL-101(Cr) in the monolithic composite a small amount of additional water was added to the pre-polymerized xerogel solution together with MIL-101 powder to achieve a proper homogenized mixture (see Supporting Information for details). The resulting monolith with 77 wt% of MIL-101(Cr) shows a BET surface which is even slightly higher (+150 m<sup>2</sup>·g<sup>-1</sup>) than the estimated BET (Table 1). The addition of water with the MIL could lead to formation of a water layer around the MIL crystallites; thereby prevent pore blocking by the xerogel. This assumption is supported by comparison of the SEM images of 35 wt% MIL-101(Cr)@xerogel-H<sub>2</sub>O (Fig. S15) and 35 wt% MIL-101(Cr)@xerogel, in which no water was added (Fig. S14). The 35 wt% MIL-101(Cr)@xerogel-H<sub>2</sub>O has the MIL crystallites slightly more separated from the xerogel, while the 35 wt% MIL-101(Cr)@xerogel (no H<sub>2</sub>O) shows the MIL and xerogel more intimately mixed.

Subsequently addition of water also significantly increased the surface areas and total pore volumes in case of the 35, 46 and 50 wt% MIL-101(Cr)@xerogel-composites (Table 1).

**Table 1. Nitrogen and water vapor sorption measurements.**

Materials <sup>a</sup>	BET surface areas <sup>b</sup> ; (Estimated) <sup>c</sup> (m <sup>2</sup> ·g <sup>-1</sup> )	Total pore volume (cm <sup>3</sup> ·g <sup>-1</sup> ) <sup>d</sup>	Water loading <sup>e</sup> ; (Estimated) <sup>f</sup> (g·g <sup>-1</sup> )
R,F-xerogel	100	0.16	0.10
MIL-100(Fe)	2200 <sup>g</sup>	0.94	0.76 <sup>h</sup>
Composites:			
43 wt%	590 (1000)	0.31	0.26 (0.38)
50 wt%	730 (1150)	0.39	0.33 (0.43)
58 wt%	770 (1320)	0.41	n.d. <sup>i</sup>
MIL-100(Cr)	1560 <sup>j</sup>	0.85	0.60 <sup>k</sup>
Composites: <sup>l</sup>			
41 wt%	400 (700)	0.28	0.23 (0.31)
51 wt%	550 (850)	0.35	0.28 (0.36)
56 wt%	570 (920)	0.40	n.d.
MIL-101(Cr)	3060 <sup>m</sup>	1.45	1.06 <sup>n</sup>
Composites: <sup>o</sup>	standard/water added	standard/water added	standard/water added
35 wt%	960/1340 (1140)	0.54/0.69	n.d./0.41 (0.44)
46 wt%	1160/1420 (1460)	0.62/0.72	n.d./0.50 (0.54)
50 wt%	1350/1500 (1580)	0.72/0.76	n.d.
77 wt%	- /2530 (2380)	- /1.27	- /0.88 (0.84)

<sup>a</sup> wt% refers to MIL amount in the composites.

<sup>b</sup> BET surface area calculated at  $0.05 < P \cdot P_0^{-1} < 0.2$  from N<sub>2</sub> sorption isotherm 77 K with a standard deviation  $\pm 20$  m<sup>2</sup>·g<sup>-1</sup>.

<sup>c</sup> BET surface area as the sum of the mass-weighted surface areas of the MILs (MIL-100(Fe) = 2200 m<sup>2</sup>·g<sup>-1</sup>; MIL-100(Cr) = 1560 m<sup>2</sup>·g<sup>-1</sup>; MIL-101(Cr) = 3060 m<sup>2</sup>·g<sup>-1</sup>) and R,F-xerogel (100 m<sup>2</sup>·g<sup>-1</sup>) calculated from the following formula (I):

$$\begin{aligned} & \text{BET (estimated)} \\ & = \frac{\text{wt\% of xerogel}}{100} \times 100 \text{ m}^2 \cdot \text{g}^{-1} + \frac{\text{wt\% of MIL}}{100} \\ & \quad \times 2200 \text{ (MIL - 100Fe) or } 1560 \text{ (MIL - 100Cr) or } 3060 \text{ (MIL - 101Cr) m}^2 \cdot \text{g}^{-1} \end{aligned}$$

<sup>d</sup> calculated from N<sub>2</sub> sorption isotherm at 77 K ( $P \cdot P_0^{-1} = 0.95$ ) for pores  $\leq 20$  nm.

<sup>e</sup> calculated from water sorption isotherm at 293 K ( $P \cdot P_0^{-1} = 0.9$ ).

<sup>f</sup> Water loading estimated as the sum of the mass-weighted uptakes at  $P \cdot P_0^{-1} = 0.9$  of the MILs (MIL-100(Fe) = 0.76 g·g<sup>-1</sup>; MIL-100(Cr) = 0.60 g·g<sup>-1</sup>; MIL-101(Cr) = 1.06 g·g<sup>-1</sup>) and R,F-xerogel (0.10 g·g<sup>-1</sup>) calculated from the following formula (II):

$$\begin{aligned} & \text{Water loading (estimated)} \\ & = \frac{\text{wt\% of xerogel}}{100} \times 0.10 \text{ g} \cdot \text{g}^{-1} + \frac{\text{wt\% of MIL}}{100} \\ & \quad \times 0.76 \text{ (MIL - 100Fe) or } 0.60 \text{ (MIL - 100Cr) or } 1.06 \text{ (MIL - 101Cr) g} \cdot \text{g}^{-1} \end{aligned}$$

<sup>g</sup> 1550–2050 m<sup>2</sup>·g<sup>-1</sup> <sup>84,85</sup>; <sup>h</sup> 0.65–0.75 g·g<sup>-1</sup> <sup>43,86</sup>.

<sup>i</sup> n.d. = not determined.

<sup>j</sup> 1770–1980 m<sup>2</sup>·g<sup>-1</sup> <sup>84,85</sup>; <sup>k</sup> 0.6–0.7 g·g<sup>-1</sup> <sup>87</sup>.

<sup>l</sup> MIL-100(Cr)@xerogel without any pre-polymerization of the xerogel solution yielded a BET surface area of 20 m<sup>2</sup>·g<sup>-1</sup> and a total pore volume of 0.03 cm<sup>3</sup>·g<sup>-1</sup> (see Supporting Information for details).

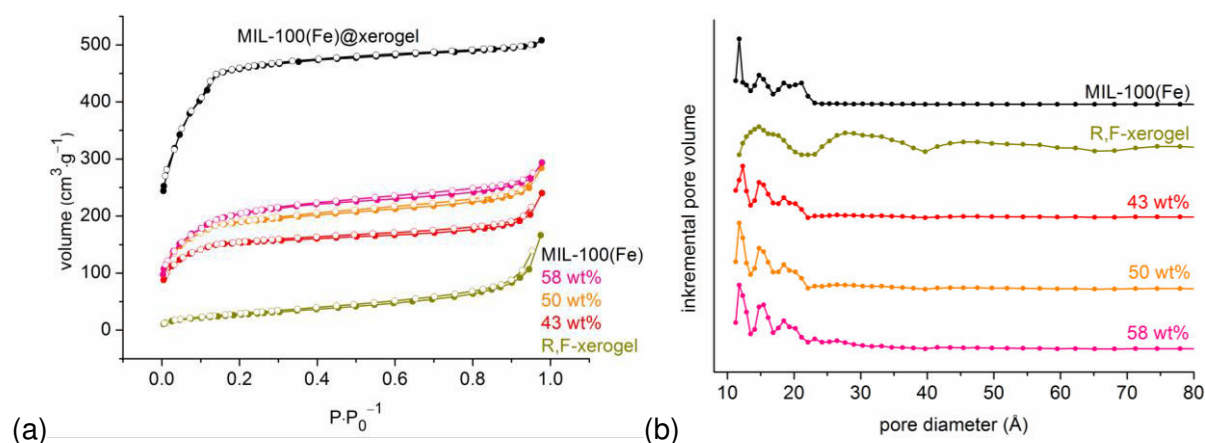
<sup>m</sup> 2060–4100 m<sup>2</sup>·g<sup>-1</sup> <sup>37,46</sup>; <sup>n</sup> 1.0–1.5 g·g<sup>-1</sup> <sup>37,86</sup>.

<sup>o</sup> The first value refers to the standard syntheses (MIL-101(Cr)@xerogel), the second value to the MIL-101(Cr)@xerogel-H<sub>2</sub>O composites.

Pore size distribution curves of the bulk MILs, can be calculated from the nitrogen adsorption isotherms (Fig. 9) using NLDFT models and show pores sizes of 12, 15, 18–19 and 20–21 Å for MIL-100(Fe) and MIL-100(Cr). The pore regions of 18–19 and 20–21 Å correspond to the MIL-100 cages (Fig. S17).

The pore size distribution curve of bulk MIL-101(Cr) shows pores of 12 and 15 Å in diameter, which are consistent with the pentagonal (12 Å) and hexagonal windows (14.7–16 Å) (Fig. S15).<sup>46</sup> The larger pores of 19 and 24 Å belong to the cages with diameters of 29 and 34 Å (Fig. S16).<sup>46</sup> Differences to the cage size from X-ray structure refinement was seen before can be explained by residual impurities of non-coordinated ligand and metal-ligand fragments inside the pores.<sup>88</sup>

Pore size distribution curves of the MIL@xerogel composites match those of the respective bulk MIL. Thus, from N<sub>2</sub> sorption isotherms, BET surface area and pore diameter distribution it is obvious that all monolithic composite materials largely retain the accessibility to the micro- and mesopores of the MIL. This is, however, only true for the materials based on pre-polymerized xerogel solutions. In contrast, a MIL-100(Cr)@xerogel composite without any pre-polymerization of the xerogel solution, presents a material which appears non-porous or without any accessible porosity (Table 1, see 'I'; Fig. S8, S9, S10).



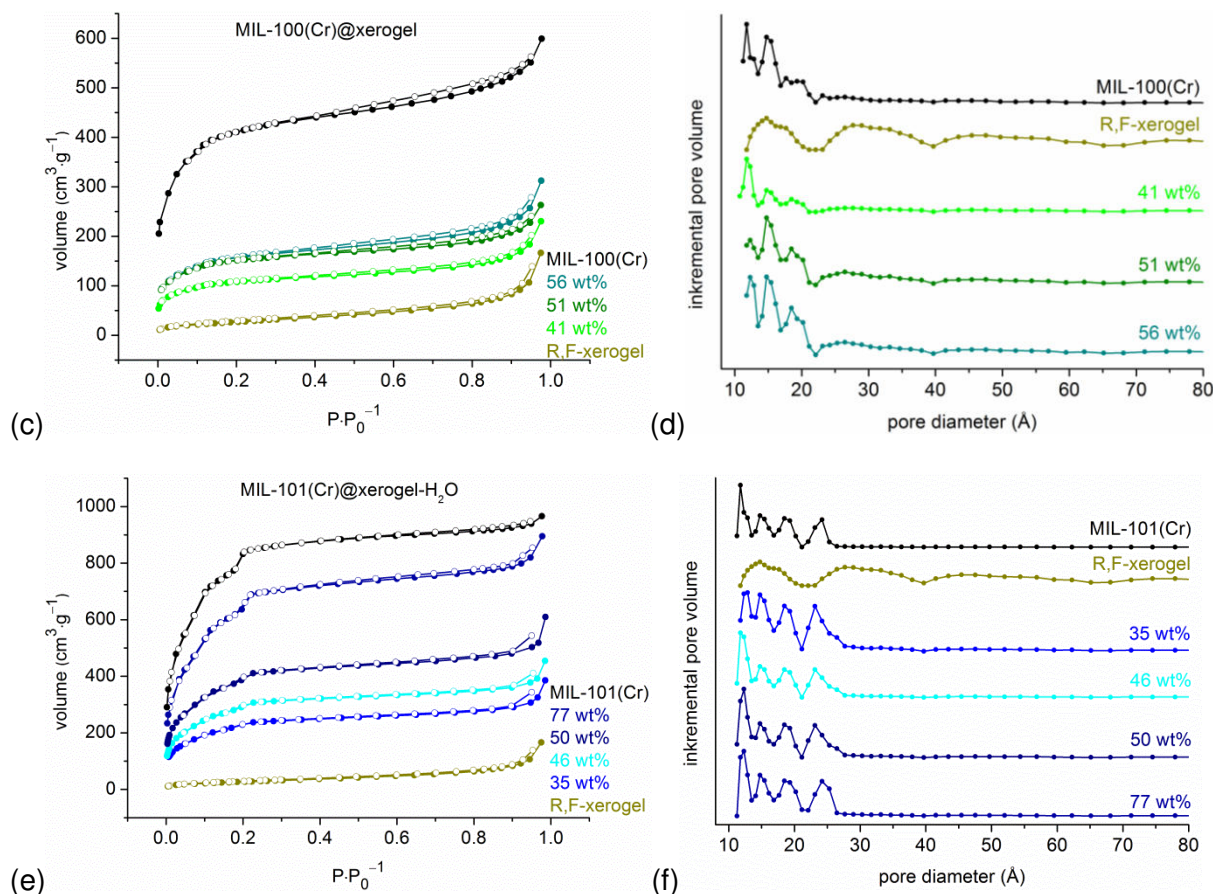


**Figure 9.** N<sub>2</sub>-sorption isotherms and pore diameter distribution of R,F-xerogel, MILs and MIL@xerogel composites. See Table 1 for BET surface areas and total pore volumes. (a,b) MIL-100Fe, (c,d) MIL-100Cr, (e,f) MIL-101Cr (a-d: MIL-100@xerogel; e,f: MIL-101(Cr)@xerogel-H<sub>2</sub>O). For enlarged pore size distribution curve of bulk MILs see Figure S2c, S4c, S6c (degassing conditions: 3 h, 423 K). Adsorption is depicted with filled, desorption with empty symbols. N<sub>2</sub> sorption data of MIL-101(Cr)@xerogel without water addition is shown in Figure S13 (a,b).

Other MOF composite materials show similar differences between experimental and estimated BET surface areas (Table 2). HKUST-1, embedded in porous carbon monoliths achieves only 40% of the estimated BET surface areas.<sup>50</sup> Composites like UiO-66@polyurethane or HKUST@HIPE reach about 60% of the calculated values.<sup>58,89</sup> These values are comparable to our pre-polymerized MIL-100(M)@xerogel (M = Fe, Cr) compounds. Yet, metal-organic frameworks in inorganic silica templates, such as HKUST-1 incorporated in silica aerogels or HKUST-1 in macro-/mesoporous silica match or even

exceed the estimated BET values similar to the MIL-101(Cr)@xerogel composites with added water reported here.<sup>57,66</sup>

**Table 2. Comparison of N<sub>2</sub> sorption data of similar composite materials from the literature.**

Composites	Experimental BET surface area (m <sup>2</sup> ·g <sup>-1</sup> )	Estimated BET surface area (m <sup>2</sup> ·g <sup>-1</sup> ) <sup>f</sup>	wt% of MOFs and quantification method	Possible application	Ref.
HKUST-1@PAM <sup>a</sup>	654 <sup>d</sup>	667	62 wt%; N <sub>2</sub> sorption data + TGA	no application investigated	90
HKUST-1 monolith <sup>b</sup>	484 <sup>e</sup>	-	No wt% given	no application investigated	56
HKUST-1@porous carbon monoliths	270; 455; 516	816; 988; 1198	19 wt%; 41 wt%; 68 wt%; Weighing method	CO <sub>2</sub> storage; Gas separation (CO <sub>2</sub> / N <sub>2</sub> )	50
HKUST-1@silica aerogel <sup>66</sup>	1025; 1036; 1138	944; 955; 1056	4.2 wt%; 16.3 wt%; 30.5 wt%; Weighing method	no application investigated	66
HKUST-1@macro-/mesoporous silica	971	907	25 wt%; TGA	catalysis	57
UiO-66@polyurethane	511 <sup>d</sup> ; 427 <sup>d</sup>	834; 752	71 wt%; 64 wt%; TGA	adsorption of organic vapors	89
HKUST-1@HIPE <sup>58</sup>	570	846	62.3 wt%; TGA	no application investigated	58
CAU-1@PMMA <sup>c</sup>	423	-	No wt% given	open-tubular capillary electrochromatography	62

<sup>a</sup> PAM = polyacrylamide. We notice that MOF wt% determination in HKUST-1@PAM composites was calculated from nitrogen sorption data based on the assumption that all of the native MOF surface area is still accessible in the composite material.

<sup>b</sup> binding agent: methoxy functionalized siloxane ether; plasticizer: methyl hydroxyl propyl cellulose.

<sup>c</sup> PMMA = polymethyl methacrylate.

<sup>d</sup> BET surface areas of pure binding agents are not considered in calculations due to their absence in the corresponding literature.

<sup>e</sup> Values decreased after several months to 287 m<sup>2</sup>·g<sup>-1</sup>.

<sup>f</sup> BET surface area as the sum of the mass-weighted surface areas of MOFs and porous binding agents calculated from the following formula:

$$\text{BET (estimated)} = \frac{\text{wt\% of MOF}}{100} \times \text{BET of pure MOF} + \frac{\text{wt\% of binding agent}}{100} \times \text{BET of pure binding agent}$$

In order to evaluate the monolithic composites as potential adsorbents for heat transformation applications, water sorption experiments were carried out to quantify their hydrophilic behavior. Water sorption isotherms of different MIL@xerogel materials are shown together with the adsorption isotherm of bulk MIL and R,F-xerogel (Fig. 10a-c). MIL-100@xerogel composites display the same stepwise adsorption isotherm, as for bulk MIL-100(M) (M = Fe, Cr) (Fig. 10a-b, Fig. S2b, Fig. S4b). This specific shape relates to the stepwise filling of the different MIL-100 cages.<sup>86,87</sup>

Water loading capacities at  $P/P_0^{-1} = 0.9$  of the MIL@xerogel compounds can be estimated from the MIL wt% based on the water uptake of bulk MIL using formula (II) in Table 1. MIL-100(M)@xerogel (M = Fe, Cr) compounds reach approximately 74 % of the calculated values. The MIL-101(Cr)@xerogel monoliths with 35 and 46 wt% of MIL loading achieve 93 % of the estimated water uptake capacities. Compared to the BET analyses given above, the MIL-101(Cr) water uptakes are closer to the calculated expected values. The 77 wt% loaded MIL-101(Cr)@xerogel-H<sub>2</sub>O matches or even slightly exceeds the estimated water uptake capacity as a result of the higher BET surface area (Table 1). As an indication of the hierarchical nature the 35 and 46 wt% MIL-101(Cr) composites achieve a near to maximum water loading already at  $P/P_0^{-1} = 0.5$  (Fig. 10c). The 77wt% MIL-101(Cr)@xerogel-H<sub>2</sub>O composites already realizes 0.79 g·g<sup>-1</sup> water uptake at  $P/P_0^{-1} = 0.5$  (Fig. 10c). Whereas for bulk MIL-101(Cr) only 0.57 g·g<sup>-1</sup>, corresponding to ~50% water uptake could be achieved at  $P/P_0^{-1} = 0.5$ .



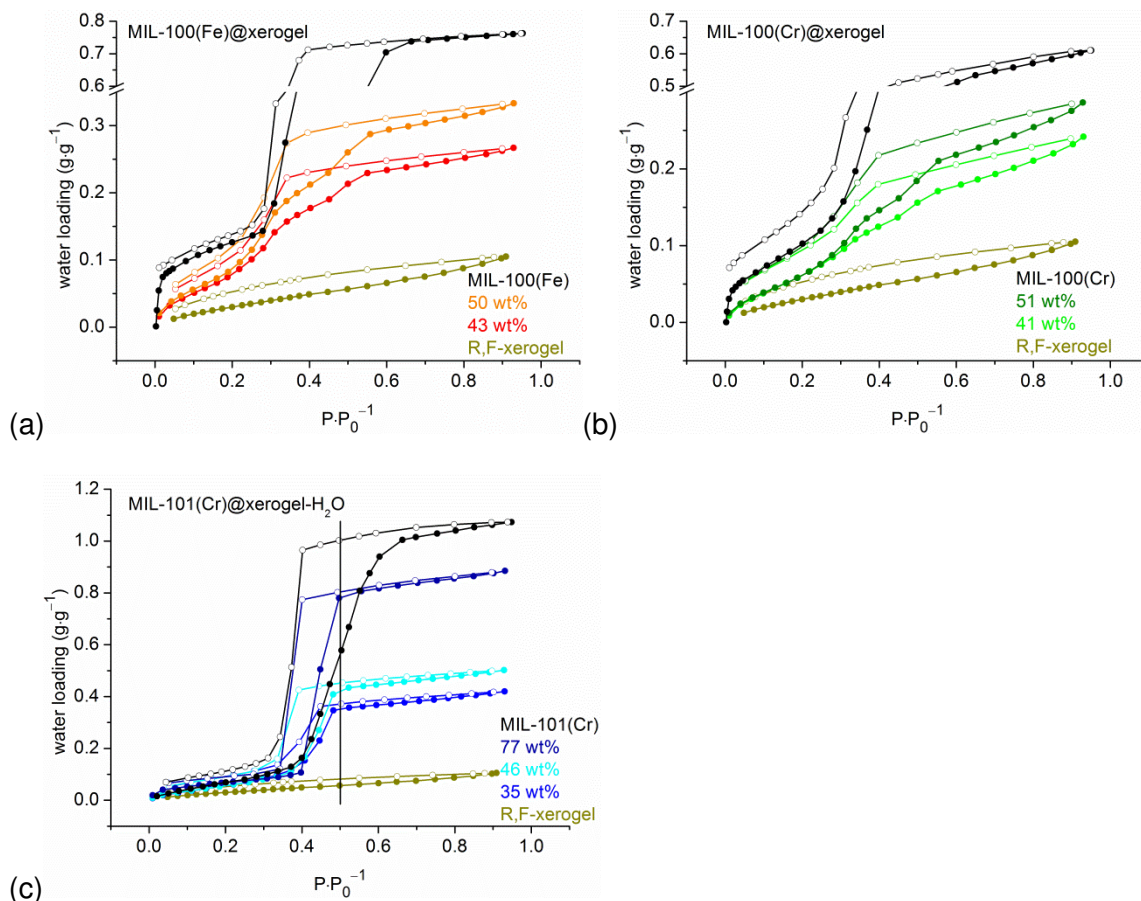


**Figure 10.** Water vapor sorption isotherms of R,F-xerogel, MILs and MIL@xerogel composites. (a) MIL-100(Fe)@xerogel, (b) MIL-100(Cr)@xerogel, (c) MIL-101(Cr)@xerogel-H<sub>2</sub>O (degassing conditions: 3 h, 423 K). Adsorption is depicted with filled, desorption with empty symbols.

#### 4. Conclusion

We presented new composite materials in monolithic shape based on a metal-organic framework part (MIL-100(M)/101(Cr), (M = Fe, Cr)) and a polymerized resorcinol-formaldehyde xerogel as the binding agent. Mesoporous resorcinol-formaldehyde (R,F-) xerogels are easily obtainable, highly tunable and the second most investigated xerogels (after silica xerogels). The MIL@xerogel composites were characterized by powder X-ray diffraction, infrared spectroscopy, nitrogen- and water sorption and scanning electron microscopy. Embedding up to 77 wt% of MIL particles is possible without the loss of the

mechanical stability of the monoliths. Pore blocking effects of the MILs through the binding agent could largely be avoided by pre-polymerization of the native xerogel solution before embedding of the MILs. The larger MIL-101(Cr) pores remain more open than the smaller MIL-100 pores during the monolith syntheses. The expected BET surface areas and water uptakes could be reached when the MIL was added together with water to the pre-polymerized xerogel solution. Formation of a water film around the MIL particles may be responsible to avoid pore blocking. These MIL-101(Cr)@xerogel-H<sub>2</sub>O composites then match the wt%-correlated BET values and water uptakes within experimental error. As an indication of the hierarchical nature the 77wt% MIL-101(Cr)@xerogel-H<sub>2</sub>O composite achieves 0.79 g·g<sup>-1</sup> water uptake at  $P/P_0 = 0.5$  while for bulk MIL-101(Cr) only 0.57 g·g<sup>-1</sup> water uptake could be achieved at  $P/P_0 = 0.5$ .

### **Associated Content**

#### **Supporting Information**

Experimental procedures for the syntheses of MIL-100(Fe,Cr), MIL-101(Cr), R,F-xerogel and MIL@xerogel composites with additional figures for PXRD, IR, sorption isotherms, pore size distributions and SEM images can be found in the Supporting Information. This material is available free of charge via the Internet at <http://pubs.acs.org>.

### **Author Information**

#### **Corresponding Authors**

\*E-Mail: [janiak@hhu.de](mailto:janiak@hhu.de).

### **Acknowledgements**

Support by the DAAD with PPP-project no 57053987 ("hierarchical structured metal-based nanocomposites") and the University of Düsseldorf through its strategic research fund (SFF) is gratefully acknowledged. We thank Mr. Steffen Köhler for help with the SEM images.

Marina Schwan and Jessica Laskowski from DLR, Cologne for the kind introduction to xerogel syntheses.

## References

- (1) (a) Batten, S. R.; Champness, N. R.; Chen, X.-M.; Garcia-Martinez, J.; Kitagawa, S.; Öhrström, L.; O'Keeffe, M.; Suh, M. P.; Reedijk, J. *CrystEngComm* **2012**, *14*, 3001–3004. (b) Batten, S. R.; Champness, N. R.; Chen, X.-M.; Garcia-Martinez, J.; Kitagawa, S.; Öhrström, L.; O'Keeffe, M.; Suh, M. P.; Reedijk, J. *Pure Appl. Chem.* **2013**, *85*, 1715–1724.
- (2) Yaghi, O. M.; Li, H. *J. Am. Chem. Soc.* **1995**, *117*, 10401–10402.
- (3) Yaghi, O. M.; Li, G.; Li, H. *Nature* **1995**, *378*, 703–705.
- (4) Long, J. R.; Yaghi, O. M. *Chem. Soc. Rev.* **2009**, *38*, 1213–1214.
- (5) Kitagawa, S.; Natarajan, S. *Eur. J. Inorg. Chem.* **2010**, *24*, 3685–3685.
- (6) Serre, C.; Kitagawa, S.; Dietzel, P. D. C. *Microporous Mesoporous Mater.* **2012**, *157*, 1–2.
- (7) Yoon, M.; Srirambalaji, R.; Kim, K. *Chem. Rev.* **2012**, *112*, 1196–1231.
- (8) Farrusseng, D.; Aguado, S.; Pinel, C.; *Angew. Chem. Int. Ed.* **2009**, *48*, 7502–7513.
- (9) Lee, J.; Farha, O. K.; Roberts, J.; Scheidt, K. A.; Nguyen, S.T.; Hupp, J. T. *Chem. Soc. Rev.* **2009**, *38*, 1450–1459.
- (10) Herbst, A.; Khutia, A.; Janiak, C. *Inorg. Chem.* **2014**, *53*, 7319–7333.
- (11) Llabrés i Xamena, F.X.; Cirujano, F.G.; Corma, A. *Microporous Mesoporous Mater.* **2012**, *157*, 112–117.
- (12) Getman, R. B.; Bae, Y.-S.; Wilmer, C. E.; Snurr, R. Q. *Chem. Rev.* **2012**, *112*, 703–723.
- (13) Chen, Z.; Xiang, S.; Arman, H. D.; Li, P.; Tidrow, S.; Zhao, D.; Chen, B. *Eur. J. Inorg. Chem.* **2010**, *24*, 3745–3749.
- (14) Ma, F.; Liu, S.; Liang, D.; Ren, G.; Zhang, C.; Wei, F.; Su, Z. *Eur. J. Inorg. Chem.* **2010**, *24*, 3756–3761.
- (15) Wu, L.; Xue, M.; Qiu, S.-L.; Chaplais, G.; Simon-Masseron, A.; Patarin, J. *Microporous Mesoporous Mater.* **2012**, *157*, 75–81.
- (16) Zhang, Z.; Zhao, Y.; Gong, Q.; Li, Z.; Li, J. *Chem. Commun.* **2013**, *49*, 653–661.
- (17) Li, J.-R.; Ma, Y.; McCarthy, M. C.; Sculley, J.; Yu, J.; Jeong, H.-K.; Balbuena, P. B.; Zhou, H.-C. *Coord. Chem. Rev.* **2011**, *155*, 1791–1823.
- (18) Li, J.-R.; Sculley, J.; Zhou, H.-C. *Chem. Rev.* **2012**, *112*, 869–932.
- (19) Herm, Z. R.; Krishna, R.; Long, J. R. *Microporous Mesoporous Mater.* **2012**, *157*, 94–100.
- (20) Plaza, M. G.; Ferreira, A. F. P.; Santos, J.C.; Ribeiro, A. M.; Müller, U.; Trukhan, N.; Loureiro, J. M.; Rodrigues, A. E. *Microporous Mesoporous Mater.* **2012**, *157*, 101–111.
- (21) Janiak, C. *Dalton Trans.* **2003**, *14*, 2781–2804.
- (22) Janiak, C.; Vieth, J. K. *New J. Chem.* **2010**, *34*, 2366–2388.
- (23) Férey, G. *Chem. Soc. Rev.* **2008**, *37*, 191–214.
- (24) Stock, N.; Biswas, S. *Chem. Rev.* **2012**, *112*, 933–969.
- (25) Kitagawa, S.; Kitaura, R.; Noro, S. *Angew. Chem. Int. Ed.* **2004**, *43*, 2334–2375.

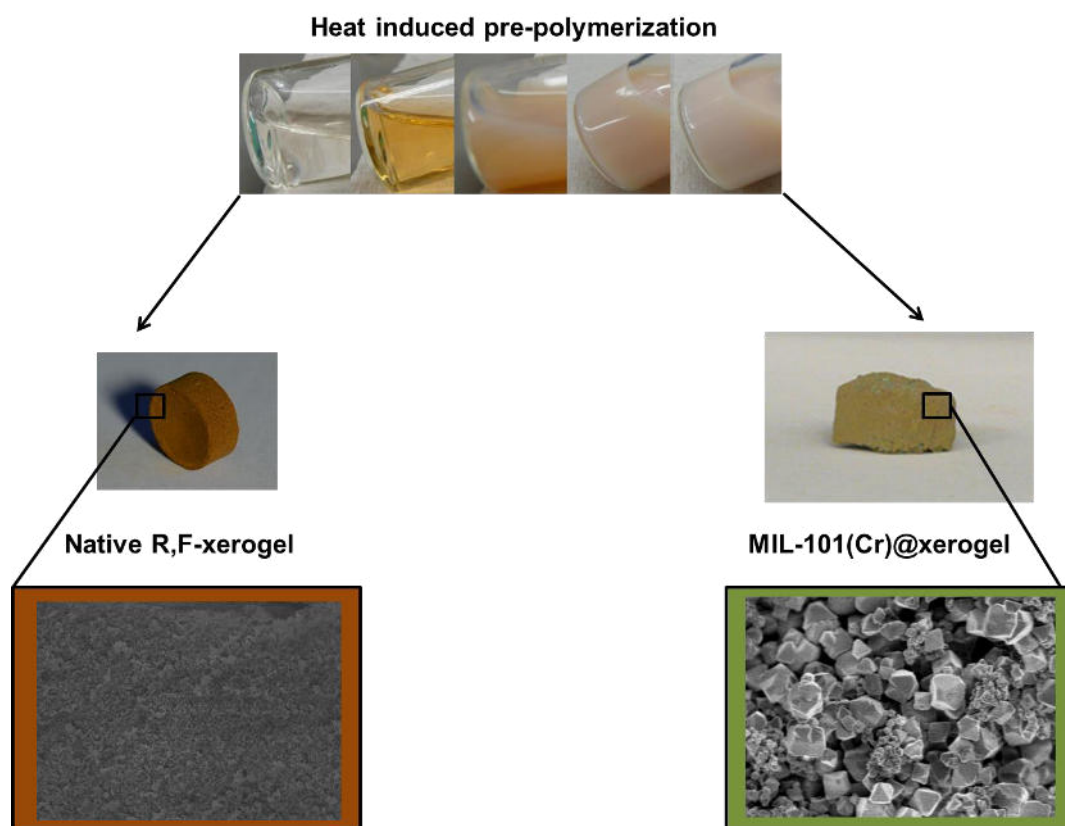
- 
- (26) Gaab, M.; Trukhan, N.; Maurer, S.; Gummaraju, R.; Müller, U. *Microporous Mesoporous Mater.* **2012**, *157*, 131–136.
- (27) Li, C.; Zhou, J.; Cao, Y.; Zhong, J.; Liu, Y.; Kang, C.; Tan, Y. *Appl. Energ.* **2014**, *117*, 149–156.
- (28)(a) Aristov, Yu. I. *Int. J. Refrigeration* **2009**, *32*, 675–686. (b) Saha, B. B.; Chakraborty, A.; Koyama, S.; Aristov, Yu. I. *Int. J. Heat Mass Transfer* **2009**, *52*, 516–524. (c) Critoph, R. E.; Tamainot-Telto, Z.; Metcalf, S. J. *Int. J. Refrigeration* **2009**, *32*, 1212–1229. (d) Veselovskaya, J. V.; Critoph, R. E.; Thorpe, R. N.; Metcalf, S.; Tokarev, M. M.; Aristov, Y. I. *Appl. Therm. Eng.* **2010**, *30*, 1188–1192. (e) Aristov, Yu. I. *Appl. Therm. Eng.* **2013**, *50*, 1610–1618. (f) Aristov, Yu. I. *J. Chem. Eng. Jpn.* **2007**, *40*, 1241–1251. (g) Aristov, Yu. I.; Dawoud, B.; Glaznev, I. S.; Elyas, A. *Int. J. Heat Mass Transfer* **2008**, *51*, 4966–4972.
- (29) Habib, K.; Saha, B. B.; Chakraborty, A.; Oh, S. T.; Koyama, S. *Appl. Therm. Eng.* **2013**, *50*, 1582–1589.
- (30) Askalany, A. A.; Salem, M.; Ismael, I. M.; Ali, A. H. H.; Morsy, M. G.; Saha, B. B. *Renew. Sust. Energ. Rev.* **2013**, *19*, 565–572.
- (31) Fröhlich, D.; Henninger, S. K.; Janiak, C. *Dalton Trans.* **2014**, *43*, 15300–15304.
- (32) Henninger, S. K.; Habib, H. A.; Janiak, C. *J. Am. Chem. Soc.* **2009**, *131*, 2776–2777.
- (33) Henninger, S. K.; Jeremias, F.; Kummer, H.; Janiak, C. *Eur. J. Inorg. Chem.* **2012**, 2625–2634.
- (34) Jeremias, F.; Lozan, L.; Henninger, S. K.; Janiak, C. *Dalton Trans.* **2013**, *42*, 15967–15973.
- (35) Canivet, J.; Fateeva, A.; Guo, Y.; Coasne, B.; Farrusseng, D. *Chem. Soc. Rev.* **2014**, *43*, 5594–5617.
- (36) Canivet, J.; Bonnefoy, J.; Daniel, C.; Legrand, A.; Coasne, B.; Farrusseng, D. *New J. Chem.* **2014**, *38*, 3102–3111.
- (37) Ehrenmann, J.; Henninger, S. K.; Janiak, C. *Eur. J. Inorg. Chem.* **2011**, 471–474.
- (38) Wickenheisser, M.; Jeremias, F.; Henninger, S. K.; Janiak, C. *Inorg. Chim. Acta* **2013**, *407*, 145–152.
- (39) Akiyama, G.; Matsuda, R.; Sato, H.; Hori, A.; Takata, M.; Kitagawa, S. *Microporous Mesoporous Mater.* **2012**, *157*, 89–93.
- (40) Khutia, A.; Rammelberg, H. U.; Schmidt, T. S.; Henninger, S.; Janiak, C. *Chem. Mater.* **2013**, *25*, 790–798.
- (41) De Coste, J. B.; Peterson, G. W.; Schindler, B. J.; Killops, K. L.; Browe, M. A.; Mahle, J. J. *J. Mater. Chem. A* **2013**, *1*, 11922–11932.
- (42) Jeremias, F.; Fröhlich, D.; Janiak, C.; Henninger, S. K. *New J. Chem.* **2014**, *38*, 1846–1852.
- (43) Jeremias, F.; Khutia, A.; Henninger, S. K.; Janiak, C. *J. Mater. Chem.* **2012**, *22*, 10148–10151.
- (44) Férey, G.; Serre, C.; Mellot-Draznieks, C.; Millange, F.; Surble, S.; Dutour, J.; Margiolaki, I. *Angew. Chem. Int. Ed.* **2004**, *43*, 6296–6301.
- (45) Horcajada, P.; Surble, S.; Serre, C.; Hong, D.-Y.; Seo, Y.-K.; Chang, J.-S.; Greneche, J.-M.; Margiolaki, I.; Férey, G. *Chem. Commun.* **2007**, *27*, 2820–2822.
- (46) Férey, G.; Mellot-Draznieks, C.; Serre, C.; Millange, F.; Dutour, J.; Surble, S.; Margiolaki, I. *Science* **2005**, *309*, 2040–2042.

- 
- (47) Böhringer, B.; Fischer, R.; Lohe, M. R.; Rose, M.; Kaskel, S.; Küsgens, P. *Metal-Organic Frameworks: Applications from Catalysis to Gas Storage*, Edited by D. Farrusseng, 1st ed., Wiley-VCH Verlag GmbH & Co. KGaA, Weinheim, 2011, chapter 15, 353–381.
- (48) (a) Jeremias, F.; Henninger, S. K.; Janiak, C. *Chem. Commun.* **2012**, *48*, 9708–9710. (b) Jeremias, F.; Fröhlich, D.; Janiak, C.; Henninger, S. K. *RSC Advances* **2014**, *4*, 24073–24082.
- (49) Ramos-Fernandez, E. V.; Garcia-Domingos, M.; Juan-Alcaniz, J.; Gascon, J.; Kapteijn, F. *Appl. Catal. A General* **2011**, *391*, 261–267.
- (50) Qian, D.; Lei, C.; Hao, G.; Li, W.; Lu, A. *ACS Appl. Mater. Interfaces* **2012**, *4*, 6125–6132.
- (51) Finsy, V.; Ma, L.; Alaerts, L.; De Vos, D. E.; Baron, G. V.; Denayer, J. F. M. *Microporous Mesoporous Mater.* **2009**, *120*, 221–227.
- (52) Zacharia, R.; Cossement, D.; Lafi, L.; Chahine, R. *J. Mater. Chem.* **2010**, *20*, 2145–2151.
- (53) Lohe, M. R.; Rose, M.; Kaskel, S. *Chem. Commun.* **2009**, 6056–6058.
- (54) Li, L.; Xiang, S.; Cao, S.; Zhang, J.; Ouyang, G.; Chen, L.; Su, C. *Nat. Comm.* **2013**, *4*, 1–9.
- (55) Tanh Jeazet, H. B.; Staudt, C.; Janiak, C. *Chem. Commun.* **2012**, *48*, 2140–2142.
- (56) Küsgens, P.; Zgaverdea, A.; Fritz, H.; Siegle, S.; Kaskel, S. *J. Am. Ceram. Soc.* **2010**, *93*, 2476–2479.
- (57) Sachse, A.; Ameloot, R.; Coq, B.; Fajula, F.; Coasne, B.; De Vos, D.; Galarneau, A. *Chem. Commun.* **2012**, *48*, 4749–4751.
- (58) Schwab, M. G.; Senkovska, I.; Rose, M.; Koch, M.; Pahnke, J.; Jonschker, G.; Kaskel, S. *Adv. Eng. Mat.* **2008**, *10*, 1151–1155.
- (59) Huang, H.; Lin, C.; Wu, C.; Cheng, Y.; Lin, C. *Anal. Chim. Acta* **2013**, *779*, 96–103.
- (60) Fu, Y.; Yan, C.; Yan, X. *Chem. Commun.* **2013**, *49*, 7162–7164.
- (61) Lin, C.; Lirio, S.; Chen, Y.; Lin, C.; Huang, H. *Chem. Eur. J.* **2014**, *20*, 3317–3321.
- (62) Li, L.; Yang, F.; Wang, H.; Yan, X. *J. Chromatogr. A* **2013**, *1316*, 97–103.
- (63) Tanh Jeazet, H. B.; Janiak, C. *Metal-Organic Framework Materials*; Edited by L. R. MacGillivray and C. M. Lukehart; John Wiley & Sons, Ltd: Chichester, 2014; pp 1–15.
- (64) Hüsing, N.; Schubert, U. *Angew. Chem.* **1999**, *110*, 22–47.
- (65) (a) Li, J.; Li, J.; Meng, H.; Xie, S.; Zhang, B.; Li, L.; Ma, H.; Zhang, J.; Yu, M. *J. Mater. Chem. A* **2014**, *2*, 2934–2941. (b) Aegerter, M. A.; Leventis, N.; Edited by M. M. Koebel, *Aerogels Handbook*, Springer, New York, **2011**.
- (66) Ulker, Z.; Erucar, I.; Keskin, S.; Erkey, C. *Microporous Mesoporous Mater.* **2013**, *170*, 352–358.
- (67) Fischer, U.; Saliger, R.; Bock, V.; Petricevic, R.; Fricke, J. *J. Porous Mater.* **1997**, *4*, 281–285.
- (68) Al-Muhtaseb, S. A.; Ritter, J. A. *Adv. Mater.* **2003**, *15*, 101–114.
- (69) Despetis, F.; Barral, K.; Kocon, L.; Phalippou, J. *J. Sol-Gel Sci. Technol.* **2000**, *19*, 829–831.
- (70) Laskowski, J.; Milow, B.; Ratke, L. *Microporous Mesoporous Mater.* **2014**, *197*, 308–315.
- (71) (a) Rey-Raap, N.; Angel Menéndez, J.; Arenillas, A. *Microporous Mesoporous Mater.* **2014**, *195*, 266–275. (b) Lin, C.; Ritter, J. A. *Carbon* **1997**, *35*, 1271–1278. (c) Mulik, S.; Sotiriou-Leventis, C.; Leventis, N. *Chem. Mater.* **2007**, *19*, 6138–6144. (d) Reuß, M.; Ratke, L. *J. Sol-Gel Sci. Technol.* **2008**, *47*, 74–80. (e) Schwan, M.; Ratke, L. *J. Mater. Chem. A* **2013**, *1*, 13462–13468.
- (72) Nagy, B.; Czakkel, O.; László, K. *Microporous Mesoporous Mater.* **2014**, *185*, 66–71.

- 
- (73) Gelb, L. D.; Gubbins, K. E.; Radhakrishnan, R.; Sliwinski-Bartowiak, M. *Rep. Prog. Phys.* **1999**, *62*, 1573–1659.
- (74) Sedron, N. A.; Walton, J. P. R. B.; Quirke, N. *Carbon* **1989**, *27*, 853–861.
- (75) Vishnyakov, A.; Ravikovitch, P.; Neimark, A. V. *Langmuir* **2000**, *16*, 2311–2320.
- (76) Yoon, J. W.; Seo, Y.-K.; Hwang, Y. K.; Chang, J.-S.; Leclerc, H.; Wuttke, S.; Bazin, P.; Vimont, A.; Daturi, M.; Bloch, E.; Llewellyn, P. L.; Serre, C.; Horcajada, P.; Grenèche, J.-M.; Rodrigues, A. E.; Férey, G. *Angew. Chem. Int. Ed.* **2010**, *49*, 5949–5952.
- (77) Vimont, A.; Goupil, J.-M.; Lavalley, J.-C.; Daturi, M.; Surblé, S.; Serre, C.; Millange, F.; Férey, G.; Audebrand, N. *J. Am. Chem. Soc.* **2006**, *128*, 3218–3227.
- (78) Yang, J.; Zhao, Q.; Li, J.; Dong, J. *Microporous Mesoporous Mater.* **2010**, *130*, 174–179.
- (79) Awadallah-F, A.; Elkhatat, A. M.; Al-Muhtaseb, S. A. *J. Mater. Sci.* **2011**, *46*, 7760–7769.
- (80) Pekala, R. W. *J. Mater. Sci.* **1989**, *24*, 3221–3227.
- (81) Sing, K. S. W.; Everett, D. H.; Haul, R. A. W.; Moscou, L.; Pierotti, R. A.; Rouquerol, J.; Siemieniowska, T. *Pure Appl. Chem.* **1985**, *57*, 603–619.
- (82) Saliger, R.; Bock, V.; Petricevic, R.; Tillotson, T.; Geis, S.; Fricke, J. *J. Non-Cryst. Solids* **1997**, *221*, 144–150.
- (83) Chen, W.; Zhang, Z.; Bao, W.; Lai, Y.; Li, J.; Gan, Y.; Wang, J. *Electrochim. Acta* **2014**, *134*, 293–301.
- (84) Lee, J. S.; Jhung, S. H.; Yoon, J. W.; Hwang, Y. K.; Chang, J.-S. *J. Ind. Eng. Chem.* **2009**, *15*, 674–676.
- (85) Kurfiřtová, L.; Seo, Y.-K.; Hwang, Y. K.; Chang, J.-S.; Čejka, J. *Catal. Today* **2012**, *179*, 85–90.
- (86) Küsgens, P.; Rose, M.; Senkovska, I.; Fröde, H.; Henschel, A.; Siegle, S.; Kaskel, S. *Microporous Mesoporous Mater.* **2009**, *120*, 325–330.
- (87) Akiyama, G.; Matsuda, R.; Kitagawa, S. *Chem. Lett.* **2010**, *39*, 360–361.
- (88) Canioni, R.; Roch-Marchal, C.; Sécheresse, F.; Horcajada, P.; Serre, C.; Hardi-Dan, M.; Férey, G.; Grenèche, J.-M.; Lefebvre, F.; Chang, J.-S.; Hwang, Y.-K.; Lebedev, O.; Turner, S.; Van Tendeloo, G. *J. Mater. Chem.* **2011**, *21*, 1226–1233.
- (89) Pinto, M. L.; Dias, S.; Pires, J. *Appl. Mater. Interfaces* **2013**, *5*, 2360–2363.
- (90) O'Neill, L. D.; Zhang, H.; Bradshaw, D. J. *J. Mater. Chem.* **2010**, *20*, 5720–5726.

---

For Table of Contents (TOC) Only



## Supporting Information

**Hierarchical MOF-xerogel monolith composites from embedding MIL-100(Fe,Cr) and MIL-101(Cr) in resorcinol-formaldehyde xerogels for water adsorption applications**

**Martin Wickenheisser,<sup>†</sup> Annika Herbst,<sup>†</sup> René Tannert,<sup>‡</sup> Barbara Milow<sup>‡</sup> and Christoph Janiak<sup>\*,†</sup>**

<sup>†</sup> *Institut für Anorganische Chemie und Strukturchemie I, Universitätsstraße 1, 40225 Düsseldorf, Germany*

<sup>‡</sup> *Deutsches Zentrum für Luft- und Raumfahrt (DLR), Institut für Werkstoff-Forschung, Aerogele, Linder Höhe, 51147 Köln, Germany*

Contact Emails:

[martin.wickenheisser@uni-duesseldorf.de](mailto:martin.wickenheisser@uni-duesseldorf.de)

[annika.herbst@uni-duesseldorf.de](mailto:annika.herbst@uni-duesseldorf.de)

[rene.tannert@dlr.de](mailto:rene.tannert@dlr.de)

[barbara.milow@dlr.de](mailto:barbara.milow@dlr.de)

[janiak@uni-duesseldorf.de](mailto:janiak@uni-duesseldorf.de)



## Experimental Section

### Synthesis of the starting materials

**MIL-100(Fe)**  $\{\text{Fe}_3(\mu_3\text{-O})(\text{F},\text{OH})(\text{H}_2\text{O})_2(\text{BTC})_2 \cdot \sim 14.5\text{H}_2\text{O}\}_n$ : MIL-100(Fe) was prepared according to the literature [1]. 665 mg of  $\text{Fe}^0$  powder (11.9 mmol), 1.65 g  $\text{H}_3\text{BTC}$  (7.85 mmol), 0.83 mL hydrofluoric acid (24 mmol; 48-51 wt% in  $\text{H}_2\text{O}$ ), 0.5 mL  $\text{HNO}_3$  (7 mmol; 65 wt%) and 60 mL of deionized  $\text{H}_2\text{O}$  were placed in a 90 mL Teflon-liner. The Teflon-liner was inserted in a steel autoclave and heated to 423 K within 2 h. After 12 h the autoclave was cooled to r.t. within 2 h. The powder was centrifuged off and washed consecutively with DMF (2 x 120 mL), EtOH (2 x 120 mL) and deionized  $\text{H}_2\text{O}$  (2 x 180 mL). Between each washing step the powder was centrifuged off and dried for 24 h at 373 K. For further activation the powder was first stirred for 12 days in 420 mL DMF at r.t., then additional 6 h at 383 K. After centrifugation and stirring for 2 days in 500 mL EtOH at r.t., the solid was further washed for 3 h at 333 K. The powder was centrifuged off, stirred again for 4 h in 500 mL of deionized water at 353 K and additional 22 h at r.t.. After centrifugation the solid was dried for 24 h at 343 K. 1.50 g of an orange-brown powder was isolated (1.64 mmol, 41 % for  $\text{Fe}_3(\mu_3\text{-O})(\text{F})(\text{H}_2\text{O})_2(\text{BTC})_2 \cdot 14.5\text{H}_2\text{O}$  ( $\text{C}_{18}\text{H}_{10}\text{FFe}_3\text{O}_{15} \cdot \text{H}_{29}\text{O}_{14.5}$ ,  $914.02 \text{ g} \cdot \text{mol}^{-1}$ )).

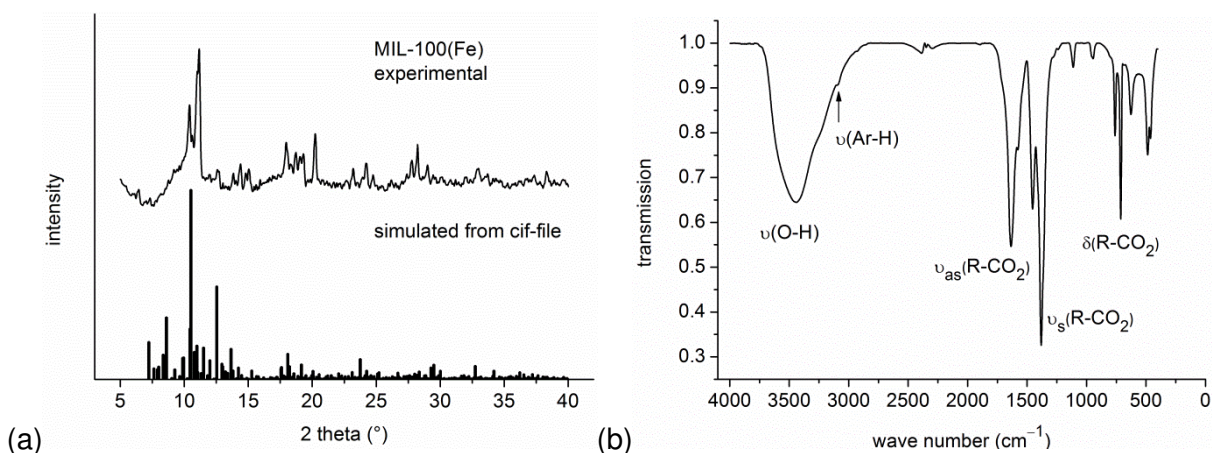


**Figure S1.** (a) Experimental powder X-ray diffraction (PXRD) pattern of activated MIL-100(Fe) and PXRD pattern simulated from the cif-file of MIL-100(Fe), CSD-Refcode CIGXIA [2]. (b) IR-spectrum (KBr) of activated MIL-100(Fe).

[1] Yoon, J. W.; Seo, Y.-K.; Hwang, Y. K.; Chang, J.-S.; Leclerc, H.; Wuttke, S.; Bazin, P.; Vimont, A.; Daturi, M.; Bloch, E.; Llewellyn, P. L.; Serre, S.; Horcajada, P.; Grenèche, J.-M.; Rodrigues, A. E.; Férey G. *Angew. Chem. Int. Ed.* **2010**, *49*, 5949–5952.

[2] Horcajada, P.; Surble, S.; Serre, C.; Hong, D.-Y.; Seo, Y.-K.; Chang, J.-S.; Grenèche, J.-M.; Margiolaki, I.; Férey, G. *Chem. Commun.* **2007**, *27*, 2820–2822.

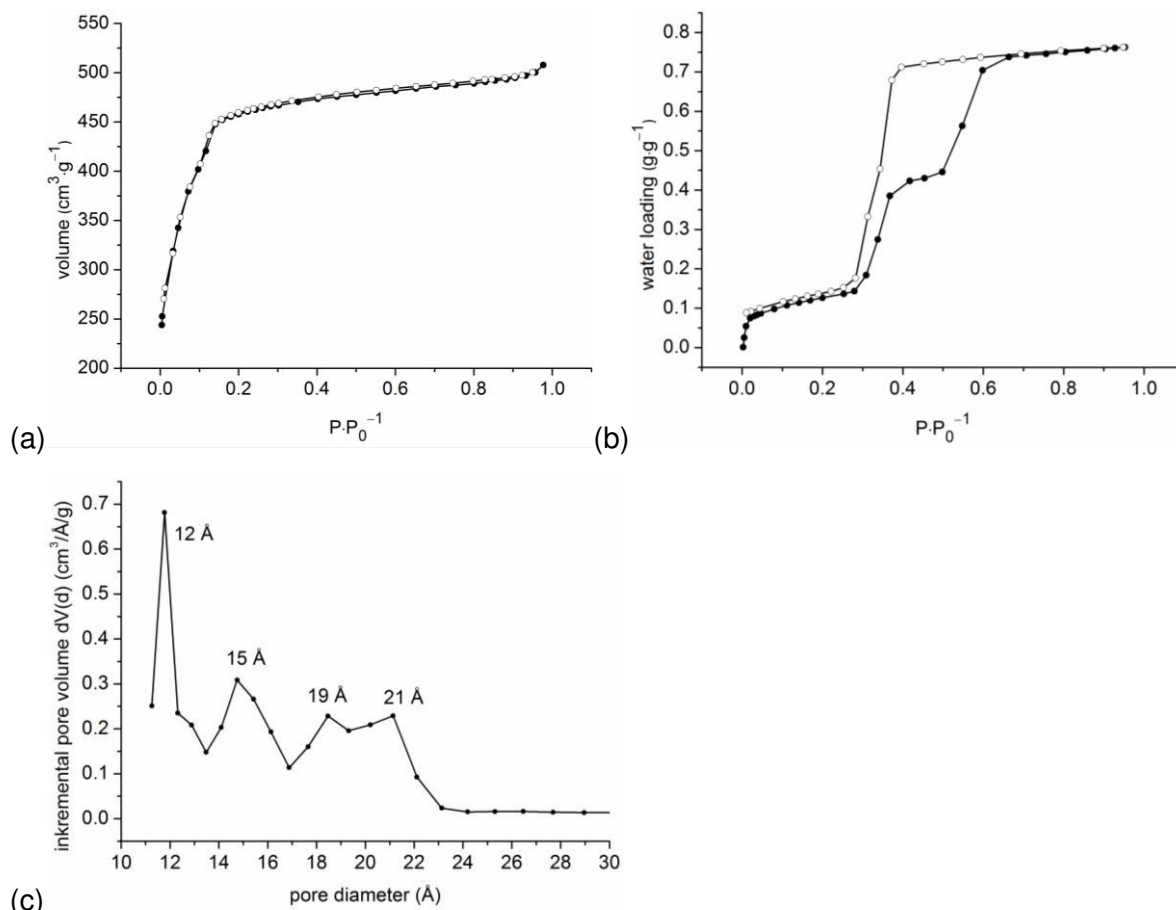


**Figure S2.** (a)  $N_2$ -sorption isotherms of activated MIL-100(Fe) (degassing conditions: 2.5 h, 423 K,  $BET = 2200 \text{ m}^2 \cdot \text{g}^{-1}$ ). (b) Water sorption isotherm of activated MIL-100(Fe) (degassing conditions: 2 h, 423 K). Adsorption is depicted with filled, desorption with empty symbols. (c) Pore size distribution curve of activated MIL-100(Fe) from ' $N_2$  at 77 K on carbon, slit pore, NLDFT equilibrium' model [3,4,5].

[3] Gelb, L. D.; Gubbins, K. E.; Radhakrishnan, R.; Sliwinski-Bartowiak, M. *Rep. Prog. Phys.* **1999**, *62*, 1573–1659.

[4] Sedron, N. A.; Walton, J. P. R. B.; Quirke, N. *Carbon* **1989**, *27*, 853–861.

[5] Vishnyakov, A.; Ravikovitch, P.; Neimark, A. V. *Langmuir* **2000**, *16*, 2311–2320.

**MIL-100(Cr)**  $\{\text{Cr}_3(\mu_3\text{-O})(\text{F},\text{OH})(\text{H}_2\text{O})_2(\text{BTC})_2 \cdot \sim 28\text{H}_2\text{O}\}_n$ : MIL-100(Cr) was prepared according to the literature [6]. 1.20 g  $\text{CrO}_3$  (12.0 mmol), 2.52 g  $\text{H}_3\text{BTC}$  (12.0 mmol), 0.42 mL hydrofluoric acid (12 mmol; 48-51 wt% in  $\text{H}_2\text{O}$ ) and 58 mL of deionized  $\text{H}_2\text{O}$  were placed in a 90 mL Teflon-liner. The Teflon-liner was inserted in a steel autoclave and heated to 473 K within 2 h. After 96 h the autoclave was cooled to r.t. within 2 h. The powder was centrifuged off and washed consecutively with DMF (2 x 120 mL), EtOH (2 x 120 mL) and deionized  $\text{H}_2\text{O}$  (2 x 180 mL). Between each washing step the powder was centrifuged off and dried for 2 h at 373 K. For further activation the powder was first stirred for 42 h in 500 mL DMF at r.t., then additional 4 h at 383 K. After centrifugation and stirring for 45 h in 500 mL EtOH at r.t., the solid was further washed for 4 h at 333 K. The powder was centrifuged off, stirred again for 69 h in 500 mL of deionized water at r.t. and additional 3 h at 353 K. After centrifugation the solid was dried for 18 h at 343 K. 3.18 g of a light green powder was isolated (2.78 mmol, 69 % for  $\text{Cr}_3(\mu_3\text{-O})(\text{F})(\text{H}_2\text{O})_2(\text{BTC})_2 \cdot 28\text{H}_2\text{O}$  ( $\text{C}_{18}\text{H}_{10}\text{Cr}_3\text{FO}_{15} \cdot \text{H}_{56}\text{O}_{28}$ ,  $1145.68 \text{ g} \cdot \text{mol}^{-1}$ )).

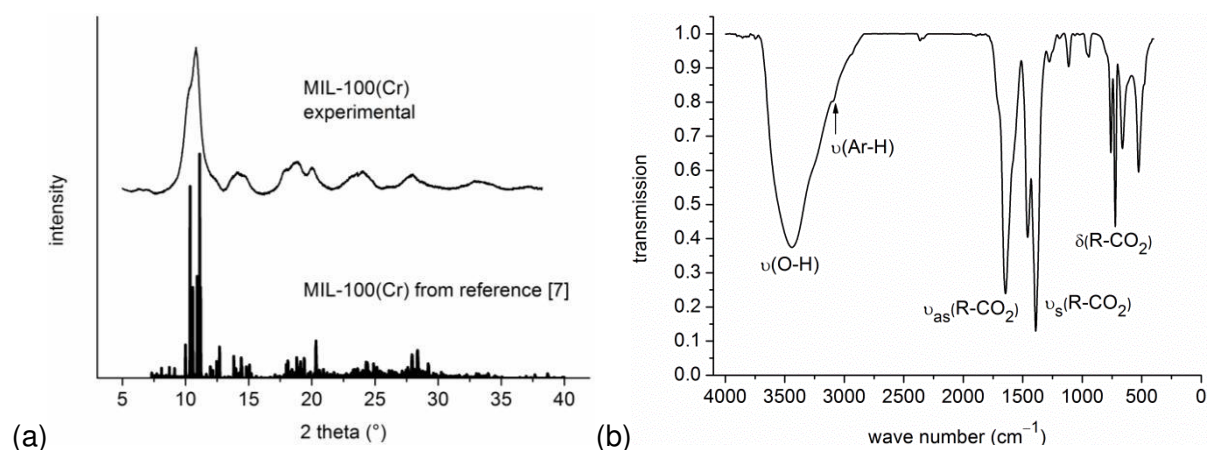


**Figure S3.** (a) Experimental powder X-ray diffraction pattern of activated MIL-100(Cr) and PXRD pattern from reference [7]. (b) IR-spectrum (KBr) of activated MIL-100(Cr).

[6] Vimont, A.; Goupil, J.-M.; Lavalley, J.-C.; Daturi, M.; Surblé, S.; Serre, C.; Millange, J.-C.; Férey, G.; Audebrand N. *J. Am. Chem. Soc.* **2006**, *128*, 3218–3227.

[7] Férey, G.; Serre, C.; Mellot-Draznieks, C.; Millange, F.; Surble, S.; Dutour, J.; Margiolaki, I. *Angew. Chem. Int. Ed.* **2004**, *43*, 6296–6301.

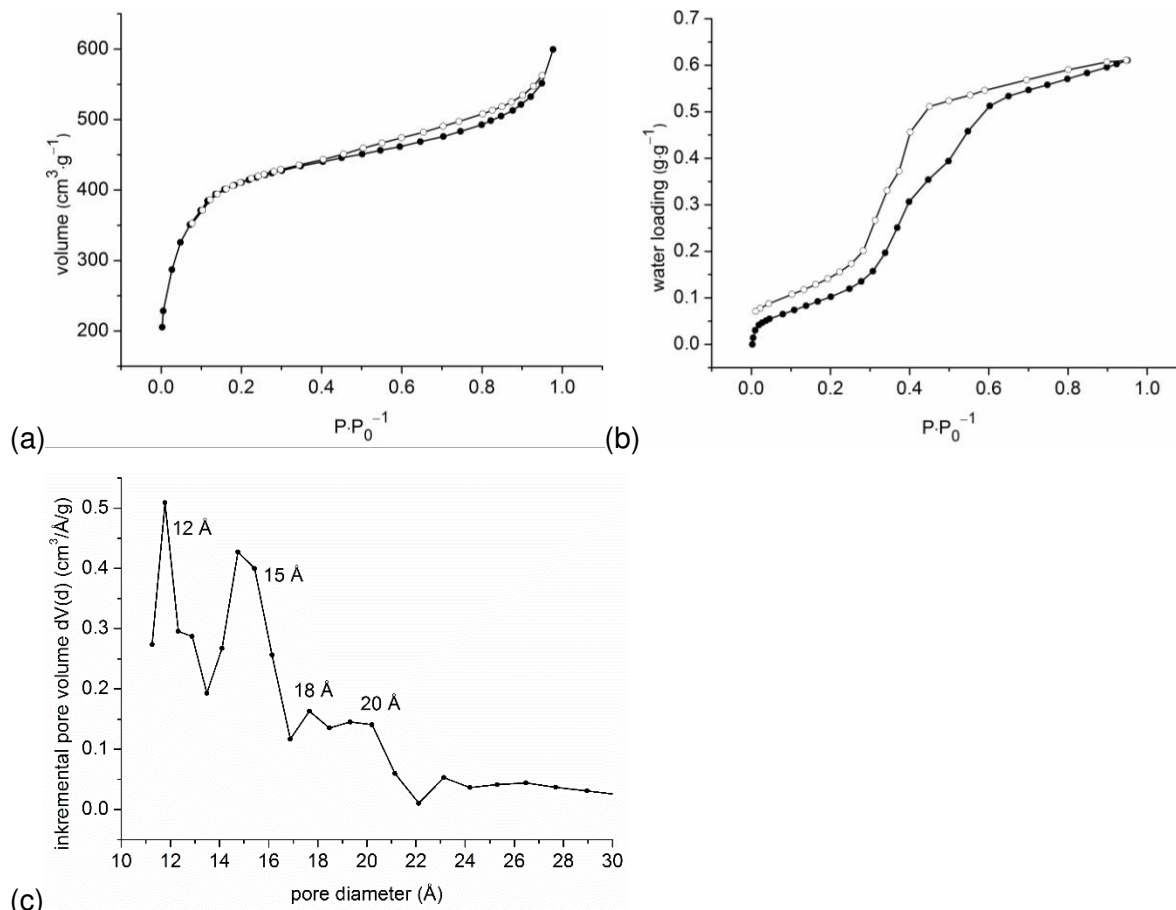


**Figure S4.** (a)  $N_2$ -sorption isotherms of activated MIL-100(Cr) (degassing conditions: 2.5 h, 473 K, BET = 1560 m<sup>2</sup>·g<sup>-1</sup>). (b) Water sorption isotherm of activated MIL-100(Cr) (degassing conditions: 2.5 h, 273 K). Adsorption is depicted with filled, desorption with empty symbols. (c) Pore size distribution curve of activated MIL-100(Cr) from ' $N_2$  at 77 K on carbon, slit pore, NLDFT equilibrium' model.

**MIL-101(Cr)**  $\{\text{Cr}_3(\mu_3\text{-O})(\text{F},\text{OH})(\text{H}_2\text{O})_2(\text{BDC})_3 \cdot \sim 25\text{H}_2\text{O}\}_n$ : MIL-101(Cr) was prepared according to the literature [8]. 4.80 g  $\text{Cr}(\text{NO}_3)_3 \cdot 9\text{H}_2\text{O}$  (12.0 mmol), 1.98 g  $\text{H}_2\text{BDC}$  (11.9 mmol), 1.1 mL TMAOH (tetramethylammonium hydroxide) (3.1 mmol;  $\rho = 1.014 \text{ g} \cdot \text{mL}^{-1}$ ; 25 wt% in  $\text{H}_2\text{O}$ ) and 60 mL of deionized  $\text{H}_2\text{O}$  were placed in a 90 mL Teflon-liner. The Teflon-liner was inserted in a steel autoclave and heated to 453 K within 10 h. After 24 h the autoclave was cooled to r.t. within 18 h. Before heating  $\text{Cr}(\text{NO}_3)_3 \cdot 9\text{H}_2\text{O}$  and  $\text{H}_2\text{BDC}$  was first stirred in deionized  $\text{H}_2\text{O}$  for 5 min, then TMAOH was dropped dropwise to the mixture and the suspension was stirred for 20 min. The green powder was centrifuged off and washed consecutively with DMF (1 x 240 mL), EtOH (1 x 240 mL) and deionized  $\text{H}_2\text{O}$  (1 x 240 mL). Between each washing step the powder was centrifuged off and dried for 22 h at 373 K. For further activation the powder was first stirred for 20 h in 400 mL DMF at 383 K. After centrifugation and stirring for 19 h in 400 mL EtOH at 333 K, the green powder was centrifuged off and stirred again for 19 h in 400 mL of deionized water at 353 K. After centrifugation the solid was dried for 24 h at 373 K. 2.34 g of a green powder was isolated (2.00 mmol, 50 % for  $\text{Cr}_3(\mu_3\text{-O})(\text{F})(\text{H}_2\text{O})_2(\text{BDC})_3 \cdot 25\text{H}_2\text{O}$  ( $\text{C}_{24}\text{H}_{16}\text{Cr}_3\text{FO}_{15} \cdot \text{H}_{50}\text{O}_{25}$ ,  $1169.74 \text{ g} \cdot \text{mol}^{-1}$ )).

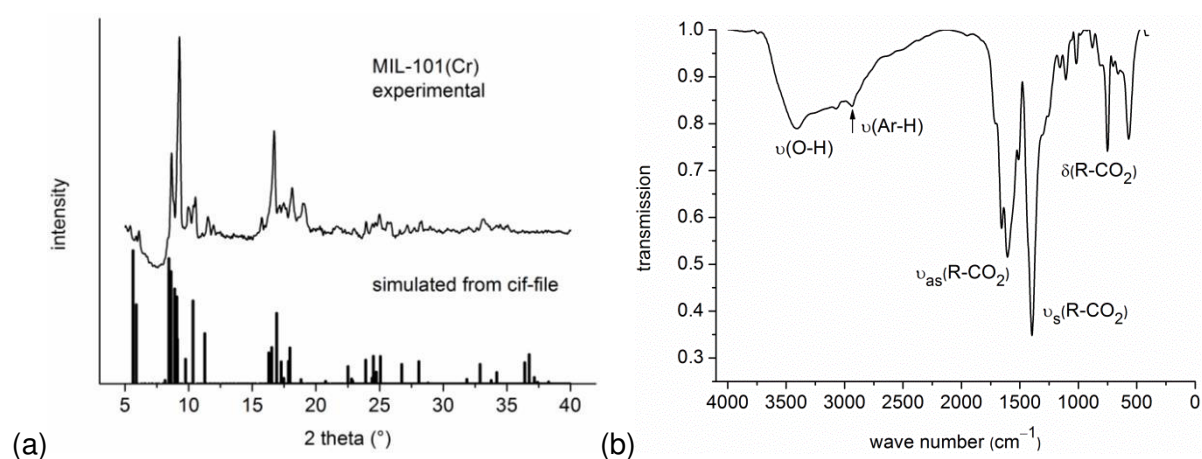


**Figure S5.** (a) Experimental powder X-ray diffraction pattern of activated MIL-101(Cr) and PXRD pattern simulated from the cif-file of MIL-101(Cr), CSD-Refcode OCUKAK [9]. (b) IR-spectrum (KBr) of activated MIL-101(Cr).

[8] Yang, J.; Zhao, Q.; Li, J.; Dong, J. *Micropor. Mesopor. Mater.* **2010**, *130*, 174–179.

[9] Férey, G.; Mellot-Draznieks, C.; Serre, C.; Millange, F.; Dutour, J.; Surblé, S.; Margiolaki, I. *Science* **2005**, *309*, 2040–2042.

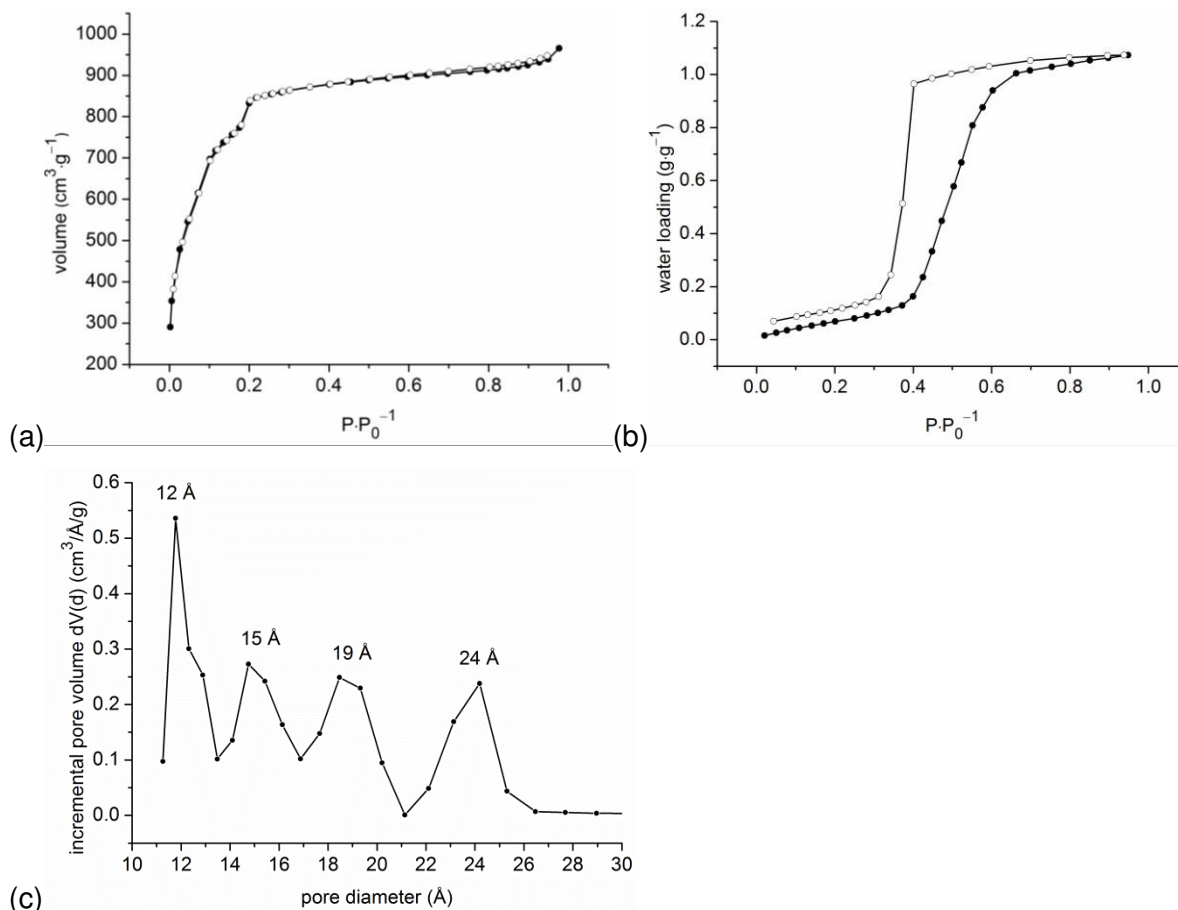


**Figure S6.** (a) N<sub>2</sub>-sorption isotherms of activated MIL-101(Cr) (degassing conditions: 2.5 h, 473 K, BET = 3060 m<sup>2</sup>·g<sup>-1</sup>). (b) Water sorption isotherm of activated MIL-101(Cr) (degassing conditions: 3 h, 473 K). Adsorption is depicted with filled, desorption with empty symbols. (c) Pore size distribution curve of activated MIL-101(Cr) from 'N<sub>2</sub> at 77 K on carbon, slit pore, NLDFT equilibrium' model.

**R,F-xerogel:** The synthesis was prepared according to the literature [10]. 2.29 g resorcinol (20.8 mmol) was dissolved in 9.87 g of an aqueous  $\text{Na}_2\text{CO}_3$  solution ( $2.1 \cdot 10^{-3} \text{ mol} \cdot \text{L}^{-1}$ ; 0.021 mmol  $\text{Na}_2\text{CO}_3$ ). Then 3.57 g of a formaldehyde solution (28.5 mmol;  $\rho = 1.06 \text{ g} \cdot \text{mL}^{-1}$ ; 24 wt% in  $\text{H}_2\text{O}$ ) was added and the solution was stirred for 5 min. The molar ratios of the starting materials were: resorcinol/formaldehyde = 0.73, resorcinol/ $\text{Na}_2\text{CO}_3$  = 1000, resorcinol/water = 0.031. The clear solution was filled into a plastic syringe, which was cut off from one side (side where the cannula is normally attached), sealed and cured for 7 days at 333 K. The brown monolith was stored in 50 mL of acetic acid (10 wt% in water) for 24 h, followed by storing it in EtOH (3 x 50 mL, min. 7 h each washing step) and drying at 313 K (21 h), 333 K (71 h) and 353 K (24 h). 820 mg of a brown monolith was isolated.

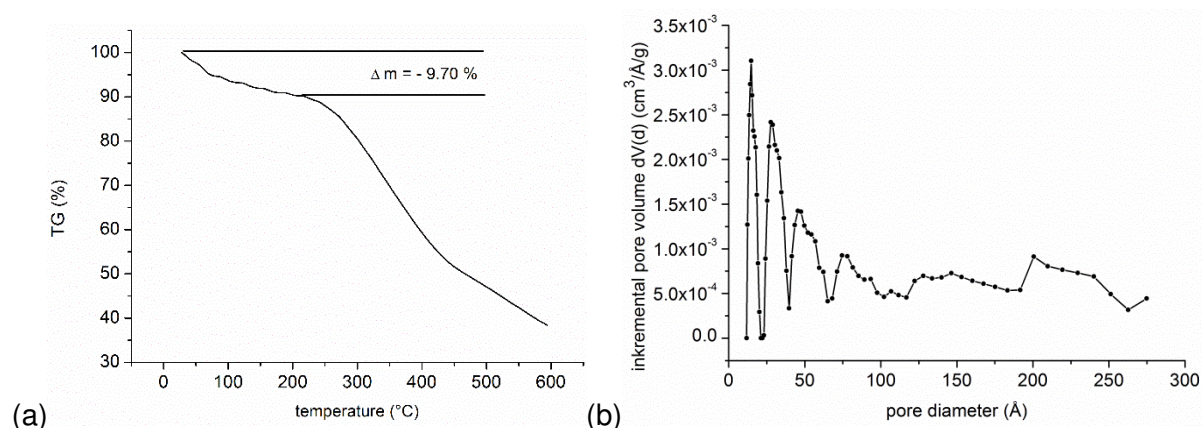


**Figure S7.** (a) Thermogravimetric analysis of R,F-xerogel. (b) Pore size distribution curve of R,F-xerogel from 'N<sub>2</sub> at 77 K on carbon, slit pore, NLDFT equilibrium' model.

[10] Al-Muhtaseb, S. A.; Ritter, J. A. *Adv. Mater.* **2003**, *15*, 101–114.

## Synthesis of the composite materials MIL-100(Cr)@xerogel without pre-polymerization of the R,F-xerogel solution

150 mg of well ground MIL-100(Cr) powder was filled into a plastic syringe, which was cut off from side (side where the cannula is normally attached). Then the just prepared, entire R,F-xerogel solution of low viscosity (Figure S11, left picture) (same amounts and same procedure like described before), was dropped onto the MIL powder. After sealing the syringe by several layers of polyethylene- and aluminum foil to avoid evaporation of the solution, homogenization of the suspension by vigorous shaking of the syringe and sedimentation of the green powder for 1 day, the reaction mixture was cured for 7 days at 333 K. The resulting monolith was light brown colored at the bottom (MIL and xerogel) and brown colored at the top (pure xerogel) (Fig. S8a). Both phases were separated and the light brown monolith from the bottom layer was stored in 40 mL of acetic acid (10 wt% in water) for 24 h, followed by storing it in EtOH (3 x 40 mL, min. 6 h each washing step) and drying at 313 K (17 h), 333 K (17 h) and 353 K (24 h). A brown monolith was isolated.

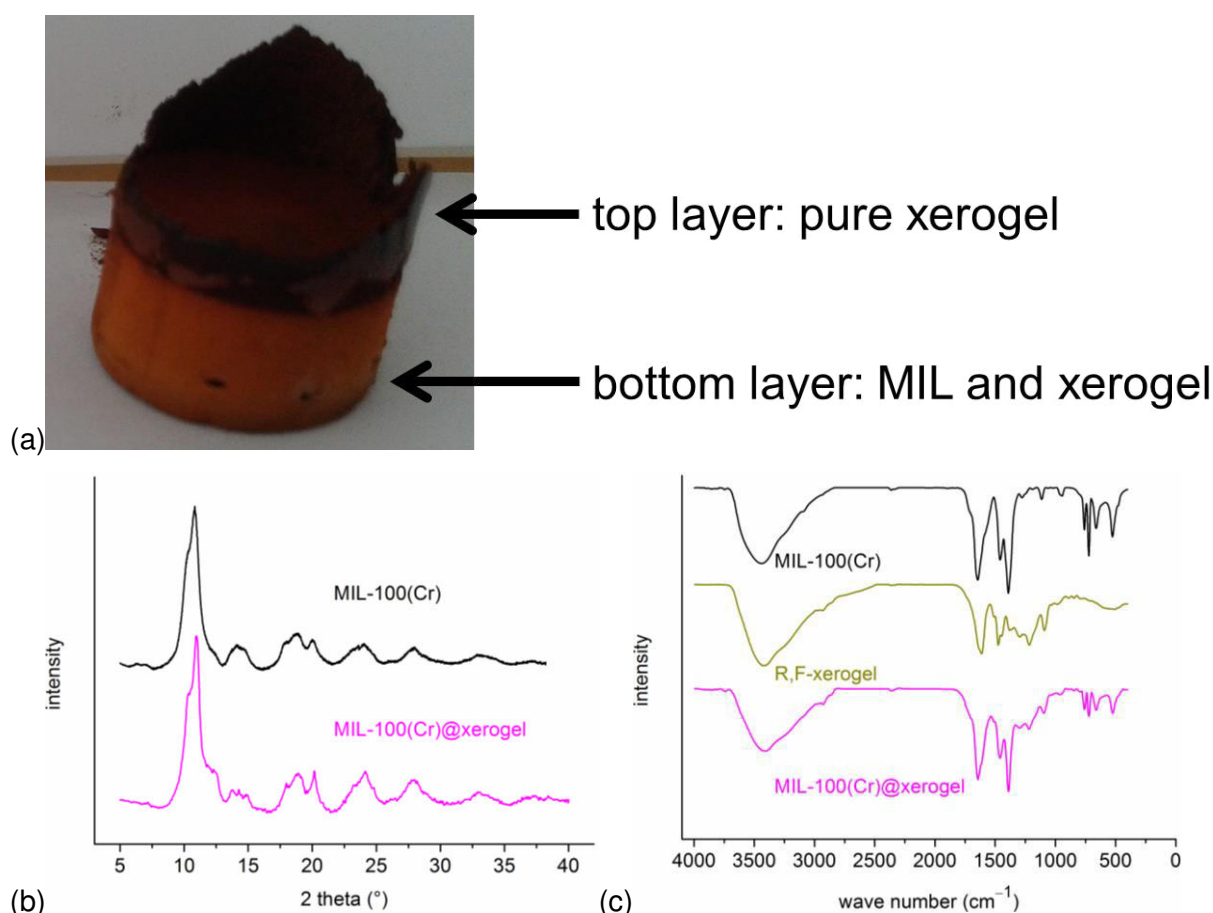


**Figure S8.** (a) Monolithic product of MIL-100(Cr)@xerogel at the bottom layer and residual parts of the pure xerogel at the top layer. (b) Experimental powder X-ray diffraction patterns of MIL-100(Cr) and MIL-100(Cr)@xerogel (bottom layer). (c) IR-spectra (KBr) of MIL-100(Cr), R,F-xerogel and MIL-100(Cr)@xerogel (bottom layer).



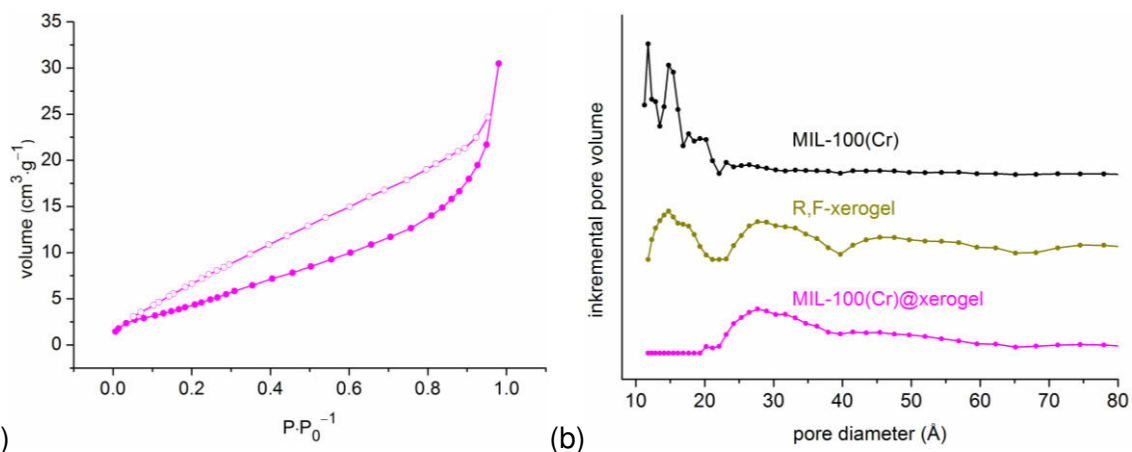


**Figure S9.** (a)  $N_2$ -sorption isotherms of MIL-100(Cr)@xerogel (bottom layer) (degassing conditions: 3 h, 423 K,  $BET = 20 \text{ m}^2 \cdot \text{g}^{-1}$ ). Adsorption is depicted with filled, desorption with empty symbols. (b) Pore size distribution curves of MIL-100(Cr), R,F-xerogel and MIL-100(Cr)@xerogel (bottom layer) from ' $N_2$  at 77 K on carbon, slit pore, NLDFT equilibrium' model.

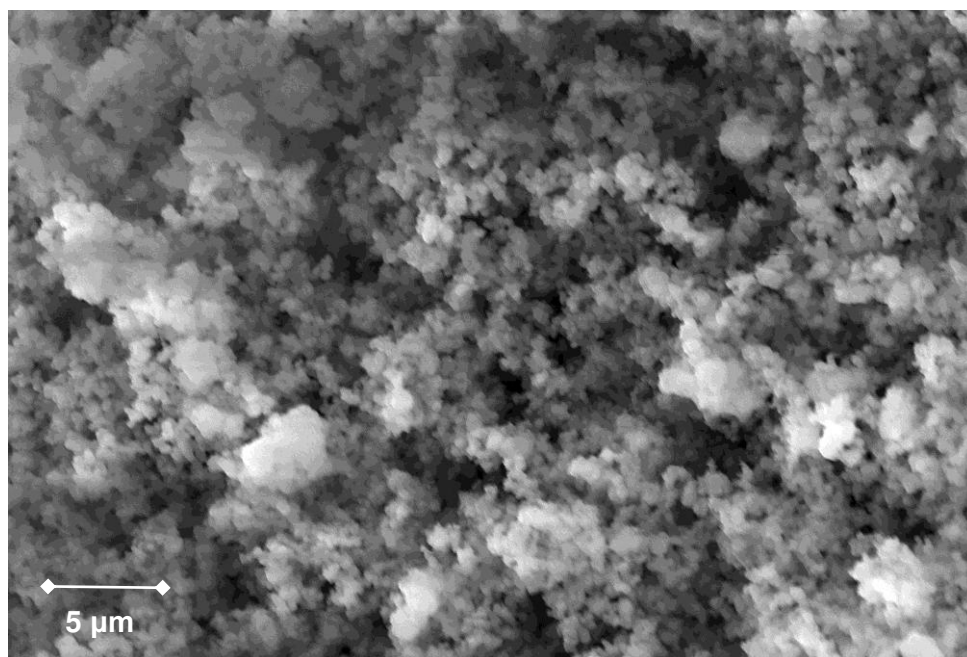


**Figure S10.** Scanning electron microscopic (SEM) image of MIL-100(Cr)@xerogel (bottom layer) without pre-polymerization of the xerogel solution.

### Pre-polymerization experiments of MIL-100(Fe)@xerogel with 11 wt% MIL-100(Fe)

4.59 g Resorcinol (41.7 mmol) was dissolved in 19.74 g of an aqueous  $\text{Na}_2\text{CO}_3$  solution ( $2.1 \cdot 10^{-3} \text{ mol} \cdot \text{L}^{-1}$ ; 0.042 mmol  $\text{Na}_2\text{CO}_3$ ). Then 7.14 g of formaldehyde solution (57.1 mmol;  $\rho = 1.06 \text{ g} \cdot \text{mL}^{-1}$ ; 24 wt% in  $\text{H}_2\text{O}$ ) was added and the solution was stirred for 5 min. The molar ratios of the starting materials are: R/F = 0.73, R/C = 1000, R/W = 0.031. The clear solution was filled into three plastic syringes (4.71 g R,F-xerogel solution per syringe), which were cut off from one side (side where the cannula is normally attached), sealed by several layers of polyethylene- and aluminum foil and cured for 3 h (syringe 1), 4 h (syringe 2) and 5 h (syringe 3) at 343 K respectively. Thermal treatment of the R,F-solutions yielded an enhanced viscosity (Fig. S11). 100 mg of well ground MIL-100(Fe) powder was then added to each syringe and the mixtures were stirred well by a spatula until homogeneous appearance is reached. After compressing and curing for 7 days at 333 K each monolith was stored in 50 mL of acetic acid (10 wt% in water) for 23 h. The monoliths were stored in EtOH (3 x 40 mL, min. 7 h each washing step) and drying at 313 K (21 h), 333 K (71 h) and 353 K (24 h). 906 mg (**11 wt%**, syringe 1), 873 mg (**11 wt%**, syringe 2) and 899 mg (**11 wt%**, syringe 3) of brown monoliths were isolated. The loading of MIL-100(Fe) in MIL-100(Fe)@xerogel was calculated from formula S1.



**Figure S11.** Pre-polymerization steps of pure R,F-xerogel solution (approx. 1 g) at 343 K. The first picture refers to the initial solution before heat treatment. The last one shows the pre-polymerized dispersion after 5 h.

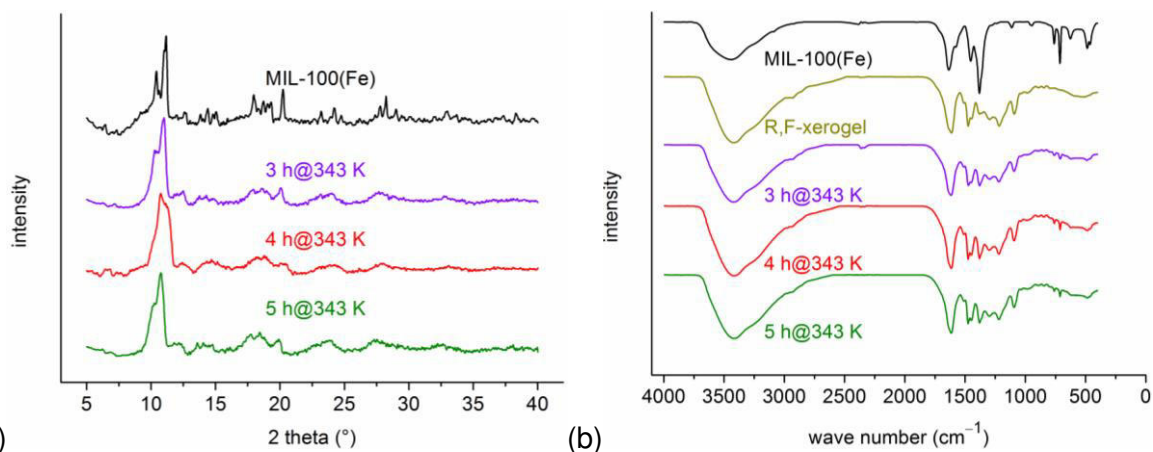


**Figure S12.** (a) Experimental powder X-ray diffraction patterns of MIL-100(Fe) and MIL-100(Fe)@xerogel with 11 wt% MIL-100(Fe). MIL-100(Fe) powders were added to the R,F-xerogel solutions after 3, 4 and 5 h of pre-polymerization time at 343 K respectively. (b) IR-spectra (KBr) of MIL-100(Fe), R,F-xerogel and MIL-100(Fe)@xerogel with 11 wt% MIL-100(Fe) (3, 4 and 5 h of polymerization at 343 K).

**Formula S1.** Used for calculations of wt% MIL in MIL@R,F-xerogel.

$$\text{wt\% (MIL in MIL@R, F- xerogel)} = \frac{m \text{ (weighted MIL)}}{m \text{ (MIL@R, F- xerogel)}} \times 100$$

### ***Standard syntheses of pre-polymerized MIL@xerogel without additional water***

#### **Standard syntheses of the composite materials MIL-100(Fe)@xerogel (no additional water) with 43, 50 and 58 wt% of MIL-100(Fe) with pre-polymerization of the R,F-xerogel solution**

2.29 g resorcinol (20.8 mmol) was dissolved in 9.87 g of an aqueous  $\text{Na}_2\text{CO}_3$  solution ( $2.1 \cdot 10^{-3} \text{ mol} \cdot \text{L}^{-1}$ ; 0.021 mmol  $\text{Na}_2\text{CO}_3$ ). Then 3.57 g of formaldehyde solution (28.5 mmol;  $\rho = 1.06 \text{ g} \cdot \text{mL}^{-1}$ ; 24 wt% in  $\text{H}_2\text{O}$ ) was added and the solution was stirred for 5 min. The molar ratios of the starting materials are: R/F = 0.73, R/C = 1000, R/W = 0.031. The clear solution was filled into a three plastic syringes (1.01 g per syringe), sealed by several layers of polyethylene- and aluminum foil and pre-polymerized for 5 h at 343 K obtaining in highly viscous solutions. 100, 150 and 180 mg of well ground MIL-100(Fe) powders were added into the syringes, stirred well by a spatula until homogenous appearance is reached, compressed and cured for 7 days at 333 K. Each monolith was stored in 40 mL of acetic acid (10 wt% in water) for 20 h. The monoliths were stored in EtOH (3 x 40 mL, min. 7 h each washing step) and drying at 313 K (21 h), 333 K (71 h) and 353 K (24 h). 230 mg (**43 wt%**, syringe 1), 300 mg (**50 wt%**, syringe 2) and 313 mg (**58 wt%**, syringe 3) of brown monoliths were isolated. The loading of the MILs in MIL@xerogel was calculated from formula S1.

#### **Standard syntheses of the composite materials MIL-100(Cr)@xerogel (no additional water) with 41, 51 and 56 wt% of MIL-100(Cr) with pre-polymerization of the R,F-xerogel solution**

The preparation, pre-polymerization of the R,F-xerogel solution, washing and drying of the monoliths are described before. 100, 150 and 180 mg of well ground MIL-100(Cr) was used yielding 246 mg (**41 wt%**), 297 mg (**51 wt%**) and 319 mg (**56 wt%**) of brown monoliths. The loading of the MILs in MIL@xerogel was calculated from formula S1.

#### **Standard syntheses of the composite materials MIL-101(Cr)@xerogel (no additional water) with 35, 46 and 50 wt% of MIL-101(Cr) with pre-polymerization of the R,F-xerogel solution**

The preparation, pre-polymerization of the R,F-xerogel solution, washing and drying of the monoliths are described before. 100, 150 and 180 mg of well ground MIL-101(Cr) was used yielding 285 mg (**35 wt%**), 325 mg (**46 wt%**) and 358 mg (**50 wt%**) of brown monoliths. The loading of the MILs in MIL@xerogel was calculated from formula S1.

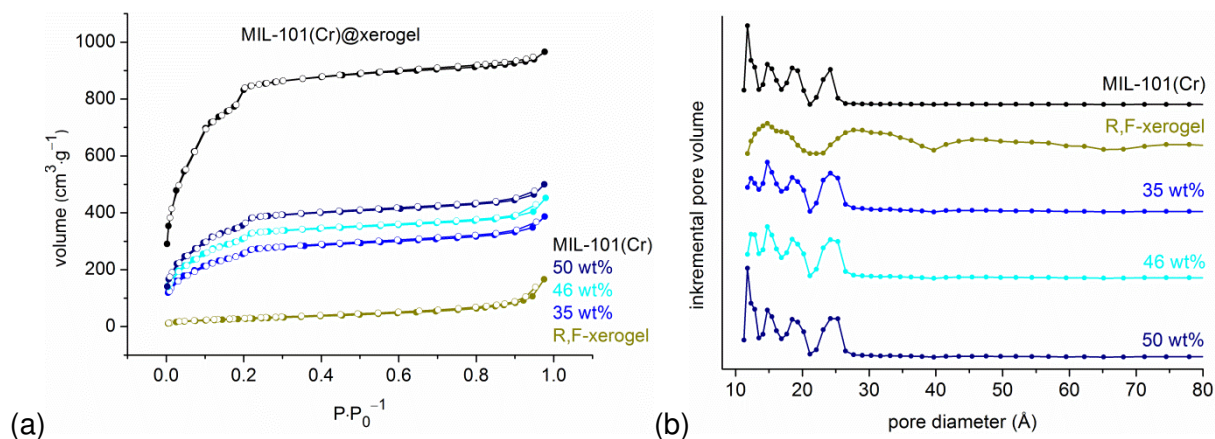


**Figure S13.** (a-b)  $N_2$ -sorption isotherms and pore diameter distribution of R,F-xerogel, MIL-101(Cr) and MIL-101(Cr)@xerogel composites (degassing conditions: 3 h, 423 K). Adsorption is depicted with filled, desorption with empty symbols.

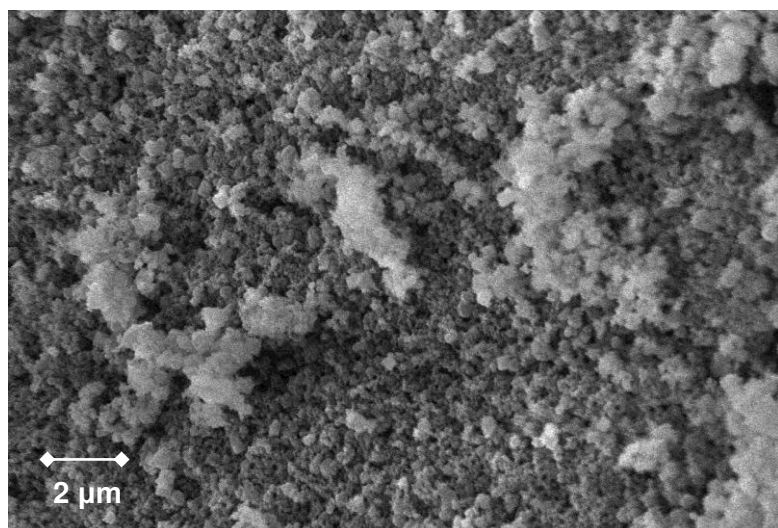


**Figure S14.** Scanning electron microscopic (SEM) images of MIL-101(Cr)@xerogel (35 wt%) with pre-polymerization of the xerogel solution.

### ***Syntheses of MIL-101(Cr)@xerogel-H<sub>2</sub>O with additional water***

#### **Syntheses of the composite material MIL-101(Cr)@xerogel-H<sub>2</sub>O (with additional water) with 35, 46 and 50 wt% of MIL-101(Cr) with pre-polymerization of the R,F-xerogel solution**

The preparation, pre-polymerization of the R,F-xerogel solution, washing and drying of the monoliths are described before for the standard syntheses. 100, 150 and 180 mg of well ground MIL-101(Cr) powders were used together with 0.6 mL of deionized water per syringe yielding brown monoliths in all cases: 288 mg (**35 wt%**), 323 mg (**46 wt%**) and 358 mg (**50 wt%**) for MIL-101(Cr) composites. The loading of the MILs in MIL@xerogel was calculated from formula S1.

#### **Synthesis of the composite material MIL-101(Cr)@xerogel-H<sub>2</sub>O (with additional water) with 77 wt% of MIL-101(Cr) with pre-polymerization of the R,F-xerogel solution**

6.88 g resorcinol (62.5 mmol) was dissolved in 29.6 g of an aqueous Na<sub>2</sub>CO<sub>3</sub> solution ( $2.1 \cdot 10^{-3}$  mol·L<sup>-1</sup>; 0.063 mmol Na<sub>2</sub>CO<sub>3</sub>). Then 10.7 g of formaldehyde solution (85.5 mmol;  $\rho = 1.06$  g·mL<sup>-1</sup>; 24 wt% in H<sub>2</sub>O) was added and the solution was stirred for 1 h. The molar ratios of the starting materials are: R/F = 0.73, R/C = 1000, R/W = 0.031. The clear solution was pre-polymerized for 5 h at 343 K until it was almost solid and cooled to room temperature. The gel can be stored at 278 K and was used for several experiments. To the pre-polymerized gel (1.03 g) well ground MIL-101Cr powder (0.46 g) and deionized water (0.6 mL) were added. The suspension was stirred for 30 min with a mechanical stirrer in a custom-made, closable glass vial, to achieve a homogenous distribution. Then the vial was closed and the gel was cured for 7 days at 343 K. The brown monolith was stored in 50 mL of acetic acid (10 wt% in water) for 24 h, followed by storing it in EtOH (3 x 50 mL, min. 7 h each washing step) and drying it without cap for 3 days at 333 K. The MIL-101Cr@xerogel composite (0.60 g, **77 wt%**) was isolated as a green monolithic solid. The loading of the MILs in MIL@xerogel was calculated from formula S1.

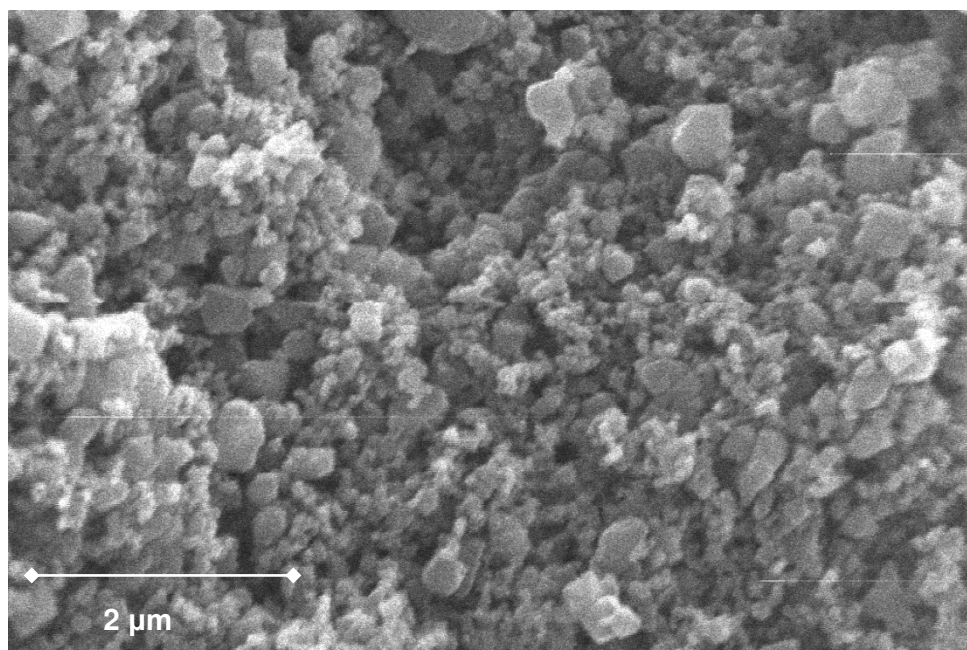


**Figure S15.** Scanning electron microscopic (SEM) images of MIL-101(Cr)@xerogel-H<sub>2</sub>O (35 wt%) with pre-polymerization of the xerogel solution.

## Porous structure of MIL-101(Cr)

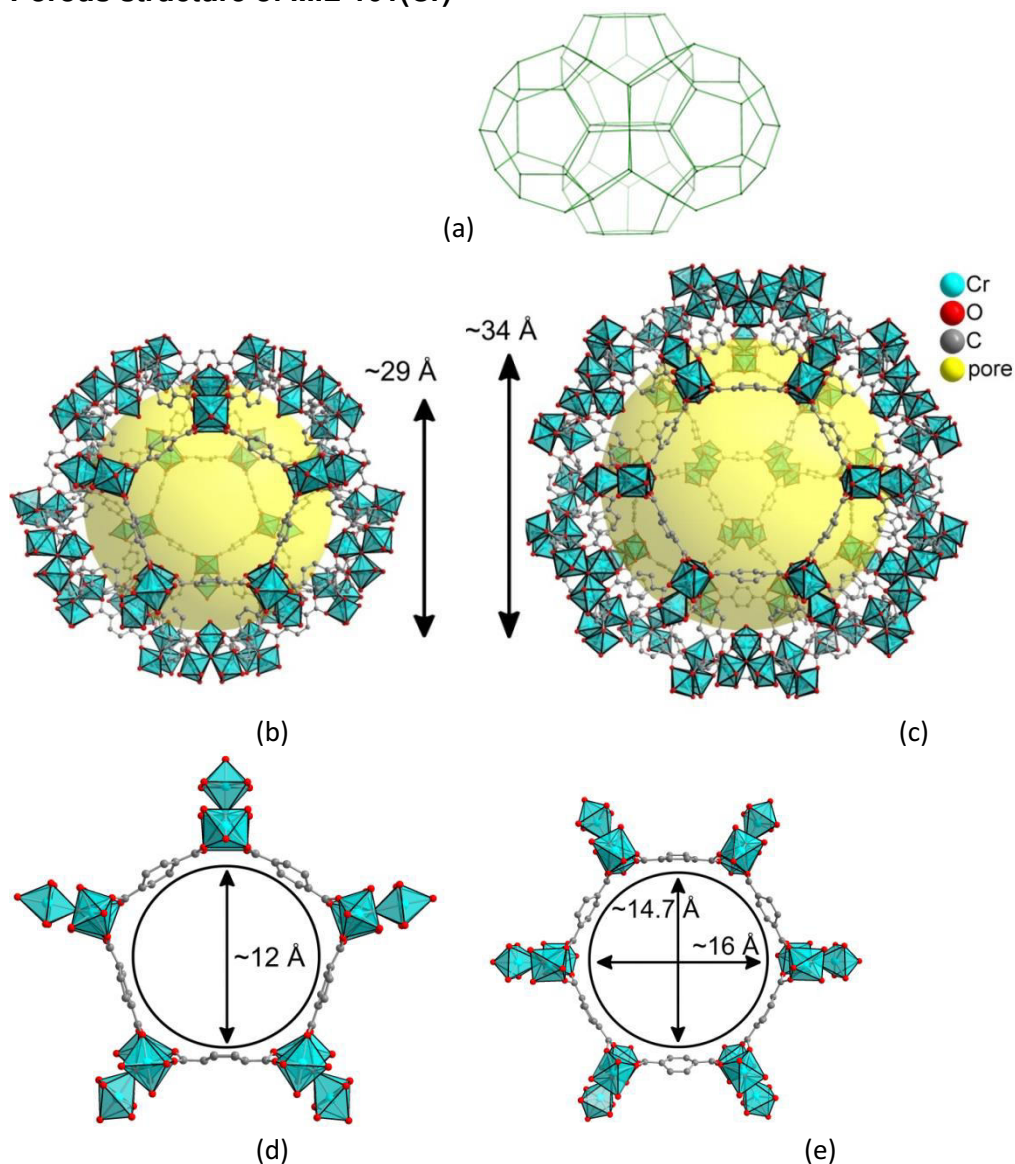


**Figure S16.** MIL-101(Cr),  $\{\text{Cr}_3(\mu_3\text{-O})(\text{F},\text{OH})(\text{H}_2\text{O})_2(\text{BDC})_3 \cdot \sim 25\text{H}_2\text{O}\}_n$  (BDC = 1,4-benzene dicarboxylate) presents a 3D framework constructed by two mesopores (in a 2:1 ratio) with diameter of 29 and 34 Å (a-c). The small cage (b) has an inner diameter 29 Å and only pentagonal windows (d). The large cage (c) has an inner diameter of 34 Å and both pentagonal and hexagonal windows (e). The MIL-101(Cr) structure is redrawn from the deposited cif file at the Cambridge Structure Database (CSD-Refcode OCUNAK [11]) using the software DIAMOND [12]. Different objects are not drawn to scale and water of crystallization is not shown.

[11] Férey, G.; Mellot-Draznieks, C.; Serre, C.; Millange, F.; Dutour, J.; Surblé, S.; Margiolaki, I. *Science* **2005**, *309*, 2040–2042.

[12] Brandenburg, K.; Diamond (Version 3.2), crystal and molecular structure visualization, Crystal Impact. K. Brandenburg & H. Putz Gbr, Bonn, Germany, 2007–2012.



### Porous structure of MIL-100(Fe)

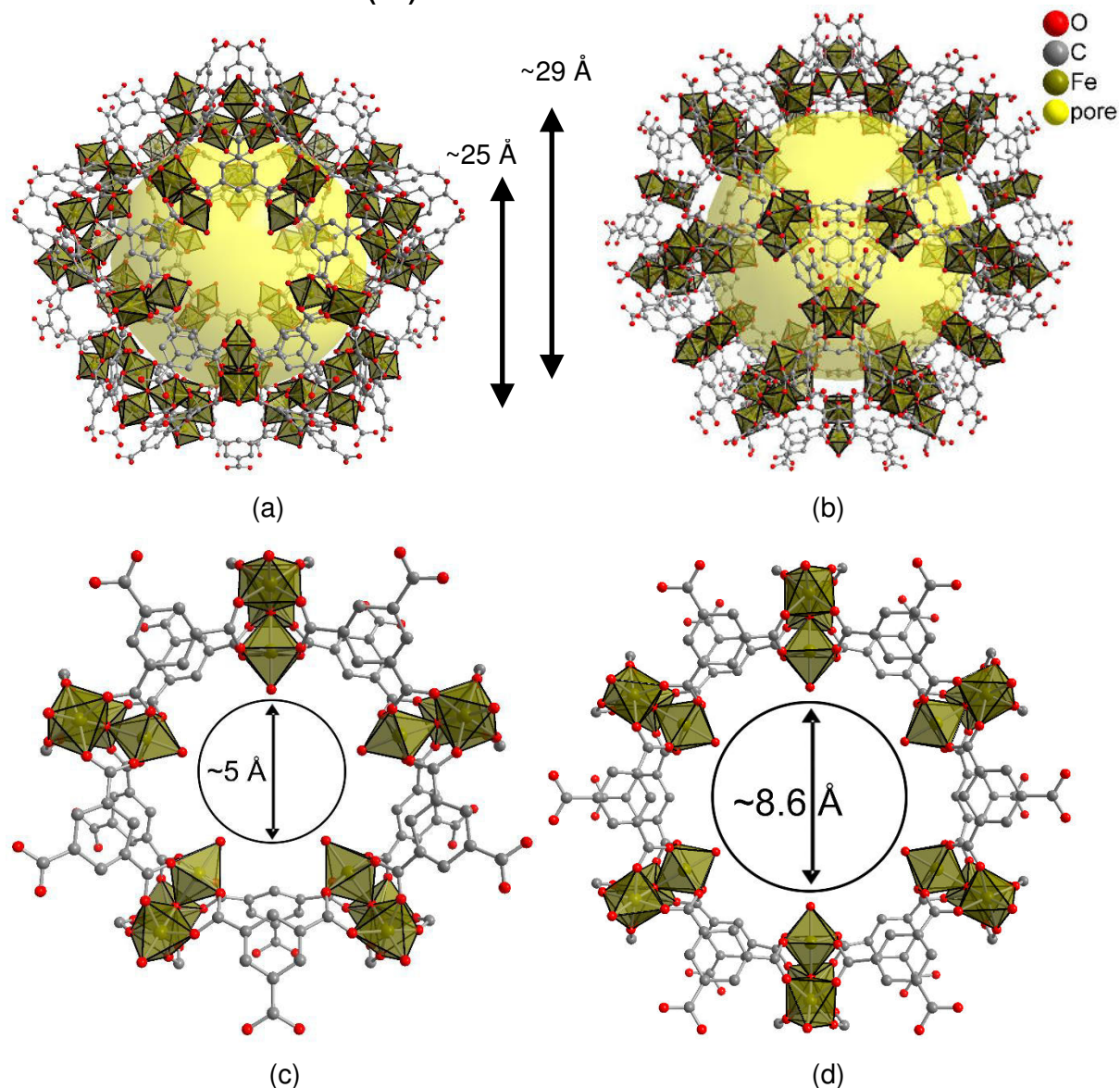


**Figure S17.** MIL-100(Fe) (isostructural to MIL-100(Cr),  $\{Fe_3(\mu_3-O)(F,OH)(H_2O)_2(BTC)_2\} \cdot \sim 14.5H_2O$  (BTC = 1,3,5-benzene tricarboxylate) presents a 3D framework constructed by two mesopores (in a 2:1 ratio) with diameter of 25 and 29 Å (a-b). The small cage (a) has an inner diameter 25 Å and only pentagonal windows (c). The large cage (b) has an inner diameter of 29 Å and both pentagonal and hexagonal windows (d). The MIL-100(Fe) structure is redrawn from the deposited cif file at the Cambridge Structure Database (CSD-Refcode CIGXIA [2]) using the software DIAMOND [12]. Different objects are not drawn to scale and water of crystallization is not shown.

## Mechanical stability test of native R,F-xerogel and composites

Monolithic, pure R,F-xerogel (177 mg), MIL-100(Fe)@xerogel (58 wt%, 159 mg), MIL-100(Cr)@xerogel (56 wt%, 161 mg) and MIL-101(Cr)@xerogel (50 wt%, 160 mg) were placed into 25 mL beakers and treated in a shaking incubator (GFL 3032) at maximum rotation ( $250 \text{ min}^{-1}$ ) for a time period of 3 hours. After 5, 10, 20, 40, 60, 120 and 180 min, the monoliths were weighed to determine the mechanical abrasion.

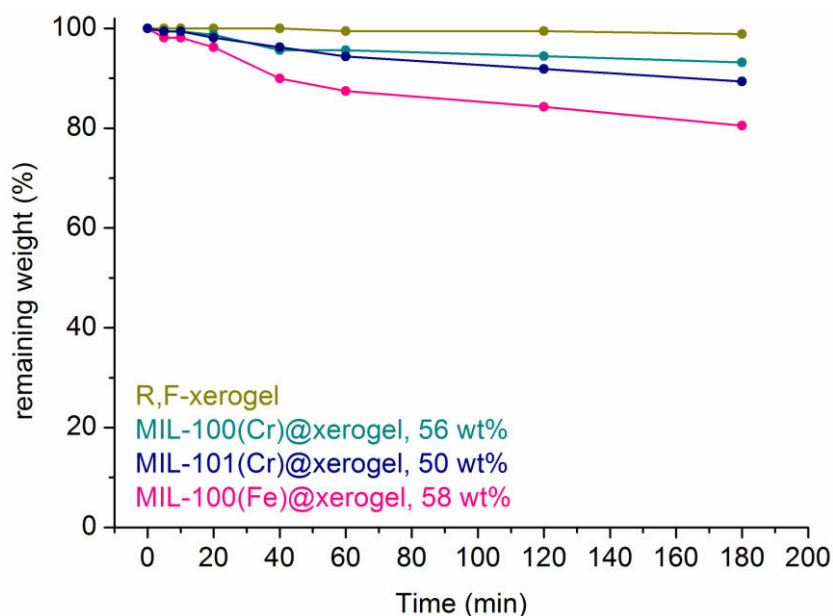


**Figure S18.** Mechanical stability test of pure R,F-xerogel and three representative MIL@xerogels in a shaking incubator at 250 rounds/min. The initial weights are set to 100 %. Mechanical abrasion after 3 hours: Pure R,F-xerogel (−1.1 wt%), MIL-100(Cr)@xerogel, 56 wt% (−6.8 wt%), MIL-101(Cr)@xerogel, 50 wt% (−10.6 wt%), MIL-100(Fe)@xerogel, 58 wt% (−19.5 wt%).

## 4. Unpublished work

### 4.1 Grafting of MIL-101(Cr) with ethylene glycols

In addition to grafting reactions of MIL-100(Cr) with small glycols and ethylenediamine as discussed in section 3.1, similar chemical modifications were carried out on MIL-101(Cr).

Therefore, activated and purified MIL-101(Cr) powders were treated *in vacuo* at 473 K for 1.5 hours to remove any adsorbed water from the metal sites, which yielded the coordinatively unsaturated metal sites (CUS). Dry toluene was added to the powders followed by the addition of pure, neat ethylene glycol (EG), diethylene glycol (DEG) and triethylene glycol solutions for each grafting modification. After stirring the suspensions overnight at 373 K and an additional 28 hours at ambient temperature, the green powders MIL-101(Cr)-X, X = EG, DEG, TEG were isolated by filtration followed by washing and drying steps.

The X-ray diffraction patterns of EG-, DEG- and TEG-modified MILs show that the crystallinity remains unchanged in comparison to native MIL-101(Cr) (Figure 25a). Infrared spectra of glycol modified MILs display the presence of new  $\nu(\text{C-H})$ - and  $\nu(\text{C-O})$  stretching vibrations, located at 2953–2884  $\text{cm}^{-1}$  for  $\nu(\text{C-H})$  and 1123–1019  $\text{cm}^{-1}$   $\nu(\text{C-O})$  (Figure 25).  $\nu(\text{C-H})$  stretching vibrations are shifted to higher wavenumbers by 9–20  $\text{cm}^{-1}$  compared to the free ligands (Figure 25b, Table 1), which is observed when a ligand is bonded to a Lewis acidic metal center.<sup>228,229</sup> This effect proves the successful grafting of EG, DEG and TEG onto the chromium(III) metal centers.

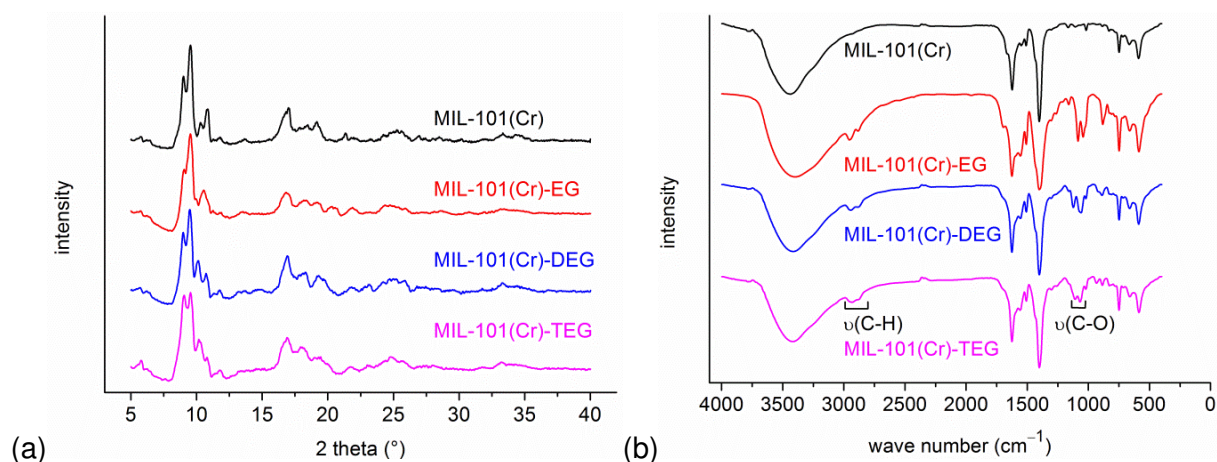


**Fig. 25.** (a) PXRD patterns of native MIL-101(Cr) and EG-, DEG- and TEG-modified MIL-101(Cr). (b) IR-spectra (KBr) of activated, native MIL-101(Cr) and EG-, DEG- and TEG-modified MIL-101(Cr).

**Table 1.**  $\nu(\text{C-H})$ - and  $\nu(\text{C-O})$ -vibration bands ( $\text{cm}^{-1}$ ) of neat EG, DEG and TEG and corresponding bands in MIL-101(Cr)-EG, MIL-101(Cr)-DEG and MIL-101(Cr)-TEG.

	EG <sup>a</sup>	DEG <sup>a</sup>	TEG <sup>a</sup>
$\nu(\text{C-H})$	2937, 2875	2924, 2871	2915, 2869
$\nu(\text{C-O})$	1083, 1033	1126, 1052	1116, 1058
	MIL-101(Cr)-EG <sup>b</sup>	MIL-101(Cr)-DEG <sup>b</sup>	MIL-101(Cr)-TEG <sup>b</sup>
$\nu(\text{C-H})$	2953, 2884	2944, 2884	2931, 2885
$\nu(\text{C-O})$	1084, 1042, 1023	1123, 1073, 1058, 1020	1109, 1068, 1019

<sup>a</sup> measured on ATR unit.

<sup>b</sup> measured in KBr disk.

Post-synthetic grafting leads to a decrease of the BET surface areas of the modified MILs by approximately 50 % compared to native MIL-101(Cr) (Table 1). Also, the available total pore volumes shrink significantly. Nitrogen sorption isotherms of modified MIL-101(Cr) show type I shapes like pure MIL-101(Cr) due to the presence of free micropores (Figure 26a). In contrast to the distinctive pore size changes of post-synthetically modified MIL-100(Cr) (section 3.1), pore size distribution curves of grafted MIL-101(Cr) only show a slight reduction of one MIL mesopore from originally 24 to 23 Å (Figure 26b).

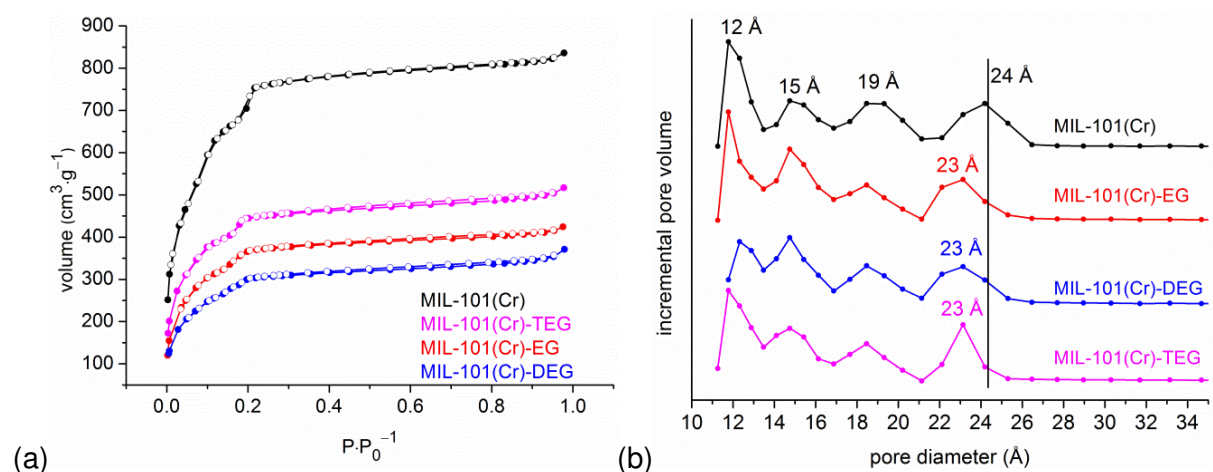


**Fig. 26.** (a)  $\text{N}_2$ -sorption isotherms of non-modified MIL-101(Cr) and EG-, DEG- and TEG-modified MIL-101(Cr) (degassing conditions: 2.5 h, 473 K). Adsorption is depicted with filled, desorption with empty symbols. (b) Pore size distribution curves of non-modified MIL-101(Cr) and EG-, DEG- and TEG-modified MIL-101(Cr).

Water sorption studies of glycol-modified MIL-101(Cr) display that only MIL-101(Cr)-TEG exhibits a slightly favored water uptake in the region of  $0.30 < P \cdot P_0^{-1} < 0.36$  compared to pure MIL-101(Cr), indicated by its higher slope (Figure 27). The total water uptakes of the grafted MILs are reduced to a large extent from  $1.02 \text{ g} \cdot \text{g}^{-1}$  for pure MIL-101(Cr) to  $0.93 \text{ g} \cdot \text{g}^{-1}$

(EG),  $0.55 \text{ g}\cdot\text{g}^{-1}$  (DEG) and  $0.75 \text{ g}\cdot\text{g}^{-1}$  (TEG) (Table 1), which is in contrast to glycol-modified MIL-100(Cr), which show almost no loss of total water uptake capacity (section 3.1).

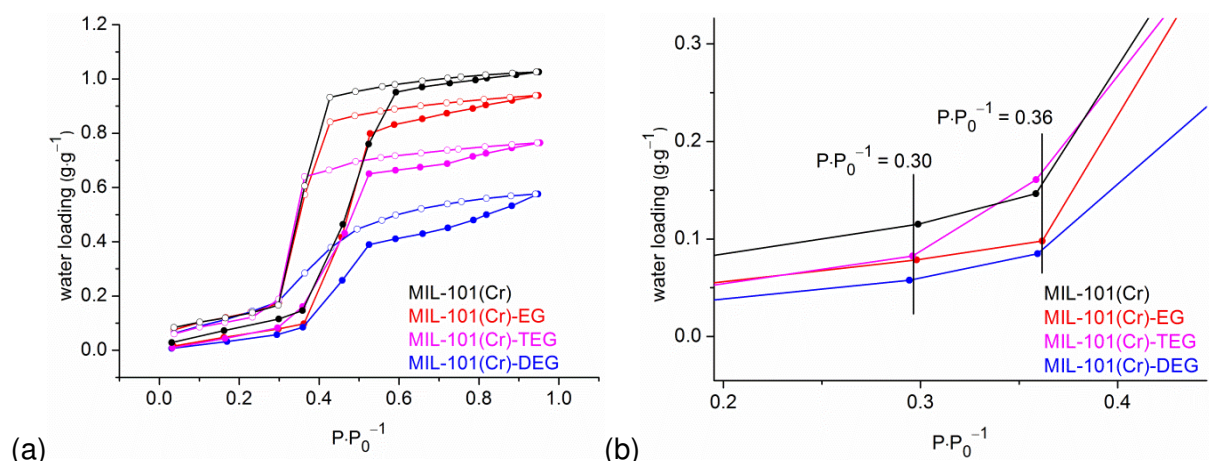


**Fig. 27.** (a) Water sorption isotherms of non-modified MIL-101(Cr) and EG-, DEG- and TEG-modified MIL-101(Cr) (degassing conditions: 2.5 h, 473 K). Adsorption is depicted with filled, desorption with empty symbols. (b) Enlargement for region  $0.2 < P\cdot P_0^{-1} < 0.4$  (only adsorption isotherms are shown).

For investigation of the stability of the chromium-glycol bonds, nitrogen sorption analyses and infrared spectra of the grafted MILs have been carried out after water sorption measurements (Figure 28a-b). BET surface areas of glycol-modified compounds reveal that MIL-101(Cr)-EG shows almost the same surface area as pure MIL-101(Cr) (Table 2). Together with the hardly visible bands for coordinated EG, most of the ethylene glycol molecules were degassed and/or washed away. Only MIL-101(Cr)-TEG possesses an almost unchanged BET surface area with clearly visible bands for coordinated TEG after water sorption measurement.

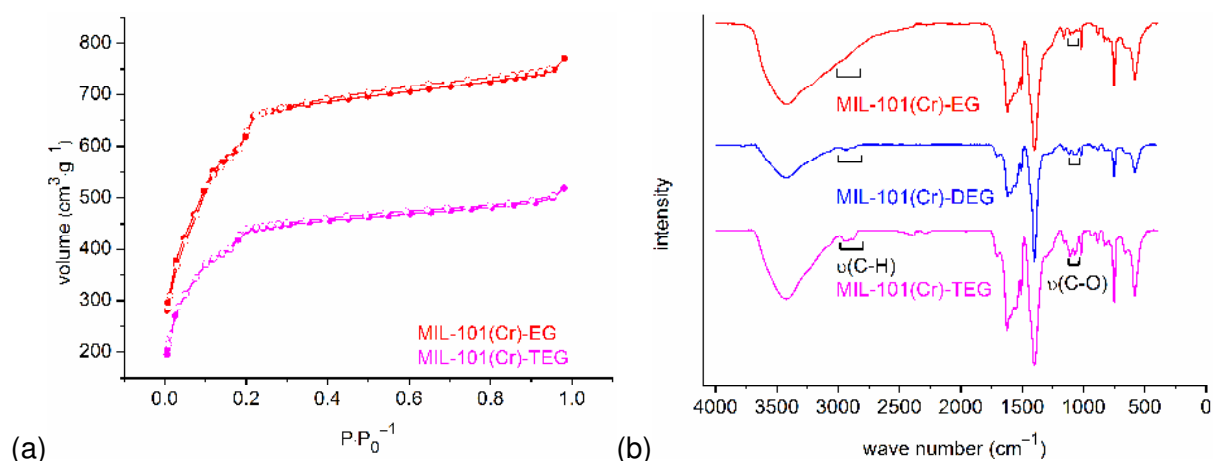


**Fig. 28.** (a)  $\text{N}_2$ -sorption isotherms of EG- and TEG-modified MIL-101(Cr) **after** water sorption measurement (degassing conditions: 2.5 h, 473 K. Adsorption is depicted with filled, desorption with empty symbols. (b) IR-spectra (KBr) of EG-, DEG- and TEG-modified MIL-101(Cr) **after** water sorption measurements.

In summary, successful grafting of MIL-101(Cr) with ethylene glycol, diethylene glycol and triethylene glycol was proven by infrared spectra and nitrogen sorption analyses without any change of the crystallinity of pure MIL-101(Cr). However, water sorption studies of glycol-modified MIL-101(Cr) have shown that the total water uptake capacities are largely reduced without any significant shifts of the water adsorption isotherms to lower partial pressures. Only TEG-modified MIL-101(Cr) shows a marginal improvement over native MIL-101(Cr), but only in a very small pressure range between  $0.30 < P \cdot P_0^{-1} < 0.36$ .

**Table 2.** Results from nitrogen and water sorption measurements (n.d. = not determined).

Compound	BET surface area ( $\text{m}^2 \cdot \text{g}^{-1}$ ) <sup>a</sup>	Total pore volume ( $\text{cm}^3 \cdot \text{g}^{-1}$ ) <sup>b</sup>	Water loading ( $\text{g} \cdot \text{g}^{-1}$ ) <sup>c</sup>	BET surface area ( $\text{m}^2 \cdot \text{g}^{-1}$ ) after single water sorption
MIL-101(Cr)	2630	1.27	1.02	-
MIL-101(Cr)-EG	1340	0.64	0.93	2320
MIL-101(Cr)-DEG	1110	0.55	0.55	n.d.
MIL-101(Cr)-TEG	1610	0.78	0.75	1560

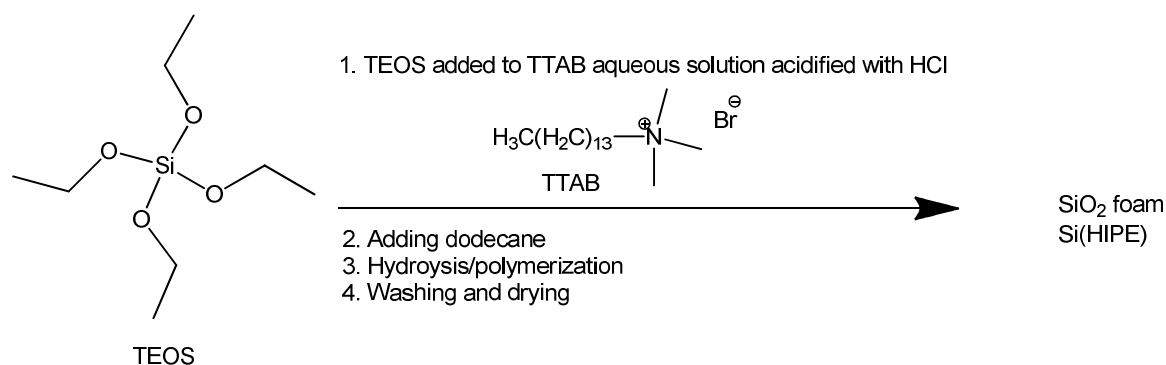
<sup>a</sup> BET surface area calculated at  $0.05 < P \cdot P_0^{-1} < 0.2$  from  $\text{N}_2$  sorption isotherm 77 K with a standard deviation  $\pm 20 \text{ m}^2 \cdot \text{g}^{-1}$ .

<sup>b</sup> calculated from  $\text{N}_2$  sorption isotherm at 77 K and  $P \cdot P_0^{-1} = 0.95$  for pores  $\leq 20 \text{ nm}$ .

<sup>c</sup> calculated from water sorption isotherm at 293 K and  $P \cdot P_0^{-1} = 0.9$ .

## 4.2 Meso-/Macroporous Si(HIPE)

As preliminary work to the MIL@Si(HIPE) composite materials, the synthesis of pure, meso-/macroporous Si(HIPE) was carried out according to the literature.<sup>230</sup> An aqueous solution, containing the surfactant tetradecyltrimethylammonium bromide (TTAB, 35 wt%), was prepared. After acidification with concentrated hydrochloric acid to initiate the hydrolysis of tetraethyl orthosilicate (TEOS), TEOS as silica precursor was added to the solution. The oily dodecane phase was slowly dropped into the aqueous solution followed by curing of the o/w emulsion for seven days at room temperature in an appropriate mold, yielding raw, white monoliths (Figure 29a). A consecutive washing procedure in deionized water and THF/acetone (1:1), followed by conventional drying in the oven led to a cracked, granulated material with pronounced shrinkage. An infrared spectrum of this material showed impurities of TTAB. Therefore the granules were further washed in DMF at 383 K followed by a final drying step at 463 K. A white, granulated Si(HIPE) material was obtained (Figure 29b). The reaction path is displayed in Scheme 3.



**Scheme 3.** Synthesis of Si(HIPE) foam using TEOS as the silica source. TTAB is used as surfactant, dodecane as the oily phase.

In contrast to the literature, in which scanning electron images predict a large void size distribution between 1–100  $\mu\text{m}$ , we observed macroporous voids with diameters in the narrow range of 4–8  $\mu\text{m}$  (Figure 29c-e).<sup>230</sup>

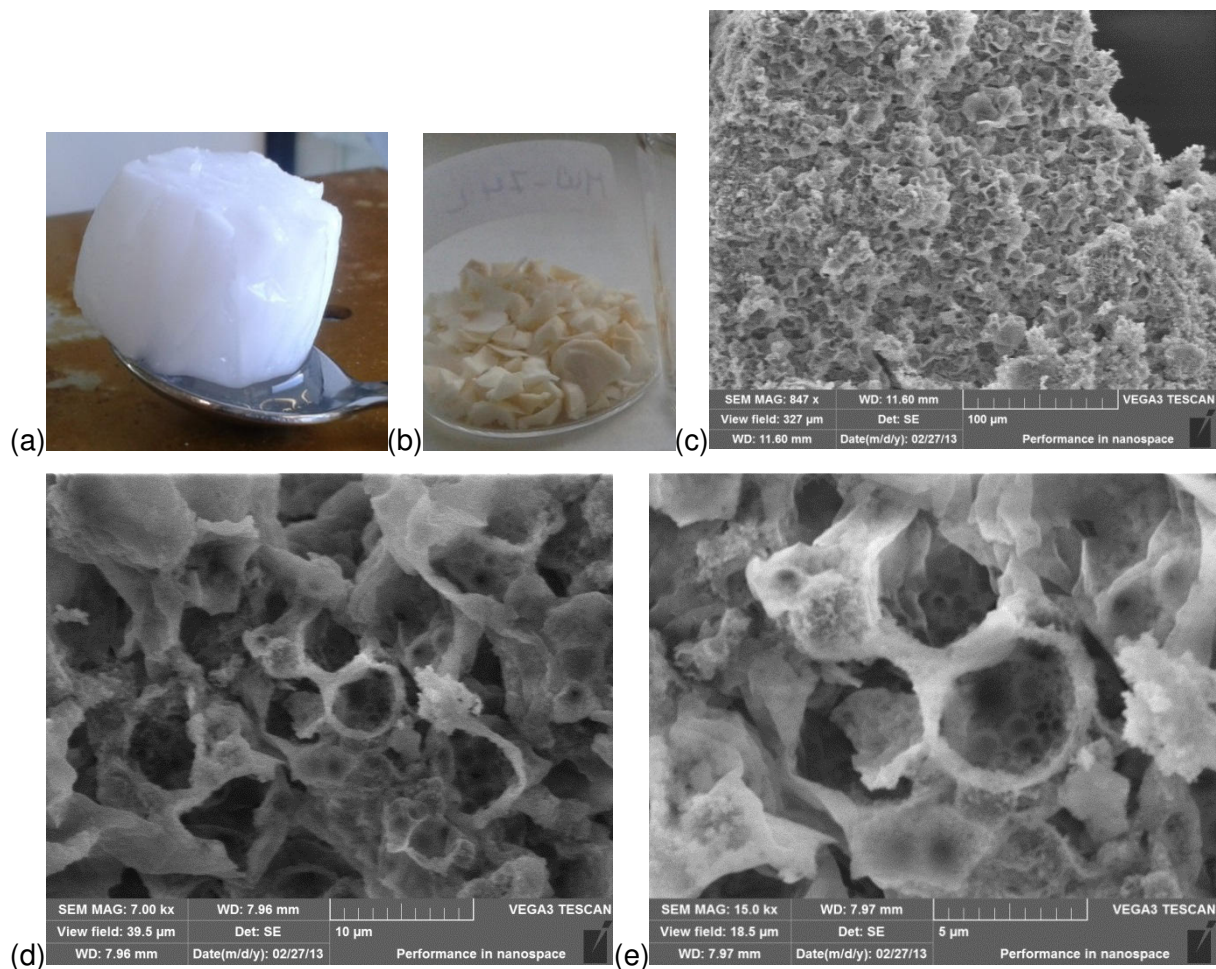


**Fig. 29.** (a) Monolithic Si(HIPE) material before washing steps (b) Granulated Si(HIPE) after washing and drying steps. (c)-(e) Scanning electron microscopic images of native Si(HIPE) (VEGA3 Easyprobe, Tescan).

Infrared data of native Si(HIPE) is shown in figure 30a. The region between  $3720$  and  $3020$   $\text{cm}^{-1}$  shows a broad band, attributed to  $\nu(\text{O-H})$  stretching vibration of physisorbed water in the HIPE pores and residual silanol groups  $\nu(\text{Si-OH})$ . The asymmetric  $\nu(\text{Si-O-Si})$  stretching vibration at  $1300\text{--}980$   $\text{cm}^{-1}$  shows the highest intensity due to the highly polar Si-O bond. Further typical vibration bands as the symmetric  $\nu(\text{Si-O-Si})$  ( $810$   $\text{cm}^{-1}$ ) and  $\delta_{\text{rocking}}(\text{Si-O-Si})$  ( $460$   $\text{cm}^{-1}$ ) band prove the presence of the anticipated functional groups. The infrared spectrum, which is identical to  $\text{SiO}_2$ , is in line with other literature data.<sup>231</sup>

Nitrogen sorption isotherm of pure Si(HIPE) reveals a high gas uptake of  $770$   $\text{cm}^3\cdot\text{g}^{-1}$  at  $P\cdot P_0^{-1} = 0.9$  (Figure 30b). The macroporous nature is illustrated by the type II shaped adsorption isotherm. A slight hysteresis loop between ad- and desorption branches presents some fraction of mesoporosity, typical for hierarchical Si(HIPE).<sup>230,231</sup> The BET surface area of  $900$   $\text{m}^2\cdot\text{g}^{-1}$  is higher, compared to other published data only presenting surface areas ranging between  $620\text{--}820$   $\text{m}^2\cdot\text{g}^{-1}$ .<sup>230,231</sup> This is probably attributed to the extensive washing



procedure. Figure 30c shows the water uptake property of pure Si(HIPE). Similar to classical silica gels, the adsorption isotherm is almost linear. Due to the high inner surface, the material shows a high water uptake of  $0.35 \text{ g}\cdot\text{g}^{-1}$  at a relative humidity of  $P\cdot P_0^{-1} = 0.9$ .<sup>23,133</sup>

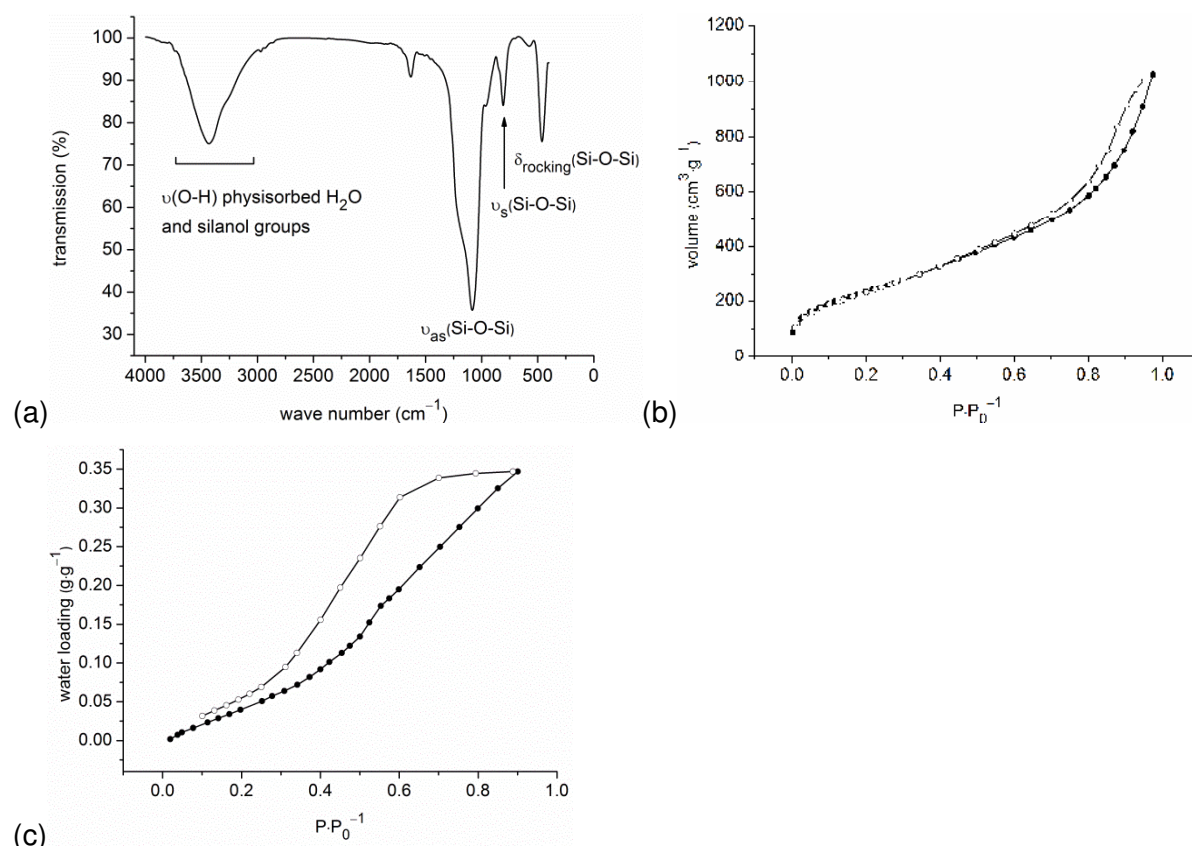


**Fig. 30.** (a) IR-spectra (KBr) of native Si(HIPE). (b) N<sub>2</sub>-sorption isotherm of native Si(HIPE) (degassing conditions: 2 h, 463 K). (c) Water sorption isotherm of pure Si(HIPE) (degassing conditions: 2 h, 463 K). Adsorption is depicted with filled, desorption with empty symbols.

In summary, pure Si(HIPE) with meso- and macroporous behavior was obtained with higher BET surface areas compared to other reports. Unfortunately, raw Si(HIPE) undergoes large shrinkage during the drying process. Conventional evaporation of water at atmospheric pressure causes drastic changes in the surface tension of the solvent upon formation of the liquid-vapor interface. This effect probably leads to a collapse of the pore structure accompanied by shrinkage of the pristine, wet monolith. Supercritical CO<sub>2</sub> drying should certainly lead to intact monolithic, crack-free structures, which has not been mentioned by Backov et al.<sup>230</sup>

**Table 3.** Results from nitrogen and water sorption measurements.

	BET surface area ( $\text{m}^2 \cdot \text{g}^{-1}$ ) <sup>a</sup>	Total pore volume ( $\text{cm}^3 \cdot \text{g}^{-1}$ ) <sup>b</sup>	Water loading ( $\text{g} \cdot \text{g}^{-1}$ ) <sup>c</sup>
Si(HIPE)	900	1.41	0.35

<sup>a</sup> BET surface area calculated at  $0.05 < P \cdot P_0^{-1} < 0.2$  from  $\text{N}_2$  sorption isotherm 77 K with a standard deviation  $\pm 20 \text{ m}^2 \cdot \text{g}^{-1}$ .

<sup>b</sup> calculated from  $\text{N}_2$  sorption isotherm at 77 K and  $P \cdot P_0^{-1} = 0.95$  for pores  $\leq 20 \text{ nm}$ .

<sup>c</sup> calculated from water sorption isotherm at 293 K and  $P \cdot P_0^{-1} = 0.9$ .

### 4.2.1 MIL-101(Cr)@Si(HIPE) (Route A)

MIL-101(Cr)@Si(HIPE) composites were synthesized through a modified procedure of the pure Si(HIPE) synthesis. Various amounts of purified MIL-101(Cr) powders were added to the reaction mixture of Si(HIPE) during the synthesis, labeled as route A. At different points of time, the MIL powders were added in order to investigate the influences on the BET surface areas and accessibility of the MIL pores in the composites. MIL-101(Cr)@Si(HIPE) were synthesized in three different ways: MIL-101(Cr) powders were added (i) before addition of hydrochloric acid *MIL-101(Cr)@Si(HIPE)-before HCl*, (ii) after addition of TEOS *MIL-101(Cr)@Si(HIPE)-after TEOS* and (iii) after adding the oily dodecane phase *MIL-101(Cr)@Si(HIPE)-after dodecane*. '50' and '100', in round brackets, stand for the weight of MIL-101(Cr) powder in mg, which was used in the synthesis. Washing and drying steps were carried out according to the synthesis of pure Si(HIPE).

Although pure Si(HIPE) exhibits shrinkage during the drying process, MIL particles, which were added during the HIPE synthesis, should hopefully lead to monolithic structures with less shrinking during the drying steps. The embedded MIL particles should help to withstand the capillary forces during the drying procedure. Against our expectations, shrinkage could not be avoided as shown in figure 31a-b. The monolithic composites shrink largely during drying to broken materials, which are full of cracks, exemplarily shown for MIL-101(Cr)(50)@Si(HIPE)-after dodecane.

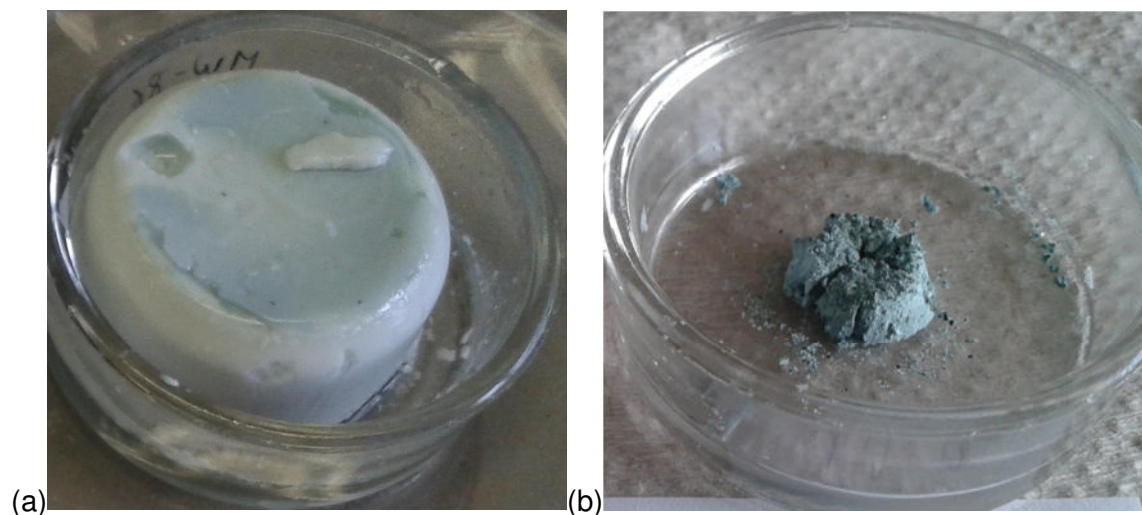


**Fig. 31.** (a) MIL-101(Cr)(50)@Si(HIPE)-after dodecane before washing steps (b) and after washing and drying steps (synthesized via route A). The large extent of shrinkage, creating pronounced cracks in the monolith, is apparent.

Scanning electron microscopic images of MIL-101(Cr)(100)@Si(HIPE) reveal that the original HIPE void sizes (4–8  $\mu\text{m}$ ) are reduced to 0.5–2  $\mu\text{m}$ , which is possibly influenced by the

addition of MIL particles (Figure 32a-b). Octahedral MIL-101(Cr) crystals with diameters of 300–500 nm adhere on the HIPE surface.<sup>232</sup>

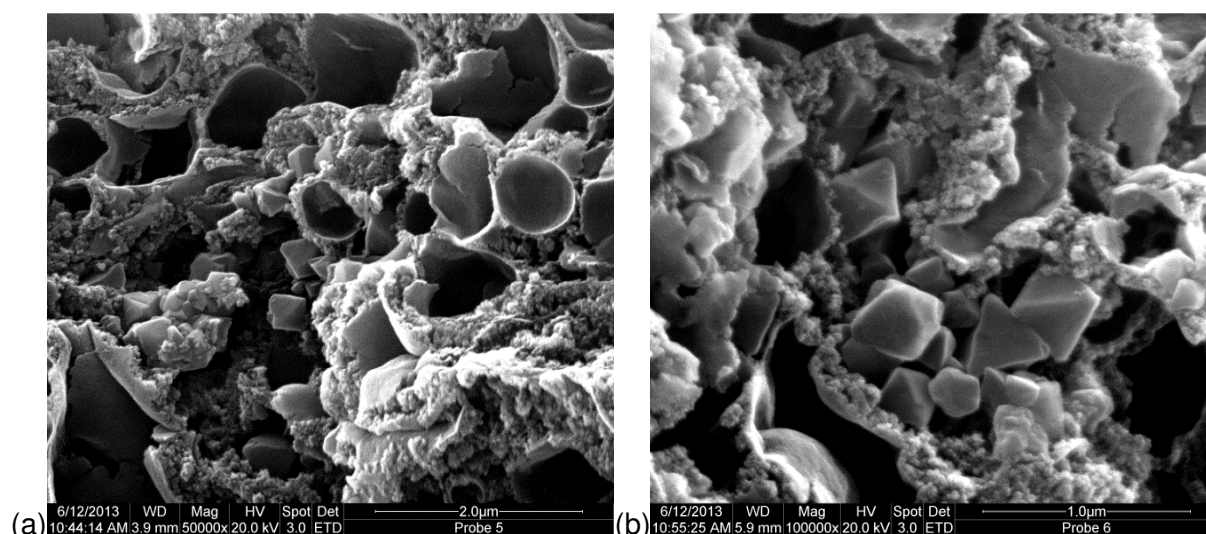


**Fig. 32.** (a)-(b) Scanning electron microscopic images of MIL-101(Cr)(100)@Si(HIPE)-after HCl (Quanta 400 FEG, Fei).

Powder patterns show the presence of crystalline MIL-101(Cr) in the composites, which is presented for MIL-101(Cr)(50/100)@Si(HIPE)-after dodecane (Figure 33a). Increasing the loading of MIL-101(Cr) changes the intensities of the reflections in the PXRD patterns from broad (50) to relatively sharp reflections (100). Infrared spectra of MIL-101(Cr)(50/100)@Si(HIPE)-after dodecane display the increasing asymmetric valence  $\nu(\text{R-CO}_2^-)$ , deformation  $\delta(\text{R-CO}_2^-)$  and stretching  $\nu(\text{Cr-O})$  vibrations of MIL-101(Cr) with increasing amount of embedded MIL, highlighted by square brackets (Figure 33b).

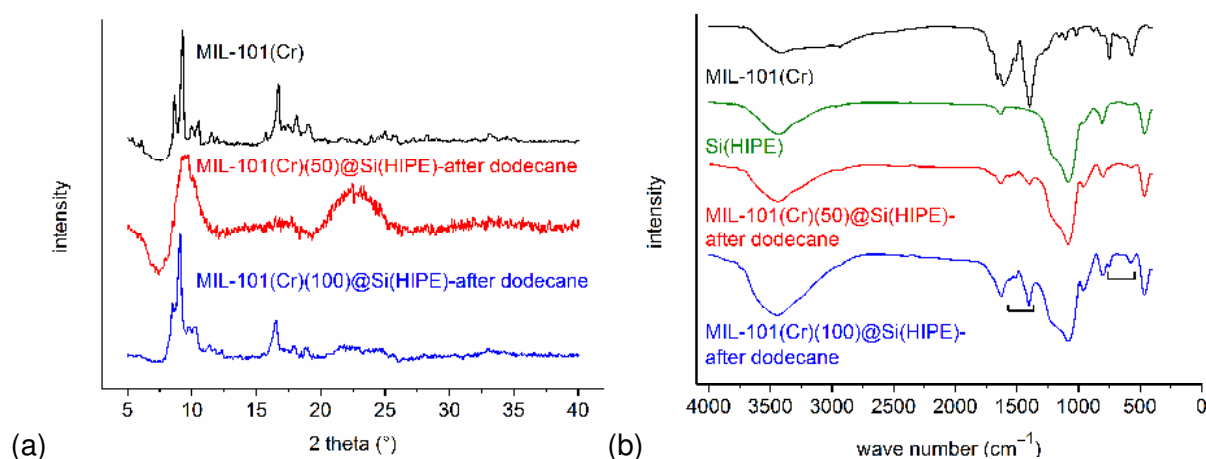


**Fig. 33.** (a) PXRD patterns of native MIL-101(Cr) and MIL-101(Cr)(50/100)@Si(HIPE)-after dodecane. (b) IR-spectra (KBr) of native MIL-101(Cr), native Si(HIPE) and MIL-101(Cr)(50/100)@Si(HIPE)-after dodecane. Square brackets highlight the bands of MIL-101(Cr) in the composite material.

Pore size distribution curves of MIL-101(Cr)(100)@Si(HIPE) composites, calculated from nitrogen sorption isotherms, show more pronounced and distinguishable MIL pores in the region of 15–25 Å with later addition of the MIL particles (Figure 34b). Nitrogen sorption isotherm of MIL-101(Cr)(100)@Si(HIPE)-before HCl, which shows a typical macroporous type II shape just like pure Si(HIPE), exhibits the highest nitrogen uptake over the entire pressure range among the MIL-101(Cr)(100)@Si(HIPE) composites (Figure 34a). The total nitrogen uptakes are decreased over the whole pressure range with later addition of MIL powder. The later addition probably leads to denser composites, which is in line with the reduced HIPE voids proven by SEM images (Figure 32).

BET surface areas of the composites show that the later addition of MIL-101(Cr) leads to a decrease of the surface areas and total pore volumes for same MIL loadings (e.g. 1370/1260/960 m<sup>2</sup>·g<sup>-1</sup> for MIL-101(Cr)(100)@Si(HIPE)-before HCl/-after TEOS/-after dodecane). If the amount of MIL powder is increased from 50 to 100 mg at the same time of MOF addition ('before HCl', 'after TEOS' or 'after dodecane'), the surface areas and total pore volumes are enlarged in the same way (e.g. 1020 m<sup>2</sup>·g<sup>-1</sup> for MIL-101(Cr)(50)@Si(HIPE)-before HCl and 1370 m<sup>2</sup>·g<sup>-1</sup> for MIL-101(Cr)(100)@Si(HIPE)-before HCl) (Table 4).

A longer stirring time of the HIPE (equivalent to a later addition of MIL) was expected to lead to an advanced state of HIPE polymerization/curing. These longer silica-oligomer and –polymer chains should be more hindered to diffuse into the MIL pores compared to shorter silica oligomers, hopefully yielding more porous composites. The later addition of MIL-101(Cr) to the HIPE reaction mixture was expected to yield composites with increased nitrogen uptakes, higher BET surface areas and more accessible MIL pores for the same MIL loading. Although the pore size distribution curves prove this statement (Figure 34b), BET surface areas reveal that the later addition leads to less porous composites.

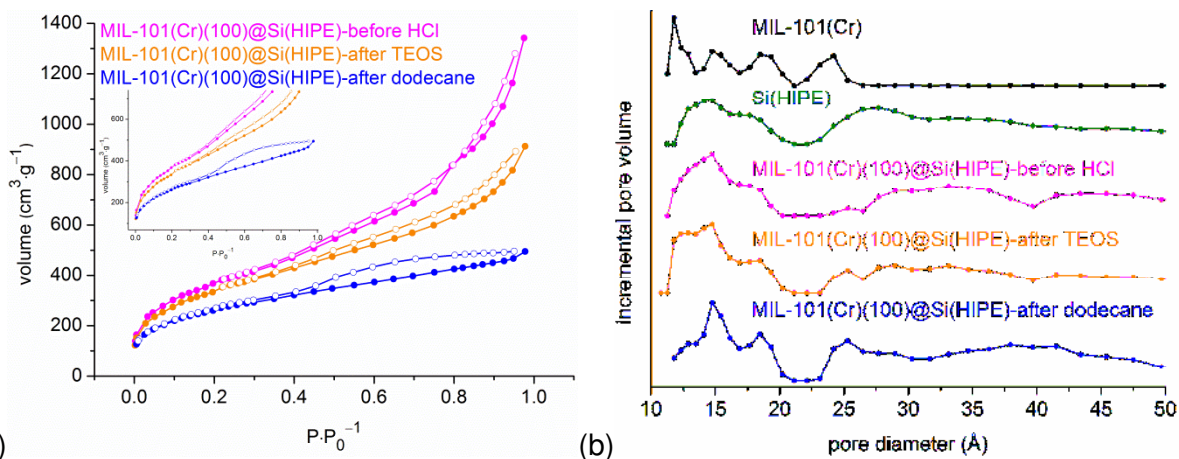


**Fig. 34.** (a)  $N_2$ -sorption isotherms of MIL-101(Cr)(100)@Si(HIPE)-X, X = before HCl, after TEOS, after dodecane (degassing conditions: 2 h, 463 K). Adsorption is depicted with filled, desorption with empty symbols. (b) Pore size distribution curves of native MIL-101(Cr), native Si(HIPE) and MIL-101(Cr)(100)@Si(HIPE)-X, X = before HCl, after TEOS, after dodecane.

To sum up the results, monolithic MIL-101(Cr)@Si(HIPE) structures could not be obtained via the direct route A due to large shrinking effects during drying. Supercritical  $CO_2$  drying could possibly avoid this problem. The presence of MIL particles was proven by powder patterns, infrared spectra and SEM images, but nitrogen sorption analyses of the composites reveal that the later addition of MOF powder yields denser and less porous composites with relatively low BET surface areas in contrast to our expectations.

**Table 4.** Results from nitrogen measurements of MIL@Si(HIPE) composites from route A.

	BET surface area ( $m^2 \cdot g^{-1}$ ) <sup>a</sup>	Total pore volume ( $cm^3 \cdot g^{-1}$ ) <sup>b</sup>
MIL-101(Cr)	3060	1.45
Si(HIPE)	900	1.41
MIL-101(Cr)(X)-Y		
X = 50, Y = before HCl	1020	1.59
X = 100, Y = before HCl	1370	1.80
X = 50, Y = after TEOS	1140	1.11
X = 100, Y = after TEOS	1260	1.26
X = 50, Y = after dodecane	760	0.57
X = 100, Y = after dodecane	960	0.72

<sup>a</sup> BET surface area calculated at  $0.05 < P \cdot P_0^{-1} < 0.2$  from  $N_2$  sorption isotherm 77 K with a standard deviation  $\pm 20 m^2 \cdot g^{-1}$ .

<sup>b</sup> calculated from  $N_2$  sorption isotherm at 77 K and  $P \cdot P_0^{-1} = 0.95$  for pores  $\leq 20$  nm.

### 4.2.2 MIL-100(Cr)/101(Cr)@Si(HIPE) (Route B)

MIL-101(Cr)@Si(HIPE) composites, synthesized via the direct route A, exhibit relatively low BET surface areas possibly due to a large extent of MIL pore blocking effects through silica mono- and oligomers. Hence, the alternative *in situ* route B was applied to maximize the BET surface areas. In addition to MIL-101(Cr), another water stable MOF, MIL-100(Cr), was incorporated into the pure Si(HIPE) material by the *in situ* method (route B).

The syntheses of MIL@Si(HIPE)-hydrothermal composites (in short: MIL@Si(HIPE)-ht) via route B were done according to the following procedure: Pre-formed Si(HIPE) granulates were firstly soaked with MIL precursors (metal source, ligand) in deionized water for at least 19 hours at ambient temperature to guarantee that the HIPE pores are fully saturated with MOF starting materials. The whole reaction slurries were then put into Teflon-liners, which were fixed into steel autoclaves, followed by hydrothermal treatment at the required temperature program for the appropriate MOF. MIL@Si(HIPE)-ht composites were isolated from the separately formed MIL powders and the products (composites and pure MIL powders) were consecutively and separately washed in DMF, ethanol and deionized water. After drying granulated composites, named as *MIL-100(Cr)@Si(HIPE)-hydrothermal* and *MIL-101(Cr)@Si(HIPE)-hydrothermal* were obtained. Separately formed MIL powders are labeled as *MIL-100(Cr)-residual* and *MIL-101(Cr)-residual*. Images of native Si(HIPE) and granulated MIL-101(Cr)@Si(HIPE)-hydrothermal are depicted in Figure 35a-b.

A scanning electron microscopic image of MIL-101(Cr)@Si(HIPE)-ht shows that the original morphology of pure Si(HIPE) is drastically changed after hydrothermal treatment. The original voids of pure Si(HIPE) with 4–8  $\mu\text{m}$  are reduced severely to non-spherical voids of 0.3–0.5  $\mu\text{m}$  most likely due to occupation of MIL particles on the HIPE surface. Isolated MIL-101(Cr) particles with diameters of 300–500 nm, which adhere on the Si(HIPE) surface, rarely show the typical octahedral shape.<sup>232</sup>

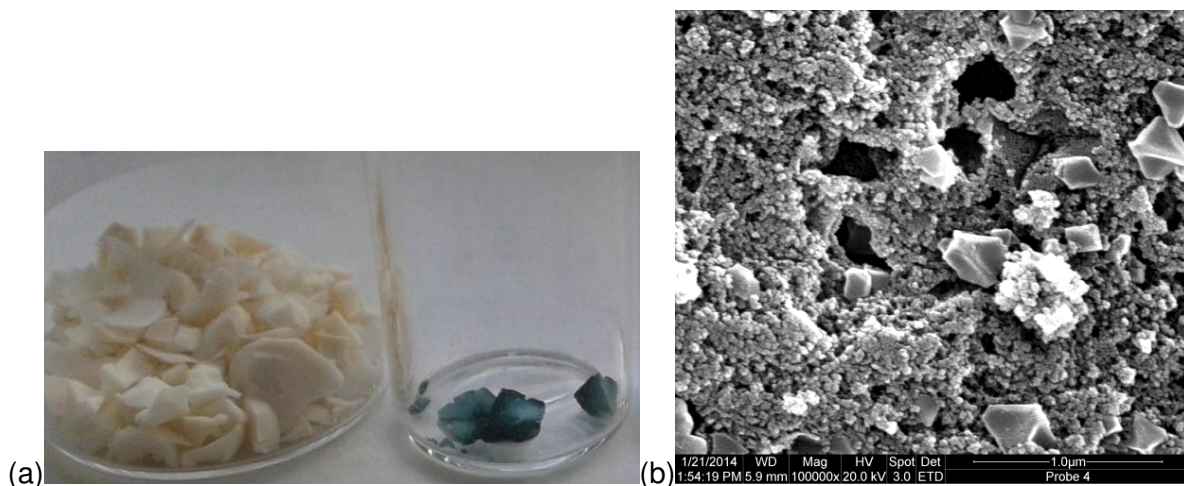


**Fig. 35.** (a) Native Si(HIPE) (left) and MIL-101(Cr)@Si(HIPE)-hydrothermal (right) synthesized via route B. (b) Scanning electron microscopic images of MIL-101(Cr)@Si(HIPE)-hydrothermal (LEO 1430 VP, Zeiss).

Figure 36a presents that the crystalline MIL-100/101(Cr) phases can be identified in MIL@Si(HIPE)-ht composites, but only for low diffraction angles up to  $2\theta = 13^\circ$ . Asymmetric valence  $\nu(\text{R-CO}_2)$ -, deformation  $\delta(\text{R-CO}_2)$ - and stretching  $\nu(\text{Cr-O})$  vibrations of the incorporated MILs are highlighted by square brackets in the infrared spectra (Figure 36b).

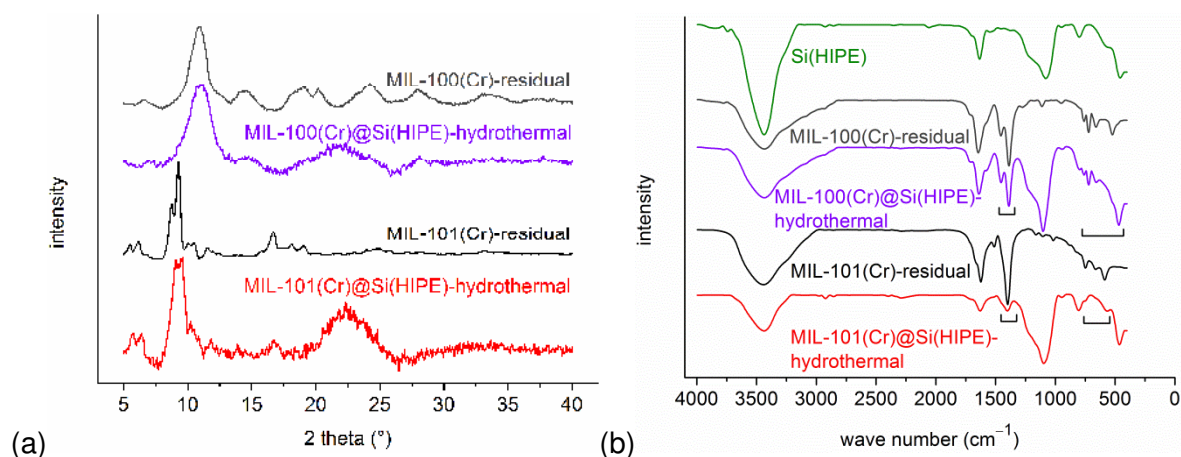


**Fig. 36.** (a) PXRD patterns of MIL-residual and MIL@Si(HIPE)-hydrothermal (MIL = MIL-100(Cr), MIL-101(Cr)). (b) IR-spectra (KBr) of native Si(HIPE), MIL-residual and MIL@Si(HIPE)-hydrothermal (MIL = MIL-100(Cr), MIL-101(Cr)). Square brackets highlight the bands of the MILs in the composite material.

Nitrogen sorption isotherms of both MIL@Si(HIPE)-ht composites present typical type II shapes, indicating mostly macroporous behavior (Figure 37a,c). A steep rise of the adsorption isotherms, which indicates the presence of a large amount of micropores as in MIL-100/101(Cr)-residual, is absent. Nevertheless, pore size distribution curves of the composites show the presence of some micropores in the region of 15–25 Å (Figure 37b,d). The BET surface areas of MIL-residual with  $1440 \text{ m}^2\cdot\text{g}^{-1}$  (MIL-100(Cr)-residual) and  $2830$



$\text{m}^2\cdot\text{g}^{-1}$  (MIL-101(Cr)-residual) show reasonable inner surfaces when compared to literature ranges of 1770–1980  $\text{m}^2\cdot\text{g}^{-1}$  for MIL-100(Cr) and 2060–4100  $\text{m}^2\cdot\text{g}^{-1}$  for MIL-101(Cr).<sup>150,151,236,237</sup> MIL@Si(HIPE)-ht with 510  $\text{m}^2\cdot\text{g}^{-1}$  (MIL-100(Cr)@Si(HIPE)-ht) and 860  $\text{m}^2\cdot\text{g}^{-1}$  (MIL-101(Cr)@Si(HIPE)-ht) show even lower BET surface areas compared to native Si(HIPE) (900  $\text{m}^2\cdot\text{g}^{-1}$ ) (Table 5). One possible explanation would be that unreacted MOF precursors (metal salt and ligand) are still located in the HIPE- and/or MIL pores, which could not be washed out by the activation steps. Another explanation is that the MIL crystals, which have been *in situ* synthesized interiorly in the HIPE macropores exhibit a low degree of crystallinity. The PXRD pattern and SEM image of MIL-101(Cr)@Si(HIPE)-hydrothermal support this statement. Compared to MIL particles, synthesized in ‘free space’ without steric limitation, the quality of the MIL-101(Cr) crystals located in the Si(HIPE) material seems to be rather low.<sup>232</sup>

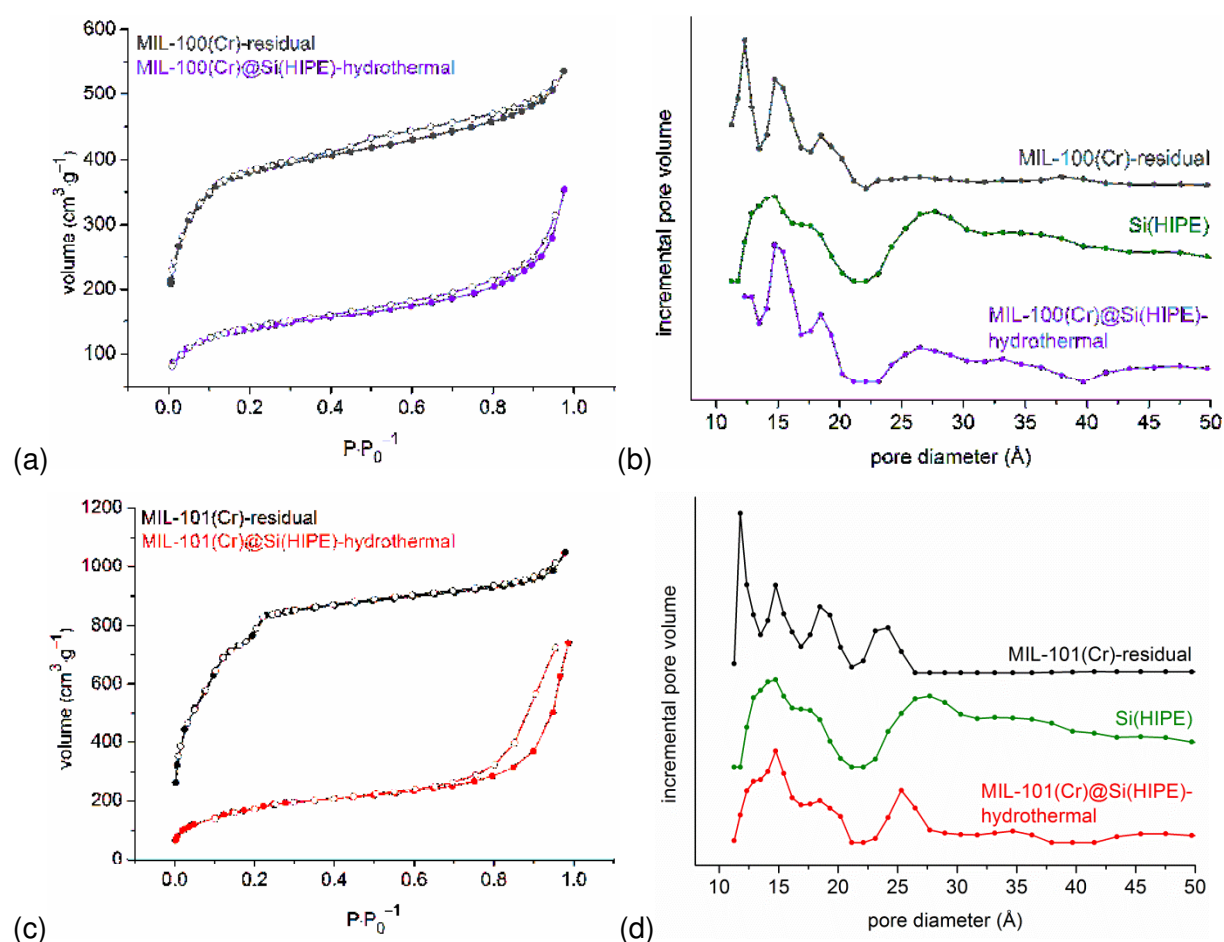


**Fig. 37.** (a) N<sub>2</sub>-sorption isotherms of MIL-100(Cr)-residual and MIL-100(Cr)@Si(HIPE)-hydrothermal (degassing conditions: 2 h, 463 K). Adsorption is depicted with filled, desorption with empty symbols. (b) Pore size distribution curves of MIL-100(Cr)-residual, Si(HIPE) and MIL-100(Cr)@Si(HIPE)-hydrothermal. (c) N<sub>2</sub>-sorption isotherms of MIL-101(Cr)-residual and MIL-101(Cr)@Si(HIPE)-hydrothermal (degassing conditions: 2 h, 463 K). (d) Pore size distribution curves of MIL-101(Cr)-residual, Si(HIPE) and MIL-101(Cr)@Si(HIPE)-hydrothermal.

In spite of the relatively low BET surface areas of both composites, water sorption measurements show that adsorption isotherms of MIL@Si(HIPE)-ht could be shifted to lower relative pressures compared to the native HIPE probably due to the presence of micropores in the composites (Figure 38). Adsorption isotherms of MIL@Si(HIPE)-ht exhibit higher slopes in the regions of  $0.25 < P \cdot P_0^{-1} < 0.37$  (for MIL-100(Cr)) and  $0.38 < P \cdot P_0^{-1} < 0.53$  (for MIL-101(Cr)) in comparison to native HIPE.

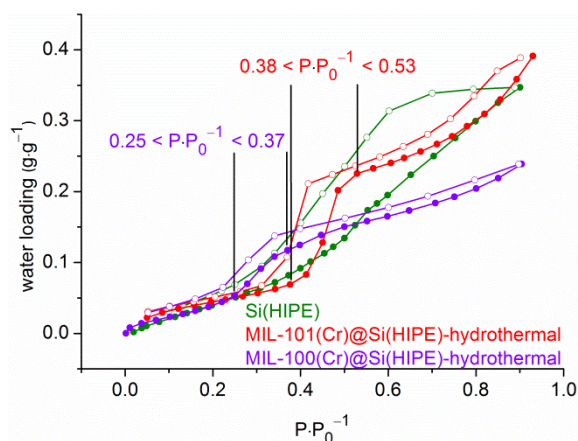


**Fig. 38.** Water sorption isotherms of pure Si(HIPE), MIL-101(Cr)@Si(HIPE)-hydrothermal and MIL-100(Cr)@Si(HIPE)-hydrothermal (degassing conditions: 2 h, 463 K). Adsorption is depicted with filled, desorption with empty symbols.

In conclusion, MIL@Si(HIPE)-ht composites, consisting of MIL-100(Cr) and MIL-101(Cr), could be obtained as green granulated materials via the *in situ* route (route B). The successful embedding could be proven by powder patterns, infrared spectra and scanning electron microscopic images. The crystallinity of the incorporated MILs, especially for MIL-101(Cr), seems to be rather low. Nitrogen sorption data of the composites reflects mostly macroporous behavior with a small amount of MIL micropores. The presence of micropores explains the partially increased hydrophilicity shown by water sorption isotherms. BET surface areas could not be maximized in comparison to route A (section 3.2). Table 5 sums up the results from nitrogen and water sorption measurements.

**Table 5.** Results from nitrogen and water sorption measurements for MIL@Si(HIPE) composites from route B (n.d. = not determined).

	BET surface area ( $\text{m}^2 \cdot \text{g}^{-1}$ ) <sup>a</sup>	Total pore volume ( $\text{cm}^3 \cdot \text{g}^{-1}$ ) <sup>b</sup>	Water loading ( $\text{g} \cdot \text{g}^{-1}$ ) <sup>c</sup>
Si(HIPE)	900	1.41	0.35
MIL-100(Cr)-residual	1440	0.78	n.d.
MIL-100(Cr)@Si(HIPE)-ht	510	0.43	0.24
MIL-101(Cr)-residual	2830	1.39	n.d.
MIL-101(Cr)@Si(HIPE)-ht	860	0.97	0.37

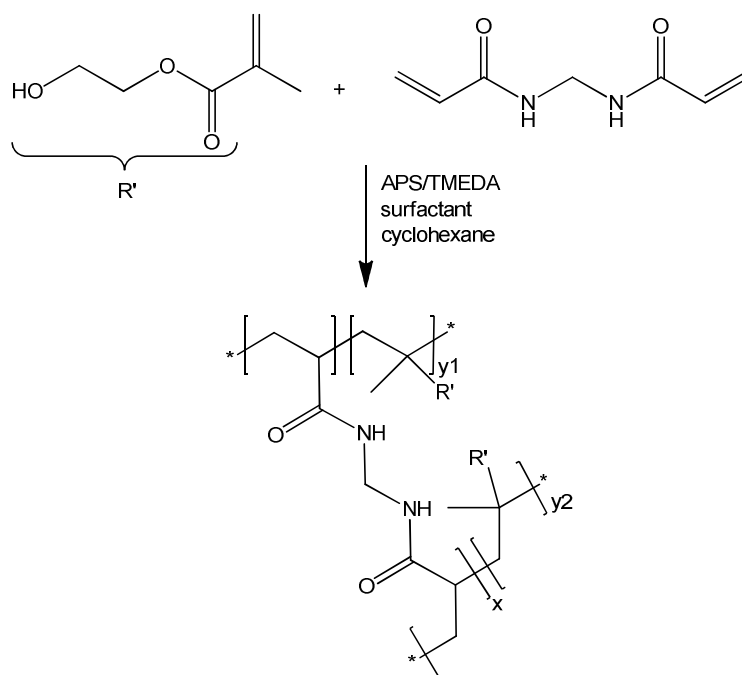
<sup>a</sup> BET surface area calculated at  $0.05 < P \cdot P_0^{-1} < 0.2$  from  $\text{N}_2$  sorption isotherm 77 K with a standard deviation  $\pm 20 \text{ m}^2 \cdot \text{g}^{-1}$ .

<sup>b</sup> calculated from  $\text{N}_2$  sorption isotherm at 77 K and  $P \cdot P_0^{-1} = 0.95$  for pores  $\leq 20 \text{ nm}$ .

<sup>c</sup> calculated from water sorption isotherm at 293 K and  $P \cdot P_0^{-1} = 0.9$ .

### 4.3 Macroporous Poly(HEMA)HIPE

Preparation of monolithic, native poly(HEMA)HIPE was done according to the literature.<sup>192</sup> 2-Hydroxyethyl methacrylate, as the monomer, was cross-linked with *N,N'*-methylenebisacrylamide. Monolithic HIPE structures were obtained with 13, 20 and 30 mol% of MBA by simply increasing the amount of cross-linker during the synthesis. The corresponding radical polymerization is shown in Scheme 4.



**Scheme 4.** Radical polymerization of 2-hydroxyethyl methacrylate (HEMA) and *N,N'*-methylenebisacrylamide (MBA) initiated by ammonium persulfate (APS) ( $x = 13, 20$  or  $30$  mol%,  $y_1 + y_2 = 87, 80$  or  $70$  mol%).

An aqueous solution, containing 2-hydroxyethyl methacrylate and the cross-linker MBA was prepared. Ammonium persulfate as the radical initiator and the surfactant Kolliphor® P188 (poly(ethylene glycol)-*block*-poly(propylene glycol)-*block*-poly(ethylene glycol)) were added to the continuous, aqueous phase. Cyclohexane, as the oily phase, was slowly dropped into the solution, creating an o/w emulsion. The addition of *N,N,N',N'*-tetramethylethylenediamine, as the second component for the redox initiation process, was necessary for an effective curing of the emulsion. After curing for three days in an appropriate mold at room temperature, followed by washing and drying, mechanically stable, rigid and white monoliths could be obtained in different shapes (Figure 39a-c).

Scanning electron microscopic images for 13, 20 and 30 mol% of cross-linked materials reveal the typical, macroporous morphology, known for HIPE systems (Figure 39d-f). The size of the voids and connecting windows of 2–6  $\mu\text{m}$  and 1–2  $\mu\text{m}$  is in line with other

literature data and seems to be independent of the amount of cross-linker.<sup>192,195</sup> This is in contrast to other known HIPE systems, where an increasing amount of cross-linker leads to an enlargement of the size of voids and connecting windows.<sup>233</sup>

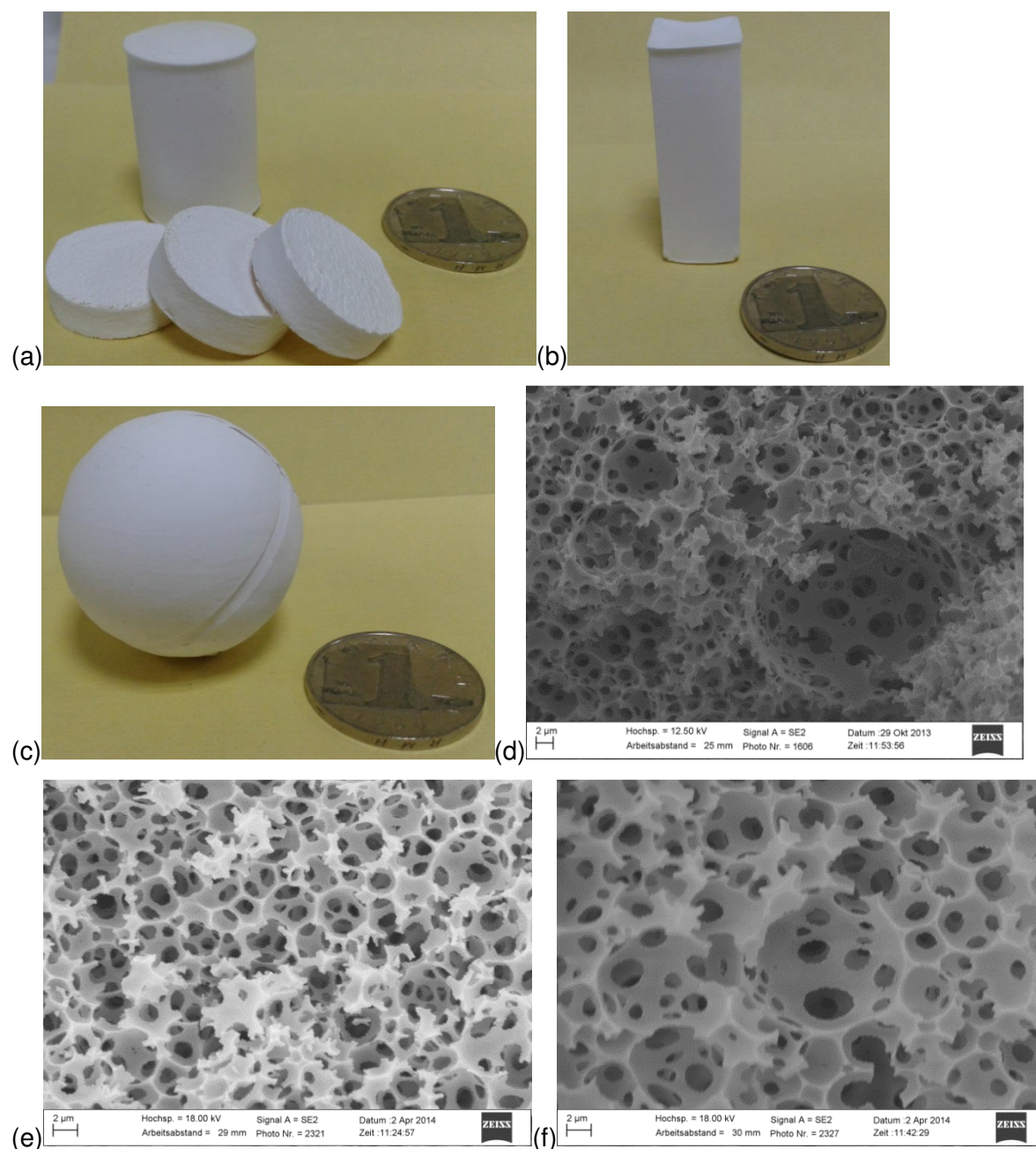


**Fig. 39.** (a)-(c) Native poly(HEMA)HIPE (13 mol% MBA) in various shapes. A ‘1 Yuan’ coin, shown in the figures, is intended for the time in Wuhan (China), where this synthetic work had been carried out. The ‘1 Yuan’ coin has approximately the same size as a ‘2 Euro’ coin. The final monoliths can be easily cut with a sharp knife. Scanning electron microscopic images of poly(HEMA)HIPEs with (d) 13 mol%, (e) 20 mol% and (f) 30 mol% *N,N'*-methylenebisacrylamide (LEO 1430 VP, Zeiss).

The increasing amount of MBA cross-linker is evidenced by infrared spectroscopic data (Figure 40). The intensities of the  $\delta(\text{N-H})$  deformation vibration (N-H functional groups are

only present in MBA) are relatively enlarged, compared to the intensities of the  $\delta(\text{C-H})$  deformation vibration (present in both monomers), by increasing the amount of MBA from 13 over 20 to 30 mol%.

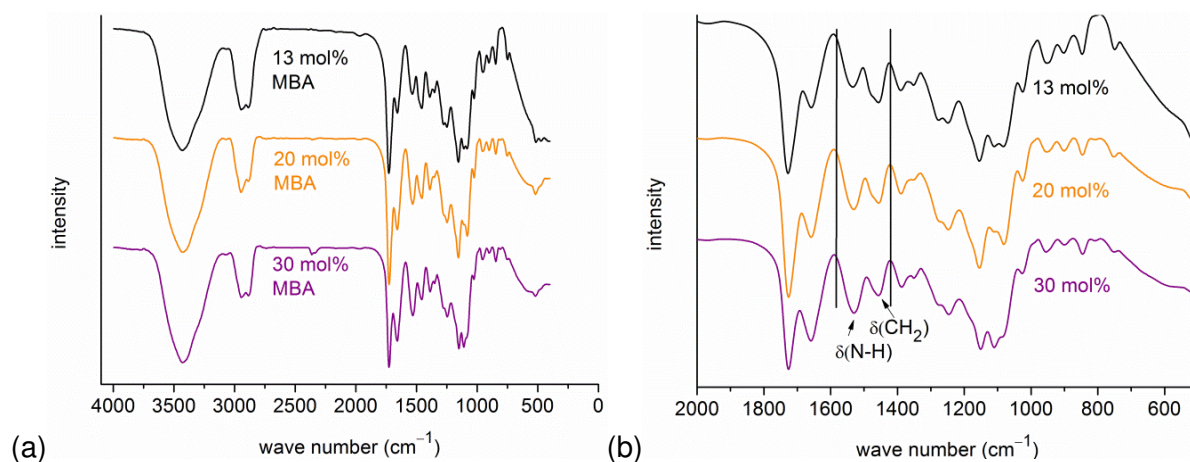


**Fig. 40.** (a) IR-spectra (KBr) of native poly(HEMA)HIPEs with 13, 20 and 30 mol% of MBA. (b) Enlargement for region 2000–600  $\text{cm}^{-1}$ .

A complete analytical characterization of the native poly(HEMA)HIPE can be found in section 3.2, consisting of infrared data, nitrogen, water and methanol sorption experiments, thermogravimetric analysis and pore size distribution from nitrogen sorption data. Essential results calculated from nitrogen and water sorption measurements, such as BET surface area, total pore volume and water loading capacity, are displayed in Table 6. The BET surface area of  $60 \text{ m}^2 \cdot \text{g}^{-1}$  is in the typical range for HIPE systems due to their macroporous nature.

**Table 6.** Results from nitrogen and water sorption measurements.

	BET surface area ( $\text{m}^2 \cdot \text{g}^{-1}$ ) <sup>a</sup>	Total pore volume ( $\text{cm}^3 \cdot \text{g}^{-1}$ ) <sup>b</sup>	Water loading ( $\text{g} \cdot \text{g}^{-1}$ ) <sup>c</sup>
Poly(HEMA)HIPE (13 mol% MBA)	60	0.05	0.16

<sup>a</sup> BET surface area calculated at  $0.05 < P \cdot P_0^{-1} < 0.2$  from  $\text{N}_2$  sorption isotherm 77 K with a standard deviation  $\pm 20 \text{ m}^2 \cdot \text{g}^{-1}$ .

<sup>b</sup> calculated from  $\text{N}_2$  sorption isotherm at 77 K and  $P \cdot P_0^{-1} = 0.95$  for pores  $\leq 20 \text{ nm}$ .

<sup>c</sup> calculated from water sorption isotherm at 293 K and  $P \cdot P_0^{-1} = 0.9$ .

### 4.3.1 MIL-100(Fe,Cr)/101(Cr)@HEMA (Route B)

Section 3.2 in this work describes the syntheses and the analytical characterization of different MIL-101(Cr)@(HEMA)HIPE composites, which were synthesized via route A. By simply adding MIL-101(Cr) powder to the pre-polymerized HEMA-HIPE emulsion, monolithic composites with maximized porosities and high vapor uptakes (H<sub>2</sub>O, MeOH) could be obtained. However, the estimated BET surface areas, based on the weight% of MIL-101(Cr) in the composites, could not be achieved due to partial blocking of the MIL pores through HIPE monomers. Therefore, the alternative *in situ* route B was chosen in order to further maximize the BET surface areas. In addition to MIL-101(Cr), other water stable MOFs like MIL-100(Fe) and MIL-100(Cr) were embedded into the poly(HEMA)HIPE template by the *in situ* method (route B).

The syntheses of MIL@poly(HEMA)HIPE-hydrothermal (in short MIL@HEMA) composites via route B were done according to the following procedure: Pre-formed native poly(HEMA)HIPE monoliths (13 mol% MBA) were firstly stirred in MIL precursors (metal source, ligand) in deionized water for at least 20 hours at room temperature to ensure that the HIPE pores were fully soaked with MOF starting materials. The whole reaction slurries were then transferred into Teflon-liners, which were put into steel autoclaves, followed by hydrothermal treatment at the needed temperature for the corresponding MOF. The obtained composites were separated from the excessive MIL powders and both products were consecutively and separately washed in DMF, ethanol and deionized water. After drying monolithic composites, labeled as *MIL-100(Fe)@HEMA*, *MIL-100(Cr)@HEMA* and *MIL-101(Cr)@HEMA* were obtained (Figure 41). Excessive MIL powders are named as *MIL-100(Fe)-residual*, *MIL-100(Cr)-residual* and *MIL-101(Cr)-residual*. Loading of the MILs in MIL@HEMA composites was estimated gravimetrically,<sup>IV</sup> assuming no MOF powder is lost during the syntheses, and additionally by AAS spectroscopy. MIL-100(Fe)@HEMA incorporates 54/58 wt% of MIL-100(Fe). In the cases of MIL-100(Cr)@HEMA and MIL-101(Cr)@HEMA, the MIL loadings are 91/93 wt% and 89/91 wt% respectively. The first value corresponds to gravimetrical analyses, the second to AAS measurements (Table 7).

<sup>IV</sup> Formula for gravimetrical quantification of MIL loading in MIL@HEMA composites:

$$\text{wt\% MIL} = \frac{m(\text{MIL@HEMA}) - m(\text{weighted poly(HEMA)HIPE})}{m(\text{MIL@HEMA})} \times 100$$

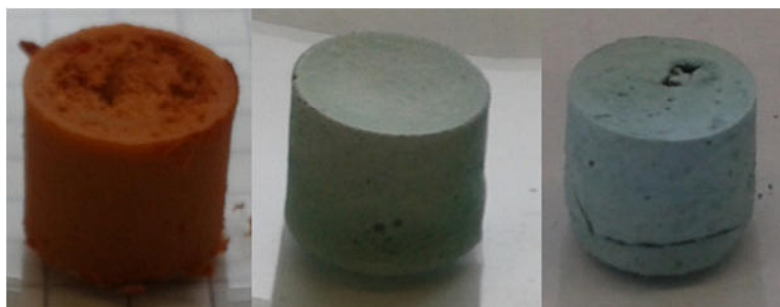


**Fig. 41.** MIL-100(Fe)@HEMA (GM: 54 wt%; AAS: 58 wt%), MIL-100(Cr)@HEMA (GM: 91 wt%; AAS: 93 wt%) and MIL-101(Cr)@HEMA (GM: 89 wt%; AAS: 91 wt%).

Scanning electron microscopic images of the MIL-100(Fe)@HEMA composite display some isolated HIPE pores with almost unchanged void diameters compared to the native poly(HEMA)HIPE (Figure 42). MIL-100(Fe) particles adhere on the HIPE surface, mainly as agglomerates. Some isolated MIL octahedrons are apparent, which is the typical morphology for MIL-100(Fe) crystals.<sup>234</sup>

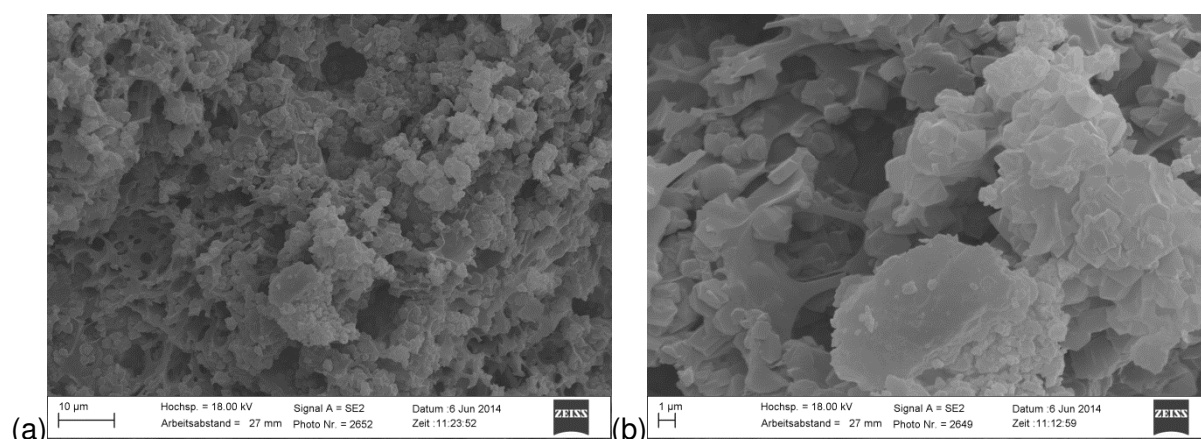


**Fig. 42.** Scanning electron microscopic images of MIL-100(Fe)@HEMA (LEO 1430 VP, Zeiss).

Figure 43a shows the powder X-ray diffraction patterns and infrared spectra of MIL@HEMA composites and the corresponding residual MILs. Powder patterns prove that the crystallinity for both MIL-100@HEMA composites remains unchanged despite the presence of amorphous poly(HEMA)HIPE. Only the MIL-101(Cr)@HEMA composite shows strongly broadened reflections even after longer measuring times. Due to the fact that quantification experiments and infrared spectra of MIL@HEMA (Figure 43b), which can be seen as an overlap of the individual spectra of MIL-residual (square brackets) and native poly(HEMA)HIPE, prove a high degree of MOF loading, MIL-101(Cr) in MIL-101(Cr)@HEMA is possibly of relatively low crystallinity. It can be assumed that only amorphous MIL-101 particles have been synthesized in the macroporous HIPE template, which is a literature-known phenomenon.<sup>235</sup>



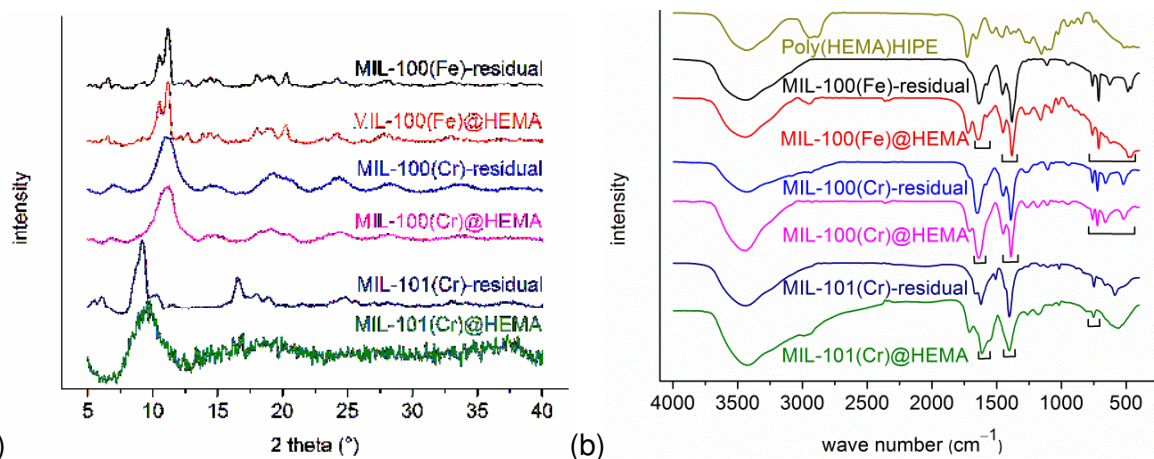


**Fig. 43.** (a) PXRD patterns of MIL-residual and MIL@HEMA (MIL = MIL-100(Fe), MIL-100(Cr), MIL-101(Cr)). (b) IR-spectra (KBr) of native poly(HEMA)HIPE (13 mol% MBA), MIL-residual and MIL@HEMA (MIL = MIL-100(Fe), MIL-100(Cr), MIL-101(Cr)). Square brackets highlight the bands of the MILs in the composite material.

Nitrogen sorption isotherms of native poly(HEMA)HIPE and MIL@HEMA composites are presented in Figure 44a. It is obvious that all composites show an increased nitrogen uptake compared to the pure HIPE over the entire pressure range. Both MIL-100@HEMA materials display a type I sorption isotherm due to the presence of free MOF micropores in the composites, which are clearly visible in the corresponding pore size distribution curves (Figure 44c-e). MIL-100(Cr)@HEMA additionally exhibits a hysteresis loop that is associated with capillary condensation in the MIL mesopores. Based on the higher loading of MIL in MIL-100(Cr)@HEMA (93 wt%), its total uptake of nitrogen is higher compared to MIL-100(Fe)@HEMA (58 wt%, Table 7). In contrast, MIL-101(Cr)@HEMA shows a mixture of a type II isotherm, reflecting the macroporous character of the HIPE, together with a type IV shaped isotherm, which indicates the presence of MIL mesopores in the composite. The missing type I shape, caused by potential MIL-101 micropores, are of rather low resolution between 12–18 Å (Figure 44e).

BET surface areas and total pore volumes of MIL@HEMA (MIL-100(Fe)@HEMA: 430 m<sup>2</sup>·g<sup>-1</sup>/0.19 cm<sup>3</sup>·g<sup>-1</sup>; MIL-100(Cr)@HEMA: 600 m<sup>2</sup>·g<sup>-1</sup>/0.34 cm<sup>3</sup>·g<sup>-1</sup>; MIL-101(Cr)@HEMA: 260 m<sup>2</sup>·g<sup>-1</sup>/0.29 cm<sup>3</sup>·g<sup>-1</sup>) are larger compared to pure poly(HEMA)HIPE (60 m<sup>2</sup>·g<sup>-1</sup>/0.05 cm<sup>3</sup>·g<sup>-1</sup>) due to the embedding of additional MOF pores into the HIPE system. Based on the weight% of MIL in the MIL@HEMA composites, BET surface areas can be expected as the sum of the mass weighted surface areas of MIL-residual and pure HIPE (see formula in Table 7). The estimated surface areas of 1150 m<sup>2</sup>·g<sup>-1</sup> (MIL-100(Fe)@HEMA), 1170 m<sup>2</sup>·g<sup>-1</sup> (MIL-100(Cr)@HEMA) and 2290 m<sup>2</sup>·g<sup>-1</sup> (MIL-101(Cr)@HEMA) could not be achieved. BET

surface areas of MIL-residual show reasonable porosity comparable to other literature data.<sup>150,151,236,237</sup>

Water sorption isotherms show an increased water uptake for all MIL@HEMA composites over the whole pressure range in comparison to native poly(HEMA)HIPE (Figure 44f). MIL-100(Cr)@HEMA shows the highest water uptake among the MIL@HEMA composites, synthesized by route B, due to the highest MIL loading (Table 7). Its uptake of  $0.30 \text{ g}\cdot\text{g}^{-1}$  ( $P\cdot P_0^{-1} = 0.9$ ) is twice the amount of native HIPE. MIL-100(Fe)@HEMA possesses an uptake of  $0.27 \text{ g}\cdot\text{g}^{-1}$  ( $P\cdot P_0^{-1} = 0.9$ ) with a stepwise adsorption isotherm, typical for pure MIL-100(Fe) through consecutive pore filling.<sup>158</sup> Although MIL-101(Cr)@HEMA has a high MIL loading of 91 wt%, its water uptake of  $0.26 \text{ g}\cdot\text{g}^{-1}$  ( $P\cdot P_0^{-1} = 0.9$ ) is relatively low.

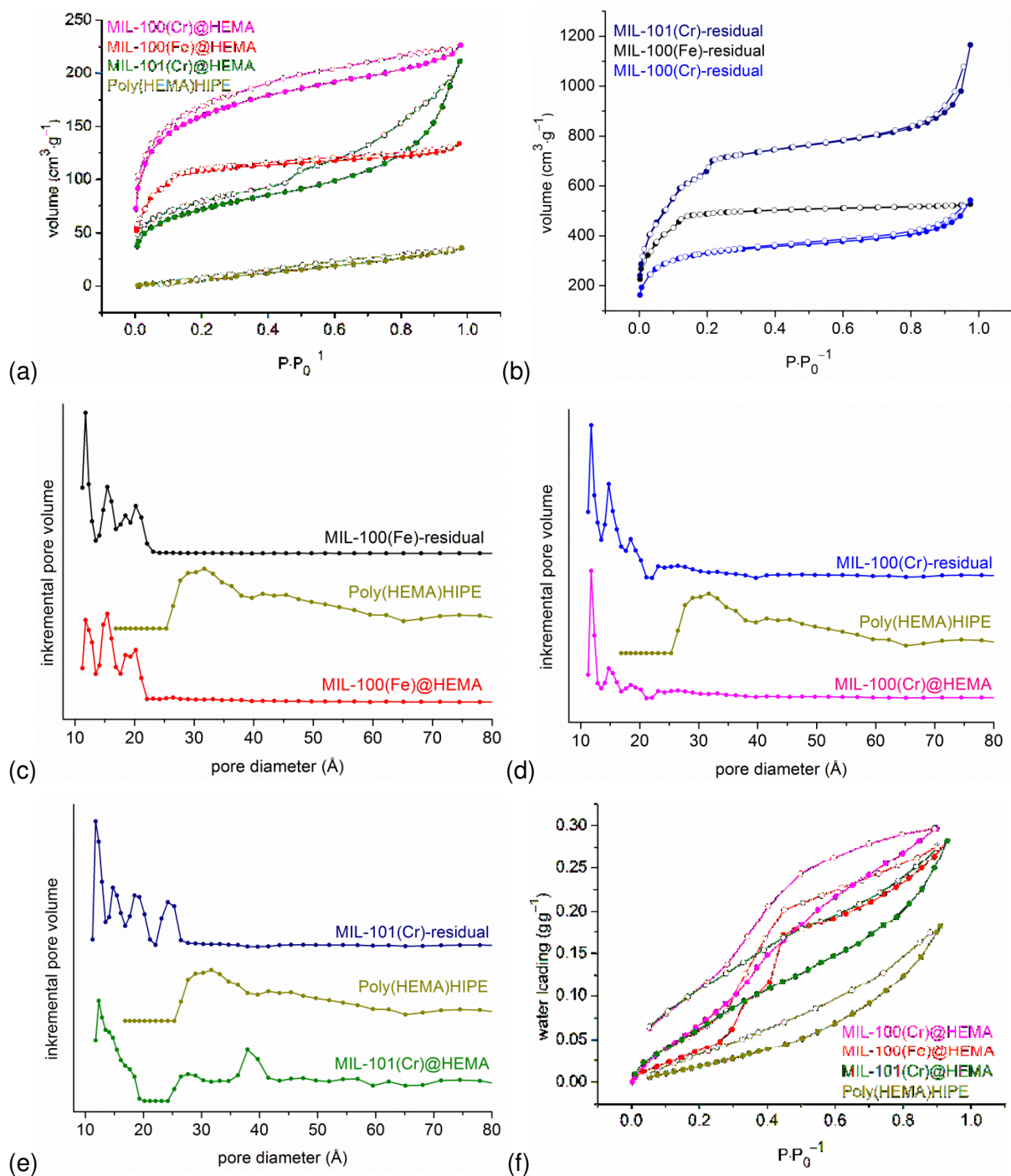


**Fig. 44.** (a)  $\text{N}_2$ -sorption isotherms of native poly(HEMA)HIPE (13 mol% MBA) and MIL@HEMA composites and (b) MILs-residual (MIL = MIL-100(Fe), MIL-100(Cr), MIL-101(Cr)) (degassing conditions: 2 h, 423 K). (c)-(e) Pore size distribution curves of native poly(HEMA)HIPE (13 mol% MBA), MIL-residual and MIL@HEMA (MIL = MIL-100(Fe), MIL-100(Cr), MIL-101(Cr)). (f) Water sorption isotherms of native poly(HEMA)HIPE (13 mol% MBA) and MIL@HEMA composites (MIL = MIL-100(Fe), MIL-100(Cr), MIL-101(Cr)) (degassing conditions: 2 h, 423 K). Adsorption is depicted with filled, desorption with empty symbols.

In conclusion three different MILs could be successfully embedded into a macroporous poly(HEMA)HIPE by the *in situ* method (route B) with retention of the monolithic shape. The highest loading of MIL with 93 wt% was achieved in MIL-100(Cr)@HEMA. Powder X-ray diffraction patterns, infrared spectra and AAS measurements confirm the presence of the MILs in the composites, although mostly amorphous MIL-101(Cr) could be synthesized inside the HIPE macropores. Nitrogen sorption isotherms and pore size distribution curves give evidence for a high amount of free MOF micropores in both MIL-100@HEMA composites. MIL-101(Cr)@HEMA contains available MIL mesopores with a negligible small amount of free MIL micropores, also reflected by the low BET surface area.

MIL-100(Fe)@HEMA and MIL-100(Cr)@HEMA, synthesized by the *in situ* method (route B), show similar results compared to the pre-polymerized MIL-101(Cr)@HEMA composites, which were obtained via route A (section 3.2). Herein, approximately 40–50 % of the estimated BET surface areas were achieved. MIL-101(Cr)@HEMA materials, synthesized via both methods, show pronounced differences. The *in situ* route leads to 91 wt% loading of MIL-101(Cr) in the macroporous HIPE template. But the embedded MIL has mostly amorphous and low porous character, leading to an inefficient material. MIL-101(Cr)@HEMA, synthesized via route A (section 3.2), lead to more porous and efficient monolithic composites with MIL loadings up to 59 wt%. Also regarding further factors such as time and energy consumption, MIL-101(Cr)@HEMA, obtained by the direct route A method, led to composites with higher performance.

**Table 7.** Results from nitrogen and water sorption measurements (n.d. = not determined).

	BET surface area <sup>a</sup> (estimated) <sup>d</sup> (m <sup>2</sup> ·g <sup>-1</sup> )	Total pore volume (cm <sup>3</sup> ·g <sup>-1</sup> ) <sup>b</sup>	Water loading (g·g <sup>-1</sup> ) <sup>c</sup>
Poly(HEMA)HIPE (13 mol% MBA)	60	0.05	0.16
MIL-100(Fe)@HEMA (58 wt% MIL)	430 (1150)	0.19	0.27
MIL-100(Fe)-residual	1930	0.81	n.d.
MIL-100(Cr)@HEMA (93 wt% MIL)	600 (1170)	0.34	0.30
MIL-100(Cr)-residual	1250	0.74	n.d.
MIL-101(Cr)@HEMA (91 wt% MIL)	260 (2290)	0.29	0.26
MIL-101(Cr)-residual	2510	1.51	n.d.

<sup>a</sup> BET surface area calculated at  $0.05 < P \cdot P_0^{-1} < 0.2$  from N<sub>2</sub> sorption isotherm 77 K with a standard deviation  $\pm 20$  m<sup>2</sup>·g<sup>-1</sup>.

<sup>b</sup> calculated from N<sub>2</sub> sorption isotherm at 77 K and  $P \cdot P_0^{-1} = 0.95$  for pores  $\leq 20$  nm.

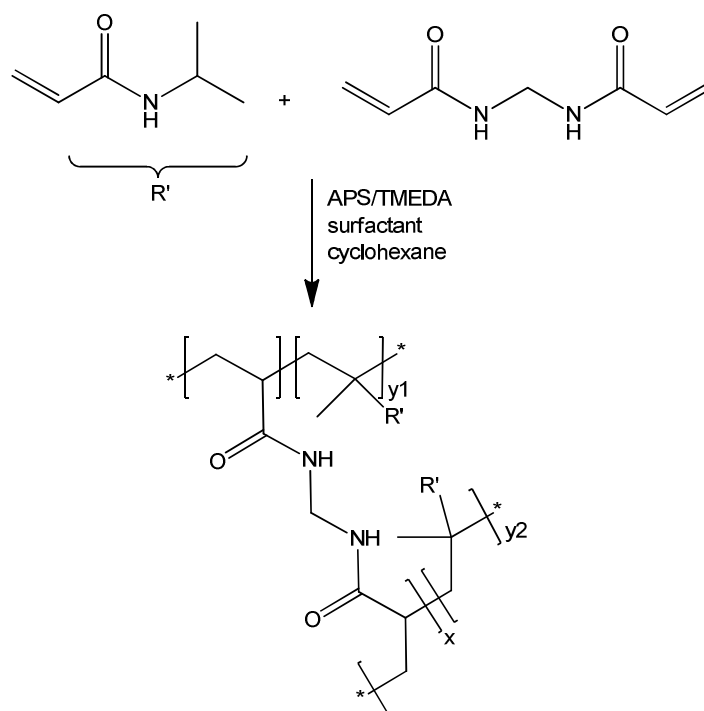
<sup>c</sup> calculated from water sorption isotherm at 293 K and  $P \cdot P_0^{-1} = 0.9$ .

<sup>d</sup> BET surface area as the sum of the mass-weighted surface areas of MIL-residual and native poly(HEMA)HIPE calculated from the following formula (wt% of the MILs were taken from AAS measurements, Table 7):

$$\begin{aligned} & \text{BET (estimated)} \\ & = \frac{\text{wt\% of native poly(HEMA)HIPE}}{100} \times 60 \text{ m}^2 \cdot \text{g}^{-1} + \frac{\text{wt\% of MIL - residual}}{100} \\ & \times 1930 \text{ (MIL - 100Fe) or } 1250 \text{ (MIL - 100Cr) or } 2510 \text{ (MIL - 101Cr) m}^2 \cdot \text{g}^{-1} \end{aligned}$$

## 4.4 Macroporous Poly(NIPAM)HIPE

The synthesis of poly(NIPAM)HIPE was carried out according to the literature.<sup>238</sup> *N*-Isopropylacrylamide was cross-linked with *N,N'*-methylenebisacrylamide in a radical polymerization (Scheme 5). To the best of our knowledge poly(NIPAM)HIPEs with MBA cross-linking of only 1–5 mol% have been reported so far. Based on our experimental experience and other literature, these reported monoliths shrank to a large extent during drying, accompanied by large cracks.<sup>238</sup> Increasing the degree of cross-linking should enhance the mechanical stability for such monoliths, yielding a more rigid and resistant material towards shrinkage.<sup>177b,239,240</sup>



**Scheme 5.** Radical polymerization of *N*-isopropylacrylamide (NIPAM) and *N,N'*-methylenebisacrylamide (MBA) initiated by ammonium persulfate (APS) ( $x = 9, 13$  or  $17$  mol%,  $y_1 + y_2 = 91, 87$  or  $73$  mol%).

An aqueous solution, containing  $1.0 \text{ mol}\cdot\text{L}^{-1}$  of NIPAM and  $0.05 \text{ mol}\cdot\text{L}^{-1}$  of MBA was prepared. Additional amounts of MBA were added for increasing the degree of cross-linking. Ammonium persulfate as the radical initiator and Triton™-X-405, as surfactant, were added to the continuous, aqueous phase. The oily cyclohexane phase and TMEDA, which act together with APS as radical initiator, were added. The o/w emulsions were cured for three days in a Teflon-liner at  $333 \text{ K}$ . After a washing procedure, the wet monoliths were carefully dried. Only poly(NIPAM)HIPE with  $17 \text{ mol}\%$  of MBA yielded a monolithic shape although shrinkage of approximately  $50 \%$  of the original volume was observed during drying (Figure

45a). Using 9 and 13 mol% of MBA led to monoliths with large shrinkage, deformation and cracks.

Scanning electron microscopic images of poly(NIPAM)HIPEs with 9, 13 and 17 mol% of MBA are displayed in Figure 45b-d. The average void sizes for all three materials are in the range of 20–110  $\mu\text{m}$ . Literature-known poly(NIPAM)HIPE with 1 and 2 mol% MBA shows a bimodal pore size distribution with voids of 1–2  $\mu\text{m}$  and 60  $\mu\text{m}$ . A cross-linking amount of 5 mol% of MBA leads to void diameters of 10  $\mu\text{m}$ .<sup>238</sup> A strict correlation between degree of cross-linking and void size seems not to be apparent in this case.

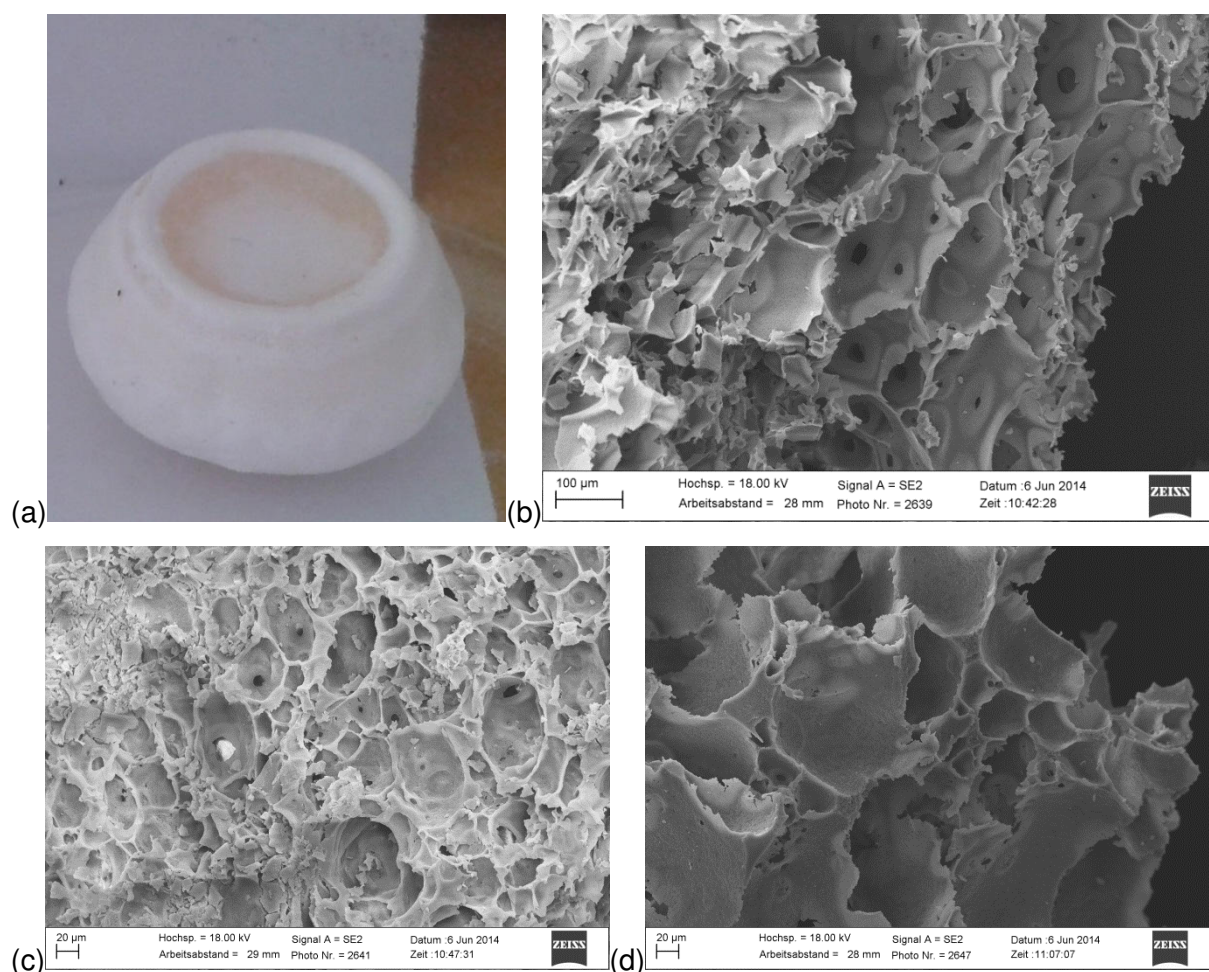


**Fig. 45.** (a) Native poly(NIPAM)HIPE (17 mol% MBA). Scanning electron microscopic images of poly(NIPAM)HIPEs with (b) 9 mol%, (c) 13 mol% and (d) 17 mol% *N,N'*-methylenebisacrylamide (LEO 1430 VP, Zeiss).

The infrared spectrum of the poly(NIPAM)HIPE (17 mol% MBA) is shown in Figure 46a-b. The region between 3700 and 3100  $\text{cm}^{-1}$  exhibits a broad band, which can be assigned to the O-H and N-H stretching vibrations of physisorbed water in the HIPE pores and N-H groups, coming from both monomers. The  $\nu(\text{C-H})$  stretching vibrations can be found at 2996–2864  $\text{cm}^{-1}$ . Typical carbonyl stretching vibration is located at 1668  $\text{cm}^{-1}$ . Further

bands, coming from the N-H deformation vibrations, can be found at  $1540\text{ cm}^{-1}$ . Additional typical vibration bands as  $\delta(\text{C-H})$  ( $1461\text{--}1359\text{ cm}^{-1}$ ),  $\nu(\text{C-N})$  ( $1282\text{--}1207\text{ cm}^{-1}$ ) and  $\nu(\text{C-O-C})$  ( $1107\text{ cm}^{-1}$ ) prove the presence of the anticipated functional groups. This is consistent with other literature data.<sup>241</sup> Infrared spectra of 9 and 13 mol% cross-linked HIPE is presented in Figure 46c. Water sorption isotherm of native poly(NIPAM)HIPE (17 mol% MBA) shows, similar to poly(HEMA)HIPE, a rather hydrophobic shape (Figure 46d). Nevertheless, the total water uptake of  $0.26\text{ g}\cdot\text{g}^{-1}$  at  $P\cdot P_0^{-1} = 0.9$  is comparatively high.

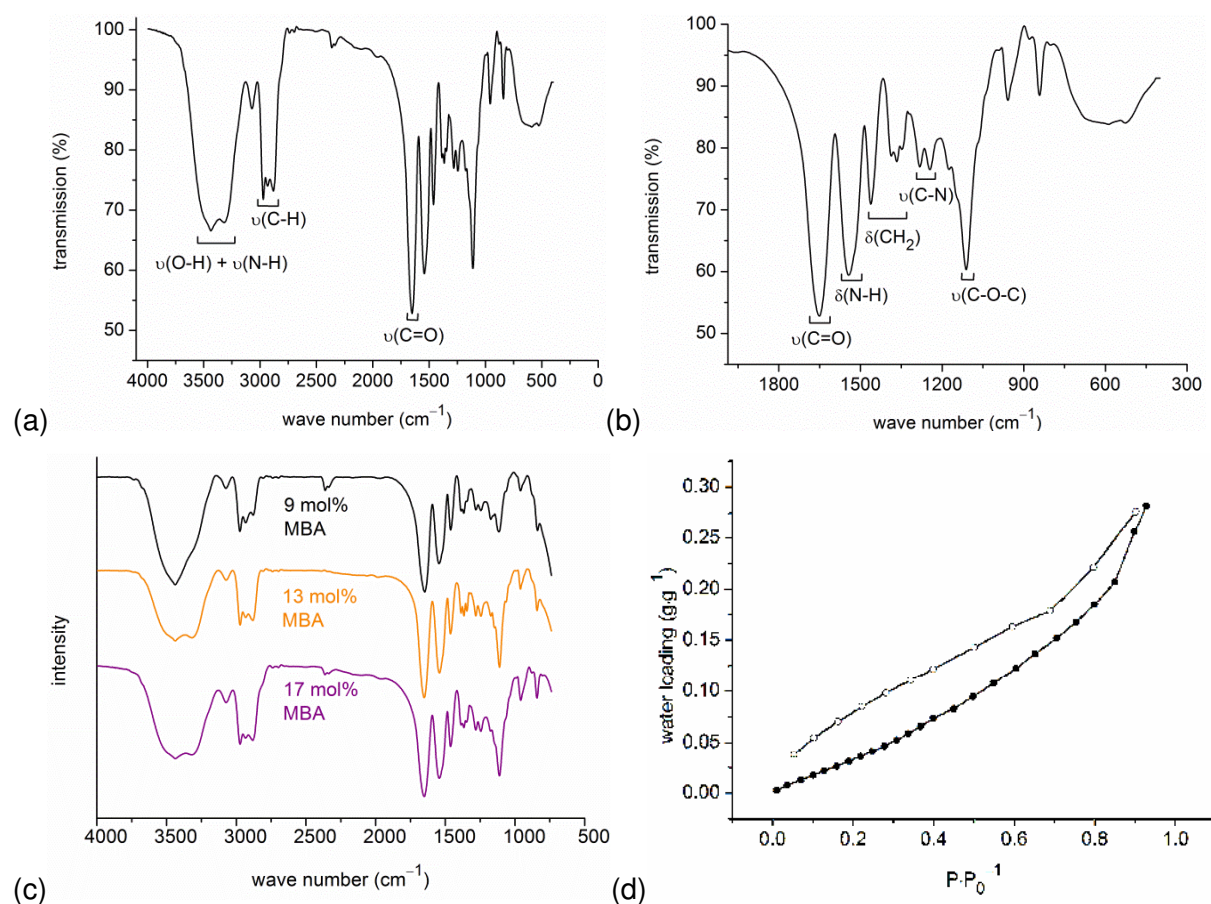


**Fig. 46.** (a) IR-spectra (KBr) of native poly(NIPAM)HIPE (17 mol% MBA). (b) Enlargement for region  $1900\text{--}300\text{ cm}^{-1}$ . (c) IR-spectra (KBr) of native poly(NIPAM)HIPEs with 9, 13 and 17 mol% of MBA. (d) Water sorption isotherms of native poly(NIPAM)HIPE (17 mol% MBA) (degassing conditions: 3 h, 393 K). Adsorption is depicted with filled, desorption with empty symbols.



The low BET surface area of  $20 \text{ m}^2\cdot\text{g}^{-1}$  is typical for HIPE systems due to their macroporous character.<sup>191</sup> Table 8 sums up the results from nitrogen and water sorption measurements.

**Table 8.** Results from nitrogen and water sorption measurements.

	BET surface area ( $\text{m}^2\cdot\text{g}^{-1}$ ) <sup>a</sup>	Total pore volume ( $\text{cm}^3\cdot\text{g}^{-1}$ ) <sup>b</sup>	Water loading ( $\text{g}\cdot\text{g}^{-1}$ ) <sup>c</sup>
Poly(NIPAM)HIPE (17 mol% MBA)	20	0.03	0.26

<sup>a</sup> BET surface area calculated at  $0.05 < P\cdot P_0^{-1} < 0.2$  from  $\text{N}_2$  sorption isotherm 77 K with a standard deviation  $\pm 20 \text{ m}^2\cdot\text{g}^{-1}$ .

<sup>b</sup> calculated from  $\text{N}_2$  sorption isotherm at 77 K and  $P\cdot P_0^{-1} = 0.95$  for pores  $\leq 20 \text{ nm}$ .

<sup>c</sup> calculated from water sorption isotherm at 293 K and  $P\cdot P_0^{-1} = 0.9$ .

#### 4.4.1 MIL-100(Fe,Cr)/101(Cr)@NIPAM (Route A)

Even though native poly(NIPAM)HIPE with 17 mol% of cross-linking features shrinkage during the drying process, the water sorption measurement shows relatively high vapor uptakes (Table 8). Different types of MIL@poly(NIPAM)HIPEs (in short MIL@NIPAM) were synthesized via the direct route A by simply adding pre-formed MIL powders to the poly(NIPAM)HIPE emulsion. Adding MOF particles to the HIPE should hopefully lead to monolithic composites with less shrinking during drying. As discussed in section 3.2, pre-polymerization of the HIPE emulsion before adding MOF powders is an indispensable factor for highly porous MIL@HIPE composites due to MOF pore blocking effects by monomer inclusion from the HIPE emulsion. Pre-polymerization experiments of the native poly(NIPAM)HIPE, which were done prior to the MIL@NIPAM syntheses, have shown that only a stirring time of 10 minutes gave reasonable curing of the emulsion yielding a monolithic shape. Separation of the emulsions occurred if the stirring time exceeded 10 minutes.

The syntheses of MIL@NIPAM composites via route A, containing different weight percentages of MIL, were done by a modified procedure of pure poly(NIPAM)HIPE. Various amounts of well-ground MIL-100(Fe), MIL-100(Cr) and MIL-101(Cr) powders were filled into 5 mL plastic syringes followed by adding specific amounts of highly pre-polymerized NIPAM-HIPE emulsion (17 mol% MBA). After homogenization, curing, washing and drying orange brown (i) MIL-100(Fe)@NIPAM (37 and 78 wt% MIL) and green (ii) MIL-100(Cr)@NIPAM (49, 58 wt% MIL), (iii) MIL-101(Cr)@NIPAM (46, 71, 92 wt%) materials were obtained. Unfortunately, all these composites were deformed and shrank during drying similar to native poly(NIPAM)HIPE, despite the usage of MOF particles. Figures 47a and 52a show two examples of MIL@NIPAM composites, in which deformation is clearly apparent. Quantification of the MIL content was done gravimetrically, supposing no MOF was lost during the synthesis.<sup>v</sup> BET surface areas of the MOF starting materials show reasonable porosities (2140 m<sup>2</sup>·g<sup>-1</sup> MIL-100(Fe); 1370 m<sup>2</sup>·g<sup>-1</sup> MIL-100(Cr); 2860 m<sup>2</sup>·g<sup>-1</sup> MIL-101(Cr), Table 9).

---

<sup>v</sup> Formula for gravimetrical quantification of MIL loading in MIL@NIPAM composites:

$$\text{wt\% (MIL in MIL@NIPAM)} = \frac{m(\text{weighted MIL})}{m(\text{MIL@NIPAM})} \times 100$$

### (i) MIL-100(Fe)@NIPAM

MIL-100(Fe) embedded into poly(NIPAM)HIPE show residual HIPE macropores with reduced void diameters in the scanning electron microscopic image (Figure 47b). Octahedral MIL-100(Fe) particles with an average size of 2–5  $\mu\text{m}$  are apparent, which adhere on the HIPE surface.<sup>234</sup>

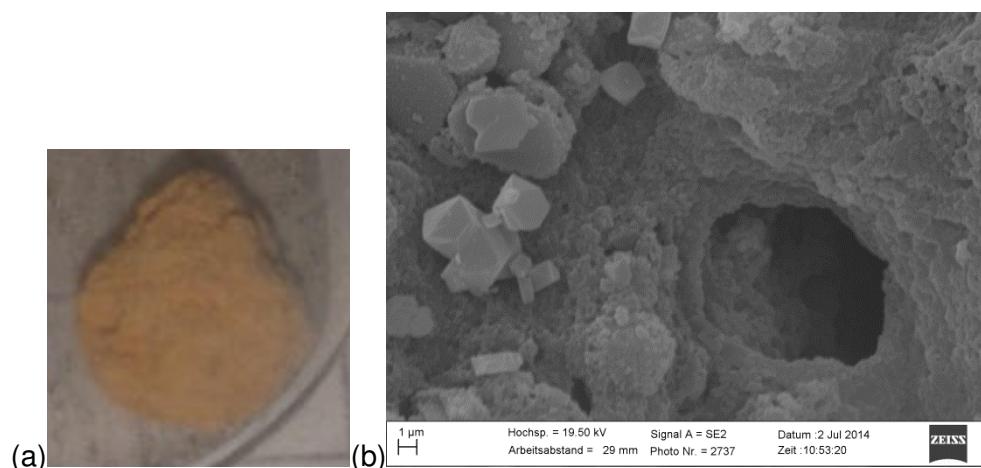


**Fig. 47.** (a) MIL-100(Fe)@NIPAM (78 wt% MIL). (b) Scanning electron microscopic images of MIL-100(Fe)@NIPAM (37 wt% MIL) (LEO 1430 VP, Zeiss).

Powder patterns evidence the presence of crystalline MIL-100(Fe) in MIL-100(Fe)@NIPAM (Figure 48a). Increasing the weight percentages of MIL lead to sharper reflections in the PXRD. Infrared spectra of both composites reveal the characteristic, asymmetric valence  $\nu(\text{R-CO}_2^-)$ , deformation  $\delta(\text{R-CO}_2^-)$  and  $\nu(\text{Fe-O})$  vibrations of incorporated MIL-100(Fe) emphasized by square brackets (Figure 48b).

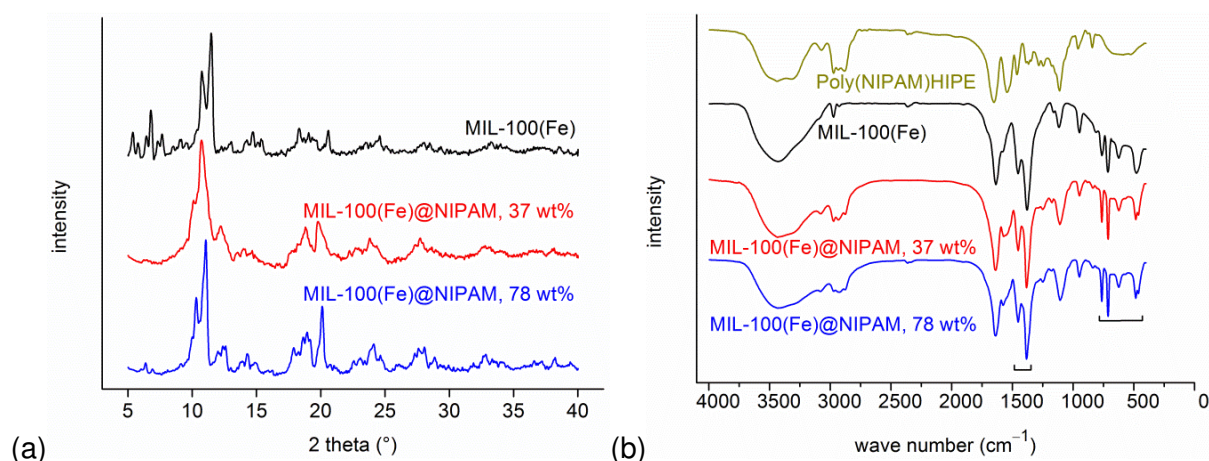


**Fig. 48.** (a) PXRD patterns of native MIL-100(Fe) and MIL-100(Fe)@NIPAM (37 and 78 wt% MIL). (b) IR-spectra (KBr) of native MIL-100(Fe), native poly(NIPAM)HIPE (17 mol% MBA) and MIL-100(Fe)@NIPAM (37 and 78 wt% MIL). Square brackets highlight the bands of MIL-100(Fe) in the composite material.

Figure 49a presents the nitrogen sorption isotherms of pure poly(NIPAM)HIPE and both MIL-100(Fe)@NIPAM composites. Embedding of MIL-100(Fe) leads to an enhanced nitrogen uptake over the entire pressure range compared to native HIPE, which is directly influenced by the MIL weight percentage. MIL-100(Fe)@NIPAMs reflect type I sorption isotherms, representative for microporous materials, with hysteresis loops that are influenced by capillary condensation in the MIL mesopores. Free and accessible micropores are proven in both composites through the corresponding pore size distribution curves (Figure 49b).

BET surface area and total pore volume of native poly(NIPAM)HIPE with  $20 \text{ m}^2\cdot\text{g}^{-1}$  and  $0.03 \text{ cm}^3\cdot\text{g}^{-1}$  are largely increased in MIL-100(Fe)@NIPAMs with  $230 \text{ m}^2\cdot\text{g}^{-1}/0.12 \text{ cm}^3\cdot\text{g}^{-1}$  (37 wt%) and  $300 \text{ m}^2\cdot\text{g}^{-1}/0.16 \text{ cm}^3\cdot\text{g}^{-1}$  (78 wt%) due to the presence of MIL micro- and mesopores in the composites (Table 9). Based on the weight percentages of MIL in MIL@NIPAM, estimated BET surface areas can be calculated according to formula d in Table 9. The expected values of  $800$  and  $1650 \text{ m}^2\cdot\text{g}^{-1}$  for 37 and 78 wt% MIL containing MIL-100(Fe)@NIPAM are far away from the experimental data probably due to a high degree of MIL pore blocking effects through NIPAM and MBA monomers. On the basis of these effects, water sorption isotherms only show a slight enhancement of water uptakes up to a relative vapor pressure of  $P/P_0 = 0.85$  (Figure 49c). Anyway, the characteristic stepwise adsorption, through the consecutive pore filling, is obvious for both composites.<sup>158</sup>

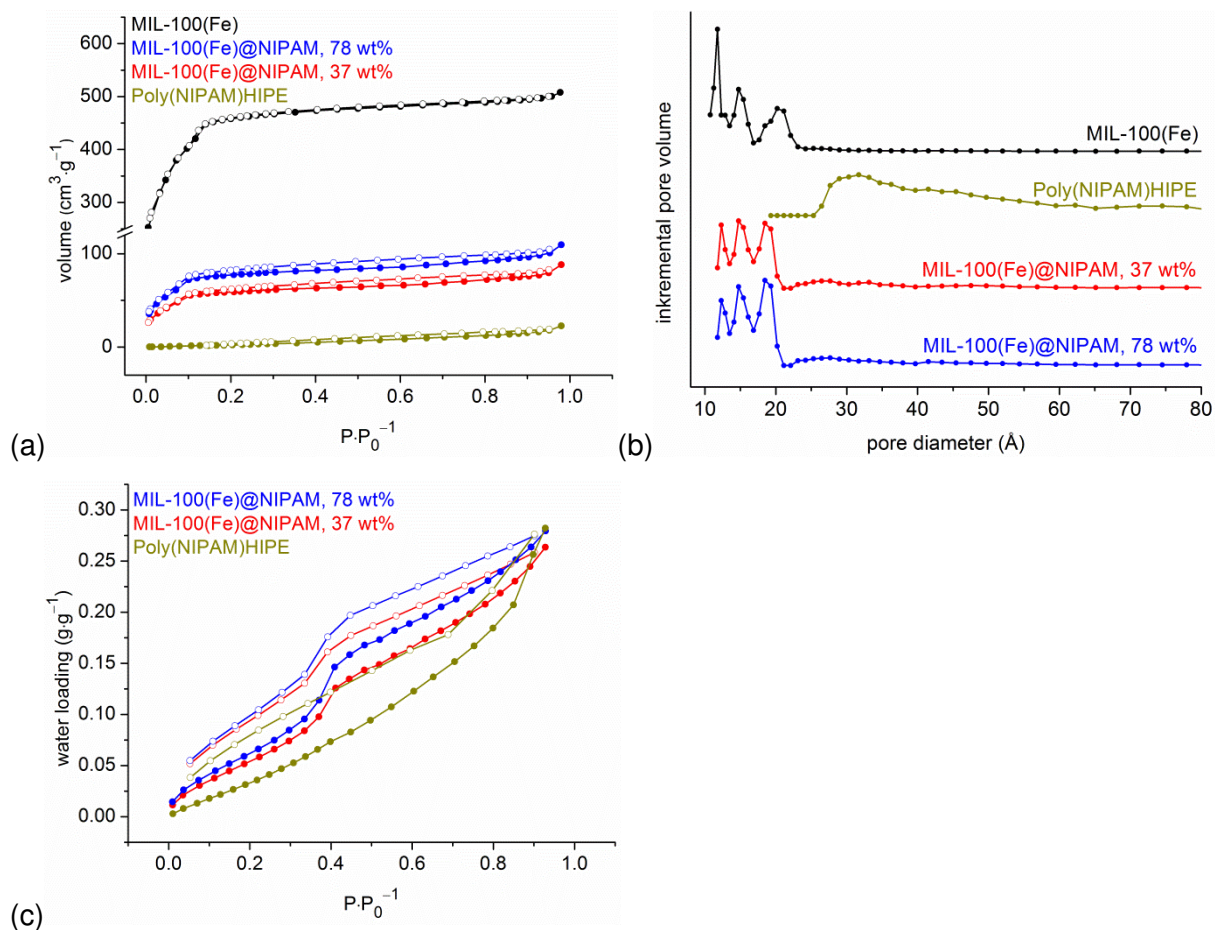


**Fig. 49.** (a)  $N_2$ -sorption isotherms of MIL-100(Fe)@NIPAM (37 and 78 wt% MIL), native MIL-100(Fe) and native poly(NIPAM)HIPE (17 mol% MBA) (degassing conditions: 3 h, 393 K). (b) Pore size distribution curves of native MIL-100(Fe), native poly(NIPAM)HIPE (17 mol% MBA) and MIL-100(Fe)@NIPAM (37 and 78 wt% MIL). (c) Water sorption isotherms of MIL-100(Fe)@NIPAM (37 and 78 wt% MIL) and native poly(NIPAM)HIPE (17 mol% MBA) (degassing conditions: 3 h, 393 K). Adsorption is depicted with filled, desorption with empty symbols.

## (ii) MIL-100(Cr)@NIPAM

Powder X-ray diffraction patterns of MIL-100(Cr)@NIPAMs indicate the unchanged, crystalline phase of pure MIL-100(Cr) (Figure 50a). Figure 50b demonstrates that the infrared spectra of both composites exhibit an additive overlap of the individual spectra of both single components (MIL and HIPE). Asymmetric valence vibrations  $\nu(\text{R-CO}_2)$  and  $\nu(\text{Cr-O})$  and deformation vibration  $\delta(\text{R-CO}_2)$  of embedded MIL-100(Cr) are highlighted by square brackets.

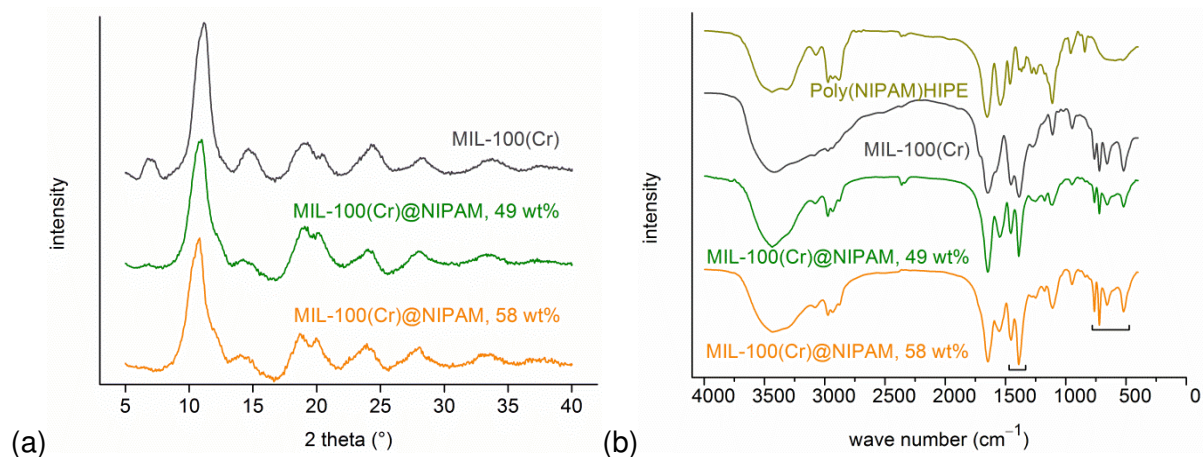


**Fig. 50.** (a) PXRD patterns of native MIL-100(Cr) and MIL-100(Cr)@NIPAM (49 and 58 wt% MIL). (b) IR-spectra (KBr) of native MIL-100(Cr), native poly(NIPAM)HIPE (17 mol% MBA) and MIL-100(Cr)@NIPAM (49 and 58 wt% MIL). Square brackets highlight the bands of MIL-100(Cr) in the composite material.

Figure 51a shows the nitrogen sorption isotherm of both MIL-100(Cr)@NIPAMs together with pure poly(NIPAM)HIPE. Increasing of the weight percentages of MIL in the composites leads to enhanced nitrogen uptake capacities over the whole  $P \cdot P_0^{-1}$  range. In contrast to MIL-100(Fe)@NIPAM, MIL-100(Cr)@NIPAMs reflect isotherms with a typical type II shape, which stand for the macroporous behavior of the HIPE. The hystereses between ad- and desorption isotherms refer to the presence of incorporated MIL mesopores. Pore size distribution curves of MIL-100(Cr)@NIPAMs document the existence of some mesopores and micropores of very poor resolution between 12–18 Å (Figure 51b). These micropores are more pronounced by increasing the MIL weight% from 49 to 58 wt%. Nevertheless, sorption isotherms of the composites do not present typical type I shapes, probably due to the low amount of MIL micropores.

BET surface areas and total pore volumes of pure poly(NIPAM)HIPE ( $20 \text{ m}^2 \cdot \text{g}^{-1} / 0.03 \text{ cm}^3 \cdot \text{g}^{-1}$ ) are only slightly enhanced in both composites ( $90 \text{ m}^2 \cdot \text{g}^{-1} / 0.14 \text{ cm}^3 \cdot \text{g}^{-1}$  (49 wt%);  $150 \text{ m}^2 \cdot \text{g}^{-1} / 0.17 \text{ cm}^3 \cdot \text{g}^{-1}$  (58 wt%), Table 9). This is far away from the estimated values of 680

$\text{m}^2\cdot\text{g}^{-1}$  (49 wt%) and  $800 \text{ m}^2\cdot\text{g}^{-1}$  (58 wt%), presumably due to tremendous HIPE polymerization inside the MIL pores. Hence, water sorption isotherms of MIL-100(Cr)@NIPAMs only show marginal improvements over native HIPE (Figure 51c).

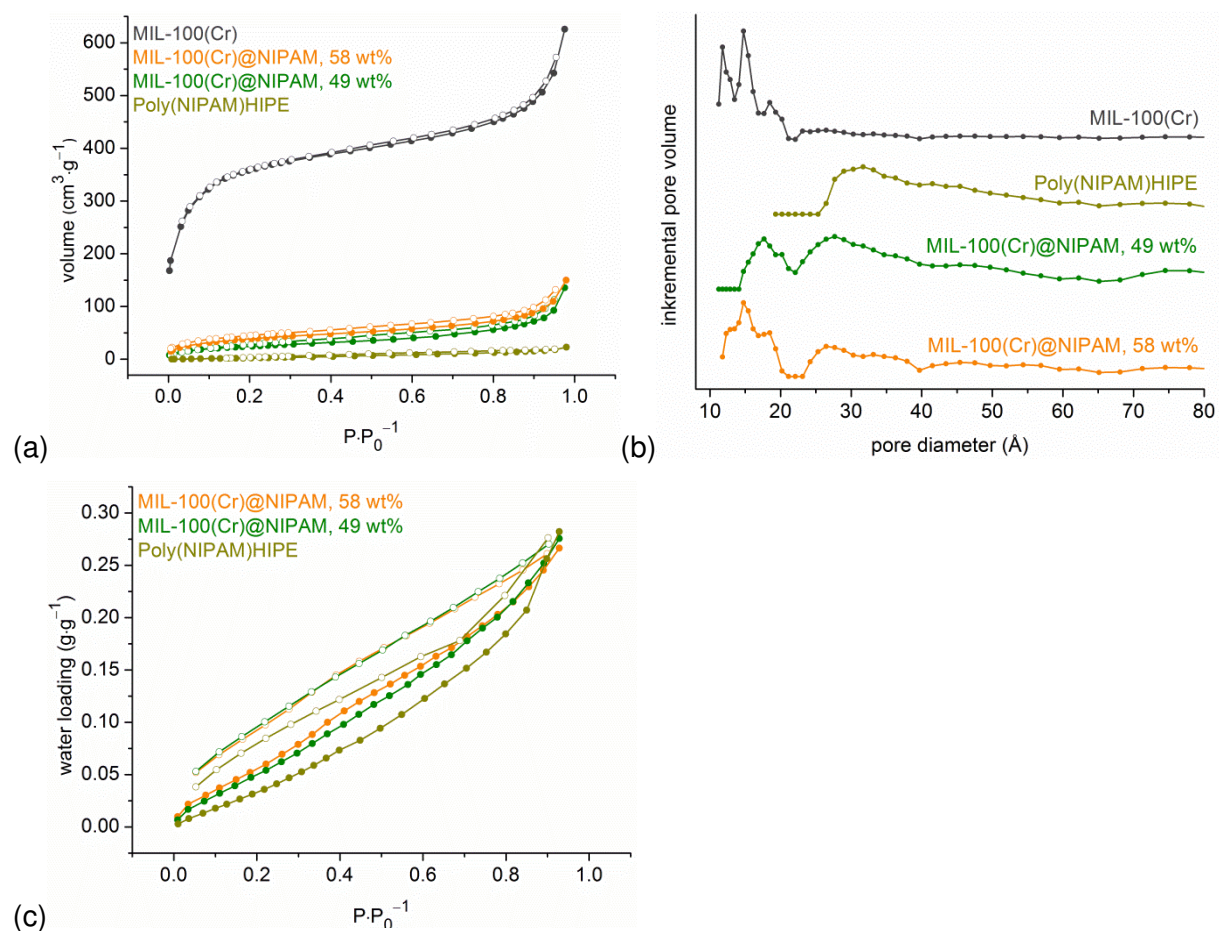


**Fig. 51.** (a)  $\text{N}_2$ -sorption isotherms of MIL-100(Cr)@NIPAM (49 and 58 wt% MIL), native MIL-100(Cr) and native poly(NIPAM)HIPE (17 mol% MBA) (degassing conditions: 3 h, 393 K). (b) Pore size distribution curves of native MIL-100(Cr), native poly(NIPAM)HIPE (17 mol% MBA) and MIL-100(Cr)@NIPAM (49 and 58 wt% MIL). (c) Water sorption isotherms of MIL-100(Cr)@NIPAM (49 and 58 wt% MIL) and native poly(NIPAM)HIPE (17 mol% MBA) (degassing conditions: 3 h, 393 K). Adsorption is depicted with filled, desorption with empty symbols.

### (iii) MIL-101(Cr)@NIPAM

The scanning electron microscopic image of MIL-101(Cr)@NIPAM (92 wt%) presents residual, macroporous HIPE pores with reduced void sizes compared to pure HIPE (Figure 52b). MIL-101(Cr) particles of octahedral morphology with sizes of 300–500 nm stick onto the surface of the NIPAM-HIPE.<sup>232</sup>

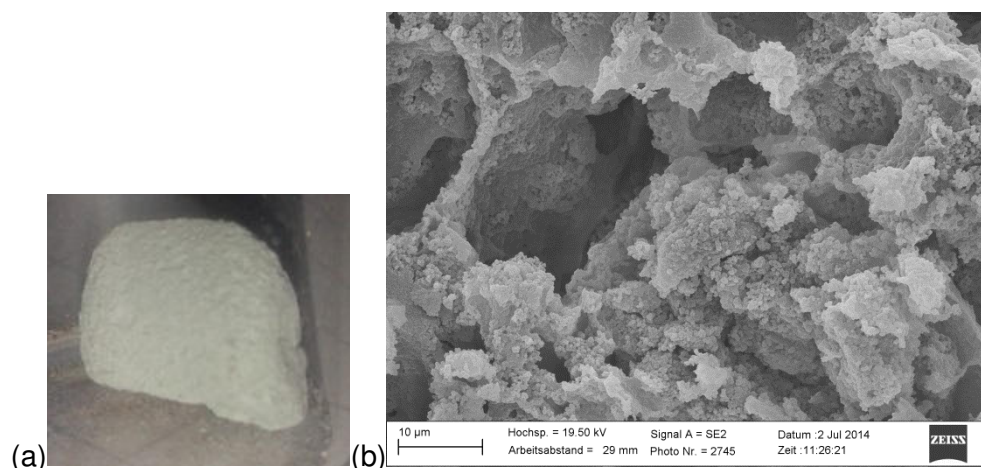


**Fig. 52.** (a) MIL-101(Cr)@NIPAM (92 wt% MIL). (b) Scanning electron microscopic images of MIL-101(Cr)@NIPAM (46 wt% MIL) (LEO 1430 VP, Zeiss).

As seen before, the crystalline MIL-101(Cr) phase in the composites is proven by the powder X-ray diffraction patterns (Figure 53a). The intensities of valence vibrations ( $\nu(\text{R-CO}_2)$ ,  $\nu(\text{Cr-O})$ ) and deformation vibration  $\delta(\text{R-CO}_2)$  of MIL-101(Cr) are increased with higher MIL loading, shown by the IR spectra (Figure 53b).

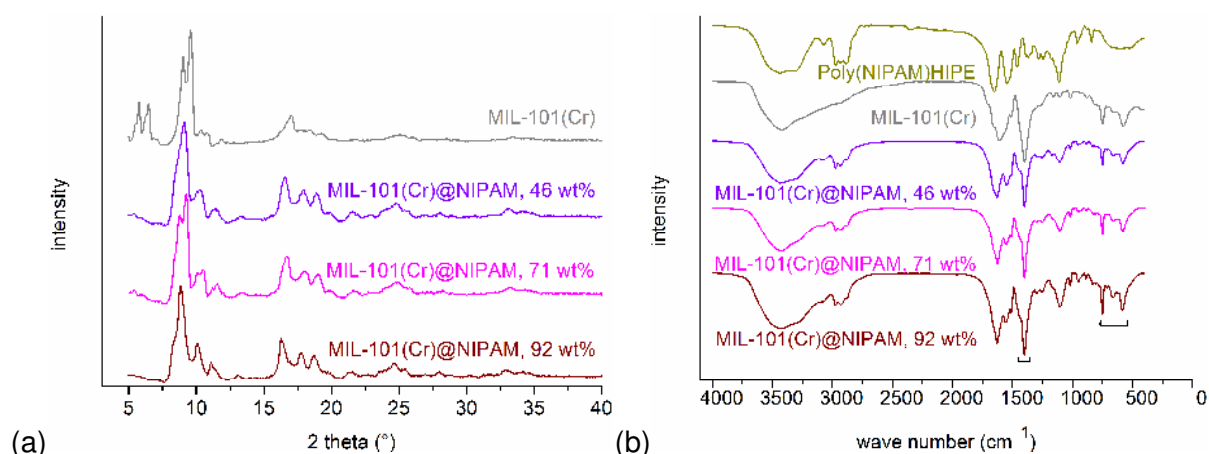


**Fig. 53.** (a) PXRD patterns of native MIL-101(Cr) and MIL-101(Fe)@NIPAM (46, 71 and 92 wt% MIL). (b) IR-spectra (KBr) of native MIL-101(Cr), native poly(NIPAM)HIPE (17 mol% MBA) and MIL-101(Cr)@NIPAM (46, 71 and 92 wt% MIL). Square brackets highlight the bands of MIL-101(Cr) in the composite material.



Nitrogen sorption analyses of MIL-101(Cr)@NIPAM reveal a vast increase of gas uptake compared to native NIPAM-HIPE in the entire pressure range (Figure 54a). Loading of MIL-101(Cr) in the composites directly determines the total nitrogen uptake. All composite materials show microporous behavior due to the type I shaped sorption isotherms. Furthermore, these micropores of almost unchanged pore sizes can be evidenced by pore size distribution curves in Figure 54b. Small hysteresis loops indicate the presence of MIL mesopores.

Experimental surface areas of MIL-101(Cr)@NIPAM with  $720 \text{ m}^2\cdot\text{g}^{-1}$  (46 wt%),  $960 \text{ m}^2\cdot\text{g}^{-1}$  (71 wt%) and  $980 \text{ m}^2\cdot\text{g}^{-1}$  (92 wt%) are closer to the estimated values of  $1320 \text{ m}^2\cdot\text{g}^{-1}$  (46 wt%),  $2030 \text{ m}^2\cdot\text{g}^{-1}$  (71 wt%) and  $2630 \text{ m}^2\cdot\text{g}^{-1}$  (92 wt%) compared to the MIL-100@NIPAM composites (Table 9). Thus, the stepwise water sorption isotherms of the composites show more satisfying results in comparison to MIL-100@NIPAMs, due to higher vapor uptakes compared to pure HIPE over the entire pressure range (Figure 54c).<sup>153</sup>

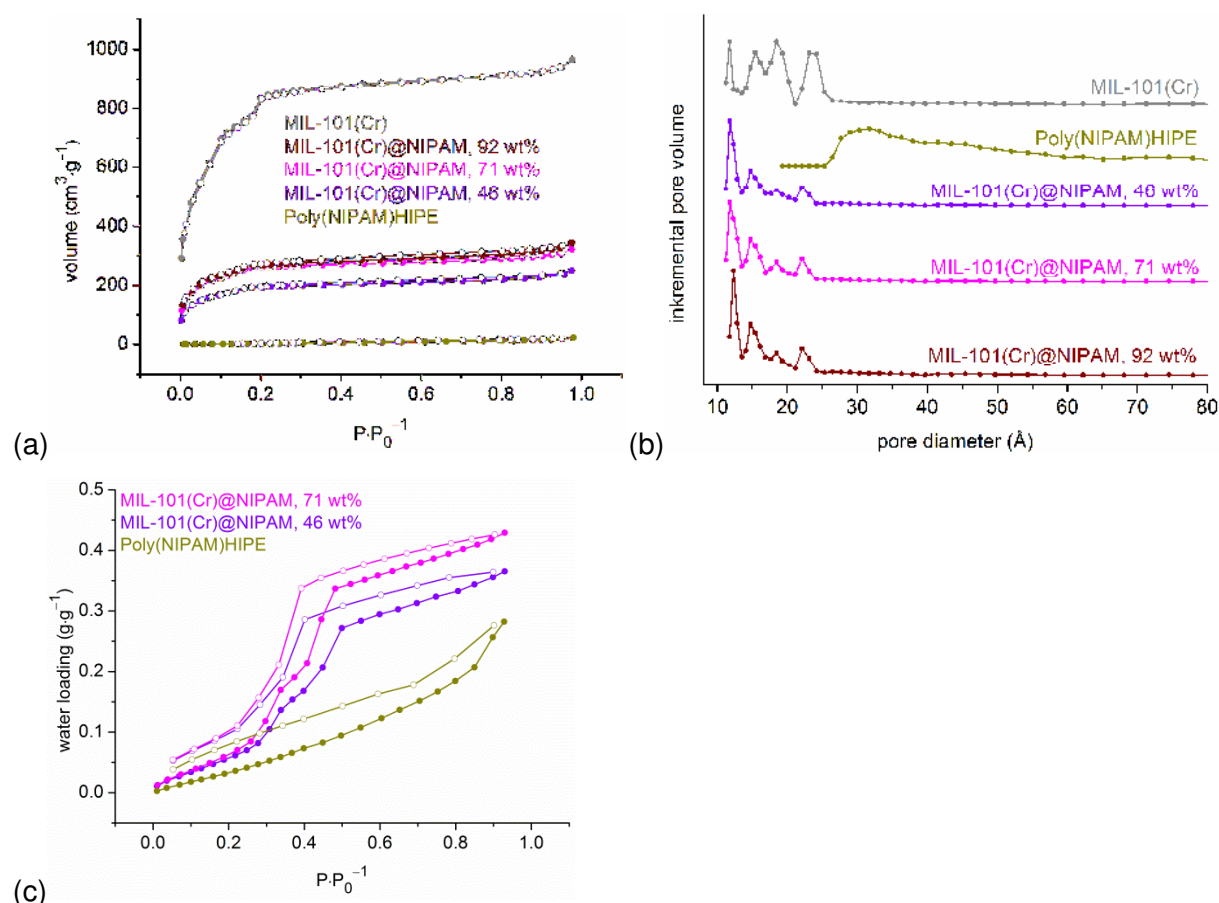



**Fig. 54.** (a) N<sub>2</sub>-sorption isotherms of MIL-101(Cr)@NIPAM (46, 71 and 92 wt% MIL), native MIL-101(Cr) and native poly(NIPAM)HIPE (17 mol% MBA) (degassing conditions: 3 h, 393 K). (b) Pore size distribution curves of native MIL-101(Cr), native poly(NIPAM)HIPE (17 mol% MBA) and MIL-101(Cr)@NIPAM (46, 71 and 92 wt% MIL). (c) Water sorption isotherms of MIL-101(Cr)@NIPAM (46 and 71 wt% MIL) and native poly(NIPAM)HIPE (17

mol% MBA) (degassing conditions: 3 h, 393 K). Adsorption is depicted with filled, desorption with empty symbols.

In conclusion MIL@NIPAM syntheses lead to monoliths with huge deformation and/or cracks during the drying procedure. Despite the usage of MOF particles, no mechanically stable monoliths were obtained. Nevertheless, powder patterns, infrared spectra and SEM images prove the presence of the MILs in the composites. Nitrogen sorption isotherms, BET surface areas and pore size distribution curves show that embedding of MIL-101(Cr) leads to higher porous and therefore more efficient composites compared to MIL-100@NIPAMs. Experimental BET surface areas of MIL-101(Cr)@NIPAM are closer to the expected surface areas in comparison to both MIL-100@NIPAMs. The free and accessible micropores in the composites lead to relatively high water vapor uptakes.

The larger BET surface areas of MIL-101(Cr)@NIPAMs, compared to the MIL-100 composites, could be explained by a higher degree of pore blocking effects in the MIL-100 containing composites. NIPAM and MBA monomers can more easily diffuse and therefore block the smaller MIL-100 pores and windows (25 and 29 Å (pores), ≈5 and ≈9 Å (windows)) through stronger capillary condensation forces. The same phenomenon was observed for the MIL@R,F-xerogel composites (section 3.3).

Among both MIL-100@NIPAM composites, surface areas of MIL-100(Fe)@NIPAMs are closer to the expected BETs. Pore diameters of pure MIL-100(Fe) and MIL-100(Cr) are theoretically of the same size (25 and 29 Å), but BET surface areas show that pure MIL-100(Fe) (2140 m<sup>2</sup>·g<sup>-1</sup>) is much more porous than pure MIL-100(Cr) (1370 m<sup>2</sup>·g<sup>-1</sup>). The less porous MIL-100(Cr), incorporated in poly(NIPAM)HIPE, probably also shows pronounced pore blocking effects through higher capillary condensation forces. In other words: Smaller pores (or materials with lower inner surfaces) are more difficult to protect than larger pores (or materials with higher inner surfaces) (Figure 55).

MIL-100(Cr)	MIL-100(Fe)	MIL-101(Cr)
BET = 1370 m <sup>2</sup> ·g <sup>-1</sup>	2140 m <sup>2</sup> ·g <sup>-1</sup>	2860 m <sup>2</sup> ·g <sup>-1</sup>
		
higher BET surface areas/porosities less capillary condensation forces easier protection for composite syntheses		

**Fig. 55.** Sequence of MIL pore protection for composite syntheses.

**Table 9.** Results from nitrogen and water sorption measurements (n.d. = not determined).

	BET surface area <sup>a</sup> (estimated) <sup>d</sup> (m <sup>2</sup> ·g <sup>-1</sup> )	Total pore volume (cm <sup>3</sup> ·g <sup>-1</sup> ) <sup>b</sup>	Water loading (g·g <sup>-1</sup> ) <sup>c</sup>
Native poly(NIPAM)HIPE (17 mol% MBA)	20	0.03	0.26
Native MIL-100(Fe)	2140	0.88	n.d.
MIL-100(Fe)@NIPAM, 37 wt%	230 (800)	0.12	0.25
MIL-100(Fe)@NIPAM, 78 wt%	300 (1650)	0.16	0.27
Native MIL-100(Cr)	1370	0.84	n.d.
MIL-100(Cr)@NIPAM, 49 wt%	90 (680)	0.14	0.25
MIL-100(Cr)@NIPAM, 58 wt%	150 (800)	0.17	0.26
Native MIL-101(Cr)	2860	1.35	n.d.
MIL-101(Cr)@NIPAM, 46 wt%	720 (1320)	0.37	0.36
MIL-101(Cr)@NIPAM, 71 wt%	960 (2030)	0.47	0.42
MIL-101(Cr)@NIPAM, 92 wt%	980 (2630)	0.50	n.d.

<sup>a</sup> BET surface area calculated at  $0.05 < P \cdot P_0^{-1} < 0.2$  from N<sub>2</sub> sorption isotherm 77 K with a standard deviation  $\pm 20 \text{ m}^2 \cdot \text{g}^{-1}$ .

<sup>b</sup> calculated from N<sub>2</sub> sorption isotherm at 77 K and  $P \cdot P_0^{-1} = 0.95$  for pores  $\leq 20 \text{ nm}$ .

<sup>c</sup> calculated from water sorption isotherm at 293 K and  $P \cdot P_0^{-1} = 0.9$ . Water sorption isotherms of native MILs have not been measured.

<sup>d</sup> BET surface area as the sum of the mass-weighted surface areas of native MILs and native poly(NIPAM)HIPE calculated from the following formula:

$$\begin{aligned} & \text{BET (estimated)} \\ &= \frac{\text{wt\% of native poly(NIPAM)HIPE}}{100} \times 20 \text{ m}^2 \cdot \text{g}^{-1} + \frac{\text{wt\% of native MILs}}{100} \\ & \times 2140 \text{ (MIL - 100Fe) or } 1370 \text{ (MIL - 100Cr) or } 2860 \text{ (MIL - 101Cr) m}^2 \cdot \text{g}^{-1} \end{aligned}$$

## 4.5 Experimental part

### 4.5.1 General section

All experiments were carried out with exposure to air except of the post-synthetic modification reactions, which were done under nitrogen atmosphere using standard Schlenk techniques.

All glassware was cleaned by storage in a KOH/isopropanol bath overnight followed by storage in a diluted HCl bath for several hours (approximately 3–6 h). Between both baths and after the HCl bath, the glassware where rinsed with deionized water and finally dried overnight in an oven at 373 K. Ultrasonic treatment of the MIL@Si(HIPE) composites were done on a Vibra Cell from Sonics. Centrifugation and filtration steps were carried out on centrifuges EBA 8S and Rotina 46 from Hettich. For moisture sensitive compounds, filtrations were done with stainless steel cannulas. MOFs or MOF composites were hydrothermally or solvothermally synthesized using an oven from Memmert with programmable temperature ramps.

Chemicals and solvents (p.a. grade) were commercially purchased and additionally purified as noted in Table 10.

**Table 10.** Chemicals and solvents.

Chemicals	Purity	Source	Additional purification
AlCl <sub>3</sub> ·6H <sub>2</sub> O	99 %	Janssen Chimica	-
2-Aminoterephthalic acid	> 99 %	Acros Organics	-
Ammonium persulfate	≥ 98 %	ROTH	-
1,3,5-Benzenetricarboxylic acid	98 %	Alfa Aesar	-
1,4-Benzenedicarboxylic acid	> 99 %	Acros Organics	-
Cr(NO <sub>3</sub> ) <sub>3</sub> ·9H <sub>2</sub> O	99 %	Acros Organics	-
CrO <sub>3</sub>	99 %	Alfa Aesar	-
Diethylene glycol	≥ 99.0 %	Sigma-Aldrich	-
Ethylenediamine	99 %	Alfa Aesar	-
Ethylene glycol	99 %	Janssen Chimica	-
Fe <sup>0</sup> powder	> 99 %	Riedel-de Haën	-
Formaldehyde	24 % in H <sub>2</sub> O, not buffered	VWR	-
Hydrochloric acid	p.a., 37 % in H <sub>2</sub> O	Fisher Chemical	-
Hydrofluoric acid	48-51 % in H <sub>2</sub> O	Acros Organics	-
2-Hydroxyethyl methacrylate	97 % stabilized with approx. 500 ppm 4-Methoxyphenol	Alfa Aesar	-
<i>N</i> -Isopropylacrylamide	> 98.0 % stabilized with 4-Methoxyphenol	TCI	-
Kolliphor ® P 188	79.9-83.7 %	Sigma-Aldrich	-
<i>N,N'</i> -Methylenebisacrylamide	99 %	Sigma-Aldrich	Recrystallized from methanol
Na <sub>2</sub> CO <sub>3</sub>	≥ 99.8 %	Riedel-de Haën	-
NaOD/D <sub>2</sub> O	40 % in D <sub>2</sub> O	Sigma-Aldrich	-
NaOH	99.99 %	VWR	-
Nitric acid	p.a., 65 % in H <sub>2</sub> O	AppliChem	-
Resorcinol	98 %	Acros Organics	-
Tetradecyltrimethylammonium bromide	98 %	Alfa Aesar	-
Tetraethyl orthosilicate	98 %	Acros Organics	-

Tetramethylammonium hydroxide	25 % in H <sub>2</sub> O	Alfa Aesar	-
<i>N,N,N',N'</i> -Tetramethylethylenediamine	> 99 %	Merck KGaA	-
Triethylene glycol	≥ 99.0 %	J. T. Baker	-
Triton™-X-405	70 % in H <sub>2</sub> O	Sigma-Aldrich	-
Solvents	Purity	Source	Additional purification
Acetic acid	p.a., 99.9 %	VWR	-
Acetone	p.a., 99.9 %	VWR	-
Cyclohexane	p.a., > 99.5 %	Applichem	-
DMF	p.a., 99.99 %	Fisher Chemical	-
Dodecane	p.a., > 99.0 %	TCI	-
Ethanol	p.a., 99.9 %	VWR	-
Methanol	p.a., ≥ 99.99 %	Fisher Chemical	-
THF	p.a., 99.6 %	VWR	-
Toluene <sup>VI</sup>	p.a., 99.99 %	Fisher Chemical	Dried over molecular sieve (4 Å)

<sup>VI</sup> Toluene was additionally dried over molecular sieve (4 Å) before usage leading to a water content of 0.015 wt% (determined by Karl Fischer titration: Analytik Jena AQUA 40.00).

## 4.5.2 Analytical methods

### 4.5.2.1 Powder X-ray diffraction (PXRD)

Powder X-ray diffraction patterns were carried out at ambient temperature on a Bruker D2 phaser (300 W, 30 kV, 10 mA) using Cu-K $\alpha$  radiation ( $\lambda = 1.54182 \text{ \AA}$ ) between  $5^\circ < 2\theta < 40^\circ$  with a scanning rate of 0.006  $^\circ/\text{s}$ . Before each measurement samples were well-ground with a pestle/mortar equipment (both made of agate). The diffractograms were obtained on a flat “low background sample holder”, in which at low angle the beam spot is strongly broadened so that only a fraction of the reflected radiation reaches the detector, hence, the low relative intensities measured at  $2\theta < 7^\circ$ . Analyses of the diffractograms were carried out with the ‘STOE WinXPOW 1.10’ software.

### 4.5.2.2 Fourier transform infrared spectroscopy (FT-IR)

Infrared spectra were measured on a Bruker TENSOR 37 IR spectrometer at ambient temperature in a wavenumber region of 4000–500  $\text{cm}^{-1}$ . Solid compounds were measured in a KBr disk, liquids on a diamond ATR unit. For preparation of the KBr disks, the samples were well-ground with an excess of KBr (20–40 fold amount) in an agate mortar followed by pressure/vacuum treatment in a RiIC England/London 30 ton press (10 ton were used). Evaluations of the spectra were done with the software ‘OPUS 7.2’.

### 4.5.2.3 Nitrogen, water and methanol sorption analyses

Nitrogen (purity 99.9990 %) physisorption isotherms were carried out on a Nova 4000e from Quantachrome at 77 K. Water and methanol physisorption isotherms were measured volumetrically on a Quantachrome Autosorb iQ MP at 293 K. Before measuring of the isotherms, the products were transferred into glass tubes capped with septa, which were weighted out before. These tubes were attached to the corresponding degassing port of the sorption analyzer, degassed under vacuum at elevated temperature, weighted out again and then transferred to the analysis port of the sorption analyzer. For determination of the cold and warm free space of the sample tubes helium gas was used. BET surface areas were calculated from the nitrogen adsorption isotherms in the  $P/P_0^{-1}$  range of 0.05–0.2. Total pore volumes were calculated from the nitrogen sorption isotherm at  $P/P_0^{-1} = 0.95$ . DFT calculations for the pore size distribution curves were done with the native ‘NovaWin 11.03’

software using the 'N<sub>2</sub> at 77 K on carbon, slit pore, NLDFT equilibrium' model.<sup>242</sup> For vapor sorption measurements the 'ASiQwin 3.01' software was applied.

#### 4.5.2.4 Water cycling measurement

Cyclic water ad- and desorption measurement of the EN grafted MIL-100(Cr) compound (see 3.1) was performed in a Setaram TG-DSC 111, where samples were exposed to an argon flow humidified by a Setaram WetSys. Ad- and desorption cycles were carried out in a temperature range of 313–413 K over 20 cycles with a constant vapor pressure of 5.6 kPa. One cycle was finished within 4 hours.

#### 4.5.2.5 NMR spectroscopy

Solution NMR spectra of the EG, DEG, TEG and EN modified MIL-100(Cr) materials were recorded on a Bruker Avance DRX200 operating at 200 MHz for <sup>1</sup>H. The proton NMR spectra were calibrated against the residual proton resonances of the deuterated solvent relative to tetramethylsilane: D<sub>2</sub>O/NaOD δ<sub>H</sub> = 4.79 ppm. Preparation of the NMR tubes was carried out with exposure to air. Processing of the <sup>1</sup>H NMR spectra were done with 'SpinWorks 3.1.7'.

#### 4.5.2.6 Scanning electron microscopy

Scanning electron microscopic images were recorded on the following devices (Information about sputtering of the samples before measuring is given in the brackets):

*VEGA3 Easyprobe* from Tescan, equipped with a tungsten cathode (no sputtering).

*LEO 982* from Zeiss with a Schottky field electron emission cathode (sputtered with chromium; approximately 10 nm thickness).

*LEO 1430 VP* from Zeiss with a tungsten cathode (coating with Au for 180 sec at 30 mA by an AGAR sputter coater).

*Quanta 400 FEG* (ESEM) from Fei. Electrons are generated by field emission (coating with Au/Pd (80:20) using an Emitech K550 sputter for 1 min at 15 mA).

*JSM-6510* from Jeol with a LaB<sub>6</sub> cathode (coating Au for 20 sec at 35 mA by Jeol JFC-1200 sputter).

Figure captions of the SEM images in this work contain the information which type of device was used.



#### 4.5.2.7 Thermogravimetric analyses

The thermogravimetric analysis curves were measured on a TG 209 F3 Tarsus from Netzsch in a temperature range of 303–873 K, with a heating rate of 3 K·min<sup>-1</sup>, using the software 'Netzsch Measurement 5.2.1'.

#### 4.5.2.8 Atomic absorption spectrometry

The quantification of the chromium and iron content of the MIL@HEMA (Route B) composites were done on a Perkin-Elmer AAnalyst 100 atomic absorption spectrometer. An acetylene/air burner was used to atomize the metals (approximately 2570 K). Hollow-cathode lamps with wavelengths of 357.9 nm (Cr) and 248.3 nm (Fe) were used. The gap widths were 0.7 nm for chromium and 0.2 nm for iron. For each metal reference solutions were prepared with concentrations of 10, 5 and 1 mg·L<sup>-1</sup>. The well-ground composites were weighted out and stirred in aqueous, saturated NaOH solution overnight. After acidification with concentrated HCl, the suspensions were filtered into volumetric flasks and diluted with deionized water. The 'AA Winlab 2.6.1' software was used.

## 4.5.3 Syntheses

### 4.5.3.1 Syntheses of MIL-101(Cr)-x, x = EG, DEG, TEG

The activated, solid MIL-101(Cr) materials (100 mg) were placed in 50 mL two-necked flasks and degassed for 1.5 h *in vacuo* at 473 K to remove any adsorbed water or solvent from the metal sites, thus giving the coordinatively unsaturated sites (CUS). After cooling to r.t., 10 mL of dry toluene (water content of 0.015 %, determined by Karl Fischer titration) and 1.0 mL of EG ( $\rho = 1.11 \text{ g}\cdot\text{mL}^{-1}$ ; 18 mmol), 1.0 mL of DEG ( $\rho = 1.12 \text{ g}\cdot\text{mL}^{-1}$ ; 11 mmol) or 1.0 mL of TEG ( $\rho = 1.12 \text{ g}\cdot\text{mL}^{-1}$ ; 7.5 mmol) were added respectively. The suspensions were stirred for 16 h at 373 K and additional 28 h at r.t. Then the green solids were filtered from the clear supernatants. The crude products were washed with acetone (2 x 5 mL) and dried for 1 h *in vacuo* at r.t. In all three cases powders were isolated with the same colors compared to the starting material. 101 mg (MIL-101(Cr)-EG, MIL-101(Cr)-DEG) and 102 mg (MIL-101(Cr)-TEG) of green powders were isolated and stored with exposure to air.

### 4.5.3.2 Synthesis of meso-/macroporous Si(HIPE)

Si(HIPE) (1-SiHIPE0.035) was synthesized according to the literature.<sup>230</sup> A 35 wt% solution of 4.0 g TTAB (12 mmol) in 7.5 mL of deionized water was prepared in a 50 mL polystyrene mold. 1.5 mL of concentrated hydrochloric acid ( $\rho = 1.19 \text{ g}\cdot\text{mL}^{-1}$ ; 18 mmol) was added under stirring. After that 1.3 mL of TEOS ( $\rho = 0.94 \text{ g}\cdot\text{mL}^{-1}$ ; 5.9 mmol) was added dropwise continued by further stirring for 15 min. After addition of TEOS, the solution became more viscous. Then 11.7 mL of dodecane was added to this solution by a dropping funnel followed by further stirring for 10 min and curing for 7 d at r.t. After one day the emulsion changed into a solid, cured monolith. The monolithic raw product was released from the mold and consecutively washed in deionized water (6 x 200 mL, 24 each washing step) under constant stirring. The white monolith was stored in THF/Aceton (1:1, ratio of volumes, 3 x 70 mL, 24 h each washing step) without stirring followed by drying for 24 h at r.t.<sup>VII</sup> During this step the monolith contracted to approximately  $1/_{10}$  of the primary volume resulting in large cracks. After oven drying for 18 h at 373 K (heating rate: 3 h), the granulated material was further washed for 4 h in 80 mL of DMF at 383 K. After a short washing step in deionized water (2 x 20 mL),

---

<sup>VII</sup> If the raw product is exclusively washed in a mixture of THF/Aceton, as described in the given literature, the final product contained large impurities of TTAB. Therefore, a modified washing procedure was applied with first washing steps in deionized water to remove TTAB and final washing steps with THF/Aceton to remove the oily phase.

the material was finally dried for 15 h at 463 K (heating rate: 2 h). 290 mg of a white, granulated material was obtained.

#### 4.5.3.3 Syntheses of MIL-101(Cr)@Si(HIPE) composites via route A

This section describes the syntheses of MIL-101(Cr)@Si(HIPE) composites via route A. This means that different amounts of pre-formed MIL powder were added during the Si(HIPE) synthesis before curing. The composites were synthesized in three different ways: The MIL powders were added (i) before addition of hydrochloric acid *MIL-101(Cr)@Si(HIPE)-before HCl*, (ii) after addition of TEOS *MIL-101(Cr)@Si(HIPE)-after TEOS* and (iii) after adding the oily dodecane phase *MIL-101(Cr)@Si(HIPE)-after dodecane*. '50' and '100', as part of the name, stand for the weight of MIL-101(Cr) powder in mg, which was added.

**(i) MIL-101(Cr)(50/100)@Si(HIPE)-before HCl:** Two separate 35 wt% solutions, each with 4.0 g of TTAB (12 mmol) in 7.5 mL of deionized water were prepared in 50 mL polystyrene vessels. 50 and 100 mg of well-ground MIL-101(Cr) powder were added to each solution respectively. The green suspensions were stirred for 10 min followed by ultrasonic treatment for further 10 min. 1.5 mL of concentrated hydrochloric acid ( $\rho = 1.19 \text{ g}\cdot\text{mL}^{-1}$ ; 18 mmol) was added under stirring to each suspension. After that 1.3 mL of TEOS ( $\rho = 0.94 \text{ g}\cdot\text{mL}^{-1}$ ; 5.9 mmol) was added dropwise into each vessel continued by further stirring for 15 min. After addition of TEOS, the suspensions became more viscous. Then 11.7 mL of dodecane was added to each suspension by a dropping funnel followed by further stirring for 10 min and curing for 7 d at r.t. After one day the suspensions changed into solid, cured, green monoliths. The monolithic raw products were released from the vessels and washed consecutively in deionized water (6 x 200 mL, 24 h each washing step) under constant stirring. The green monoliths were stored in THF/Aceton (1:1, ratio of volumes, 3 x 80 mL, 24 h each washing step) without stirring followed by drying for 24 h at r.t. During this step the monoliths contracted to approximately  $1/10$  of the primary volume resulting in large cracks. After oven drying for 18 h at 373 K (heating rate: 3 h), the granulated materials were further washed for 4 h in 80 mL of DMF at 383 K. After a short washing step in deionized water (2 x 20 mL), the materials were finally dried for 15 h at 463 K (heating rate: 2 h). 338 and 390 mg of green, granulated materials were obtained. Both composite materials were labeled as *MIL-101(Cr)(X)@Si(HIPE)-before HCl*,  $X = 50, 100$ .

**(ii) MIL-101(Cr)(50/100)@Si(HIPE)-after TEOS:** Two separate 35 wt% solutions, each with 4.0 g of TTAB (12 mmol) in 7.5 mL of deionized water were prepared in 50 mL polystyrene vessels. 1.5 mL of concentrated hydrochloric acid ( $\rho = 1.19 \text{ g}\cdot\text{mL}^{-1}$ ; 18 mmol) was added under stirring to each solution. After that 1.3 mL of TEOS ( $\rho = 0.94 \text{ g}\cdot\text{mL}^{-1}$ ; 5.9 mmol) was added dropwise into each vessel continued by further stirring for 10 min. 50 and 100 mg of well-ground MIL-101(Cr) powder were added to each solution respectively continued by further stirring for 5 min. Then 11.7 mL of dodecane was added to each suspension by a dropping funnel followed by further stirring for 10 min and curing for 7 d at r.t. The monolithic raw products were washed consecutively in deionized water (6 x 200 mL, 24 each washing step) under constant stirring. The green monoliths were stored in THF/Aceton (1:1, ratio of volumes, 3 x 70 mL, 24 h each washing step) without stirring followed by drying for 24 h at r.t. After oven drying for 18 h at 373 K (heating rate: 3 h), the granulated materials were further washed for 4 h in 70 mL of DMF at 383 K. After a short washing step in deionized water (2 x 20 mL), the materials were finally dried for 15 h at 463 K (heating rate: 2 h). 336 and 398 mg of green, granulated materials were obtained. Both composite materials were labeled as *MIL-101(Cr)(X)@Si(HIPE)-after TEOS*,  $X = 50, 100$ .

**(iii) MIL-101(Cr)(50/100)@Si(HIPE)-after dodecane:** Two separate 35 wt% solutions, each with 4.0 g of TTAB (12 mmol) in 7.5 mL of deionized water were prepared in 50 mL polystyrene vessels. 1.5 mL of concentrated hydrochloric acid ( $\rho = 1.19 \text{ g}\cdot\text{mL}^{-1}$ ; 18 mmol) was added under stirring to each solution. After that 1.3 mL of TEOS ( $\rho = 0.94 \text{ g}\cdot\text{mL}^{-1}$ ; 5.9 mmol) was added dropwise into each vessel continued by further stirring for 15 min. Then 11.7 mL of dodecane was added to each solution by a dropping funnel followed by further stirring for 10 min. 50 and 100 mg of well-ground MIL-101(Cr) powder were added to each solution, which were further stirred for 15 min and cured for 10 d at r.t. The monolithic raw products were washed in deionized water (6 x 200 mL, 24 h each washing step) under constant stirring. The green monoliths were stored in THF/Aceton (1:1, ratio of volumes, 3 x 70 mL, 24 h each washing step) without stirring followed by drying for 24 h at r.t. After oven drying for 18 h at 373 K (heating rate: 3 h), the granulated materials were further washed for 3 h in 70 mL of DMF at 383 K. After a short washing step in deionized water (2 x 20 mL), the materials were finally dried for 15 h at 463 K (heating rate: 2 h). 340 and 392 mg of green, granulated materials were obtained. Both composite materials were labeled as *MIL-101(Cr)(X)@Si(HIPE)-after dodecane*,  $X = 50, 100$ .

#### 4.5.3.4 Syntheses of MIL-100(Cr)/101(Cr)@Si(HIPE) composites via route B

Syntheses of MIL@Si(HIPE) composites via route B are depicted in this section. Therefore the pre-formed Si(HIPE) granulates were firstly soaked with MIL precursors (metal source, ligand) followed by hydrothermal treatment at the appropriate temperature program. The obtained composites are labeled as (i) *MIL-100(Cr)@Si(HIPE)-hydrothermal* and (ii) *MIL-101(Cr)@Si(HIPE)-hydrothermal*. Excessive MIL powders were additionally obtained in both syntheses, which are named as (i) *MIL-100(Cr)-residual* and (ii) *MIL-101(Cr)-residual*.

**(i) MIL-100(Cr)@Si(HIPE)-hydrothermal:**<sup>243</sup> 0.21 g CrO<sub>3</sub> (2.1 mmol), 0.44 g H<sub>3</sub>BTC (2.1 mmol), 0.07 mL hydrofluoric acid (2 mmol; 48-51wt% in H<sub>2</sub>O) and 64 mg of Si(HIPE) were stirred in 8 mL of deionized water for 19 h at r.t. in a 25 mL round bottom flask to ensure that the Si(HIPE) is fully soaked with starting materials. The entire reaction slurry is transferred into a Teflon-liner and the flask is washed with deionized water (2 x 1 mL). The Teflon-liner was placed in an autoclave and heated to 473 K within 10 h. After 96 h the autoclave was cooled to r.t. within 2 h. The composite material was separated from the residual MIL powder and shortly washed in deionized water (3 x 10 mL). MIL-100(Cr)@Si(HIPE)-hydrothermal and MIL-100(Cr)-residual, which was centrifuged off, were consecutively and separately washed in DMF [1 x 20 mL (composite) and 1 x 50 mL (residual MIL), 2 h, 383 K], EtOH [1 x 20 mL (composite) and 1 x 50 mL (residual MIL), 2 h, 333 K] and deionized water [1 x 20 mL (composite) and 1 x 50 mL (residual MIL), 2 h, 353 K]. After drying for 19 h at 353 K 71 mg of green, granulated MIL-100(Cr)@Si(HIPE)-hydrothermal and 643 mg of green MIL-100(Cr)-residual powder were obtained.

**(ii) MIL-101(Cr)@Si(HIPE)-hydrothermal:**<sup>232</sup> 1.20 g Cr(NO<sub>3</sub>)<sub>3</sub>·9H<sub>2</sub>O (3.0 mmol), 0.50 g H<sub>2</sub>BDC (3.0 mmol), 0.27 mL TMAOH (0.75 mmol; ρ = 1.014 g·mL<sup>-1</sup>; 25 wt% in H<sub>2</sub>O) and 178 mg of Si(HIPE) were stirred in 13 mL of deionized water for 72 h at r.t. in a 50 mL round bottom flask to ensure that the Si(HIPE) is fully soaked with starting materials. The entire reaction slurry is transferred into a Teflon-liner and the flask is washed with deionized water (2 x 1 mL). The Teflon-liner was placed in an autoclave and heated to 453 K within 10 h. After 24 h the autoclave was cooled to r.t. within 18 h. The composite material was separated from the residual MIL powder and shortly washed in deionized water (3 x 10 mL). MIL-101(Cr)@Si(HIPE)-hydrothermal and MIL-101(Cr)-residual, which was centrifuged off, were consecutively and separately washed in DMF [1 x 30 mL (composite) and 1 x 50 mL (residual MIL), 2 h, 383 K], EtOH [1 x 30 mL (composite) and 1 x 50 mL (residual MIL), 2 h, 333 K] and deionized water [1 x 30 mL (composite) and 1 x 50 mL (residual MIL), 2.5 h, 353

K]. After drying for 25 h at 353 K 198 mg of green, granulated MIL-101(Cr)@Si(HIPE)-hydrothermal and 558 mg of green MIL-101(Cr)-residual powder were obtained.

#### 4.5.3.5 Synthesis of macroporous Poly(HEMA)HIPEs

Poly(HEMA)HIPEs with 13, 20 and 30 mol% of *N,N'*-methylenebisacrylamide were prepared according to the literature.<sup>192</sup> 2-Hydroxyethyl methacrylate (HEMA) was added dropwise to deionized water. After adding different amounts of *N,N'*-methylenebisacrylamide (MBA), ammonium persulfate (APS) and the surfactant Kolliphor® P188 to the aqueous solution, the mixtures were stirred for 10 min. Then cyclohexane was added to the clear solutions via a dropping funnel. After that, the mixtures were further stirred for 30 min. *N,N,N',N'*-Tetramethylethylenediamine (TMEDA) was then added dropwise to the emulsions and the mixtures were further stirred for 3 min. The white, viscous crude products were filled into appropriate molds and cured for 3 days at r.t. A washing procedure with deionized water (6 x 150 mL, min. 14 h for each washing step) for each product was followed by drying the monoliths for 23 h at 353 K.<sup>viii</sup> 1.61 g (13 mol% MBA), 1.10 g (20 mol% MBA) and 1.83 g (30 mol% MBA) of mechanically stable white monoliths with different shapes were isolated (see Table 11 for precise masses/volumes of the starting materials).

**Table 11.** Syntheses of poly(HEMA)HIPEs with different mol% of MBA.

Starting materials	Poly(HEMA)HIPE (13 mol% MBA)	Poly(HEMA)HIPE (20 mol% MBA)	Poly(HEMA)HIPE (30 mol% MBA)
HEMA ( $\rho = 1.071 \text{ g}\cdot\text{mL}^{-1}$ )	1.03 mL (8.45 mmol)	1.03 mL (8.45 mmol)	1.03 mL (8.45 mmol)
MBA	200 mg (1.30 mmol)	326 mg (2.11 mmol)	558 mg (3.62 mmol)
Deionized water	2.60 g	2.60 g	2.60 g
APS	35 mg (0.15 mmol)	35 mg (0.15 mmol)	35 mg (0.15 mmol)
Kolliphor® P188	750 mg	750 mg	750 mg
TMEDA	0.15 mL (0.20 mmol) <sup>a</sup>	30 $\mu\text{L}$ (0.20 mmol) <sup>b</sup>	30 $\mu\text{L}$ (0.20 mmol) <sup>b</sup>
Cyclohexane	11.0 mL	11.0 mL	11.0 mL

<sup>a</sup> 20 vol% TMEDA (TMEDA : deionized water: 1 : 4;  $c = 1.3 \text{ mmol}\cdot\text{mL}^{-1}$ ).

<sup>b</sup> Pure TMEDA was used ( $\rho = 0.78 \text{ g}\cdot\text{mL}^{-1}$ ).

<sup>viii</sup> The washing procedure differed from that described in the literature. Instead of 2-propanol, deionized water was used due to the better solubility of HEMA, MBA, APS, surfactant and TMEDA in water.

#### 4.5.3.6 Syntheses of MIL-100(Fe,Cr)/101(Cr)@HEMA composites via route B

Syntheses of MIL@poly(HEMA)HIPE-hydrothermal (in short MIL@HEMA) composites via route B are presented in this section. The pre-formed native poly(HEMA)HIPE monoliths (13 mol% MBA) were firstly stirred in MIL precursors (metal source, ligand) in deionized water followed by hydrothermal treatment at the needed temperature. The obtained composites are labeled as (i) *MIL-100(Fe)@HEMA-hydrothermal*, (ii) *MIL-100(Cr)@HEMA-hydrothermal* and (iii) *MIL-101(Cr)@HEMA-hydrothermal*. Excessive MIL powders were additionally obtained in the syntheses, which are named as (i) *MIL-100(Fe)-residual*, (ii) *MIL-100(Cr)-residual* and (iii) *MIL-101(Cr)-residual*.

**(i) MIL-100(Fe)@HEMA-hydrothermal:**<sup>244</sup> 665 mg of Fe<sup>0</sup> powder (11.9 mmol), 1.65 g H<sub>3</sub>BTC (7.85 mmol), 0.83 mL hydrofluoric acid (24 mmol; 48-51 wt% in H<sub>2</sub>O), 0.5 mL HNO<sub>3</sub> (7 mmol; 65 wt%) and 340 mg of monolithic, native poly(HEMA)HIPE (13 mol% MBA) were stirred in 50 mL of deionized water for 22 h at r.t. in a round bottom flask to ensure that the native poly(HEMA)HIPE is fully soaked with starting materials. The entire reaction slurry is transferred into a Teflon-liner and the flask is additionally washed with deionized water (2 x 5 mL). The Teflon-liner was placed in an autoclave and heated to 423 K within 2 h. After 12 h the autoclave was cooled to r.t. within 2 h. The composite material was separated from the residual MIL powder and shortly washed in deionized water (2 x 10 mL). MIL-100(Fe)@HEMA-hydrothermal and MIL-100(Fe)-residual, which was centrifuged off, were consecutively and separately washed in DMF [1 x 100 mL, 22 h, 383 K], EtOH [1 x 100 mL, 20 h, 333 K] and deionized water [1 x 100 mL, 24 h, 353 K]. MIL-100(Fe)-residual was dried for 24 h at 333 K. The composite was first dried for 24 h at 333 K, then additional 24 h at 353 K. 739 mg of MIL-100(Fe)@HEMA-hydrothermal as an orange brown monolith and 600 mg of orange-brown MIL-100(Fe)-residual powder were obtained.

**(ii) MIL-100(Cr)@HEMA-hydrothermal:**<sup>243</sup> 1.80 g CrO<sub>3</sub> (18.0 mmol), 3.78 g H<sub>3</sub>BTC (18.0 mmol), 0.63 mL hydrofluoric acid (18 mmol; 48-51 wt% in H<sub>2</sub>O) and 340 mg of monolithic, native poly(HEMA)HIPE (13 mol% MBA) were stirred in 80 mL of deionized water for 20 h at r.t. in a round bottom flask to ensure that the native poly(HEMA)HIPE is fully soaked with starting materials. The entire reaction slurry is transferred into a Teflon-liner and the flask is additionally washed with deionized water (2 x 4 mL). The Teflon-liner was placed in an autoclave and heated to 473 K within 10 h. After 96 h the autoclave was cooled to r.t. within 2 h. The composite material was separated from the residual MIL powder and shortly washed in deionized water (2 x 10 mL). MIL-100(Cr)@HEMA-hydrothermal and

MIL-100(Cr)-residual, which was centrifuged off, were consecutively and separately washed in DMF [1 x 100 mL, 23 h, 383 K], EtOH [1 x 100 mL, 24 h, 333 K] and deionized water [1 x 100 mL, 23 h, 353 K]. MIL-100(Cr)-residual was dried for 96 h at 333 K. The composite was first dried for 96 h at 333 K, then additional 24 h at 353 K. 3.96 g of MIL-100(Cr)@HEMA-hydrothermal as a green monolith and 240 mg of green MIL-100(Cr)-residual powder were obtained.

**(iii) MIL-101(Cr)@HEMA-hydrothermal.**<sup>232</sup> 4.80 g Cr(NO<sub>3</sub>)<sub>3</sub>·9H<sub>2</sub>O (12.0 mmol), 1.98 g H<sub>2</sub>BDC (11.9 mmol), 1.1 mL TMAOH (3.1 mmol; ρ = 1.014 g·mL<sup>-1</sup>; 25 wt% in H<sub>2</sub>O) and 305 mg of monolithic, native poly(HEMA)HIPE (13 mol% MBA) were stirred in 50 mL of deionized water for 20 h at r.t. in a round bottom flask to ensure that the native poly(HEMA)HIPE is fully soaked with starting materials. The entire reaction slurry is transferred into a Teflon-liner and the flask is additionally washed with deionized water (2 x 5 mL). The Teflon-liner was placed in an autoclave and heated to 453 K within 10 h. After 24 h the autoclave was cooled to r.t. within 18 h. The composite material was separated from the residual MIL powder and shortly washed in deionized water (2 x 10 mL). MIL-101(Cr)@HEMA-hydrothermal and MIL-101(Cr)-residual, which was centrifuged off, were consecutively and separately washed in DMF [1 x 100 mL, 23 h, 383 K], EtOH [1 x 100 mL, 22 h, 333 K] and deionized water [1 x 100 mL, 24 h, 353 K]. MIL-101(Cr)-residual was dried for 22 h at 333 K. The composite was first dried for 22 h at 333 K, then additional 24 h at 353 K. 2.89 g of MIL-101(Cr)@HEMA-hydrothermal as a green monolith and 250 mg of green MIL-101(Cr)-residual powder were obtained.

The loadings of the MILs in MIL@HEMA-hydrothermal were estimated gravimetrically, assuming no MOF powder is lost during the syntheses and additional by AAS spectroscopy (Table 12).

**Table 12.** wt% of MILs in MIL@(HEMA)-hydrothermal composites (in short MIL@HEMA).

MIL@HEMA-hydrothermal composites	Gravimetrical analysis <sup>a</sup>	AAS spectroscopy
MIL-100(Fe)	54 wt%	58 wt%
MIL-100(Cr)	91 wt%	93 wt%
MIL-101(Cr)	89 wt%	91 wt%

<sup>a</sup>

$$\text{wt\% (MIL in MIL@HEMA)} = \frac{m(\text{MIL@HEMA}) - m(\text{weighted poly(HEMA)HIPE})}{m(\text{MIL@HEMA})} \times 100$$



#### 4.5.3.7 Synthesis of macroporous Poly(NIPAM)HIPEs

Poly(NIPAM)HIPEs with 9, 13 and 17 mol% of *N,N'*-methylenebisacrylamide were prepared according to the literature.<sup>238a</sup> 4.0 mL of an aqueous solution, containing 1.0 mol·L<sup>-1</sup> of *N*-isopropylacrylamide (4.0 mmol) and 0.05 mol·L<sup>-1</sup> of *N,N'*-methylenebisacrylamide (0.2 mmol) was added into 50 mL beakers respectively. 30 mg (0.19 mmol; 9 mol% MBA), 62 mg (0.40 mmol; 13 mol% MBA) and 92 mg (0.60 mmol; 17 mol% MBA) of MBA were then added additionally to the solutions under constant stirring for 5 min. 0.6 mL of Triton™-X-405 ( $\rho = 1.096 \text{ g}\cdot\text{mL}^{-1}$ ; 70 wt% in H<sub>2</sub>O;  $c = 0.39 \text{ mol}\cdot\text{L}^{-1}$ ; 0.2 mmol) was added respectively followed by addition of 0.20 mL of an aqueous ammonium persulfate solution for each solution (10 wt% in H<sub>2</sub>O;  $c = 0.49 \text{ mol}\cdot\text{L}^{-1}$ ; 0.098 mmol). After stirring for 10 min, 12.0 mL of cyclohexane was slowly dropped into each solution continued by further stirring for 10 min. 60  $\mu\text{L}$  of *N,N,N',N'*-tetramethylethylenediamine ( $\rho = 0.78 \text{ g}\cdot\text{mL}^{-1}$ ; 0.40 mmol) was added respectively followed by stirring for 10 min. The white, viscous crude products were filled into Teflon-liners and cured for 3 days at 333 K. A washing procedure with deionized water (6 x 150 mL, min. 6 h for each washing step) for each product was followed by drying the monoliths consecutively for 24 h at 313 K, 333 K and 353 K. 0.54 g (9 mol% MBA), 0.29 g (13 mol% MBA) and 0.53 g (17 mol% MBA) of white materials were isolated. Poly(NIPAM)HIPE with 17 mol% of MBA led to a monolithic shape even though shrinkage of approximately 50 % of the original volume was noted during drying. Using 9 and 13 mol% of cross-linking led to monoliths with pronounced shrinkage, deformation and cracks.

#### 4.5.3.8 Syntheses of MIL-100(Fe,Cr)/101(Cr)@NIPAM composites via route A

Herein, the syntheses of MIL@poly(NIPAM)HIPEs composites (in short MIL@NIPAM) via route A are described. Different amounts of pre-formed MIL-100(Fe), MIL-100(Cr) and MIL-101(Cr) powders were added during the poly(NIPAM)HIPE synthesis before curing, yielding composites labeled as (ii) *MIL-100(Fe)@(NIPAM)HIPE*, (iii) *MIL-100(Cr)@(NIPAM)HIPE* and (iv) *MIL-101(Cr)@(NIPAM)HIPE*. Before synthesizing MIL@NIPAM composites, pre-polymerization experiments with native poly(NIPAM)HIPE have been carried out (i).

##### (i) Pre-polymerization experiments with native poly(NIPAM)HIPE emulsion

Poly(NIPAM)HIPE emulsions (17 mol% MBA) were prepared according to section 4.5.3.7. After adding TMEDA, the emulsions were further stirred for 10 min, 20 min, 30 min, 1 h and 2 h before curing for 3 days at 333 K. Only a stirring time of 10 min gave reasonable curing of the emulsion yielding a monolithic shape. Separation of the emulsions occurred if the stirring time exceeded 10 min.

##### (ii) MIL-100(Fe)@NIPAM

2.0 mL of an aqueous solution containing  $1.0 \text{ mol}\cdot\text{L}^{-1}$  of *N*-isopropylacrylamide (2.0 mmol) and  $0.05 \text{ mol}\cdot\text{L}^{-1}$  of *N,N'*-methylenebisacrylamide (0.1 mmol) was added into a 50 mL beaker. 46 mg of MBA (0.30 mmol; 17 mol% MBA) was then added additionally to the solution under constant stirring for 5 min. 0.3 mL of Triton<sup>TM</sup>-X-405 ( $\rho = 1.096 \text{ g}\cdot\text{mL}^{-1}$ ; 70 wt% in  $\text{H}_2\text{O}$ ;  $c = 0.39 \text{ mol}\cdot\text{L}^{-1}$ ; 0.1 mmol) was added followed by addition of 0.10 mL of an aqueous ammonium persulfate solution (10 wt% in  $\text{H}_2\text{O}$ ;  $c = 0.49 \text{ mol}\cdot\text{L}^{-1}$ ; 0.049 mmol). After stirring for 10 min, 6.0 mL of cyclohexane was slowly dropped into the solution continued by further stirring for 10 min. 30  $\mu\text{L}$  of *N,N,N',N'*-tetramethylethylenediamine ( $\rho = 0.78 \text{ g}\cdot\text{mL}^{-1}$ ; 0.20 mmol) was added followed by stirring for 5 min. For preparing the composite materials, plastic syringes (5 mL) were prepared in advance. They were cut off from one side and filled with a specific mass of well-ground MIL-100(Fe) powder and the just prepared emulsion (syringe 1: 100 mg MIL + 1008 mg emulsion, syringe 2: 75 mg MIL + 1002 mg emulsion, syringe 3: 50 mg MIL + 1025 mg emulsion, syringe 4: 25 mg MIL + 1012 mg emulsion). Each syringe was stirred well by a spatula for further 5 min (total stirring time after adding TMEDA: 10 min). The orange-brown, crude products were compressed and cured for 2 days at 333 K. A washing procedure with deionized water (6 x 150 mL, min. 7 h for each washing step) for

each product was followed by drying the monoliths consecutively for 24 h at 313 K, 333 K and 353 K. The orange-brown monoliths from syringes 1 and 2 crumbled during the washing procedure. 64 mg (**78 wt%**, syringe 3) and 68 mg (**37 wt%**, syringe 4) of orange-brown materials with pronounced shrinkage and deformation were isolated. The loadings of the MILs in MIL@(NIPAM)HIPEs were calculated from formula 5.

**Formula 5.** Used for calculations of wt% MIL in MIL@(NIPAM)HIPEs (in short MIL@NIPAM).

$$\text{wt\% (MIL in MIL@NIPAM)} = \frac{m(\text{weighted MIL})}{m(\text{MIL@NIPAM})} \times 100$$

### (iii) MIL-100(Cr)@NIPAM

Preparation of the poly(NIPAM)HIPE emulsions, curing, washing and drying were done in the same way like described in (i). Syringes were filled with different amounts of well-ground MIL-100(Cr) powder and pre-polymerized emulsions in the following way (syringe 1: 100 mg MIL + 1005 mg emulsion, syringe 2: 75 mg MIL + 1002 mg emulsion, syringe 3: 50 mg MIL + 1013 mg emulsion, syringe 4: 25 mg MIL + 1027 mg emulsion). The green monoliths from syringes 1 and 2 crumbled during the washing procedure. 86 mg (**58 wt%**, syringe 3) and 51 mg (**49 wt%**, syringe 4) of green materials with pronounced shrinkage and deformation were isolated.

### (iv) MIL-101(Cr)@NIPAM

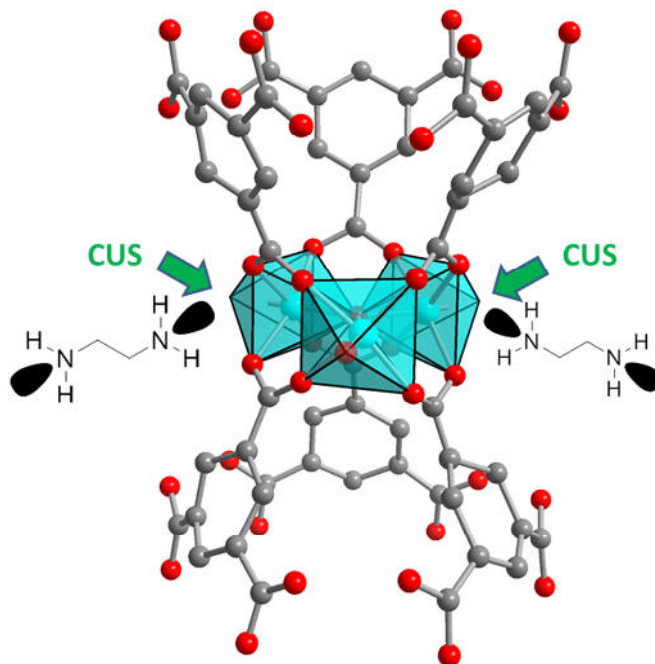
Preparation of the poly(NIPAM)HIPE emulsions, curing, washing and drying were done in the same way like described in (i). Syringes were filled with different amounts of well-ground MIL-101(Cr) powder and pre-polymerized emulsions in the following way (syringe 1: 100 mg MIL + 1006 mg emulsion, syringe 2: 75 mg MIL + 1022 mg emulsion, syringe 3: 50 mg MIL + 1002 mg emulsion. 109 mg (**92 wt%**, syringe 1), 105 mg (**71 wt%**, syringe 2) and 109 mg (**46 wt%**, syringe 3) of green materials with pronounced shrinkage and deformation were isolated.

## 5. Summary

The following six sections give a short overview about the work, which has been done in this thesis. Section 5.1 sums up the results of the post-synthetic modifications of MIL-100(Cr) and MIL-101(Cr) with small glycols and amines. Sections 5.2–5.5 abstract the type of composites, synthesized in this work, ordered by the corresponding template materials: Si(HIPE), poly(HEMA)HIPE, poly(NIPAM)HIPE and R,F-xerogel. Section 5.6 gives an overall summary.

### 5.1 Grafting of MIL-100(Cr) and MIL-101(Cr)

Grafting of coordinatively, unsaturated chromium sites in MIL-100(Cr) and MIL-101(Cr) with EG (ethylene glycol), DEG (diethylene glycol) and TEG (triethylene glycol) were carried out successfully by simply adding the grafting reagents to powdery MILs after activated in vacuum and high temperature. MIL-100(Cr) could be additionally modified with EN (Scheme 6).



**Scheme 6.** Schematic illustration of grafting of ethylenediamine to coordinatively, unsaturated metal sites (CUS) at the secondary building unit of MIL-100(Cr).<sup>128</sup>

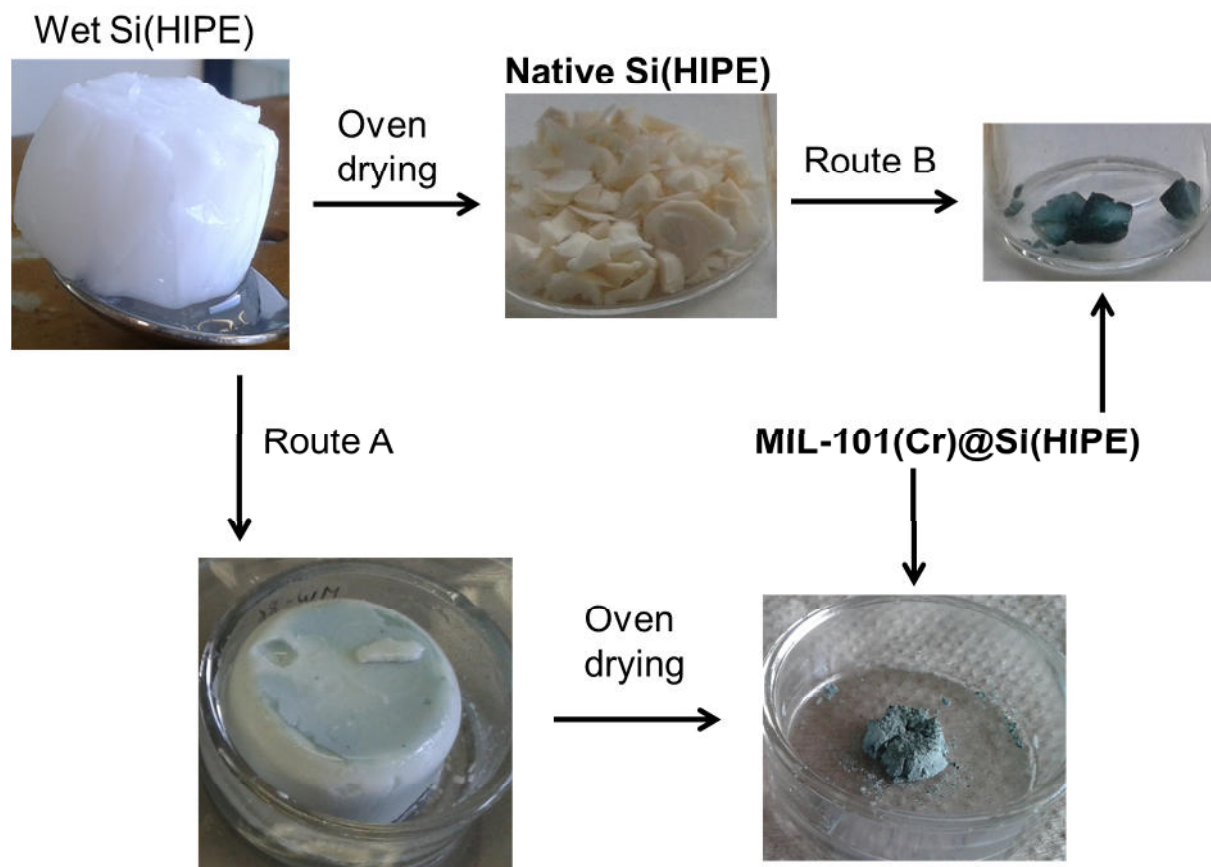
Powder X-ray diffraction patterns of both modified MILs show no loss in crystallinity and infrared spectroscopic analyses reveal the presence of the anticipated, newly introduced groups with a shift to higher wavenumbers, therefore proving the successful coordination onto chromium(III). The BET surface areas of both modified MILs are decreased to

approximately 50 % compared to the BET surface areas of the pure MILs. Pore size distribution curves show that grafting of MIL-100(Cr) leads to formation of novel, smaller pores in addition to the original pores, whereas grafting of MIL-101(Cr) with glycols only shows a slight reduction of one single pore. Water sorption measurements of EG-, DEG- and TEG grafted MIL-101(Cr) have shown that modifications lead to a pronounced loss of total water uptakes in comparison to native MIL-101 without any significant shift of the water adsorption isotherms to lower partial pressures. Only MIL-101(Cr)-TEG presents a slight improvement over pure MIL, but only in a very small pressure range between  $0.30 < P \cdot P_0^{-1} < 0.36$ . Stability tests have proven that TEG-modified MIL shows the least degradation among the glycol-modified MIL-101(Cr).

More satisfying results were obtained by grafting of MIL-100(Cr). In spite of the reduction of the BET surface areas after grafting, the water loadings remain comparatively high. Water loading capacity is not only determined by the available surface area, but also by the hydrophilicity or hydrophobicity of the ligand, hydrogen bonding, directing and interference effects of functional groups, site preference and possible structure transition of the MOF. The high water loadings in combination with the decrease of the BET surface areas can only be stated by the fact that the size of the MIL-100 pores is not the essential factor for high water uptakes. MIL-100(Cr)-EG, MIL-100(Cr)-DEG and MIL-100(Cr)-EN even show a slightly favored water uptake in comparison to pure MIL due to the higher slopes of the adsorption isotherms of the grafted materials in a region of  $0.17 < P \cdot P_0^{-1} < 0.30$  compared to non-modified MIL-100(Cr). The demonstrated proof of concept displays the possibility to shift water adsorption isotherms to lower partial pressures by simply substitution of terminal water molecules by hydrophilic grafting reagents at the CUS without linker modification. Ethylenediamine has shown a more stable bond to chromium(III) over glycol ligands. An ad-, desorption cycling stability test of MIL-100(Cr)-EN shows some sort of degradation after 20 cycles with a partial loss of EN. Therefore, the usage of EN-modified MIL-100(Cr) for possible practical applications has to be critically regarded.

## 5.2 MIL@Si(HIPE)

Native, porous Si(HIPE) was synthesized in pure form without visible impurities and a relatively high BET surface area. The granulated, native HIPE displays spherical voids in  $\mu\text{m}$  range and high water loading capacities. Unfortunately, drying in the oven leads to large shrinkage of the wet monolith (Scheme 7). The collapse of the pore structure through shrinking could possibly be avoided by supercritical  $\text{CO}_2$  drying.



**Scheme 7.** Synthetic routes A and B to synthesize MIL-101(Cr)@Si(HIPE).

The direct route A was carried out, whereat various amounts of activated MIL-101(Cr) powders were simply added to the Si(HIPE) at different points of time during the HIPE synthesis. Unfortunately, the MIL powders did not minimize or avoid shrinkage during the drying process, against our expectation. Granulated MIL-101(Cr)@Si(HIPE) composites (Scheme 7), obtained by the direct route A, reflect decreased HIPE voids, compared to pure Si(HIPE). The presence of MIL-101(Cr) crystals could be evidenced by PXRD, IR and SEM analyses.

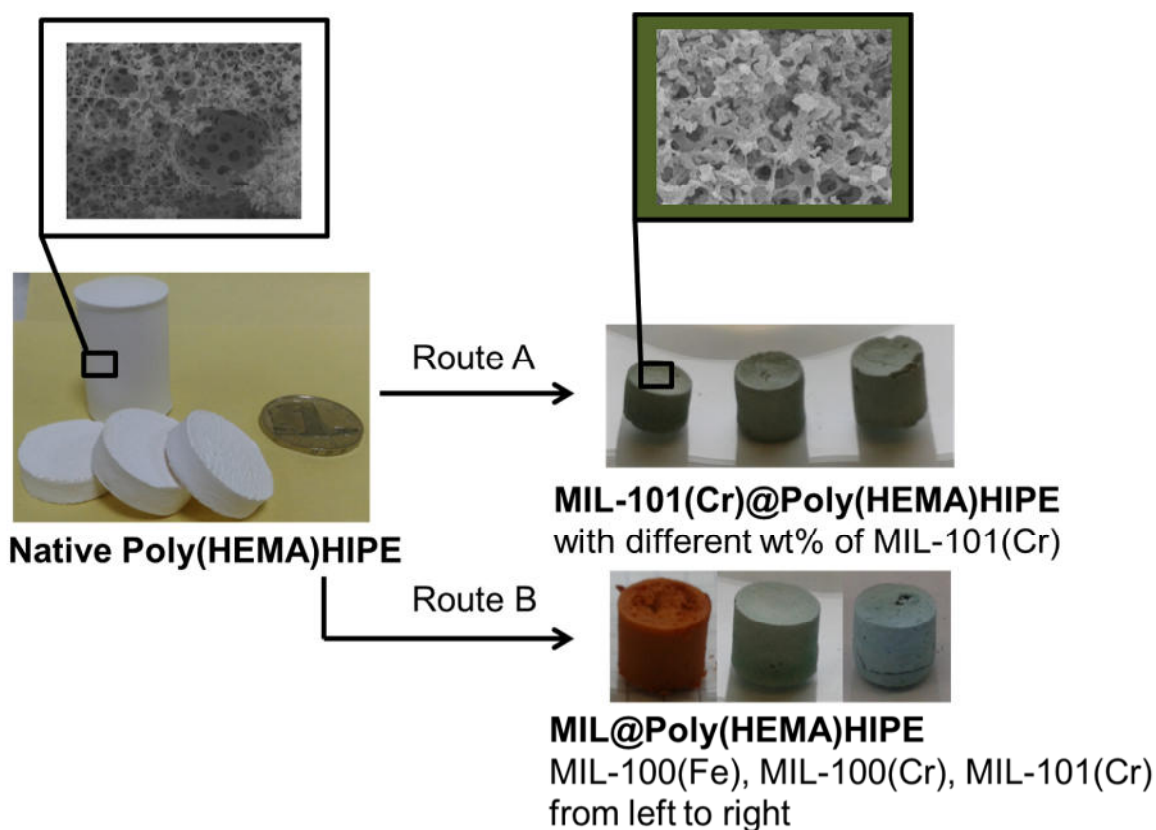
Later addition of MIL-101(Cr) to the HIPE was anticipated to yield composites with increased nitrogen uptakes, higher BET surface areas and more accessible MIL pores for the same MOF loading, according to an advanced state of HIPE polymerization. Experimental nitrogen

sorption measurements have clearly disproved these working hypotheses, which show that the later addition of MOF powder yield less porous composites, although the MIL micro- and mesopores are more pronounced and distinguishable in the pore size distribution curves with later MOF addition.

An alternative *in situ* route was also performed (route B), in which granulated, native Si(HIPE) was firstly soaked with MIL precursors followed by hydrothermal treatment at the appropriate temperature. Granulated MIL-100(Cr)@Si(HIPE)-ht and MIL-101(Cr)@Si(HIPE)-ht composites (Scheme 7) were obtained ('ht' stands for hydrothermal). SEM images of MIL-101(Cr)@Si(HIPE)-ht reveal that the original HIPE morphology is drastically changed from spherical (native Si(HIPE)) to non-spherical voids with reduced pore sizes. Typical MIL-101(Cr) octahedrons are scarcely visible in the scanning electron microscopic images. PXRD and IR analyses suggest the presence of MIL-100/101 crystals in the composites, but nitrogen sorption measurements have shown that both composites are of relative low porosity with mostly macroporous behavior. BET surface areas are even lower compared to the pure HIPE. Nevertheless, water adsorption isotherms of both MIL@Si(HIPE)-ht are shifted to lower partial pressures in comparison to pure HIPE in the regions of  $0.25 < P \cdot P_0^{-1} < 0.37$  (for MIL-100(Cr)@Si(HIPE)-ht) and  $0.38 < P \cdot P_0^{-1} < 0.53$  (for MIL-101(Cr)@Si(HIPE)-ht), due to the presence of some MIL micro- and mesopores, but a complete consideration of the analytical data suggest that both *in situ* embedded MIL crystals are of rather low quality.

### 5.3 MIL@Poly(HEMA)HIPE

Monolithic, native poly(HEMA)HIPE was successfully synthesized by using HEMA as monomer and MBA as cross-linker through an o/w emulsion (Scheme 8). The amount of cross-linker could easily be varied and the final monoliths were obtained in versatile shapes. SEM images reveal typical, spherical voids in the  $\mu\text{m}$  range with connecting windows. Water and methanol vapor sorption analyses showed that native poly(HEMA)HIPE is rather hydrophobic.



**Scheme 8** Synthetic routes A and B to synthesize MIL@poly(HEMA)HIPE (Route A: MIL-101(Cr). Route B: MIL-100(Fe,Cr), MIL-101(Cr)).

MIL-101(Cr)@poly(HEMA)HIPE (Scheme 8), synthesized via the direct route A, were obtained with up to 59 wt% of MIL in monolithic and mechanically stable shape by simply adding various amounts of MIL-101(Cr) powders to the HIPE emulsion before curing. Different strategic, synthetic routes have been carried out in order to maximize the BET surface areas of the final composites and avoid pore blocking effects through HIPE monomers. Pre-polymerization of the HIPE emulsion before addition of the MIL leads to the best results and was shown to be the indispensable factor for highly porous composites, in which the micro- and mesopores of MIL-101(Cr) remain partially unblocked, proven by pore size distribution curves. BET surface areas of MIL-101(Cr)@poly(HEMA)HIPE composites



are lower than the expected from the MOF weight percentage. Nevertheless, these composites show higher methanol and water uptake capacities in comparison to pure poly(HEMA)HIPE. Due to the rather hydrophobic nature of native poly(HEMA)HIPE, corresponding composites from route A show a favored methanol adsorption compared to water.

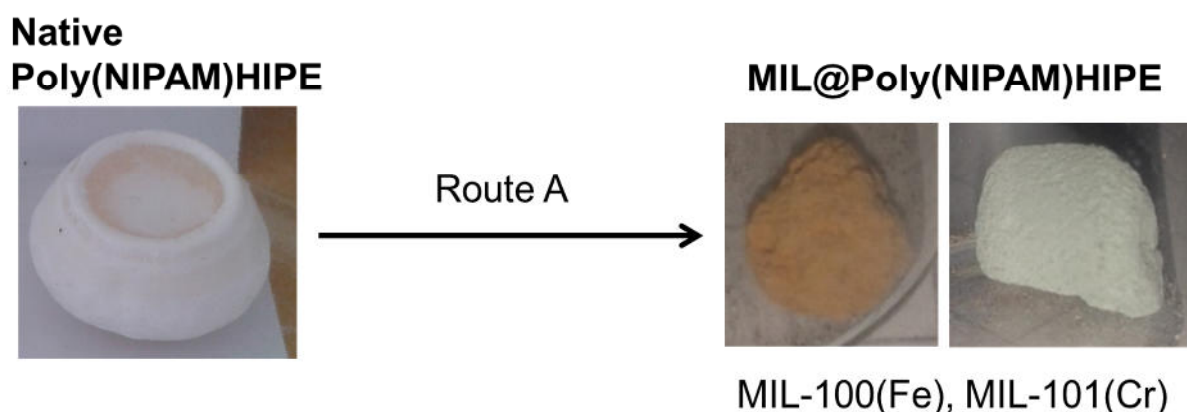
In order to further maximize the BET surface areas of MIL@poly(HEMA)HIPE composite, the *in situ* route B was chosen. Starting materials of MIL-100(Fe,Cr) and MIL-101(Cr) were *in situ* crystallized directly inside the macroporous voids of the native HIPE. Monolithic, colored composites were obtained in all cases with MOF loadings up to 93 wt%, proven by gravimetric and AAS measurements (Scheme 8).

Both *in situ* synthesized MIL-100@poly(HEMA)HIPE composites show similar results compared to pre-polymerized MIL-101(Cr)@poly(HEMA)HIPEs, which were obtained from the direct route A based on PXRD, IR and nitrogen sorption studies. Herein, approximately 40–50 % of the estimated BET surface areas were reached.

Mostly amorphous and low porous MIL-101(Cr) was *in situ* synthesized in the HIPE voids due to broad reflections in the powder pattern and the relatively low BET surface area. MIL-101(Cr)@poly(HEMA)HIPE composites, which were obtained via both methods (route A and B), show huge discrepancies. The *in situ* route B leads to 91 wt% loading of embedded MIL-101, but the incorporated MIL-101 has mostly amorphous character with low porosity. MIL-101(Cr)@poly(HEMA)HIPEs from route A exhibit higher BET surface areas and have therefore the higher performance with MIL loadings up to 59 wt%.

## 5.4 MIL@Poly(NIPAM)HIPE

Pure poly(NIPAM)HIPE was obtained by an o/w emulsion using NIPAM as main monomer and MBA as cross-linker. Different mol% of cross-linkers were introduced into the porous polymers. It has been shown that only the highest amount of MBA with 17 mol% provided monolithic bodies in spite of strong shrinking effects (Scheme 9). Nevertheless, scanning electron microscopic images reveal the typical morphology with voids in  $\mu\text{m}$  range. Water sorption measurements have proven the rather hydrophobic nature of this pure HIPE, similar to poly(HEMA)HIPE.



**Scheme 9.** Synthetic route A to synthesize MIL@poly(NIPAM)HIPE (MIL-100(Fe,Cr), MIL-101(Cr)). Only MIL-100(Fe)@NIPAM and MIL-101(Cr)@NIPAM composites are shown.

Pre-polymerization of the HIPE emulsions before adding the MOF powders has turned out to be an indispensable step in synthesizing highly porous composites via route A, as seen before (section 3.2). Various amounts of MIL-100(Fe,Cr) and MIL-101(Cr) powders were added to the highly pre-polymerized HIPE emulsion. Unfortunately, addition of MOF powders did not avoid or minimize the expected shrinking effects of the composites, also seen for pure poly(NIPAM)HIPE. The direct route A yielded composites with a maximum MOF loading of 92 wt% for MIL-101(Cr)@NIPAM, but deformation and shrinking was apparent in all MIL@NIPAM composites (Scheme 9).

In spite of the presence of MIL crystals, proven by powder patterns, infrared spectra and SEM images, nitrogen sorption studies reveal that pore blocking effects of the MIL pores by HIPE monomers occurred to a large extent, especially for both MIL-100@NIPAM composites.

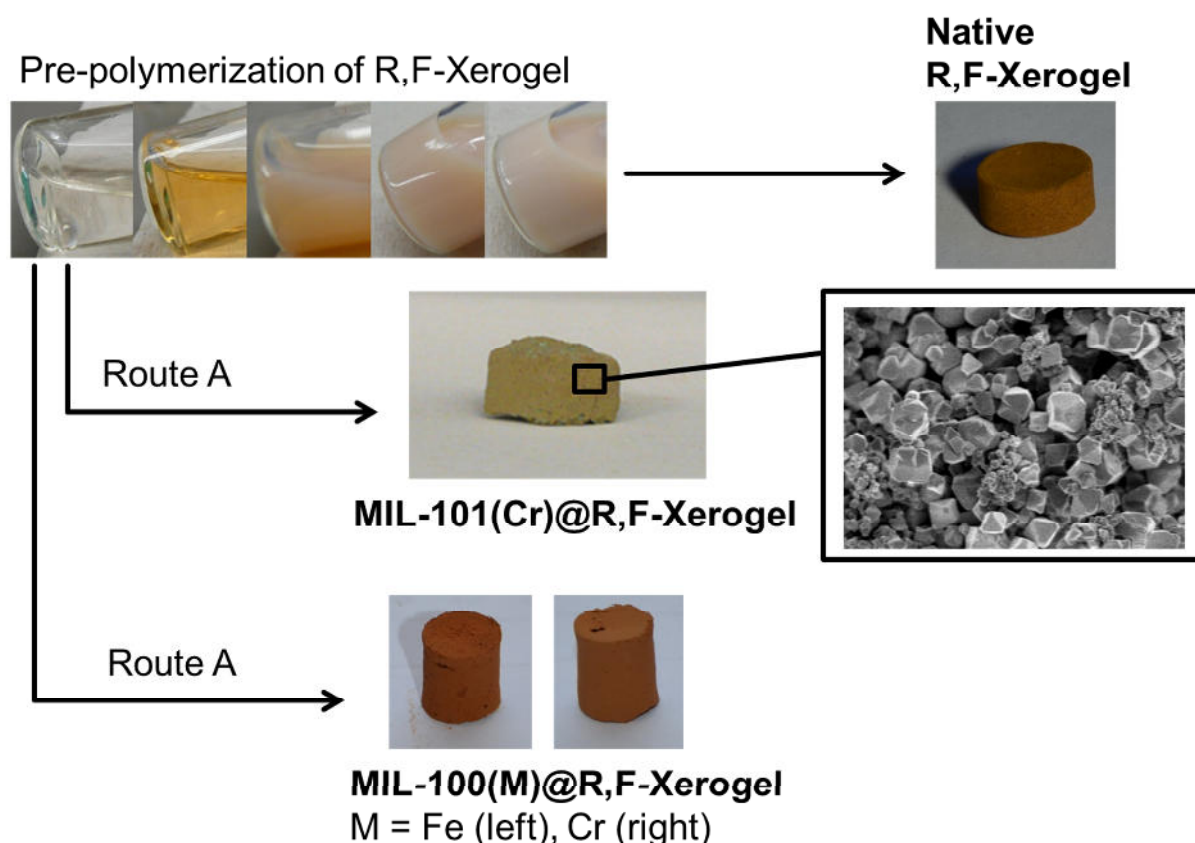
Sorption analyses have shown that the experimental BET surface areas of MIL-100@NIPAM are below the estimated surface areas, based on the MOF weight percentages in the

composites due to large pore blocking effects of the MIL-100 pores and windows by NIPAM and MBA monomers. MIL-100(Fe)@NIPAMs show more accessible and free MIL micropores compared to MIL-100(Cr)@NIPAMs, based on BET and pore size distribution analyses. Due to the large pore blocking effects, water sorption measurements of MIL-100@NIPAMs reveal only slightly enhanced water uptakes over the entire pressure range in comparison to the pure HIPE.

In contrast, experimental surface areas of MIL-101(Cr)@NIPAMs are closer to the estimated BETs, when compared to MIL-100@NIPAM. Pore blocking effects seem to be less pronounced, possibly due to lower capillary condensation forces because of the larger MIL-101 pores and windows. A similar effect was observed for MIL@R,F-xerogel composites (section 3.3). Therefore, water sorption isotherms of MIL-101(Cr)@NIPAM show increased water vapor uptakes compared to MIL-100@NIPAMs.

## 5.5 MIL@R,F-Xerogel

Native, porous R,F-xerogel was obtained by polycondensation of resorcinol and formaldehyde in aqueous solution under basic conditions via a sol-gel approach. The sol was filled into an appropriate mold and thermally polymerized for one week at 333 K. Subcritical drying led to mechanically stable, porous monolithic bodies with a BET surface area of  $100 \text{ m}^2 \cdot \text{g}^{-1}$  and maximum water adsorption uptake of  $0.10 \text{ g} \cdot \text{g}^{-1}$  with a linear rise of the adsorption isotherm (Scheme 10).



**Scheme 10.** Synthetic route A to synthesize MIL@R,F-xerogel (MIL-100(Fe,Cr), MIL-101(Cr)).

Based on the experiences from MIL@HIPE composites, mechanically stable, monolithic MIL@R,F-xerogels were synthesized via the direct route A using powdery MIL-100(Fe,Cr) and MIL-101(Cr) and the xerogel as the binding agent with MOF loadings up to 77 wt% (Scheme 10). Combining MIL powders with non-pre-polymerized xerogel solutions, led to composites with quite low porosity. Furthermore, nitrogen sorption measurements have shown, that the later addition of MOF powders yield composites with enhanced porosities for the same MOF loadings.

Only thermally initiated pre-polymerization of the pure xerogel solution before adding different amounts of MOF powders yield composites with high BET surface areas close to the estimated surface areas based on the MOF weight percentages. Pore blocking effects of the MILs through monomers of the binding agent could be avoided to a large extent by this pre-polymerization method, especially for the MIL-101(Cr) composites. Protection of the larger MIL-101 pores and windows is easier feasible compared to the smaller MIL-100 pores and windows during the composite syntheses.

MIL-101(Cr)@R,F-xerogel, with a MIL loading of 77 wt% features a slightly increased water vapor uptake compared to pure MIL-101(Cr) up to  $P \cdot P_0^{-1} = 0.5$ . Highly porous MIL@R,F-xerogel composites show higher water uptakes compared to the pure xerogel over the entire pressure range and vapor adsorption is close to the expected water vapor amount according to the MIL weight percentage.

## 5.6 Overall summary

Two members of the MIL-family (MIL = Matériaux de l'Institut Lavoisier), MIL-100(Cr) and MIL-101(Cr), were post-synthetically modified by substitution of coordinated water molecules through small glycols and ethylenediamine. In case of glycol-grafting of bulk MIL-101(Cr) to MIL-101(Cr)-glycol products, water sorption measurements have proven that grafting of native MIL-101 lead to an intense loss of total water uptakes in comparison to the pure MIL and water adsorption isotherms were not significantly shifted of to lower partial pressures. In comparison to MIL-101, glycol and amine-grafting of MIL-100(Cr) leads to products with almost the same water loading uptakes as pure MIL-100, although the modified MILs show a decrease of the BET surface areas and pore volumes. MIL-100(Cr)-EG, MIL-100(Cr)-DEG and MIL-100(Cr)-EN (EG = ethylene glycol, DEG = diethylene glycol, EN = ethylenediamine) exhibit slightly favored water vapor uptakes in the partial pressure range of  $0.17 < P \cdot P_0^{-1} < 0.30$  with a higher slope of the water adsorption isotherms compared to non-modified MIL-100.

The relatively high water uptakes together with the loss of the surface areas can only be interpreted by the assumption that the size of the MIL-100(Cr) pores is not the fundamental parameter for high water uptakes. This proof of concept shows the prospects to shift water adsorption isotherms of metal-organic frameworks to lower partial pressures through a simple substitution of coordinated water molecules by hydrophilic glycols and amines.

The synthetic approach to obtain monolithic materials were done by incorporation of powdery MIL particles into porous binding agents such as Si(HIPE), poly(HEMA)HIPE (HEMA = 2-hydroxyethyl methacrylate), poly(NIPAM)HIPE (NIPAM = *N*-Isopropylacrylamide) and a xerogel, based on resorcinol and formaldehyde. Two different synthetic techniques were applied to obtain monolithic composites for the potential application as thermally driven adsorption chiller or heat pump. The first direct route, or 'Route A', describes the direct addition of powdery MOF particles to the porous binding agent before curing into monolithic shape. In the second route, 'Route B', MOF particles were *in situ* crystallized in the pores of the pre-formed, monolithic polymers.

Si(HIPE) as well as poly(NIPAM)HIPE have shown to be unsuitable materials for the syntheses of monolithic MIL composites. Both, native materials are largely deformed by conventional oven drying. The resulting polymers feature big cracks or a granulated shape and the addition of MIL particles does not avoid or minimize the large shrinking effects. Only poly(HEMA)HIPE and R,F-xerogel have proven to be mechanically stable monolithic

products and are suitable for the syntheses of composites with high MOF loadings. The native porous polymers and the MIL composites offer sufficient mechanical stability, good manageability and negligible shrinking effects through conventional drying techniques.

The later addition of MOF particles to the liquid binding agents yield composites with higher inner surfaces and more pronounced and distinguishable MIL pores in the direct route (route A). Pore blocking effects of the MIL pores through monomers of the HIPE or xerogel could be avoided to a large extent in the direct route by this pre-polymerization technique. Pre-polymerization of the binding agents before addition of the powdery MOF powders is an essential requirement for highly porous composites with good vapor loading lifts. Due to the larger windows and pores in MIL-101, MOF pore blocking effects are less pronounced possibly because of the lower capillary condensation forces compared to MIL-100.

Water and methanol sorption experiments have proven that R,F-xerogel is more hydrophilic than poly(HEMA)HIPE. For intended applications as a water-sorption based adsorption chiller or heat pump, the highly porous MIL-101(Cr)@R,F-xerogel composites with high water loading lifts reflect the most suitable candidates.

## 6. Outlook

### 6.1 Water sorption based applications

Section 3.1 has shown that grafting of MIL-100(Cr) with ethylenediamine (EN) results in more stable products compared to grafting with glycols due to the higher stability of the Cr-nitrogen(EN) coordinative bond over Cr-oxygen(glycol) bond. Further post-synthetic modifications with amines such as diethylenetriamine (DETA) or triethylenetetramine (TETA) should be carried out on water-stable MOFs like MIL-100(Cr) or MIL-101(Cr). The enhanced number of hydrophilic N-H groups in DETA and TETA should lead to stronger Cr-amine bonds and possibly have a greater influence on the water adsorption isotherms of these modified MILs probably resulting in an earlier water adsorption. Water ad-/desorption cycling stability tests have to prove whether these compounds are suitable candidates for intended water sorption applications.

The successful embedding of MIL-101(Cr) particles into poly(HEMA)HIPE via the direct route A is discussed in section 3.2. A wider range of MIL@poly(HEMA)HIPE composites could be obtained by the *in situ* route B using MOFs like MIL-100(Fe,Cr) and MIL-101(Cr). For a complete understanding of this 'MIL@HEMA chemistry', MIL-100(Fe,Cr) should also be incorporated into the macroporous Poly(HEMA)HIPE via the direct route. MIL@NIPAM and MIL@R,F-xerogel, synthesized by the direct route A, have shown stronger MIL pore blocking effects for the MIL-100 systems in comparison to MIL-101. It would be interesting to further understand these pronounced pore blocking effects for MOFs with smaller pore sizes through the direct synthesis and characterization of MIL-100(Fe,Cr)@poly(HEMA)HIPE composites.

Water sorption analyses of organic HIPEs, as poly(HEMA)HIPE and poly(NIPAM)HIPE have shown their rather hydrophobic behavior. When it should come to the intended applications for water sorption, it is necessary to increase the hydrophilicity of these HIPE materials. Therefore, different solutions are conceivable: (i) other o/w HIPEs based on acrylic acid,<sup>245</sup> polyacrylamide,<sup>188,246</sup> gelatin or polysaccharide<sup>247</sup> could be synthesized and their water adsorption behavior has to be classified. (ii) The relatively low hydrophilicity could be connected to the low BET surface areas of the macroporous HIPEs, which are typically below  $50 \text{ m}^2 \cdot \text{g}^{-1}$ . Increasing of the poly(HIPE) surface areas can be performed by addition of porogenic solvents into the continuous phase of the HIPE during HIPE formation. Introduction these solvents should lead to the formation of secondary pores in the HIPE matrix, because of phase separation effects during polymerization of the emulsion, which



could yield to HIPE systems with surface areas up to  $720 \text{ m}^2\cdot\text{g}^{-1}$ .<sup>248</sup> Even higher surface areas can be obtained through hyper-crosslinking of the HIPE material, the so-called ‘Davankov approach’, which is done post-synthetically and results in HIPE systems with surface areas up to  $1100 \text{ m}^2\cdot\text{g}^{-1}$ .<sup>182</sup> (iii) Another possibility to increase the hydrophilicity of HIPEs can also be carried out post-synthetically. 4-Vinylbenzyl chloride (VBC) can be introduced as a cross-linker into HIPE systems followed by functionalization of the reactive benzyl chloride groups via nucleophilic substitutions with e.g. different amines. Surface functionalization is well known for hydrophobic styrene based HIPEs, but the concept could also be tried to adapt on more hydrophilic monomers, e.g. 2-hydroxyethyl methacrylate, using VBC as cross-linker.<sup>193,240,249</sup>

Porous polymer beads are used in a wide range of applications, such as stationary phase in separations<sup>250</sup> or supports for catalysts immobilization.<sup>251</sup> Poly(HIPE) beads can be obtained using a sedimentation polymerization technique described by Cooper et al.<sup>252</sup> Herein o/w emulsion droplets are added into a third oily medium forming an o/w/o three phase system. The o/w droplets are instantly solidified by contact with the third oily phase. Through this method MIL@HIPE composites could be obtained in spherical shape.

Section 3.3 presents the sorption properties of MIL@R,F-xerogels, which have been synthesized by the direct route A. Pore blocking effects could be largely avoided by pre-polymerization of the pure xerogel. Nevertheless, further *in situ* MIL@R,F-xerogel syntheses should be performed for an advanced understanding of the ‘MIL@R,F-xerogel chemistry’ hopefully yielding to more porous composites with almost no MIL pore blocking. R,F-xerogel materials have shown good properties concerning mechanical performance and sorption behavior but when it should come to intended water-sorption applications, a high degree of thermal conductivity is a required physical parameter. Unfortunately, xerogels exhibit relatively low heat conductivity, but pyrolysis of native xerogels at high temperature under nitrogen atmosphere leads to hierarchical porous carbon monoliths with enhanced thermal conductivity.<sup>198</sup> These porous carbons could be used for *in situ* syntheses of different metal-organic frameworks. Similar experiments have already been done by Lu et al. in which HKUST-1 was embedded into porous carbons for carbon dioxide storage applications.<sup>213</sup>

## 6.2 Other applications

Poly(HIPE) and xerogel materials have found use in a wide variety of applications. One area in which they have been exploited extensively is as support for solid phase synthesis due to their monolithic shape.<sup>250</sup> Our MIL@HIPE and MIL@xerogel composites could be interesting materials as stationary phase for chromatography in separation experiments. The preparation of these composite columns by in-mold polymerization could yield to effective materials concerning separation of e.g. organic components as shown for other polymeric MOF composites.<sup>253</sup>

A further interesting research topic is the quest of suitable materials for gas storage or gas separation for a wide range of industrial applications. Native HIPE and xerogel compounds have been studied as adsorbents for the storage of gases like carbon dioxide or hydrogen.<sup>182,254,255</sup> The accessible micro- and mesopores of our MIL@HIPE and MIL@xerogel could have a positive influence on the kinetic properties and uptake capacities of industrial relevant gases. The hierarchical porosity of our composites, possessing pores in the micro-meso-macro porous range, should allow for fast gas diffusion rates and high uptakes.

Pure poly(NIPAM)HIPE is well studied as thermoresponsive 'particle pump' through a temperature-controlled release of different kind of particles.<sup>238</sup> At first the porous material is swollen in water, which can contain active particles, below 31 °C. Heating above 31 °C then causes a rapid contraction of the polymer and 'pumping' of the adsorbed particles into the surrounding aqueous phase. The effect of containing a second component like our MIL@NIPAM composites should be investigated in detail. These new composites could have interesting properties as a potential thermoresponsive trigger for the reversible uploading and release of active particles.

## 7. References

---

- (1) D. M. Le Van, Adsorption Processes and Modeling: Present and Future, article in Fundamentals of Adsorption 6 (FOA6), F. Meunier (Eds.), Elsevier, Paris, 1998, p. 19–29.
- (2) F. Rodriguez-Reinoso, B. Mc Enaney, J. Rouquérol, K. Unger (Eds.), Characterization of Porous Solids VI, Proceedings of the 6th Int. Symposium on the Characterization of Porous Solids, (COPS-VI), Alicante, May 2002, Studies in Surface Science and Catalysis, Volume 144, Elsevier, Amsterdam, 2002.
- (3) A. Dabrowski (Eds.), Adsorption and its Application in Industry and Environmental Protection Volume 1 Application in Industry, Elsevier Science & Technology, Amsterdam, 1998, p. 95–116.
- (4) D. M. Ruthven, Principles of Adsorption and Adsorption Processes, Wiley-Interscience, New York, 1984.
- (5) R. T. Yang, Gas Separation by Adsorption Processes, Imperial College Press, London, 1997.
- (6) D. Bathen, M. Breitbach, Adsorptionstechnik, VDI-Buch, Springer, Berlin, 2001.
- (7) F. Notaro, M. W. Ackley, J. Smolarek, *Chem. Eng. (New York)* **1999**, *106*, 104–108.
- (8) S. Sircar, Drying Processes, in ‘F. Rodriguez-Reinoso, B. Mc Enaney, J. Rouquérol, K. Unger (Eds.), Characterization of Porous Solids VI, Proceedings of the 6th Int. Symposium on the Characterization of Porous Solids, (COPS-VI), Alicante, May 2002, Studies in Surface Science and Catalysis, Volume 144, Elsevier, Amsterdam, 2002.’, p. 2533–2567.
- (9) F. Meunier, Adsorption for Environment, in ‘B. Crittenden, W. J. Thomas, Adsorption Technology and Design, Butterworth-Heinemann, Oxford, 1998.’, p. 1–12.
- (10) Ullman’s Encyclopaedia of Industrial Chemistry, 6th Ed., Wiley-VHC, Weinheim, 2002.
- (11) F. Meunier, *Appl. Therm. Eng.* **1998**, *18*, 715–729.
- (12) L. L. Vasiliev, D. A. Mishkinis, A. A. Antukh, L. L. Vasiliev Jr., *Adsorption* **2001**, *7*, 149–161.
- (13) B. Crittenden, W. J. Thomas (Eds.), Adsorption Technology and Design, Butterworth-Heinemann, Oxford, 1998.
- (14) F. Rouquérol, J. Rouquérol, K. S. W. Sing, Adsorption by Powders and Porous Solids: Principles Methodology and Applications, Academic Press, San Diego, 1998.
- (15) S. Lowell, J. E. Shields, M. A. Thomas, M. Thommes, Characterization of Porous Solids and Powders: Surface Area, Pore Size and Density, Springer, Heidelberg, 2006.
- (16) S. J. Gregg, K. S. W. Sing, Adsorption, Surface Area and Porosity, Academic Press, London, 1982.
- (17) W. Steele, The Interaction of Gases with Solid Surfaces, Pergamon, New York, 1974.
- (18) A. W. Adamson, A. P. Cast, Physical Chemistry of Surfaces, 6th Ed., J. Wiley & Sons, New York, 1997.
- (19) R. Kümmel, E. Worch, Adsorption aus wässrigen Lösungen, VEB Verlag für Grundstoffindustrie, Leipzig, 1990.
- (20) S. Brunauer, L. S. Deming, W. Edwards Deming, E. Teller, *J. Am. Chem. Soc.* **1940**, *62*, 1723–1732.

- 
- (21) K. S. W. Sing, D. H. Everett, R. A. W. Haul, L. Moscou, R. A. Pierotti, J. Rouquérol, T. Siemieniowska, *Pure Appl. Chem.* **1985**, *57*, 603–619.
- (22) For more information: <http://www.iupac.org/web/ins/2010-009-1-100>.
- (23) E.-P. Ng, S. Mintova, *Microporous Mesoporous Mater.* **2008**, *114*, 1–26.
- (24) W. Kast, Adsorption aus der Gasphase, VCH Verlagsgesellschaft, Weinheim, 1988.
- (25) M. Huggahalli, J. R. Fair, *Ind. Eng. Chem. Res.* **1996**, *35*, 2071–2074.
- (26) I. Langmuir, *J. Am. Chem. Soc.* **1918**, *40*, 1361–1403.
- (27) S. Brunauer, P. H. Emmett, E. Teller, *J. Am. Chem. Soc.* **1938**, *60*, 309–319.
- (28) M. N. Golubovic, H. D. M. Hettiarachchi, W. M. Worek, *Int. J. Heat Mass Transfer* **2006**, *49*, 2802–2809.
- (29) H. Yang, H. Zhu, M. M. R. M. Hendrix, N. J. H. G. M. Lousberg, G. de With, A. C. C. Esteves, J. H. Xin, *Adv. Mater.* **2013**, *25*, 1150–1154.
- (30) (a) I. Gur, K. Sawyer, R. Prasher, *Science* **2012**, *335*, 1454–1455. (b) H. Demir, M. Mobedi, S. Ülkü, *Renew. Sust. Energ. Rev.* **2008**, *12*, 2381–2403. (c) A. Hepbasli, Y. Kalinci, *Renew. Sust. Energ. Rev.* **2009**, *13*, 1211–1229. (d) S. K. Henninger, F. P. Schmidt, H. M. Henning, *Appl. Therm. Eng.* **2010**, *30*, 1692–1702. (e) S. K. Henninger, F. Jeremias, H. Kummer, C. Janiak, *Eur. J. Inorg. Chem.* **2012**, *16*, 2625–2634.
- (31) R. T. Yang, Adsorbents: Fundamentals and Applications, John Wiley & Sons, Inc., New Jersey, 2003.
- (32) M. Ito, F. Watanabe, M. Hasatani, *Heat Transf. Jpn. Res.* **1996**, *25*, 420–433.
- (33) C. X. Jia, Y. J. Dai, J. Y. Wu, R. Z. Wang, *Int. J. Refrig.* **2007**, *30*, 345–253.
- (34) B. Dawoud, Y. I. Aristov, *Int. J. Heat Mass Transfer* **2003**, *46*, 273–281.
- (35) H. T. Chua, K. C. Ng, A. Chakraborty, N. M. Oo, M. A. Othman, *J. Chem. Eng. Data* **2002**, *47*, 1177–1181.
- (36) E. A. Levitskij, Y. I. Aristov, M. M. Tokarev, V. N. Parmon, *Sol. Energy Mater. Sol. Cells* **1996**, *44*, 219–235.
- (37) L. G. Gordeeva, M. M. Tokarev, V. N. Parmon, Y. I. Aristov, *React. Kinet. Catal. Lett.* **1998**, *65*, 153–159.
- (38) D. Balköse, U. Köktürk, H. Yilmaz, *Appl. Surf. Sci.* **1999**, *147*, 77–84.
- (39) A. V. Rao, N. D. Hedge, H. Hirashima, *J. Colloid Interface Sci.* **2007**, *305*, 124–132.
- (40) S. D. Bhagat, C. S. Oh, Y. H. Kim, Y. S. Ahn, J. G. Yeo, *Microporous Mesoporous Mater.* **2006**, *96*, 237–244.
- (41) C. A. M. Mulder, J. G. van Lierop, *Springer Proc. Phys.* **1986**, *6*, 68–75.
- (42) N. Hüsing, U. Schubert, *Angew. Chemie* **1998**, *110*, 22–47.
- (43) Ž. Knez, Z. Novak, *J. Chem. Eng. Data* **2001**, *46*, 858–860.
- (44) M. R. Miner, B. Hosticka, P. M. Norris, *J. Non-Cryst. Solids* **2004**, *350*, 285–289.
- (45) J. M. Bialon, A. B. Jarzębski, A. I. Lachowski, J. J. Malinowski, Y. I. Aristov, *Chem. Mater.* **1997**, *9*, 2486–2490.
- (46) J. M. Bialon, A. I. Lachowski, A. B. Jarzębski, L. G. Gordeeva, Y. I. Aristov, *J. Colloid Interface Sci.* **1999**, *218*, 500–503.
- (47) Atlas of zeolite framework types: <http://www.iza-structure.org>.

- 
- (48) R. Szostak, Handbook of Molecular Sieves, Van Norstrand Reinhold, New York, 1992.
- (49) H. Stach, J. Mugele, J. Jänchen, E. Weiler, *Adsorption* **2005**, *11*, 393–404.
- (50) A. Jentys, G. Warecka, M. Derewinski, J. A. Lercher, *J. Phys. Chem.* **1989**, *93*, 4837–4843.
- (51) B. Hunger, O. Klepel, C. Kirschhock, M. Heuchel, H. Toufar, H. Fuess, *Langmuir* **1999**, *15*, 5937–5941.
- (52) O. M. Dzhigit, A. V. Kiselev, K. N. Mikos, G. G. Muttik, T. A. Rahmanova, *Trans. Faraday Soc.* **1971**, *67*, 458–467.
- (53) S. Yang, A. Navrotsky, *Microporous Mesoporous Mater.* **2000**, *37*, 175–186.
- (54) J. Jänchen, D. Ackermann, H. Stach, W. Brösicke, *Sol. Energy* **2004**, *76*, 339–344.
- (55) D. H. Olson, W. O. Haag, W. S. Borghard, *Microporous Mesoporous Mater.* **2000**, *35–36*, 435–446.
- (56) S. T. Wilson, B. M. Lok, C. A. Messina, T. R. Cannan, E. M. Flanigen, *J. Am. Chem. Soc.* **1982**, *104*, 1146–1147.
- (57) O. Kitao, K. E. Gubbins, *J. Phys. Chem.* **1996**, *100*, 12424–12430.
- (58) B. L. Newalkar, R. V. Jasra, V. Kamath, S. G. T. Bhat, *Microporous Mesoporous Mater.* **1998**, *20*, 129–137.
- (59) (a) S. Shimooka, K. Oshima, H. Hidaka, T. Takewaki, H. Kakiuchi, A. Kodama, M. Kubota, H. Matsuda, *J. Chem. Eng. Jpn.* **2007**, *40*, 1330–1334. (b) H. Kakiuchi, S. Shimooka, M. Iwade, K. Oshima, M. Yamazaki, S. Terada, H. Watanabe, T. Takewaki, *Kagaku Kogaku Ronbunshu* **2005**, *31*, 361–364. (c) H. van Heyden, S. Mintova, T. Bein, *J. Mater. Chem.* **2006**, *16*, 514–518. (d) A. Ristic, N. Z. Logar, S. K. Henninger, V. Kaucic, *Adv. Funct. Mater.* **2012**, *22*, 1952–1957.
- (60) S. G. Izmailova, E. A. Vasiljeva, I. V. Karetina, N. N. Feoktistova, S. S. Khvoshchev, *J. Colloid Interface Sci.* **1996**, *179*, 374–379.
- (61) A. Dyer, Introduction to Zeolite Molecular Sieves, John Wiley & Sons, Great Britain, 1988.
- (62) G. Liu, P. Tian, J. Li, D. Zhang, F. Zhou, Z. Liu, *Microporous Mesoporous Mater.* **2008**, *111*, 143–149.
- (63) B. M. Lok, C. A. Messina, R. L. Patton, R. T. Gajek, T. R. Cannan, E. M. Flanigen, *J. Am. Chem. Soc.* **1984**, *106*, 6092–6093.
- (64) F. Jeremias, D. Fröhlich, C. Janiak, S. K. Henninger, *New. J. Chem.* **2014**, *38*, 1846–1852.
- (65) A. M. Prakash, S. Unnikrishnan, *J. Chem. Soc. Faraday Trans.* **1994**, *90*, 2291–2296.
- (66) S. Wilson, P. Barger, *Microporous Mesoporous Mater.* **1999**, *29*, 117–126.
- (67) C. T. Kresge, M. E. Leonowicz, W. J. Roth, J. C. Vartuli, J. S. Beck, *Nature* **1992**, *359*, 710–712.
- (68) J. S. Oh, W. G. Shim, J. W. Lee, J. H. Kim, H. Moon, G. Seo, *J. Chem. Eng. Data* **2003**, *48*, 1458–1462.
- (69) A. Y. Khodakov, V. L. Zholobenko, M. I. Clerc, D. Durand, *J. Phys. Chem. B* **2005**, *109*, 22780–22790.
- (70) H.-M. Kao, C.-C. Cheng, C.-C. Ting, L.-Y. Hwang, *J. Mater. Chem.* **2005**, *15*, 2989–2992.
- (71) P. L. Llewellyn, F. Schüth, Y. Grillet, F. Rouquero, J. Rouquero, K. K. Unger, *Langmuir* **1995**, *11*, 574–577.
- (72) Y. Long, T. Xu, Y. Sun, W. Dong, *Langmuir* **1998**, *14*, 6173–6178.

- 
- (73) H. Naono, M. Hakuman, T. Tanaka, N. Tamura, K. Nakai, *J. Colloid Interface Sci.* **2000**, *225*, 411–420.
- (74) C. Nguyen, C. G. Sonwane, S. K. Bhatia, D. D. Do, *Langmuir* **1998**, *14*, 4950–4952.
- (75) X. S. Zhao, F. Audley, G. Q. Lu, *J. Phys. Chem. B* **1998**, *102*, 4143–4146.
- (76) R. Mokaya, *Chem. Commun.* **2001**, 933–934.
- (77) (a) S. Kitagawa, R. Kitaura, S. Noro, *Angew. Chem. Int. Ed.* **2004**, *43*, 2334–2375. (b) S. Kitagawa, R. Kitaura, S. Noro, *Angew. Chem.* **2004**, *116*, 2388–2430.
- (78) (a) S. R. Batten, N. R. Champness, X.-M. Chen, J. Garcia-Martinez, S. Kitagawa, L. Öhrström, M. O’Keeffe, M. P. Suh, J. Reedijk, *CrystEngComm* **2012**, *14*, 3001–3004. (b) S. R. Batten, N. R. Champness, X.-M. Chen, J. Garcia-Martinez, S. Kitagawa, L. Öhrström, M. O’Keeffe, M. P. Suh, J. Reedijk, *Pure Appl. Chem.* **2013**, *85*, 1715–1724.
- (79) (a) S. R. Batten, B. F. Hoskins, R. Robson, *J. Am. Chem. Soc.* **1995**, *117*, 5385–5386. (b) B. F. Abrahams, B. F. Hoskins, D. M. Michail, R. Robson, *Nature* **1994**, *369*, 727–729. (c) B. F. Hoskins, R. Robson, *J. Am. Chem. Soc.* **1990**, *112*, 1546–1554. (d) B. F. Hoskins, R. Robson, *J. Am. Chem. Soc.* **1989**, *111*, 5962–5964.
- (80) (a) S. Decurtins, H. W. Schmalle, P. Schneuwly, H. R. Oswald, *Inorg. Chem.* **1993**, *32*, 1888–1892. (b) G. De Munno, M. Julve, F. Nicolo, F. Lloret, J. Faus, R. Ruiz, E. Sinn, *Angew. Chem. Int. Ed. Engl.* **1993**, *32*, 613–615. (c) P. Brandt, A. K. Brinah, R. D. Fischer, *Angew. Chem. Int. Ed. Engl.* **1988**, *27*, 1521–1523.
- (81) O. M. Yaghi, H. Li, *J. Am. Chem. Soc.* **1995**, *117*, 10401–10402.
- (82) O. M. Yaghi, G. Li, H. Li, *Nature* **1995**, *378*, 703–705.
- (83) H. Furukawa, N. Ko, Y. B. Go, N. Aratani, S. B. Choi, E. Choi, A. Ö. Yazaydin, R. Q. Snurr, M. O’Keeffe, J. Kim, O. M. Yaghi, *Science* **2010**, *329*, 424–428.
- (84) O. K. Farha, A. Ö. Yazaydin, I. Eryazici, C. D. Malliakas, B. G. Hauser, M. G. Kanatzidis, S. T. Nguyen, R. Q. Snurr, J. T. Hupp, *Nat. Chem.* **2010**, *2*, 944–948.
- (85) C. Janiak, J. K. Vieth, *New J. Chem.* **2010**, *34*, 2366–2388.
- (86) K. Seri, W. Mori, *J. Phys. Chem. B* **2002**, *106*, 1380–1385.
- (87) G. Férey, C. Serre, *Chem. Soc. Rev.* **2009**, *38*, 1380–1399.
- (88) S. M. Cohen, *Chem. Rev.* **2012**, *112*, 970–1000.
- (89) N. Stock, S. Biswas, *Chem. Rev.* **2012**, *112*, 933–969.
- (90) J. R. Long, O. M. Yaghi, *Chem. Soc. Rev.* **2009**, *38*, 1213–1214.
- (91) S. Kitagawa, S. Natarajan, *Eur. J. Inorg. Chem.* **2010**, *24*, 3685–3685.
- (92) C. Serre, S. Kitagawa, P. D. C. Dietzel, *Microporous Mesoporous Mater.* **2012**, *157*, 1–2.
- (93) M. Yoon, R. Srirambalaji, K. Kim, *Chem. Rev.* **2012**, *112*, 1196–1231.
- (94) D. Farrusseng, S. Aguado, C. Pinel, *Angew. Chem. Int. Ed.* **2009**, *48*, 7502–7513.
- (95) J. Lee, O. K. Farha, J. Roberts, K. A. Scheidt, S. T. Nguyen, J. T. Hupp, *Chem. Soc. Rev.* **2009**, *38*, 1450–1459.
- (96) A. Herbst, A. Khutia, C. Janiak, *Inorg. Chem.* **2014**, *53*, 7319–7333.
- (97) F. X. Llabrés i Xamena, F. G. Cirujano, A. Corma, *Microporous Mesoporous Mater.* **2012**, *157*, 112–117.
- (98) R. B. Getman, Y.-S. Bae, C. E. Wilmer, R. Q. Snurr, *Chem. Rev.* **2012**, *112*, 703–723.

- 
- (99) Z. Chen, S. Xiang, H. D. Arman, P. Li, S. Tidrow, D. Zhao, B. Chen, *Eur. J. Inorg. Chem.* **2010**, *24*, 3745–3749.
- (100) F. Ma, S. Liu, D. Liang, G. Ren, C. Zhang, F. Wei, Z. Su, *Eur. J. Inorg. Chem.* **2010**, *24*, 3756–3761.
- (101) L. Wu, M. Xue, S.-L. Qiu, G. Chaplais, A. Simon-Masseron, J. Patarin, *Microporous Mesoporous Mater.* **2012**, *157*, 75–81.
- (102) Z. Zhang, Y. Zhao, Q. Gong, Z. Li, J. Li, *Chem. Commun.* **2013**, *49*, 653–661.
- (103) J.-R. Li, Y. Ma, M. C. McCarthy, J. Sculley, J. Yu, H.-K. Jeong, P. B. Balbuena, H.-C. Zhou, *Coord. Chem. Rev.* **2011**, *155*, 1791–1823.
- (104) J.-R. Li, J. Sculley, H.-C. Zhou, *Chem. Rev.* **2012**, *112*, 869–932.
- (105) Z. R. Herm, R. Krishna, J. R. Long, *Microporous Mesoporous Mater.* **2012**, *157*, 94–100.
- (106) M. G. Plaza, A. F. P. Ferreira, J. C. Santos, A. M. Ribeiro, U. Müller, N. Trukhan, J. M. Loureiro, A. E. Rodrigues, *Microporous Mesoporous Mater.* **2012**, *157*, 101–111.
- (107) C. Janiak, *Dalton Trans.* **2003**, *14*, 2781–2804.
- (108) G. Férey, *Chem. Soc. Rev.* **2008**, *37*, 191–214.
- (109) M. Gaab, N. Trukhan, S. Maurer, R. Gummaraju, U. Müller, *Microporous Mesoporous Mater.* **2012**, *157*, 131–136.
- (110) J. L. C. Rowsell, O. M. Yaghi, *J. Am. Chem. Soc.* **2006**, *128*, 1304–1315.
- (111) Z. Wang, S. M. Cohen, *Chem. Soc. Rev.* **2009**, *38*, 1315–1329.
- (112) Y.-H. Kiang, G. B. Gardner, S. Lee, Z. Xu, E. B. Lobkovsky, *J. Am. Chem. Soc.* **1999**, *121*, 8204–8215.
- (113) J. S. Seo, D. Whang, H. Lee, S. I. Jun, J. Oh, Y. J. Jeon, K. Kim, *Nature* **2000**, *404*, 982–986.
- (114) R. K. Deshpande, J. L. Minnaar, S. G. Telfer, *Angew. Chem. Int. Ed.* **2010**, *49*, 4598–4602.
- (115) K. K. Tanabe, Z. Wang, S. M. Cohen, *J. Am. Chem. Soc.* **2008**, *130*, 8508–8517.
- (116) M. J. Ingleson, J. P. Barrio, J. B. Guilhaud, Y. Z. Khimyak, M. J. Rosseinsky, *Chem. Commun.* **2008**, 2680–2682.
- (117) E. Dugan, Z. Wang, M. Okamura, A. Medina, S. M. Cohen, *Chem. Commun.* **2008**, 3366–3368.
- (118) Z. Wang, S. M. Cohen, *Angew. Chem. Int. Ed.* **2008**, *47*, 4699–4702.
- (119) W. Morris, C. J. Doonan, H. Furukawa, R. Banerjee, O. M. Yaghi, *J. Am. Chem. Soc.* **2008**, *130*, 12626–12627.
- (120) Y. Goto, H. Sato, S. Shinkai, K. Sada, *J. Am. Chem. Soc.* **2008**, *130*, 14354–14355.
- (121) M. J. Ingleson, J. P. Barrio, J. Bacsá, C. Dickinson, H. Park, M. J. Rosseinsky, *Chem. Commun.* **2008**, 1287–1289.
- (122) Z. Wang, S. M. Cohen, *J. Am. Chem. Soc.* **2007**, *129*, 12368–12369.
- (123) Z. Wang, S. M. Cohen, 235th American Chemical Society National Meeting, New Orleans, LA, United States, April 6–10, 2008.
- (124) M. Savonnet, E. Kockrick, A. Camarata, D. Bazer-Bachi, N. Bats, V. Lecocq, C. Pinel, D. Farrusseng, *New. J. Chem.* **2011**, *35*, 1892–1897.
- (125) S. S. Y. Chui, S. M. F. Lo, J. P. H. Charmant, A. G. Orpen, I. D. Williams, *Science*, **1999**, *283*, 1148–1150.

- 
- (126) Y. K. Hwang, D.-Y. Hong, J.-S. Chang, S. H. Jung, Y.-K. Seo, J. Kim, A. Vimont, M. Daturi, C. Serre, G. Férey, *Angew. Chem. Int. Ed.* **2008**, *47*, 4144–4148.
- (127) A. Demessence, D. M. D'Alessandro, M. L. Foo, J. R. Long, *J. Am. Chem. Soc.* **2009**, *131*, 8784–8786.
- (128) M. Wickenheisser, F. Jeremias, S. K. Henninger, C. Janiak, *Inorg. Chim. Acta* **2013**, *407*, 145–152.
- (129) C.-D. Wu, A. Hu, L. Zhang, W. Lin, *J. Am. Chem. Soc.* **2005**, *127*, 8940–8941.
- (130) C. Li, J. Zhou, Y. Cao, J. Zhong, Y. Liu, C. Kang, Y. Tan, *Appl. Energ.* **2014**, *117*, 149–156.
- (131) K. Habib, B. B. Saha, A. Chakraborty, S. T. Oh, S. Koyama, *Appl. Therm. Eng.* **2013**, *50*, 1582–1589.
- (132) A. A. Askalany, M. Salem, I. M. Ismael, A. H. H. Ali, M. G. Morsy, B. B. Saha, *Renew. Sust. Energ. Rev.* **2013**, *19*, 565–572.
- (133) C. Janiak, S. K. Henninger, *Chimia* **2013**, *67*, 419–424.
- (134) W. M. Raldow, W. E. Wentworth, *Sol. Energy* **1979**, *23*, 75–79.
- (135) H. Furukawa, F. Gándara, Y.-B. Zhang, J. Jiang, W. L. Queen, M. R. Hudson, O. M. Yaghi, *J. Am. Chem. Soc.* **2014**, *136*, 4369–4381.
- (136) S. K. Henninger, F. Jeremias, H. Kummer, P. Schossig, H.-M. Henning, *Energy Procedia* **2012**, *30*, 279–288.
- (137) S. K. Henninger, G. Munz, K.-F. Ratzsch, P. Schossig, *Adsorption* **2011**, *17*, 833–843.
- (138) Y.-K. Seo, J. W. Yoon, J. S. Lee, Y. K. Hwang, C.-H. Jun, J.-S. Chang, S. Wuttke, P. Bazin, A. Vimont, M. Daturi, S. Bourrelly, P. L. Llewellyn, P. Horcajada, C. Serre, G. Férey, *Adv. Mater.* **2012**, *24*, 806–810.
- (139) J. J. Low, A. I. Benin, P. Jakubczak, J. F. Abrahamian, S. A. Faheem, R. R. Willis, *J. Am. Chem. Soc.* **2009**, *131*, 15834–15842.
- (140) S. K. Henninger, G. Munz, K.-F. Ratzsch, P. Schossig, *Renew. Energy* **2011**, *36*, 3043–3049.
- (141) A. Rezk, R. Al-Dadah, S. Mahmoud, A. Elsayed, *Int. J. Heat Mass Transfer* **2012**, *55*, 7366–7374.
- (142) Y. I. Aristov, *Appl. Therm. Eng.* **2013**, *50*, 1610–1618.
- (143) T. Núñez, W. Mittelbach, H.-M. Henning, *Appl. Therm. Eng.* **2007**, *27*, 2205–2212.
- (144) Y. I. Aristov, G. Restuccia, G. Cacciola, V. N. Parmon, *Appl. Therm. Eng.* **2002**, *22*, 191–204.
- (145) Y. I. Aristov, *J. Chem. Eng. Jpn.* **2007**, *40*, 1242–1251.
- (146) Y. Wang, M. D. LeVan, *J. Chem. Eng. Data* **2009**, *54*, 2839–2844.
- (147) P. M. Schoenecker, C. G. Carson, H. Jasuja, C. J. J. Flemming, K. S. Walton, *Ind. Eng. Chem. Res.* **2012**, *51*, 6513–6519.
- (148) S. K. Henninger, H. A. Habib, C. Janiak, *J. Am. Chem. Soc.* **2009**, *131*, 2776–2777.
- (149) P. Küsgens, M. Rose, I. Senkovska, H. Fröde, A. Henschel, S. Siegle, S. Kaskel, *Microporous Mesoporous Mater.* **2009**, *120*, 325–330.
- (150) G. Férey, C. Mellot-Draznieks, C. Serre, F. Millange, J. Dutour, S. Surblé, I. Margiolaki, *Science* **2005**, *309*, 2040–2042.
- (151) J. Ehrenmann, S. K. Henninger, C. Janiak, *Eur. J. Inorg. Chem.* **2011**, *4*, 471–474.
- (152) S. Bernt, V. Guillermin, C. Serre, N. Stock, *Chem. Commun.* **2011**, *47*, 2838–2840.



- 
- (153) G. Akiyama, R. Matsuda, H. Sato, A. Hori, M. Takata, S. Kitagawa, *Microporous Mesoporous Mater.* **2012**, *157*, 89–93.
- (154) A. Khutia, H. U. Rammelberg, T. Schmidt, S. Henninger, C. Janiak, *Chem. Mater.* **2013**, *25*, 790–798.
- (155) G. Férey, C. Serre, C. Mellot-Draznieks, F. Millange, S. Surble, J. Dutour, I. Margiolaki, *Angew. Chem. Int. Ed.* **2004**, *43*, 6296–6301.
- (156) P. Horcajada, S. Surble, C. Serre, D.-Y. Hong, Y.-K. Seo, J.-S. Chang, J.-M. Greneche, I. Margiolaki, G. Férey, *Chem. Commun.* **2007**, *27*, 2820–2822.
- (157) C. Volkringer, D. Popov, T. Loiseau, G. Férey, M. Burghammer, C. Riekell, M. Haouas, F. Taulelle, *Chem. Mater.* **2009**, *21*, 5695–5697.
- (158) F. Jeremias, A. Khutia, S. K. Henninger, C. Janiak, *J. Mater. Chem.* **2012**, *22*, 10148–10151.
- (159) G. Akiyama, R. Matsuda, S. Kitagawa, *Chem. Lett.* **2010**, *39*, 360–361.
- (160) F. Jeremias, V. Lozan, S. K. Henninger, C. Janiak, *Dalton Trans.* **2013**, *42*, 15967–15973.
- (161) J. H. Cavka, S. Jakobsen, U. Olsbye, N. Guillou, C. Lamberti, S. Bordiga, K. P. Lillerud, *J. Am. Chem. Soc.* **2008**, *130*, 13850–13851.
- (162) M. Kandiah, M. H. Nilsen, S. Usseglio, S. Jakobsen, U. Olsbye, M. Tilset, C. Larabi, E. A. Quadrelli, F. Bonino, K. P. Lillerud, *Chem. Mater.* **2010**, *22*, 6632–6640.
- (163) S.-N. Kim, J. Kim, H.-Y. Kim, H.-Y. Cho, W.-S. Ahn, *Catal. Today* **2013**, *204*, 85–93.
- (164) M. Dan-Hardi, C. Serre, T. Frot, L. Rozes, G. Maurin, C. Sanchez, G. Férey, *J. Am. Chem. Soc.* **2009**, *131*, 10857–10859.
- (165) (a) T. Ahnfeldt, N. Guillou, D. Gunzelmann, I. Margiolaki, T. Loiseau, G. Férey, J. Senker, N. Stock, *Angew. Chem. Int. Ed.* **2009**, *48*, 5163–5166. (b) T. Ahnfeldt, J. Moellmer, V. Guillerme, R. Staudt, C. Serre, N. Stock, *Chem. Eur. J.* **2011**, *17*, 6462–6468. (c) H. Reinsch, M. Krüger, J. Marrot, N. Stock, *Inorg. Chem.* **2013**, *52*, 1854–1859. (d) H. Reinsch, M. A. van der Veen, B. Gil, B. Marszalek, T. Verbiest, D. de Vos, N. Stock, *Chem. Mater.* **2012**, *25*, 17–26. (e) H. Reinsch, M. Feyand, T. Ahnfeldt, N. Stock, *Dalton Trans.* **2012**, *41*, 4164–4171. (f) H. Reinsch, B. Marszalek, J. Wack, J. Senker, B. Gil, N. Stock, *Chem. Commun.* **2012**, *48*, 9486–9488.
- (166) D. Fröhlich, S. K. Henninger, C. Janiak, *Dalton Trans.* **2014**, *43*, 15300–15304.
- (167) M. F. de Lange, C. P. Ottevanger, M. Wiegman, T. J. H. Vlugt, J. Gascon, F. Kapteihn, *CrystEngComm* **2015**, *17*, 281–285.
- (168) B. B. Saha, I. I. El-Sharkawy, T. Miyazaki, S. Koyama, S. K. Henninger, A. Herbst, C. Janiak, *Energy* **2015**, *79*, 363–370
- (169) N. C. Burtch, H. Jasuja, K. S. Walton, *Chem. Rev.* **2014**, *114*, 10575–10612.
- (170) J. Canivet, A. Fateeva, Y. Guo, B. Coasne, D. Farrusseng, *Chem. Soc. Rev.* **2014**, *43*, 5594–5617.
- (171) J. Canivet, J. Bonnefoy, C. Daniel, A. Legrand, B. Coasne, D. Farrusseng, *New. J. Chem.* **2014**, *38*, 3102–3111.
- (172) K. Tan, N. Nijem, Y. Gao, S. Zuluaga, J. Li, T. Thonhauser, Y. J. Chabal, *CrystEngComm* **2015**, *17*, 247–260.
- (173) D. Bradshaw, A. Garai, J. Huo, *Chem. Soc. Rev.* **2012**, *41*, 2344–2381.
- (174) O.-L. Zhu, Q. Xu, *Chem. Soc. Rev.* **2014**, *43*, 5468–5512.

- 
- (175) (a) H. B. Tanh Jeazet, C. Staudt, C. Janiak, *Chem. Commun.* **2012**, *48*, 2140–2142. (b) H. B. Tanh Jeazet, C. Janiak, *Metal-Organic Framework Materials*, Edited by L. R. MacGillivray and C. M. Lukehart, John Wiley & Sons, Ltd, Chichester, 2014, pp 1–15.
- (176) D. Barby, Z. Haq, *Eur. Pat.* **1982**, EP 60138 A1 19820915.
- (177) (a) S. D. Kimmins, N. R. Cameron, *Adv. Funct. Mater.* **2011**, *21*, 211–225. (b) H. Zhang, A. I. Cooper, *Soft Matter* **2005**, *1*, 107–113.
- (178) I. Gurevitch, M. S. Silverstein, *Macromolecules* **2011**, *44*, 3398–3409.
- (179) E. Lovelady, S. D. Kimmins, J. Wu, N. R. Cameron, *Polym. Chem.* **2011**, *2*, 559–562.
- (180) S. Kovačič, P. Krajnc, C. Slugovc, *Chem. Commun.* **2010**, *46*, 7504–7506.
- (181) F. Audouin, M. Birot, É. Pasquinet, H. Deleuze, O. Besnard, D. J. Poullain, *Appl. Polym. Sci.* **2008**, *108*, 2808–2813.
- (182) M. G. Schwab, I. Senkovska, M. Rose, N. Klein, M. Koch, J. Pahnke, G. Jonschker, B. Schmitz, M. Hirscher, S. Kaskel, *Soft Matter* **2009**, *5*, 1055–1059.
- (183) P. Krajnc, N. Leber, D. Stefanec, S. Kontrec, A. J. Podgornik, *Chromatogr. A* **2005**, *1065*, 69–73.
- (184) E. M. Christenson, W. Soofi, J. L. Holm, N. R. Cameron, A. G. Mikos, *Biomacromolecules* **2007**, *8*, 3806–3814.
- (185) S. J. Pierre, J. C. Thies, A. Dureault, N. R. Cameron, J. C. M. van Hest, N. Carette, T. Michon, R. Weberskirch, *Adv. Mater.* **2006**, *18*, 1822–1826.
- (186) C. Zhao, E. Danish, N. R. Cameron, R. Katakay, *J. Mater. Chem.* **2007**, *17*, 2446–2453.
- (187) N. Cohen, M. S. Silverstein, *Polymer* **2011**, *52*, 282–287.
- (188) S. Kovačič, K. Jeřábek, P. Krajnc, *Macromol. Chem. Phys.* **2011**, *212*, 2151–2158.
- (189) (a) J. Y. Lee, B. Tan, A. I. Cooper, *Macromolecules* **2007**, *40*, 1955–1961. (b) C. Palocci, A. Barbetta, A. La Grotta, M. Dentini, *Langmuir* **2007**, *23*, 8243–8251. (c) B. Tan, J. Y. Lee, A. I. Cooper, *Macromolecules* **2007**, *40*, 1945–1954.
- (190) (a) V. O. Ikem, A. Menner, A. Bismarck, *Langmuir* **2010**, *26*, 8836–8841. (b) P. J. Colver, S. A. F. Bon, *Chem. Mater.* **2007**, *19*, 1537–1539.
- (191) D. Wu, F. Xu, B. Sun, R. Fu, H. He, K. Matyjaszewski, *Chem. Rev.* **2012**, *112*, 3959–4015.
- (192) S. Kovačič, D. Štefanec, P. Krajnc, *Macromolecules* **2007**, *40*, 8056–8060.
- (193) I. Pulko, P. Krajnc, *Macromol. Rapid Commun.* **2012**, *33*, 1731–1746.
- (194) D. Štefanec, P. Krajnc, *Polym. Int.* **2007**, *56*, 1313–1319.
- (195) O. Kulygin, M. S. Silverstein, *Soft Matter* **2007**, *3*, 1525–1529.
- (196) X. Lu, M. C. Arduini-Schuster, J. Kuhn, O. Nilsson, J. Fricke, R. W. Pekala, *Science* **1991**, *255*, 971–972.
- (197) L. W. Hrubesh, *J. Non-Cryst. Solids* **1998**, *225*, 335–342.
- (198) (a) S. T. Mayer, R. W. Pekala, J. L. Kaschmitter, *J. Electrochem. Soc.* **1993**, *120*, 446–451. (b) U. Fischer, R. Saliger, V. Bock, R. Petricevic, J. Fricke, *J. Porous Mater.* **1997**, *4*, 281–285. (c) F. Carrasco-Marín, D. Fairén-Jiménez, C. Moreno-Castilla, *Carbon* **2009**, *47*, 463–469.
- (199) R. W. Pekala, *J. Mater. Sci.* **1989**, *24*, 3221–3227.
- (200) (a) S. Mulik, C. Sotiriou-Leventis, M. A. Aegerter, L. Leventis, M. M. Koebel (Eds.), *Aerogels Handbook – Advances in Sol–Gel Derived Materials and Technologies*, Springer, New York,

- 
- Dordrecht, Heidelberg, London, 2011, 215–234. (b) R. B. Durairaj, *Resorcinol: Chemistry, Technology and Applications*, Springer, Berlin, Heidelberg, New York, 2005.
- (201) (a) A. M. Elkhatat, S. A. Al-Muhtaseb, *Adv. Mater.* **2001**, *23*, 2887–2903. (b) S. S. Al-Muhtaseb, J. A. Ritter, *Adv. Mater.* **2003**, *15*, 101–114.
- (202) (a) O. Czakkel, M. Katalin, E. Geissler, L. Krisztina, *Microporous Mesoporous Mater.* **2005**, *86*, 124–133. (b) X. Lu, R. Caps, J. Fricke, C. T. Alviso, R. W. Pekala, *J. Non-Cryst. Solids* **1995**, *188*, 226–234.
- (203) C. Lin, J. A. Ritter, *Carbon* **1997**, *35*, 1271–1278
- (204) J. Laskowski, B. Milow, L. Ratke, *Microporous Mesoporous Mater.* **2014**, *197*, 308–315.
- (205) P. Küsgens, A. Zgaverdea, H. G. Fritz, S. Siegle, S. Kaskel, *J. Am. Ceram. Soc.* **2009**, *93*, 2476–2479.
- (206) M. G. Schwab, I. Senkovska, M. Rose, M. Koch, J. Pähnke, G. Jonschker, S. Kaskel, *Adv. Eng. Mater.* **2008**, *10*, 1151–1155.
- (207) M. Wickenheisser, C. Janiak, *Microporous Mesoporous Mater.* **2015**, *204*, 242–250.
- (208) L. D. O'Neill, H. Zhang, D. Bradshaw, *J. Mater. Chem.* **2010**, *20*, 5720–5726.
- (209) L. Li, J. Yao, P. Xiao, J. Shang, Y. Feng, P. Webley, H. Wang, *Colloid Polym. Sci.* **2013**, *291*, 2711–2717.
- (210) M. L. Pinto, S. Dias, J. Pires, *Appl. Mater. Interfaces* **2013**, *5*, 2360–2360.
- (211) Z. Ulker, I. Erucar, S. Keskin, C. Erkey, *Microporous Mesoporous Mater.* **2013**, *170*, 352–358.
- (212) A. Sachse, R. Ameloot, B. Coq, F. Fajula, B. Coasne, D. De Vos, A. Galarneau, *Chem. Commun.* **2012**, *48*, 4749–4751.
- (213) D. Qian, C. Lei, G.-P. Hao, W.-C. Li, A.-H. Lu, *Appl. Mater. Interfaces* **2012**, *4*, 6125–6132.
- (214) M. Wickenheisser, A. Herbst, R. Tannert, B. Milow, C. Janiak, *submitted*.
- (215) D. Li, Y. Xia, *Adv. Mater.* **2004**, *16*, 1151–1170.
- (216) R. Ostermann, J. Cravillon, C. Weidmann, M. Wiebcke, B. M. Smarsly, *Chem. Commun.* **2011**, *47*, 442–444.
- (217) M. Rose, B. Bohringer, M. Jolly, R. Fischer, S. Kaskel, *Adv. Eng. Mater.* **2011**, *13*, 356–360.
- (218) Q. Wei, S. L. James, *Chem. Commun.* **2005**, *12*, 1555–1556.
- (219) M. R. Lohe, M. Rose, S. Kaskel, *Chem. Commun.* **2009**, 6056–6058.
- (220) A. Vimont, H. Leclerc, F. Maugé, M. Daturi, J.-C. Lavalley, S. Surblé, C. Serre, G. Férey, *J. Phys. Chem. C* **2007**, *111*, 383–388.
- (221) H. Leclerc, A. Vimont, J.-C. Lavalley, M. Daturi, A.D. Wiersum, P.L. Llewellyn, P. Horcajada, G. Férey, C. Serre, *J. Phys. Chem. Chem. Phys.* **2011**, *13*, 11748–11756.
- (222) C. Volkringer, H. Leclerc, J.-C. Lavalley, T. Loiseau, G. Férey, M. Daturi, A. Vimont, *J. Phys. Chem. C* **2012**, *116*, 5710–5719.
- (223) F. Jeremias, S. K. Henninger, C. Janiak, *Chem. Commun.* **2012**, *48*, 9708–9710.
- (224) F. Jeremias, D. Fröhlich, C. Janiak, S. K. Henninger, *RSC Adv.* **2014**, *4*, 24073–24082.
- (225) S. Zhou, A. Bismarck, J. H. G. Steinke, *J. Mater. Chem. B* **2013**, *1*, 4736–4745.
- (226) F. Audouin, A. Heise, *Eur. Polym. J.* **2013**, *49*, 1073–1079.
- (227) I. G. Escalona, C. J. Gommès, N. Job, S. Blacher, C. G. Olivera-Fuentes, J.-P. Pirard, A. Léonard, *Microporous Mesoporous Mater.* **2009**, *117*, 61–66.

- 
- (228) K. Krishnan, R. A. Plane, *Inorg. Chem.* **1966**, *5*, 852–857.
- (229) D. A. Young, T. B. Freedman, E. D. Lipp, L. A. Nafie, *J. Am. Chem. Soc.* **1986**, *108*, 7255–7263.
- (230) F. Carn, A. Colin, M.-F. Achard, H. Deleuze, E. Sellier, M. Birot, R. Backov, *J. Mater. Chem.* **2004**, *14*, 1370–1376.
- (231) (a) S. Ungureanu, G. Sigaud, G. L. Vignoles, C. Lorrette, M. Birot, A. Derré, O. Babot, H. Deleuze, A. Soum, G. Pécastaings, R. Backov, *J. Mater. Chem.* **2011**, *21*, 14732–14740. (b) N. Brun, P. Hesemann, G. Laurent, C. Sanchez, M. Birot, H. Deleuze, R. Backov, *New J. Chem.* **2013**, *37*, 157–168. (c) S. Ungureanu, G. Laurent, H. Deleuze, O. Babot, M. F. Achard, M. I. Popa, C. Sanchez, R. Backov, *Colloids and Surfaces A: Physicochem. Eng. Aspects* **2010**, *360*, 85–93.
- (232) J. Yang, Q. Zhao, J. Li, J. Dong, *Microporous Mesoporous Mater.* **2010**, *130*, 174–179.
- (233) S. Zhang, J. Chen, *Polymer* **2007**, *48*, 3021–3025.
- (234) W. Chen, Z. Zhang, W. Bao, Y. Lai, J. Li, Y. Gan, J. Wang, *Electrochimica Acta* **2014**, *134*, 293–301.
- (235) T. D. Bennett, A. K. Cheetham, *Acc. Chem. Res.* **2014**, *47*, 1555–1562.
- (236) J. S. Lee, S. H. Jung, J. W. Yoon, Y. K. Hwang, J.-S. Chang, *J. Ind. Eng. Chem.* **2009**, *15*, 674–676.
- (237) L. Kurfiřtová, Y.-K. Seo, Y. K. Hwang, J.-S. Chang, J. Čejka, *Catal. Today* **2012**, *179*, 85–90.
- (238) (a) N. C. Grant, A. I. Cooper, H. Zhang, *Appl. Mater. Interfaces* **2010**, *2*, 1400–1406. (b) H. Zhang, A. I. Cooper, *Adv. Mater.* **2007**, *19*, 2439–2444.
- (239) N. Brun, S. Ungureanu, H. Deleuze, R. Backov, *Chem. Soc. Rev.* **2011**, *40*, 771–788.
- (240) N. Cameron, *Polymer* **2005**, *46*, 1439–1449.
- (241) T. Hasegawa, S. Tatsuta, Y. Katsumoto, *Anal. Bioanal. Chem.* **2010**, *398*, 2203–2209.
- (242) (a) L. D. Gelb, K. E. Gubbins, R. Radhakrishnan, M. Sliwinski-Bartowiak, *Rep. Prog. Phys.* **1999**, *62*, 1573–1659. (b) N. A. Sedron, J. P. R. B. Walton, N. Quirke, *Carbon* **1989**, *27*, 853–861. (c) A. Vishnyakov, P. Ravikovitch, A. V. Neimark, *Langmuir* **2000**, *16*, 2311–2320.
- (243) A. Vimont, J.-M. Goupil, J.-C. Lavalley, M. Daturi, S. Surblé, C. Serre, F. Millange, G. Férey, N. Audebrand, *J. Am. Chem. Soc.* **2006**, *128*, 3218–3227.
- (244) J. W. Yoon, Y.-K. Seo, Y. K. Hwang, J.-S. Chang, H. Leclerc, S. Wuttke, P. Bazin, A. Vimont, M. Daturi, E. Bloch, P. L. Llewellyn, S. Serre, P. Horcajada, J.-M. Grenèche, A. E. Rodrigues, G. Férey, *Angew. Chem. Int. Ed.* **2010**, *49*, 5949–5952.
- (245) P. Krajnc, D. Štefanec, I. Pulko, *Macromol. Rapid Commun.* **2005**, *26*, 1289–1293
- (246) R. Butler, C. M. Davies, A. I. Cooper, *Adv. Mater.* **2001**, *13*, 1459–1463.
- (247) (a) A. Barbetta, M. Dentini, E. M. Zannoni, M. E. De Stefano, *Langmuir* **2005**, *21*, 12333–12342. (b) A. Barbetta, M. Dentini, M. S. De Vecchis, P. Filippini, G. Formisano, S. Caiazza, *Adv. Funct. Mater.* **2005**, *15*, 118–124. (c) A. Barbetta, M. Massimi, L. C. Devirgiliis, M. Dentini, *Biomacromolecules* **2006**, *7*, 3059–3068.
- (248) K. Jerábek, I. Pulko, K. Soukupova, D. Štefanec, P. Krajnc, *Macromolecules* **2008**, *41*, 3543–3646.
- (249) I. Pulko, P. Krajnc, *Chem. Commun.* **2008**, *37*, 4481–4483.

- 
- (250) (a) M. Slater, M. Snauko, F. Svec, J. M. Frechet, *J. Anal. Chem.* **2006**, *78*, 4969–4975. (b) N. Fontanals, R. M. Marce, P. A. G. Cormack, D. C. Sherrington, F. Borrull, *J. Chromatogr. A* **2008**, *1191*, 118–124.
- (251) R. Haag, S. Roller, *Top. Curr. Chem.* **2004**, *242*, 1–42.
- (252) H. Zhang, A. I. Cooper, *Chem. Mater.* **2002**, *14*, 4017–4020.
- (253) (a) H.-Y. Huang, C.-L. Lin, C.-Y. Wu, Y.-J. Cheng, C.-H. Lin, *Anal. Chim. Acta* **2013**, *779*, 96–103. (b) S. Aguado, J. Canivet, D. Farrusseng, *J. Mater. Chem.* **2011**, *21*, 7582–7164. (c) C.-L. Lin, S. Lirio, Y.-T. Chen, C.-H. Lin, H.-Y. Huang, *Chem. Eur. J.* **2014**, *20*, 3317–3321. (d) L.-M. Li, F. Yang, H.-F. Wang, X.-P. Yan, *J. Chromatogr. A* **2013**, *1316*, 97–103. (e) S. Yang, F. Ye, Q. Lv, C. Zhang, S. Shen, S. Zhao, *J. Chromatogr. A* **2014**, *1360*, 143–149. (f) Y.-Y. Fu, C.-X. Yang X.-P. Yan, *Chem. Commun.* **2013**, *49*, 7162–7164.
- (254) (a) F. Su, C. L. Bray, B. Tan, A. I. Cooper, *Adv. Mater.* **2008**, *20*, 2663–2666. (b) H. He, W. Li, M. Zhong, D. Konkolewicz, D. Wu, K. Yaccato, T. Rappold, G. Sugar, N. E. David, K. Matyjaszewski, *Energy Environ. Sci.* **2013**, *6*, 488–493. (c) P. Muchuan, C. Saiwan, D. deMontigny, P. Tontiwachwuthikul, *Energy Procedia* **2013**, *37*, 151–158. (d) H. He, W. Li, M. Lamson, M. Zhong, D. Konkolewicz, C. M. Hui, K. Yaccato, T. Rappold, G. Sugar, N. E. David, K. Damodaran, S. Natesakhawat, H. Nulwala, K. Matyjaszewski, *Polymer* **2014**, *55*, 385–394.
- (255) (a) K. Wörmeyer, I. Smirnova, *Chem. Eng. J.* **2013**, *225*, 350–357. (b) N. N. Linneen, R. Pfeffer, Y. S. Lin, *Chem. Eng. J.* **2014**, *254*, 190–197. (c) S. Cui, W. Cheng, X. Shen, M. Fan, A. Russell, Z. Wuab, X. Yiab, *Energy Environ. Sci.* **2011**, *4*, 2070–2074.